NONLINEAR SEISMIC ANALYSIS OF QUASI-ISOLATION SYSTEMS FOR EARTHQUAKE PROTECTION OF BRIDGES

BY

EVGUENI T. FILIPOV

THESIS

Submitted in partial fulfillment of the requirements
for the degree of Master of Science in Civil Engineering
in the Graduate College of the
University of Illinois at Urbana-Champaign, 2012

Urbana, Illinois

Advisers:

Assistant Professor Larry A. Fahnestock, Co-Director of Research
Associate Professor James M. LaFave, Co-Director of Research
Professor Jerome F. Hajjar – Northeastern University
Professor Emeritus Douglas A. Foutch

ABSTRACT

Quasi-isolation is a modern bridge seismic design philosophy where nonlinearity is permitted to occur in specific bearing components such that forces transferred into the substructure are reduced and isolation is achieved by sliding of the bearings. The system is a pragmatic approach for providing earthquake resilient bridges in locations such as the eastern and central United States, as well as in many locations around the world where there is significant earthquake risk at long recurrence periods. Such a seismic risk does not typically justify the design of a rigorous classical isolation system, but instead, a low-complexity, low-cost quasi-isolation approach could provide significant mitigation of earthquake effects.

The proposed system employs a set of fixed bearings at one intermediate substructure, and all other substructures are instrumented with isolation bearings that permit thermal expansion such as elastomeric bearings with an elastomer-concrete sliding interface or elastomeric bearings with a PTFE (Teflon) to stainless steel sliding interface. L-shaped steel side retainers are placed in the transverse direction of the elastomeric bearings, and along with the low-profile fixed bearings, these components prevent bridge movement during service loading, but break-off and permit sliding at high earthquake loads.

This thesis outlines a base bridge prototype, with the anticipated nonlinear behaviors in the structural components defined in a finite element model of the global structure. New nonlinear elements have been formulated to capture the bi-directional stick-slip behaviors in the bridge bearings and the bilinear (and eventual fracture) behavior of steel retainers and fixed bearings. Longitudinal and transverse static pushover analyses are performed to demonstrate local limit states and progression of damage in the bridge structure. A large scale parametric study carried out to investigate the quasi isolated system performance on different superstructure types, substructure types, substructure heights, foundations and isolation bearing types. Different suites of ground motions are scaled and incremental dynamic analyses (IDA) are carried out for each parametric variation such that the sequence of damage and global seismic performance can be evaluated. Results indicate that the bearing systems with the flat PTFE slider, would likely result in critical damage from the unseating of bearings at moderate and high seismic events in the New Madrid Seismic Zone (NMSZ). The sequence of damage for many bridge cases indicates yielding of piers at low-earthquake hazards which justifies further

calibration of the quasi-isolation bearing systems. Finally the, type of ground motion, foundation stiffness, pier height and bearing type were noted to have significant influence on the global bridge response.

ACKNOWLEDGEMENTS

I would first like to express my profound gratitude to my advisors Dr. Jerome Hajjar, Dr. Larry Fahnestock , Dr. James LaFave and Dr. Douglas Foutch. I am thankful for their guidance, support and encouragement through the past three years. I have been inspired by their commitment to this project and their dedication to the profession of structural engineering. I have thoroughly enjoyed working with them and feel that I have profited greatly.

I would like to give special thanks to my parents and sister who have taught me the value of education and hard work, but have also reminded me to relax and enjoy life. I am greatly indebted to my friends and colleagues Mark Denavit, Dan Borello, Jeff Meissner and many others who have helped me with thousands of issues and questions. I am also grateful to the members of my project team, Joshua Steelman, Carlos Meléndez Gimeno, and Jessica Revell, you have all given me great help and input on this research.

I would like to thank the Illinois Department of Transportation (IDOT) Technical Review Panel for their valuable input through the course of this project. In particular Dan Tobias, Ralph Anderson, Mark Shaffer and Chad Hodel, I thank you greatly for your insight on the practicality of this research.

I am grateful to Professor James Long for performing the foundation analysis for the project, as well as the software vendors ENSOFT, INC. who provided the geotechnical analysis software for that part of the project. I would like to acknowledge the staff and resources at the Texas Advanced Computing Center (TACC) at The University of Texas at Austin that helped in the large scale computational needs for the parametric study.

Funding for this research was provided partly by IDOT, and the National Science Foundation Graduate Research Fellowship Program. The material presented is based on result of ICT R27-70, *Calibration and Refinement of Illinois' Earthquake Resisting System Bridge Design Methodology*. ICT R27-70 was conducted in cooperation with the Illinois Center for Transportation (ICT); IDOT; Division of Highways; and the U.S. Department of Transportation, Federal Highway Administration (FHWA). Any opinions, findings and conclusions expressed herein are those of the author, and do not necessarily reflect the views or policies of the sponsors and collaborating agencies.

TABLE OF CONTENTS

CHAPTER 1

INTRODUCTION

1.1 Background

Recent editions of bridge design codes, such as the Guide Specifications for LRFD Seismic Bridge Design (AASHTO 2009), have provided modernized provisions that alter the quantification of earthquake hazard. These design provisions have incorporated a design earthquake of 1000 year recurrence period (5% in 50 years), in comparison to the 500 year recurrence period (10% in 50 years) earthquake that was used in bridge design historically (FEMA 1988). Philosophies, innovation and seismic design techniques have been influenced primarily by the western United States, where there is a widely recognized risk of earthquakes. Significant earthquakes are known to have occurred in the eastern and mid-western United States, so it has become accepted that there is a seismic risk characterized by high-magnitude, low recurrence earthquakes. Although this risk is now well accepted, many agencies east of the Rocky Mountains have been reluctant to adopt the same procedures that are used in high seismic regions, as they tend to be more expensive and complex for design and construction. Alternative design procedures suited to the high-magnitude, low recurrence hazard, can allow engineers to provide inexpensive systems that although not perfect for seismic loading will prevent collapse and limit damage during an earthquake.

The modernization efforts in Illinois have brought forward the idea of quasi-isolation for highway bridges where the structure is intended to respond predictably, reliably, and elastically under service loading (including small seismic events). For larger seismic events on the other hand, certain bridge bearing components are intended to “fuse” and experience nonlinear behaviors that can allow for passive quasi-isolation of the bridge superstructure. The quasi isolation system is intended to be a low-complexity, low-cost approach that would not follow the rigorous design necessary for a classical isolation systems (Buckle 1990; Naeim and Kelly 1999), yet would provide significant mitigation of earthquake effects.

1.2 Calibration and refinement of the ERS strategy

The concept for this project stems from the Earthquake Resisting System (ERS) methodology currently in use by the Illinois Department of Transportation (IDOT). The project is a joint effort of the Illinois Center for Transportation (ICT) and IDOT, and aims at investigating systems with prescribed sequential fusing, which occurs when the ultimate capacities of specific components are exceeded. More critical elements are designed based on the ultimate capacities of the fusing components so that the critical elements remain in service after an earthquake and prevent structural collapse of the bridge (Tobias et al. 2008). The concept of this proposed system is an extension of a common bridge design methodology employed in high seismic regions of the United States, where the substructure and superstructure should remain elastic while a fusing mechanism is implemented at the interface between the two (AASHTO 2010; AASHTO 2009). The IDOT ERS allows for three distinct levels of fusing and redundancy, namely: (Level 1): permitting damage and failure of the bearing components to allow quasi-isolation; (Level 2): providing sufficient seat widths to permit the required sliding; (Level 3): permitting damage to the substructure elements so long as there is no span loss.

To evaluate the performance of the quasi-isolated system, and to develop methods for improved calibration, a research project is underway at the University of Illinois with an oversight panel comprised of engineers from IDOT and from the Federal Highway Administration. The three year project is comprised of three overlapping and interconnected stages of research.

Stage 1: *Refinement and calibration of the fuse capacities and seismic redundancy that exists between superstructure and substructure.*

This stage includes rigorous experimental testing carried out in the Newmark Civil Engineering Laboratory (NCEL) at the University of Illinois (Filipov et al. 2010). The experiments are aimed at investigating the nonlinear behavior of bridge bearings and auxiliary components that would create a quasi-isolated system. Experimental results documented in part by (Steelman et al. 2011) are followed by a comprehensive set of component analyses using Abaqus (Abaqus FEA 2010) and the findings will be used to finalize phenomenological models for simulating the bearings and ancillary components.

Stage 2: *Computational Simulation of Response of Bridge Systems*

This thesis focuses on the second phase of the project, which is the computational study used to characterize global bridge behavior of the quasi-isolated system. An initial part of this stage is to understand the bearing and component behaviors, and to incorporate these as part of a finite element analysis framework. Global bridge models are created that capture nonlinear behaviors in various elements and the system behavior is investigated using different analysis types.

Stage 3: *Refinement of Strength Reduction Factors φ and R-factors*

The final stage of the project will include processing of the system analyses results from Stage 2 to find improved design procedures for the current system and to find appropriate seismic strength reduction factors for common bridge systems. Furthermore, this stage will investigate adequate, yet simplified nonlinear analysis methods and design procedures to be used by consultants for future bridge designs of typical Illinois bridges.

1.3 The quasi-isolated bridge system

There are an increasing number of bridge systems in Illinois that have the potential to reach a quasi-isolated seismic response although they have not been specifically designed to do so. Elastomeric expansion bearings are becoming the preferred type of thermal expansion bearings, since they are easier to inspect and maintain than regular steel rocker bearings that have been used historically. Figure 1.1 shows plan and elevation views of a typical bridge in Illinois where elastomeric bearings are used at the abutments and the first intermediate substruture, and a set of low-profile steel bearings are used at the second intermediate substructure.

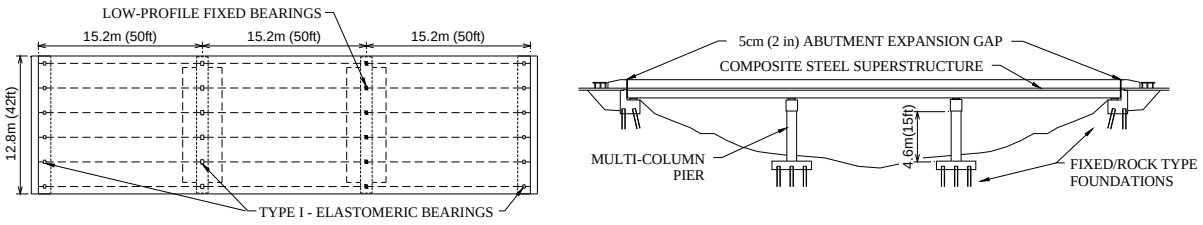

(a) Plan (b) Elevation

Figure 1.1 Modern bridge system with a potential for a quasi-isolated response

Global bridge movements from serviceability loads are resisted by the low-profile bearings, attached to the substructure with anchor bolts, as well as L – shaped steel retainers that restrain transverse movement of the elastomeric bearings. Within typical bridge design in Illinois two common types of elastomeric bearings are often implemented: (i) IDOT Type I bearings, fabricated using an elastomer reinforced with steel shims and placed directly on the concrete substructure (vulcanized to only a top steel plate); and (ii) IDOT Type II bearings, which consist of a bottom steel plate connected to the substructure and vulcanized to a steel-reinforced elastomeric bearing, a middle plate vulcanized to the elastomer and coated on the top side with polytetrafluoroethylene (PTFE), and a top plate with a stainless steel mating surface carrying the girder load directly onto the PTFE surface. Figure 1.2 shows details of the low profile steel bearings and the elastomeric bearings with side retainers.

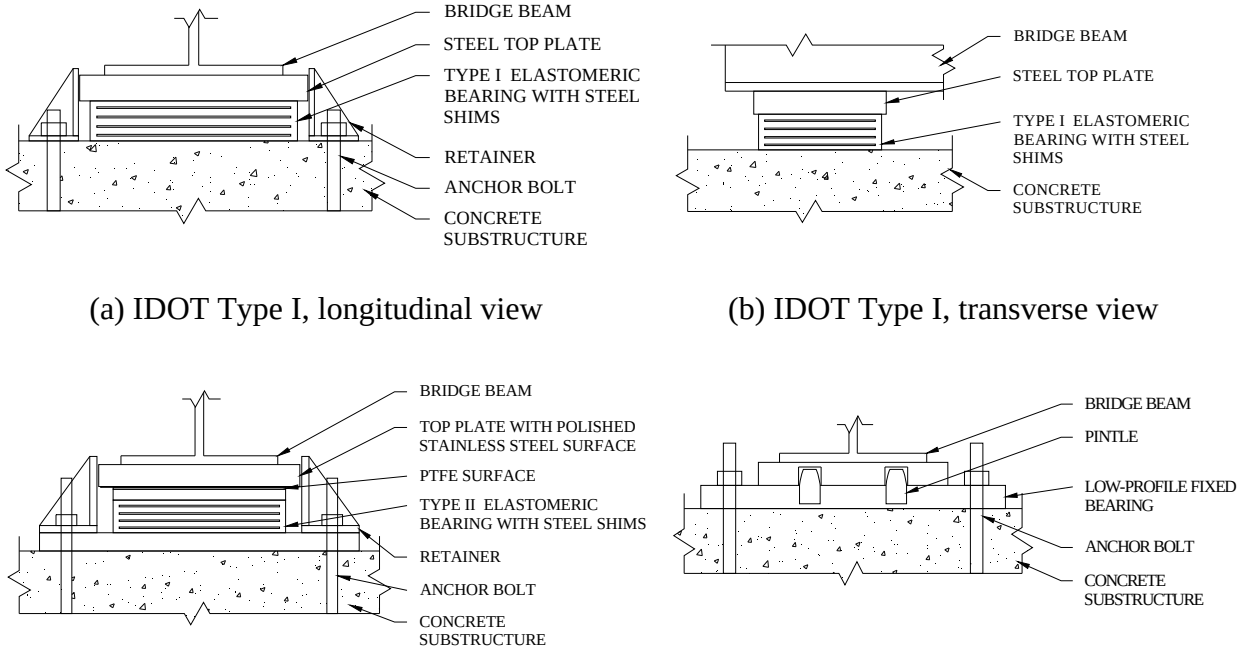

(a) IDOT Type I, longitudinal view (b) IDOT Type I, transverse view

(c) IDOT Type II, longitudinal view (d) Low-profile fixed, longitudinal view

Figure 1.2 Bridge bearing types under consideration for quasi-isolated systems

During a moderate to large earthquake, the low-profile bearings as well as the fixed bearings are intended to fail thereby allowing all bearings to slide. This response would limit the forces that are transferred into the substructure, and would potentially result in period elongation

that would further reduce the seismic response of the structure. Having large enough seat widths at the abutments and piers, the bearings would ideally slide freely causing no damage to the substructure and superstructure components. Having followed a successful and limited sequence of damage, the bridge would remain serviceable even after a large seismic event, allowing for critical post-earthquake emergency response to occur.

1.4 Motivation and objectives

The purpose of the research outlined in this thesis is to better understand the performance of different bridge structures that implement bearing systems with the potential for a quasi-isolated response. These systems, while providing adequate seismic performance would not require complex design procedures and would be more cost effective than classical isolation systems that are used in high seismic risk regions. Numerical models have been developed to capture the nonlinearities for bearings and other bridge components, and have been used to study the system behavior. The analyses have been used to determine the sequence of damage, and general global performance of various bridge systems subject to increasing earthquake hazard typical for the New Madrid Seismic Zone (NMSZ). The results from this study are intended to inform the future calibration of seismic design procedures for bridges in Illinois.

1.5 Organization of this thesis

- *Chapter 1 - Introduction*

  This chapter provides a summary of the research project and motivation for the study of the quasi-isolated bridge system.

- *Chapter 2 – Base bridge model for nonlinear analyses*

  A numerical bridge model is built using OpenSees (McKenna, Mazzoni, and Fenves 2006), that can capture a variety of nonlinear behaviors expected to occur during a seismic event.

- *Chapter 3 – Computational modeling of nonlinear bearing components*

  The formulation of new element models that can capture nonlinear bearing behaviors is shown and validation and calibration for each model is provided.

- *Chapter 4 – Static pushover analyses of prototype bridge system*

  The prototype bridge is subjected to lateral pushover analyses to investigate local nonlinear behaviors in the system.

- *Chapter 5 – Overview of parametric study*

  This chapter presents the bridge variations used for a parametric study, and presents ground motions with appropriate scaling procedures to simulate seismic hazard for the NMSZ.

- *Chapter 6 – Dynamic analyses of quasi-isolated systems*

  Sample dynamic analyses of a single bridge system are presented, and procedures for incremental hazard analysis and sequence of damage identification are shown.

- *Chapter 7 – Results of parametric study*

  This chapter summarizes the results and findings of the parametric study.

- *Chapter 8 – Conclusions*

  Final conclusions and observations are presented and future paths of research are identified.

CHAPTER 2

BASE BRIDGE MODEL FOR NONLINEAR ANALYSES

The global system models were analyzed using the open source, nonlinear seismic analysis program Open System for Earthquake Engineering Simulation (OpenSees 2006). One base prototype bridge model was developed with the capability to capture a variety of nonlinear behaviors that may be encountered in the event of an earthquake. The model was further modified and expanded as part of the later parametric study to simulate different element capacities and to capture different nonlinear behaviors. This chapter presents and explains the assumptions and measures taken to create valid global models for the various bridges considered herein. Table 2.1 shows the variety of parametric variations that will be considered in Chapter 5.

Table 2.1 Variations to be considered in large scale parametric study in Chapter 5

		Bridge Type 1 Steel - Short				**Bridge Type 2 Steel - Long**				**Bridge Type 3 Concrete - Short**				Variations
Parameter	**Alternatives**	1	2	3	4	5	6	7	8	9	10	11	12	
Span Length & Bridge Type (ft)	50' - 50' - 50'	*	*	*	*									3
	60' - 60' - 60'									*	*	*	*	
	80' - 120' - 80'					*	*	*	*					
Intermediate Sub-Structure	Continuous Wall	*	*			*	*			*	*			2
	Multi Column Pier			*	*			*	*			*	*	
Intermediate Sub-Structure Height	Short - 15'	*		*		*		*		*		*		2
	Tall - 40'		*		*		*		*		*		*	
Movement Bearings	Type I Elastomeric	All (12) of the above bridges are modeled with Elastomeric Type I and Type II Bearings												2
	Type II Elastomeric													
Foundations	Fixed Foundation	All (24) of the above bridges are modeled with Fixed and Flexible Foundations												2
	Flexible Foundation													

The research focused on continuous bridge structures with steel and concrete superstructures and simply supported abutment conditions. Substructures considered include

multi-column and wall piers of different heights. The parametric study further considers both the IDOT Type I and Type II bearings which differ in coefficient of friction and overall global response. Two cases of soil stiffness are considered, but only for pile driven foundation structures. Integral abutment bridges, bridges with very flexible foundation types (single row piles or spread footing foundations) and bridges with skew are not considered. Although the quasi isolation system may be applicable to those bridge configurations, there would likely be many other considerations which should be taken as part of a seismic analysis.

In the past years many researchers have modeled typical highway bridges which are in ways similar to what is considered in this project(Wang, Chung, and Liao 1998; Choi, DesRoches, and Nielson 2004; Bignell and LaFave 2010; Aviram, Mackie, and Stojadinovic 2008). Some similar approaches have been taken into this prototype model and alternative methods have been used as needed. An important goal of this bridge model is that all important aspects of behavior are captured, while the model remains computationally efficient. For the global parametric study each bridge model would be run hundreds of times for different intensities of various ground motions.

2.1 Basic bridge prototype

The base prototype bridge (shown in Figure 1.1) is a three-span continuous steel I-girder composite stringer superstructure on multi-column (4) pier substructures (all proportioned in accordance with the IDOT bridge manual (IDOT 2009)). The bridge deck allows for two lanes of traffic, and it is constructed with six girders that act compositely with a 20.3 cm (8 in.) thick concrete deck. All deck elements are calibrated and modeled with appropriate elastic stiffness. The prototype bridge has multi-column piers that are 4.5 m (15 ft) tall and are modeled with beam-column elements with hinges and fiber sections that capture material nonlinearities in the concrete and reinforcing steel. The bearings elements are modeled explicitly for each girder at each substructure to consider the important nonlinear effects. The prototype system is modeled with a fixed base, representing a stiff rocky substrate and steadfast foundation elements, but the model is also capable of capturing nonlinear behavior for more flexible foundation boundary condition scenarios. The nonlinear behavior of the abutment backwalls is modeled with a 5cm (2in.) gap from the bridge deck allowing for a thermal expansion cavity at the abutments, and a hyperbolic material is used to capture the backfill behavior. For the typical three-span bridge

configuration used in this parametric study, low-profile fixed bearings are installed at the second intermediate pier (Pier 2), while Type I or Type II elastomeric expansion bearings are used at the other pier and abutment locations. The prototype bridge uses Type I isolation bearings where sliding occurs at the elastomer to concrete interface. Figure 2.1 shows the finite element mesh for the prototype bridge, when the superstructure is loaded to the left in the longitudinal direction (the right pier experiences a larger deflection than the left, since it is equipped with fixed bearings).

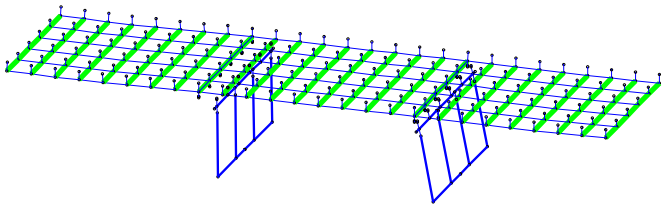

Figure 2.1. Mesh of base bridge model created using OpenSees

2.2 Overview of the modeling of bearing elements

The bearing elements presented in Figure 1.2 are the primary connection between the superstructure and substructure, and are considered to be of primary importance to the global behavior of the bridge structure. To accurately capture three-dimensional bridge behavior in a numerical simulation, the bearing element models must be capable of properly representing movement in any arbitrary direction in plan. As a result, a bearing model that is defined by uncoupled behavior in two orthogonal directions would not be fully suitable, and would likely result in underestimating system displacements and overestimating forces. The importance of bi-directional bearing implementation has been shown in previous research (Mosqueda, Whittaker, and Fenves 2004), and is partially portrayed through the pushover analyses shown in Chapter 4.

The typical bearings for quasi-isolated systems were investigated using experimental tests to better quantify the various nonlinear behaviors (Filipov et al. 2010; Steelman et al. 2011). The elastomeric bearings exhibited typical friction sliding behaviors for both the elastomer to concrete and the PTFE to stainless steel sliding interfaces. The steel retainers showed elasto-plastic yield characteristics followed by fracture, and the low-profile fixed bearings exhibit somewhat similar behaviors as observed in prior research. To model these nonlinear behaviors new elements were formulated to effectively simulate the three-dimensional bearing behaviors.

Further discussion on the experimental testing, results, model formulation, validation and calibration are presented in Chapter 3 of this thesis.

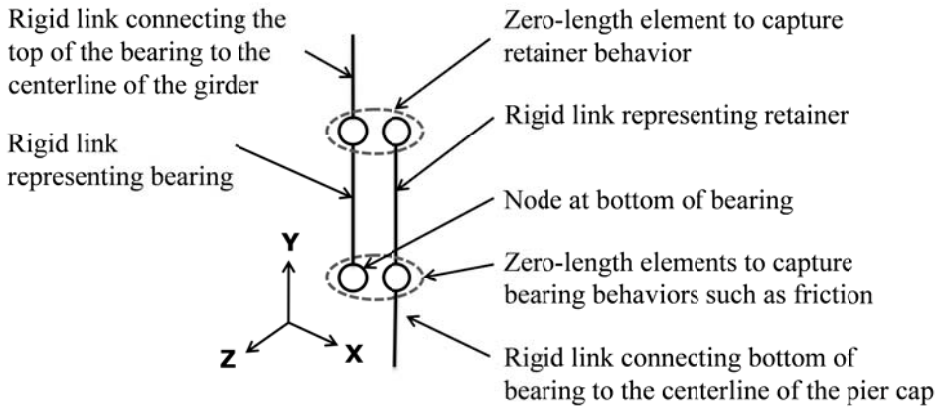

Figure 2.2 Modeling scheme and orientation for bearing and retainer models

The bearing elements provide a connection between the superstructure and substructure of the bridge, and are implemented in the global bridge model as shown in Figure 2.2. Rigid links are used to connect the bearings to the centerlines of the bridge girders and pier cap, such that all elements are modeled at an appropriate height. Two rigid links are used to simulate the height of the bearing and retainers (if necessary) separately, such that the nonlinear behaviors could be modeled independently. The zero-length elements capture the various nonlinear behaviors and are discussed in further detail in Chapter 3 and Appendix A.

2.3 Modeling of bridge superstructure

A common bridge deck modeling approach is one where a single beam is used with equivalent mass and stiffness, to simulate the behavior of the entire bridge deck, including girders, deck slab and side parapets (B. G. Nielson and DesRoches 2007; Ian G. Buckle et al. 2006). Although this modeling approach is efficient, it fails to capture the mass distribution along the height and width of the bridge superstructure. Alternatively a shell-beam model where the slab is modeled explicitly using shell elements tends to be computationally expensive. A bridge deck model that can easily capture both stiffness and mass distribution of a superstructure is a grid deck model as has been shown by past research (Chang and White 2008; Barth and Wu 2006). This type of model considers the girders and tributary concrete area for vertical flexural stiffness of the deck, and the transverse stiffness is estimated based on the equivalent total deck

area. Flexural stiffnesses are reduced by a factor of 0.75 to account for deck cracking. Axial stiffness of the deck includes both the concrete and steel components, and the torsional stiffness of the deck is modeled using the bare steel or precast concrete areas, while neglecting any contribution from the slab.

Diaphragm elements for the bridges are included per the IDOT bridge design manual (IDOT 2009) using linear elastic beam elements. The short and long steel superstructures use C12x25 U.S. and C15x40 U.S. shapes respectively, while the precast concrete girders are assumed to be cast together at support locations. It is noted that the deck diaphragms can be a location of critical damage if they are inadequate to transfer forces from the slab deck to the bearing supports. The most critical location would likely be at the intermediate piers, since the bearing components are designed for much higher dead loads there than at the abutments. The diaphragm capacities are evaluated as part of Stage 3 of this project, which will be reported in future publications. Tables with the expected diaphragm forces will be produced as a result of the computational study shown in this thesis. These demands are presented in Chapter 7 and can later be compared to the appropriate diaphragm capacities to determine if diaphragm failure is likely. Failure or inelasticity of the diaphragm elements can lead to local damage of the bridge girders, and potential local or global collapse. Diaphragm damage should be avoided at all costs to permit for an effective quasi isolated response.

To model the bridge deck, properties have been based on typical bridge designs observed in Illinois. The concrete capacity of the slab is f_c'=24 MPa (3500 psi), the reinforcement is assumed to have a yield strength of F_y= 410 MPa (60 ksi) but its contribution is neglected for most calculations. The steel girders are ASTM A572 with a yield capacity of F_y= 345 MPa (50 ksi). The precast girder used for one of the parametric cases is assumed to have a concrete strength capacity of f_c'=41 MPa (6000 psi). The stiffness of steel components is assumed to be E_s = 200 GPa (29000 ksi) and the concrete stiffness is calculated as $E_C = 4730\sqrt{f_c'}$ in MPa ($57,000\sqrt{f_c'}$ in psi). The shear modulus for both steel and concrete is calculated as $G = \frac{E}{2*(1+\upsilon)}$.

A cross-section view of the bridge deck is shown in Figure 2. 3 with some basic dimensions used for all superstructures in the parametric study. The deck is 12.8 m (42 ft) wide

to carry two lanes of traffic. The deck concrete slab is 20 cm (8 in.) thick and an additional 3.8cm (1.5 in.) of asphalt topping is applied on top for the road surface. The asphalt and concrete are assumed to weigh 2400kg/m^3 (150 pcf), but only the stiffness of the concrete is considered to contribute to the deck's flexural stiffness. The bridge has two side parapets which are 30 cm (1 ft) wide and 75 cm (30 in.) tall. The parapet stiffness is neglected, thus making the conservative assumption that the parapet and deck are cast separately in construction. If there is a good connection between the deck and the parapet and if the two components were to move integrally, then it is possible that the parapet would further increase the transverse stiffness of the already essentially rigid structure.

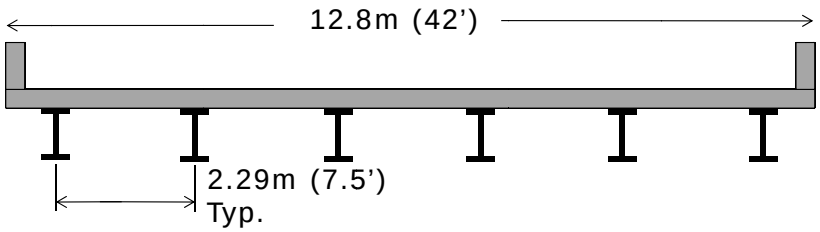

Figure 2. 3. Longitudinal cross-section view of bridge deck

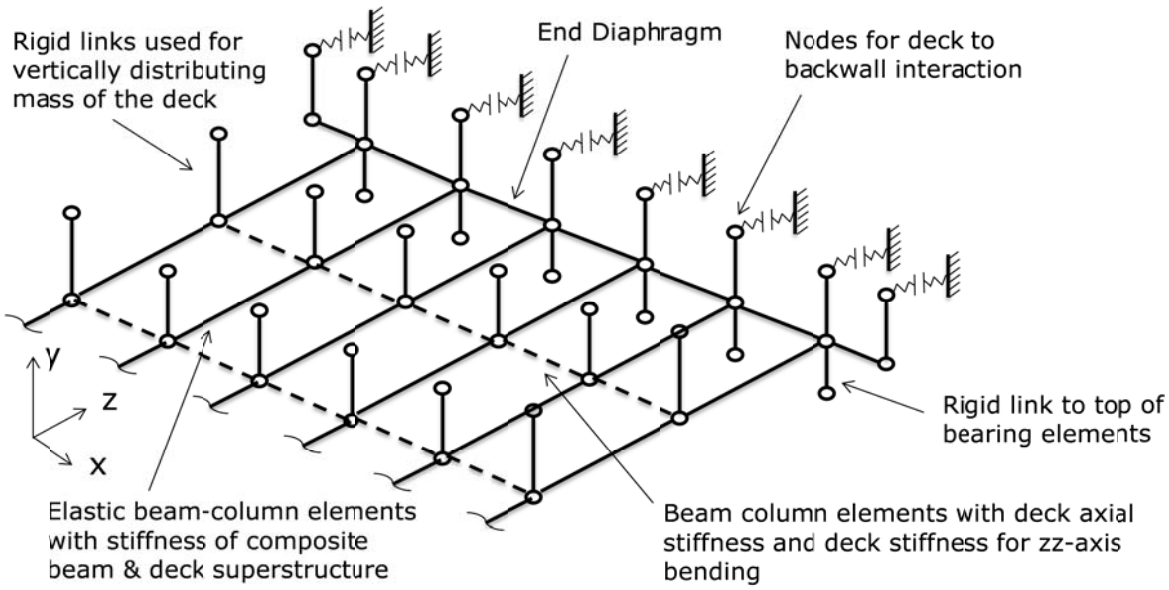

Figure 2.4 Grid model used to model the deck superstructure

The final bridge model that was used in the analytical study is shown in Figure 2.4. Equivalent section properties of the deck slab and girders are calculated for each bridge, and the

equivalent stiffness of the entire deck is reduced by a factor of 0.75 and is distributed evenly among the six longitudinal girders. The deck stiffness is modeled in the transverse members such that the girders are linked for torsional stiffness and out of plane deformation. The bridge deck properties for the three types of bridges considered in the parametric study are shown in Table 2.2.

Table 2.2 Deck propertied to be considered in parametric study

	Bridge Type		
Basic Deck Properties	**Ss - Steel Short**	**Sl - Steel Long**	**Cs - Concrete Short**
Deck width - m (ft)	13 (42)	13 (42)	13 (42)
Deck thickness - cm (in)	20 (8)	20 (8)	20 (8)
Girder type	W690x125 (W27x84 U.S.)	W1000x272 (W40x183 U.S.)	91.4cm (36 in.) PPC I-Girder
Span lengths - m (ft)	15.2-15.2-15.2 (50-50-50)	24.4-36.6-24.4 (80-120-80)	18.3-18.3-18.3 (60-60-60)
Girder Depth - cm (in)	68 (26.7)	99 (39)	975 (384)
Girder Area - cm^2 (in^2)	160 (24.8)	344 (53.3)	332805 (51584.84)
Girder Ixx - cm^4 (in^4)	18387 (2850)	85161 (13200)	35951 (5572.38)
Girder Iyy - cm^4 (in^4)	684 (106)	2135 (331)	332805 (51584.84)
Girder J - cm^4 (in^4)	18 (2.81)	125 (19.3)	332805 (51584.84)
Girder Weight - kN/m (kips/ft)	7 (0.504)	16 (1.098)	35 (2.4)
Concrete Deck Weight - kN/m (kips/ft)	67 (4.575)	67 (4.575)	67 (4.575)
Asphalt Topping Weight - kN/m (kips/ft)	11 (0.75)	11 (0.75)	11 (0.75)
Parapets Weight - kN/m (kips/ft)	11 (0.75)	11 (0.75)	11 (0.75)
Total deck weight - kN/m (kips/ft)	96 (6.579)	105 (7.173)	124 (8.475)
Deck Modeling Properties (Based on concrete stiffness of 23.2 MPa / 3370 ksi)			
Transvere composite modulus Iyy - m^4 (ft^4)	42 (4845.7)	63 (7250.367)	65 (7555.212)
Vertical composite modulus Ixx - m^4 (ft^4)	0.19 (22.2)	0.67 (77.42816)	0.53 (60.8576)
Composite area - m^4 (ft^2)	0.26 (30.2)	0.32 (37.54985)	0.33 (38.47497)
Shear stiffness of slab only GA - kN/m (kip)/in	640080 (5664960.0)	640080 (5664960)	640080 (5664960)
K/GA for slab - 1/kN (1/kip)	4.76E-08 (2.12E-07)	4.76E-08 (2.12E-07)	4.76E-08 (2.12E-07)
Transverse flex. stiffness EIyy - MN*m^2 (kip*in^2)	971717 (3.39E+11)	1453942 (5.07E+11)	1515074 (5.28E+11)
Vertical flex. stiffness EIxx - MN*m^2 (kip*in^2)	4458 (1.55E+09)	15527 (5.41E+09)	12204 (4.25E+09)

The superstructure model for each parametric variation has been compared and validated with elastic approximations of an equivalent elastic deck subject to nominal loads.

Figure 2.5 (a) shows the superstructure model of the Short steel variation subjected to vertical loading. A 24 m (80 ft) span is fixed on one end, simulating a cantilever, and is loaded in the vertical direction with the distributed dead load of the deck. The theoretical elastic deformations used for comparison of the deck performance in

Figure 2.5 (b) are calculated based Euler beam theory. Generally there is a good match between the OpenSees model and the idealistic approximation.

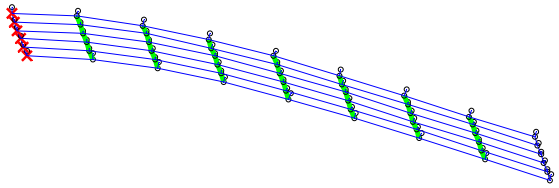

(a) Isotropic view of deflected cantilever bridge deck subject to pure gravity load

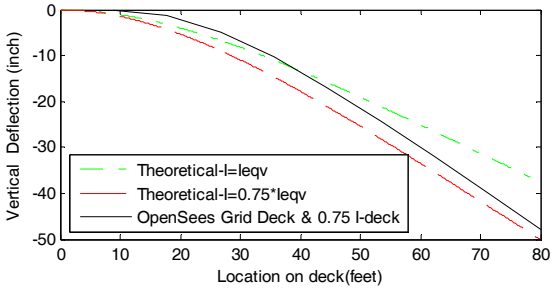

(b) Deformation of OpenSees model compared to idealistic equations

Figure 2.5 Validation of deck model for 1.0D vertical loading

The grid model was subjected to a distributed transverse load of 2.5 times the dead load, and a 200 times scaled deformation plot is shown in

Figure 2.6 (a). The theoretical shear deformations are estimated using Timoshenko beam theory and Euler equations are again used to calculate the flexural deformations. The grid model that uses only flexural stiffness of elements provides a reasonable approximation of the deck behavior. Although shear deformations are noted for the transverse loading of the deck, their magnitude is low enough, that they are considered negligible in the overall seismic response. The discretization of the bridge was refined several times, and 3 m (10 ft) long elements were chosen as the final deck segments. This discretization was shown to be sufficient in capturing all necessary bridge behavior.

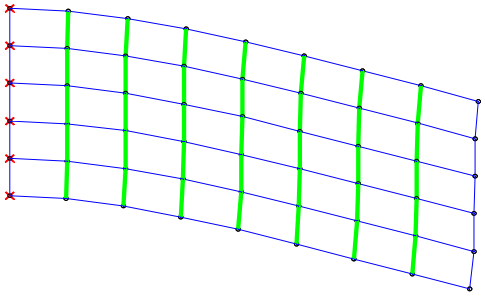

(a) Plan view of deflected bridge deck subject to transverse load

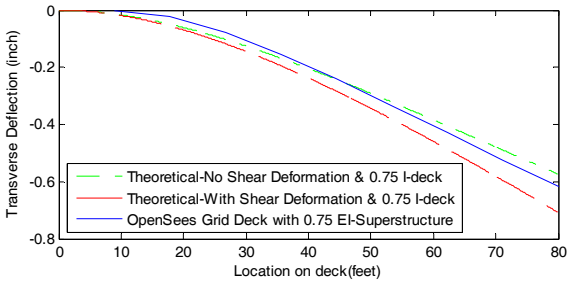

(b) Deformation of OpenSees model compared to theoretical equations

Figure 2.6 Validation of deck model for 2.5D transverse loading

A final consideration for the deck model was the mass distribution along the height and width of the superstructure. In addition to the grid model outlined above, a different model of the bridge superstructure was created using beam and shell elements, where mass was distributed accurately in all three dimensions. The shell model was computationally expensive and was replaced by the much more computationally efficient grid model, however, it did show that mass distribution was not uniform along the bridge width. Since the parapets are offset in the transverse direction from the center of the bridge deck, they typically cause the highest gravity loads to be seen in the outside girders, and alter the load distribution of the inside girders as well. This load distribution influences individual bearing loads, and thereby friction break-off forces. This behavior is briefly illustrated with lateral pushover analyses in Chapter 4. To capture the appropriate distribution of loads along the bridge width, a simplified model was built to simulate the slab and parapet load distribution along the six beam lines. The reactions shown in Figure 2.7 represent girder loads in US kips per 30 cm (1 ft) of deck length. The reactions obtained from the analysis are distributed proportionally along the length of the grid superstructure model as shown in Figure 2.8. Furthermore, rigid links are used to distribute the loads vertically to capture the vertical center of mass of the concrete deck. The vertical mass distribution causes overturning effects and changes the bearing load pattern along the bridge width. Chapter 4 shows the overturning effects and the variation of bearing loads due to a transverse pushover analysis, however it should be noted that full uplift of bearings was not observed in any of the analyses presented in this thesis.

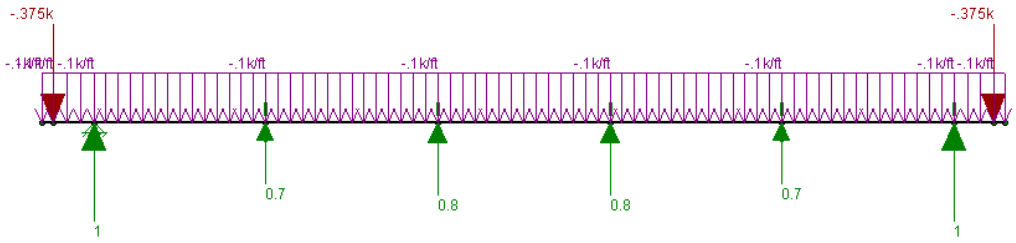

Figure 2.7 Distribution of parapet and uniform loads along bridge width

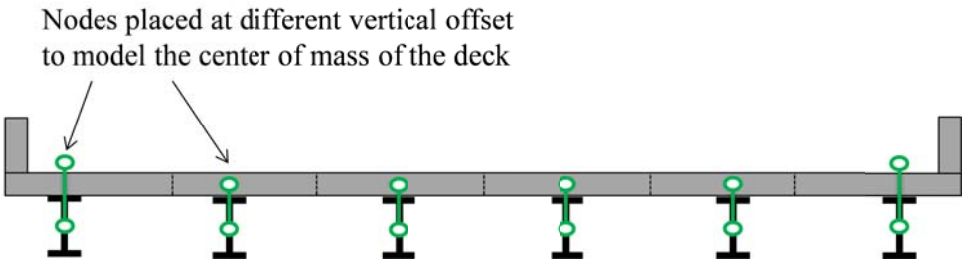

Figure 2.8 Distribution of deck mass along width and height of bridge

2.4 Modeling of intermediate substructures

Multi-column and wall piers are the two types of intermediate substructures considered in the parametric bridge study. Each substructure is also studied with two different clear heights, 4.6 m (15 ft) for short and 12.3 m (40 ft) for tall structures. The substructures were all reinforced concrete and were analyzed and designed per the IDOT design manual (IDOT 2009) and the ACI code (ACI 318 2008). The indicated clear pier heights are taken from the top of the foundation pile cap to the bottom of the pier cap. The pier cap is modeled as a 1 m (39 in.) high and 1.1 m (42 in.) wide beam for all analyses. This member is significantly stiffer than the pier column and wall and is modeled as linear elastic. The foundation pile cap is also much stiffer and is also model as linear elastic. A schematic detail of the components used for substructure modeling is shown in Figure 2.9 and the nonlinear models used and considered are discussed in this section. Note that Section 2.4.1 contains most of the details on the materials and nonlinear elements for both multi-column piers and wall substructures.

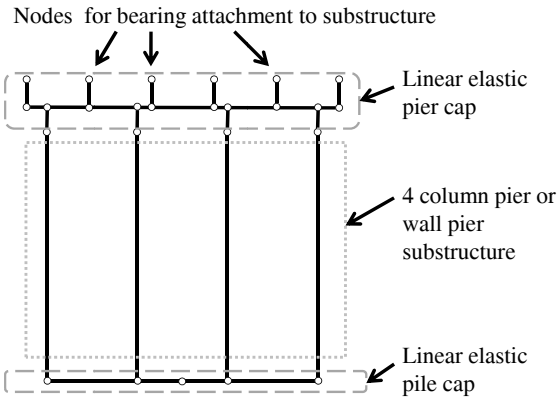

Figure 2.9 Schematic representation of substructure model

2.4.1 Multi-column piers

The column (and wall piers) can experience nonlinear phenomena such as cracking and flexural and shear yielding when subjected to high lateral loads. Different elements, element discretization and fiber sections were investigated to find an appropriate method for modeling a single cantilever, and dual curvature columns. The distributed plasticity model proposed by (Scott and Fenves 2006) was used, as it captures the curvature in the plastic hinge regions as shown in Figure 2.10 (a), which well matches concrete column behavior. The plastic hinge length is defined per (Berry, Lehman, and Lowes 2008), as $l_p = 0.05L + 0.1 f_y d_b / \sqrt{f_c'}$ in MPa ($l_p = 0.05L + 0.008 f_y d_b / \sqrt{f_c'}$ in psi) is used, where L is distance from the critical section to the point of contraflexure, f_y is the longitudinal rebar yield strength, d_b is the longitudinal rebar diameter, and f_c' is the concrete strength.

A fiber section (Figure 2.10 (b)), was used to model the nonlinear material behavior in the plastic hinge regions of the column. To provide consistently reliable results the section was discretized to have 15 fiber wedges, 15 fiber rings of confined concrete, 5 fiber rings of un-confined concrete and the necessary number of fibers to simulate each rebar individually. The reinforcement was modeled by using the OpenSees Steel 02 - material model (Figure 2.11(a)), while the un-confined and confined concrete were modeled using the OpenSees Concrete 02 material model (Figure 2.11(b)). Concrete properties were defined as follows: a confined-to-unconfined concrete strength ratio of 1.25, concrete tensile capacity $f_t = 0.12 f_c'$, and concrete modulus of elasticity $E_C = 4730\sqrt{f_c'}$ in MPa ($57{,}000\sqrt{f_c'}$ in psi). Sufficient transverse confining reinforcement is assumed present, such that the full moment capacity of the pier can be developed without bar buckling, and before shear failure occurs in the system. Modifying the material properties, as well as column and section geometries, it was possible to validate the distributed plasticity model against experimental findings (PEER 2003).

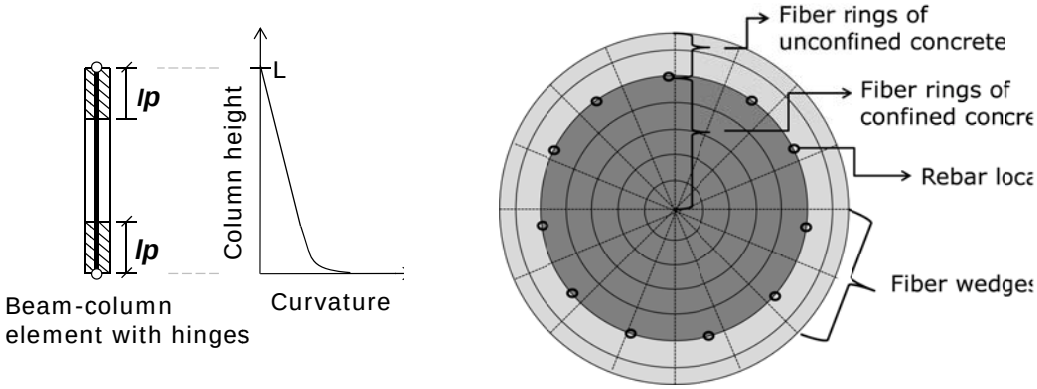

(a) Element and curvature distribution

(b) Fiber sections used at for pier modeling

Figure 2.10 Definitions for pier column substructure

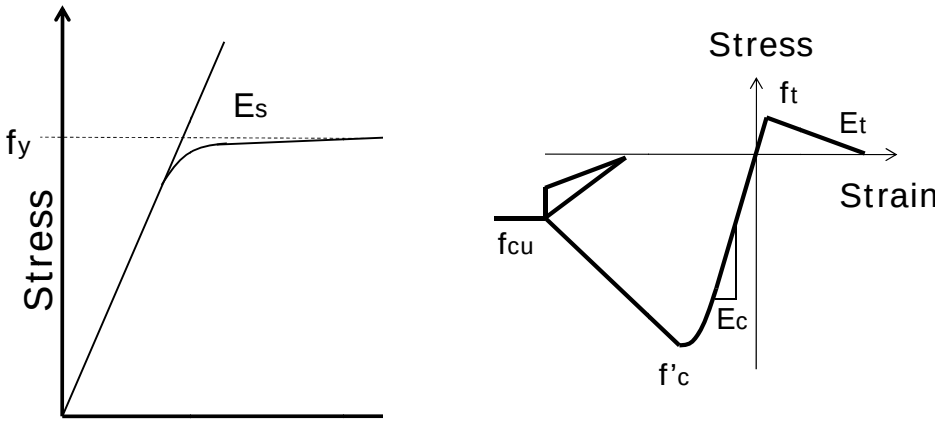

(a) Steel 02 model

(b) Concrete 02 model

Figure 2.11 Steel and concrete materials used for nonlinear model

Model validation with cyclic force-displacement experiment data for a 460 mm (18 in.) diameter concrete column with a vertical reinforcement ratio of 3.62% is shown in Figure 2.12 (Test FL3)(Kowalsky, Priestly, and Seible 1999). The test had an axial load of 1780 kN (400 kips) and the lateral load was applied at 370 cm (144 in.) from the base of the column. Figure 2.13 shows the fiber model validated with Test 3 from another set of experiments, (Chai, Priestley, and Seible 1991), where 61 cm (24 in.) columns with 2.54% vertical reinforcement were investigated. These columns had spiral reinforcement ratio of 0.17 and the lateral load was applied at 365 cm (143 in.) from the column base. A third validation shown from experimental

results of (Ang, Priestley, and Paulay 1989) is shown in Figure 2.14. The model properties used to match these results include: a pier diameter of 40 cm (16 in.), pier height of 100 cm (39 in.), an axial load of 750 kN (170 kips), and a vertical reinforcement ratio of 3.2%

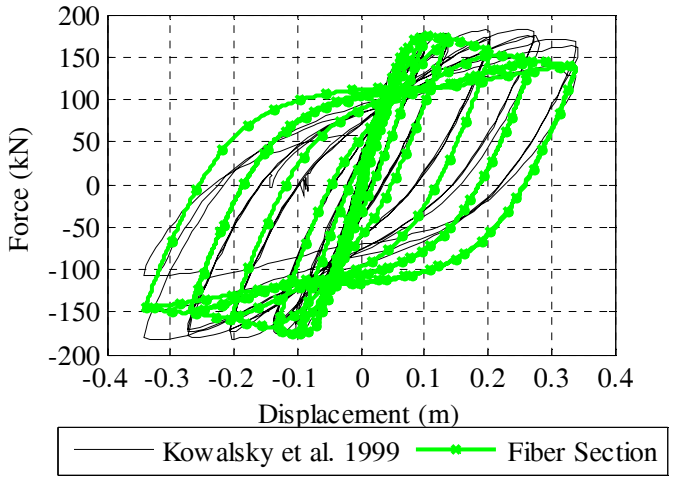

Figure 2.12 Validation of bridge column model with results from Kowalsky et al.1999 – Experiment FL3

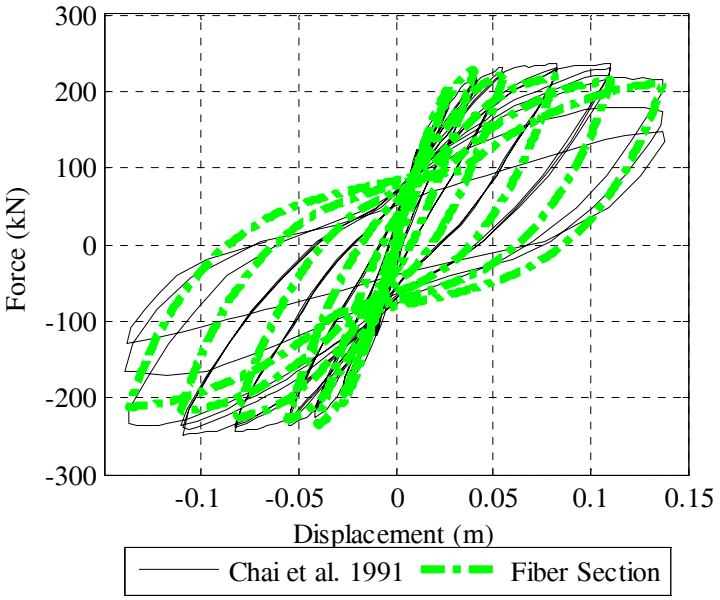

Figure 2.13 Validation of bridge column model with results from Chai et al. 1991 – Test 3

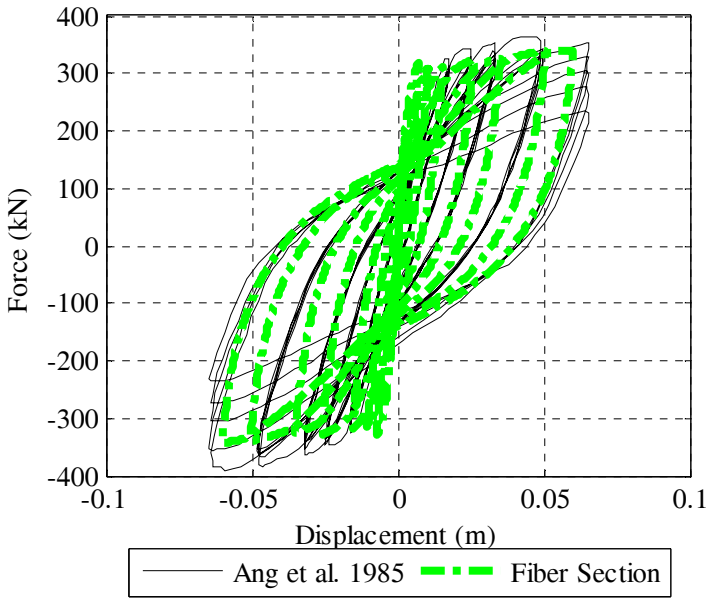

Figure 2.14 Validation of bridge column model with results from Ang et al. 1985

The columns used for the basic bridge prototype are spaced at 3.05 m (10 ft), and they are 4.6 m (15 ft) tall from the top of pile cap to the bottom of the pier cap. They have a 0.91 m (3 ft) diameter, are constructed of 24.1 MPa (3500 psi) normal-weight concrete, and are reinforced with eleven 29 mm (U.S. #9) longitudinal bars (with 3.8 cm (1.5 in.) clear cover). Design specifications for the remainder of bridges in the parametric study are available in Chapter 5. The stiffness of the columns is reduced by 0.75 to account for initial cracking effects. For the parametric study it was important to define the limit states of concrete piers, so cracking, and more importantly steel yielding effects were monitored. Figure 2.15 shows a force-displacement hysteresis for a typical IDOT cantilever column that would be used for a short bridge structure. The same column subjected to double curvature bending is shown in Figure 2.16. The double curvature scenario is more typical for the column capacity and stiffness when the bridge is subject to transverse loads.

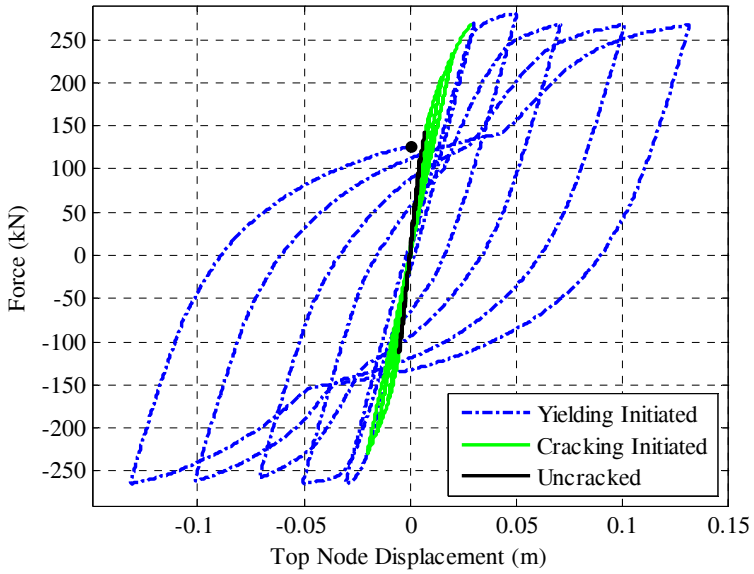

Figure 2.15. Force-displacement hysteresis and limit states for typical 4.6 m (15 ft) IDOT column subject to single curvature cyclic loading

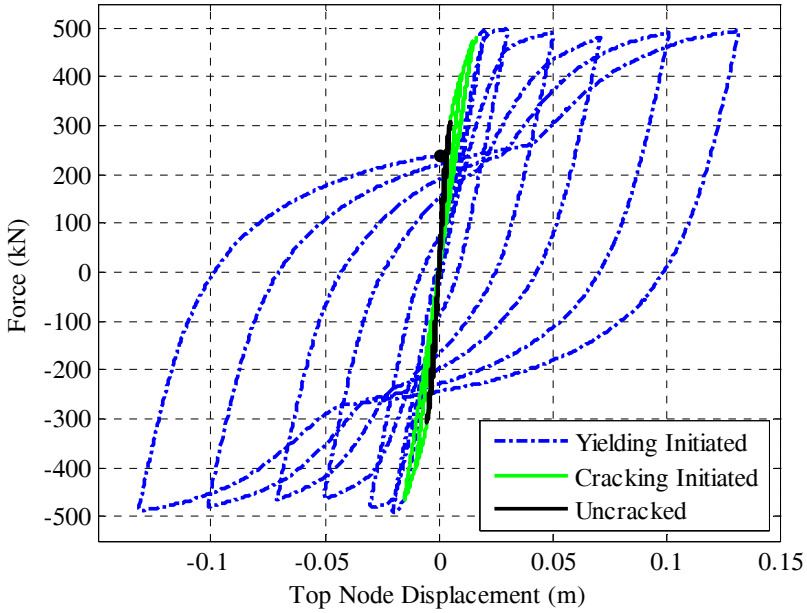

Figure 2.16. Force-displacement hysteresis and limit states for typical 4.6 m (15 ft) IDOT column subject to double curvature cyclic loading

2.4.2 Wall substructures

A wall that was 9.45m (35ft) wide and 91.4cm (3 ft) thick was chosen to be used for all cases with wall substructures, with vertical reinforcement placed at 3.81 cm (1.5 in) clear cover .

The clear height of the wall between the pile cap and the pier cap were varied for the tall and short substructure cases, and varied between 4.5 m (15 ft) and 12.2 m (40 ft). Basic analysis of this type of substructure as well as observance of some existing bridge drawings showed that relatively low reinforcement ratios ($\rho = 0.001$ to $\rho = 0.005$) were necessary to provide the design capacity for this system. Reinforcement was designed for the various parametric systems resulting in the use of two reinforcement configurations. One system employed a reinforcement ratio of $\rho = 0.0015$ which is applicable for most designs and $\rho = 0.0019$ was used for tall 12.2m (40 ft) bridges with the long or concrete superstructure configurations. To provide these ratios 22mm (U.S. #7) and 25mm (U.S. #8) bars were used and were assumed to be placed at 30 cm (12 in) center to center spacing for the entire width of the wall resulting in final reinforcement ratios of the wall to be 0.0015 and 0.0019 respectively (0.15% and 0.19%).

Based on the specified wall dimensions and reinforcements some basic calculations were carried out to determine what limit states were important to consider and to develop a reliable model that can capture various linear and nonlinear behaviors that are to be expected from the wall substructures. Loading of the wall substructures was assumed to occur predominantly in the two orthogonal directions of the bridge deck, therefore longitudinal movement would cause out-of-plane loading of the wall and transverse deck movement would cause in plane loading. Figure 2.17 shows the assumed loading directions of the wall substructure.

(a) Out-of-plane loading (b) In-plane loading

Figure 2.17. Loading of wall substructures

The shear capacity of the wall was calculated to equal φV_c =5350 kN (1200kips) for both directions based on the concrete capacity alone. Typical horizontal reinforcement for wall substructures in Illinois can range widely with typical values in the range of 0.0010 to 0.0025, thereby providing additional shear strength due to the steel reinforcement of φV_s = 220 to 580kN

(50 to 130kips) for out-of plane loading and φV_s = 2540 to 6500 kN (570 to 1450 kips) for in-plane loading. The shear friction capacity of the wall was also relatively high at φV_n =10,000 kN (8,000 kips).

The nominal moment capacity of the wall substructures for out of plane loading was φM_n = 4300 kN-m (3170 kip-ft) and 5600 kN-m (4120 kip-ft) for the two reinforcement cases. The in-plane nominal moment capacity of the ρ = 0.0015 reinforced wall was calculated to be φM_n = 110500 kN-m (81500 kip-ft) when only a sixth of the reinforcement was considered active. This moment capacity is much greater than expected loads and leads to shear being the more likely failure mechanism for the in-plane loading condition.

In comparison to the capacity of the retainers and fixed bearings used on the different parametric variations the shear capacity of the wall is significantly higher than any lateral load that can be developed at the top of the substructure. Maximum lateral loads that can be expected at top of the substructure should be no more than 3500 kN (800 kips), therefore the only likely type of nonlinearity that is to occur is that due to flexural bending due to out-of plane loads. A fiber model similar to that used for the circular columns is developed as shown in Figure 2.18. The reinforcement and concrete are modeled in the same fashion as for the circular column and the same distributed plasticity model is used to capture the hinge formation at critical loads.

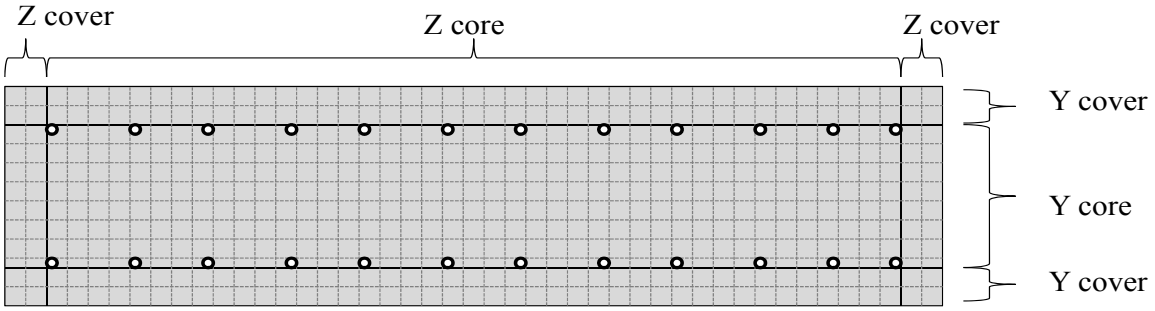

Figure 2.18. Fiber section used for wall substructures

The elastic stiffness of the wall is evaluated assuming cracked initial conditions. For out-of-plane loading the wall stiffness was calculated to be I_{yy} =0.7*I_g=4760 m^4 (1143000 in^4), and for in-plane the stiffness was I_{zz} = 0.7*I_g = 647656 m^4 (155600000 in^4). The concrete stiffness was estimated to be E_c =23.2 MPa (3372ksi) and G_c = 14.5 MPa (2107ksi). Based on linear calculations for a cantilever beam it was determined that even when the tall 12.2m (40ft) structure was loaded in-plane with a maximum load of 3500 kN (800kips) it would deflect at

most 1.8 mm (0.07 in) due to flexural and 0.3 mm (0.013 in) due to shear deformation. These deflections are considered negligible to the overall bridge performance, so only the elastic flexural stiffness of the element is used to model deformations for the in-plane direction. For out of plane loading, the element stiffness is expected to have more of an effect. A 100 kip load would result in 5 mm (0.2 in) elastic deformation for the short 4.5m (15 ft) bridge and up to 60 mm (2.4 in) of deflection for the tall 12.2 m (40 ft) bridge. Shear deformations are again negligible in comparison to flexural deformation, and the beam column element with hinges will be capable to capture all necessary effects.

Validation of the model was carried out considering two sets of experimental data from (Haroun et al. 1993) and (Abo-Shadi, Saiidi, and Sanders 1999) for the cyclic out-of-plane loading of walls. Figure 2.19 shows the OpenSees fiber model used to simulate an experiment of a 30 x 150 cm (12 x 59 in.) wall test with 0.78% vertical reinforcement. Figure 2.20 shows the same dimensions wall with a reinforcement ratio of 1.47% vertical reinforcement. Both of those elements had 0.14% shear reinforcement, an axial load of 650 kN (146 kN) and the lateral load was applied at 255cm above the top of the base. The plot in Figure 2.21 shows the OpenSees model validated with a 25 x 97 cm. (10 x38 in.) wall with 0.56% vertical reinforcement. That test had 0.15% horizontal reinforcement, the out of plane load was applied at 290 cm (114 in.), an axial load of 275 kN (62 kips) was applied for the duration of the experiment. The model was adapted to the walls used in the parametric study and cyclic element testing was carried out to observe the behavior. Figure 2.22 shows the walls tested for out of plane behavior.

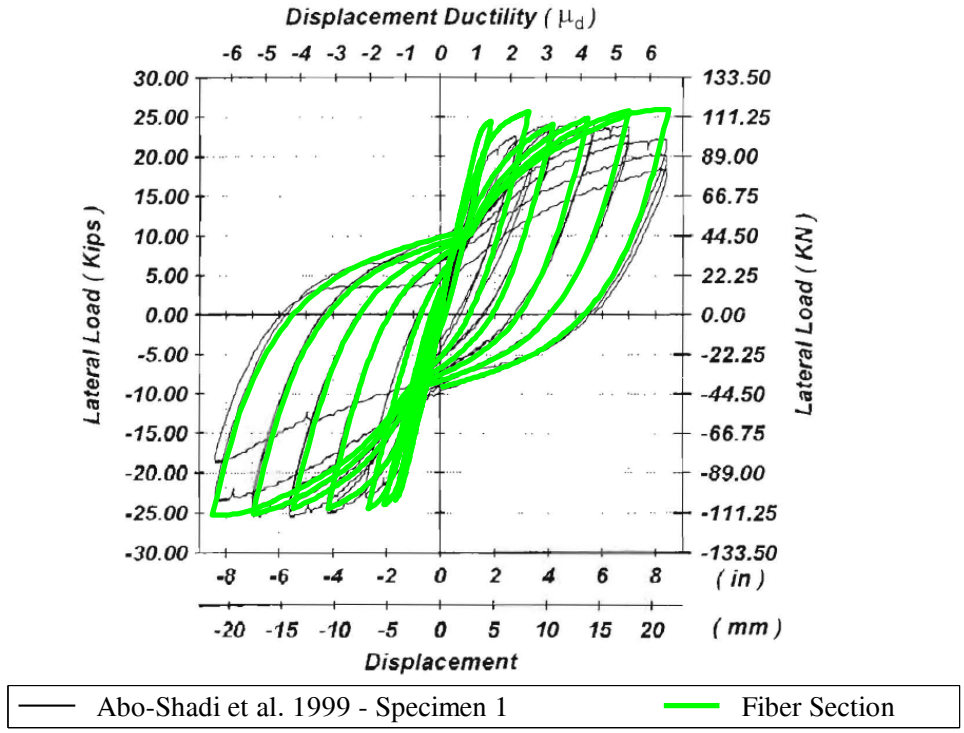

Figure 2.19. Validation of wall model with results from Abo-Shadi et al. 1999 - Specimen 1

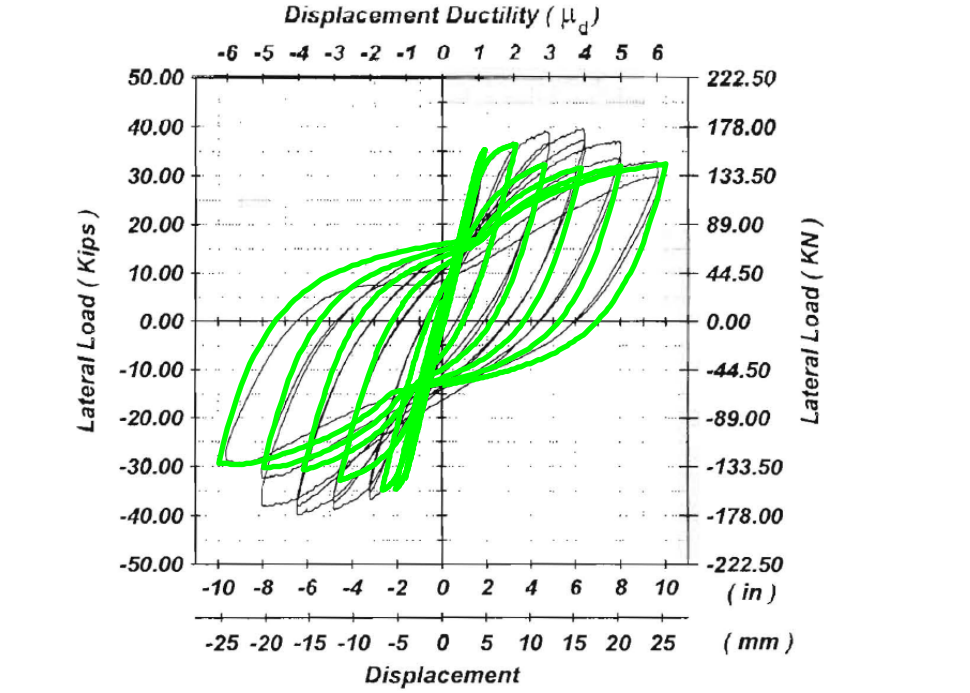

Figure 2.20. Validation of wall model with results from Abo-Shadi et al. 1999 - Specimen 4

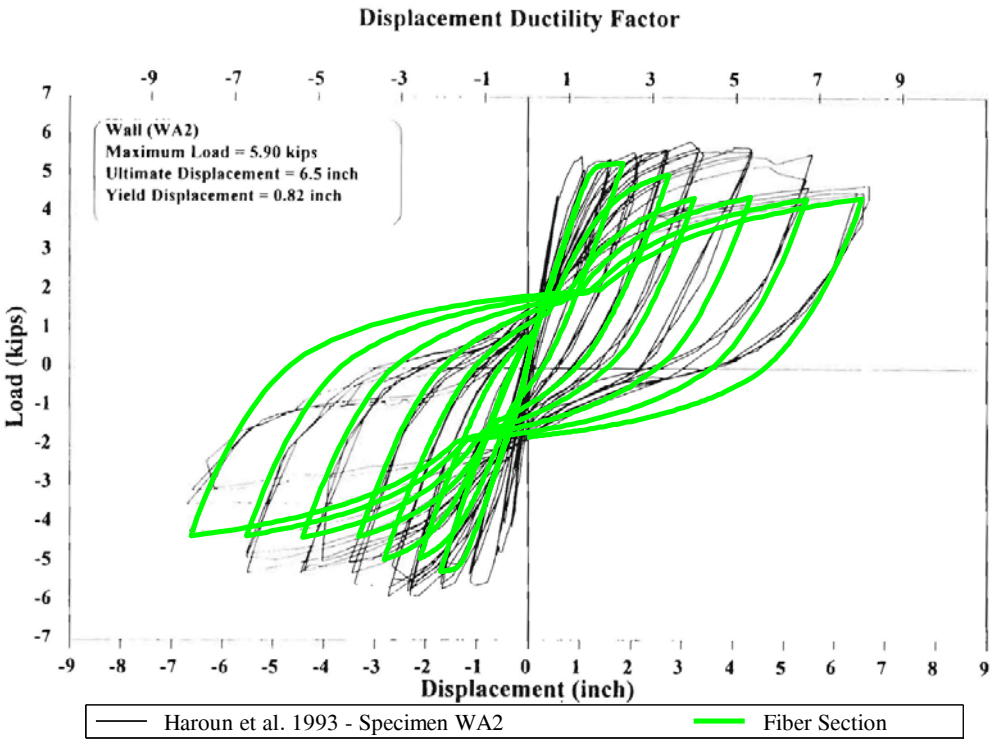

Figure 2.21. Validation of wall model with results from Haroun et al. 1993 Specimen WA2

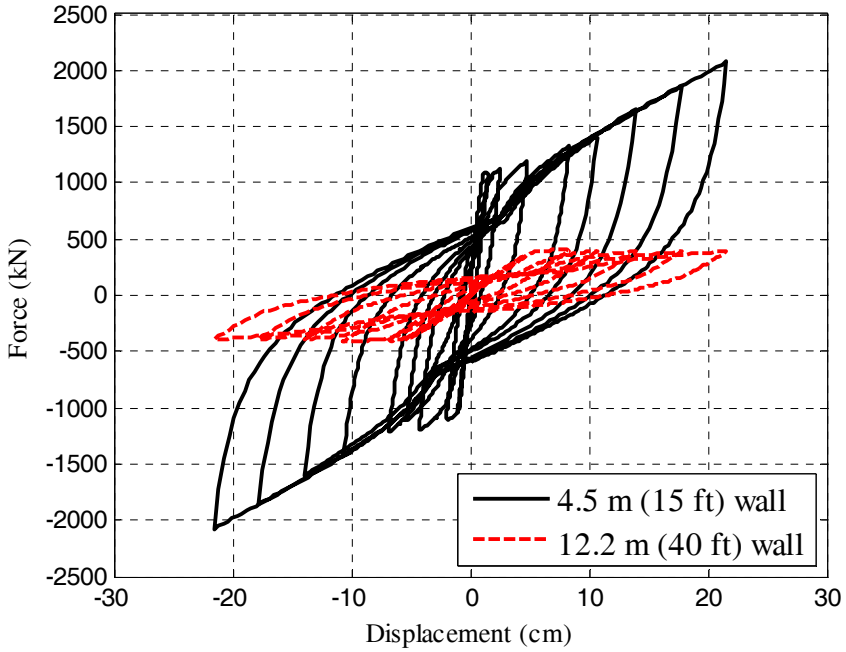

Figure 2.22. Out of plane cyclic pushover analysis for wall elements with 22mm (U.S. #7) reinforcement

2.5 Foundations

Intermediate substructure and abutment foundation response is included in the system models based on a separate study of common representative bridge foundations and soils that was carried out with a geotechnical pile group analysis program, GROUP 7.0 provided by (Ensoft Inc. 2010). The pile group response was verified using the single pile analysis software LPILE 5.0, that was provided from the same vendor. Foundations to be used for the parametric analysis were designed for the base bridge model, and were verified to be characteristic for typical Illinois foundations. The pile group and pile cap response was modeled for three different soil conditions and the global foundation response was simulated in OpenSees using linear and nonlinear spring materials.

The abutment foundation were defined as (11) HP12x63 piles at a 13.7m (45') depth, with a 1.2m x 1.8m x 12.8m (4'x6'x42') concrete pile cap. The abutment has a row of four piles battered towards the superstructure at a 1 to 3 slope, a row of five piles placed straight and two piles placed in the wing walls as shown in Figure 2.23. The typical foundation for the intermediate substructure has three rows of four HP12x63 straight piles driven to a depth of 13.7m (45'), and the pile group is covered with a 0.76m x 3.7m x 10.7m (2.5'x12'x35') cap as shown in Figure 2.24.

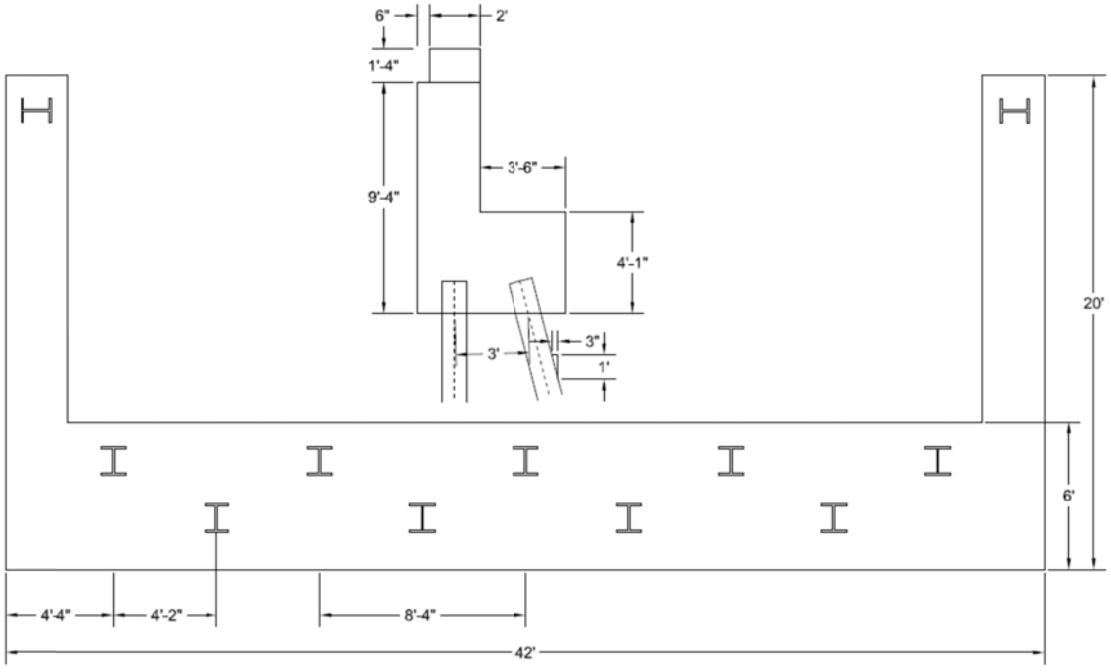

Figure 2.23 Abutment foundation

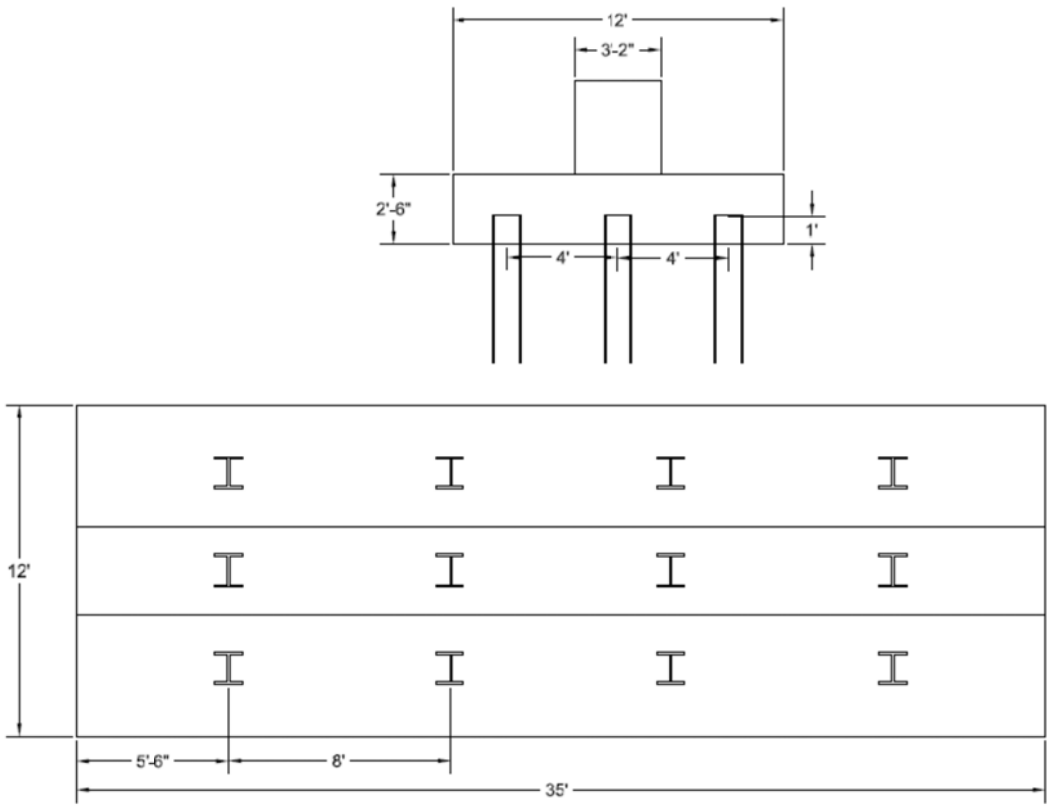

Figure 2.24 Intermediate substructure foundation

The foundation assemblies were modeled with the following soil types:

(i) soft clay or loamy soil, modeled with a 0.014-0.024MPa (300–500psf) shear strength. (Flexible foundation boundary condition)

(ii) medium to stiff sand, modeled with 0.072–0.096MPa (1500–2000psf) shear strength; and

(iii) stiff rock, modeled as a fixed base; (Fixed foundation boundary condition)

Although nonlinear soil-foundations models were developed for three different soil conditions, it was decided to only use conditions (i) and (iii) in the analyses in order to limit the size of the parametric study. Hereafter, these two conditions are noted as "Fixed foundation boundary conditions" assuming the large pile group placed in a stiff rock substrate, and "Flexible foundation boundary condition" assuming the same foundation placed in soft soil conditions. The soil types used to model the foundation are an independent variable from the characteristics of the earthquake ground motions. As will be shown in Chapter 5, two sets of ground motions are considered separately, where the soil class has an influence on the spectral acceleration and

displacement. Finally, although these naming conventions imply that one foundation condition is much less stiff than the other, they are not intended to cover the entire collection of foundation conditions for bridges in Illinois. Other foundation types such as single row piles or mat foundations, if placed in soft soils may exhibit different characteristics from the flexible foundation condition considered herein.

The soil-foundation interaction behavior was calculated for the foundations and different soil types as curvilinear force-displacement relations. Figure 2.25 shows the modeling scheme for the different foundation stiffnesses. The foundation is simulated in OpenSees as a zero-length element that restrains the bottom node of each substructure using springs for lateral and rotational stiffness as recommended per (Liam Finn 2005). Figure 2.26 represents the flexible foundation boundary conditions where the nonlinear force-displacement and moment-rotation behaviors for the abutment and intermediate substructures are modeled based on soft soil substrate. Figure 2.27 shows the axial behavior of the abutment foundation which is entirely governed by the yield strength of the piles. The high vertical stiffness and capacity of the foundations indicate that the vertical foundation response is not of significant influence. The nonlinear force - displacement curves are fit using the P-y uniaxial material in OpenSees as defined by (Boulanger et al. 1999), and the axial behavior is simulated using the Steel 02 uniaxial material model.

As a final note, the foundation modeling considered herein is in no sense fully comprehensive. Although soft soil-springs are used there is also the possibility of different foundation types and different soil conditions. Furthermore, potentially critical limit states such as soil liquefaction or localized foundation damage are not considered. Base shears provided from the seismic analysis (Chapters 6 and 7) in this project could potentially be compared to capacities for other foundation components. For more information on substructure, foundation and soil interaction, the reader can refer to a wide range of literature (PoLam and Law 2000; Tongaonkar and Jangid 2003; Ciampoli and Pinto 1995; Bignell and LaFave 2010).

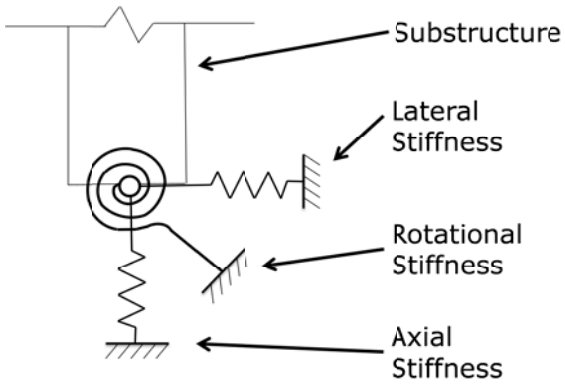

Figure 2.25 Schematic for foundation modeling

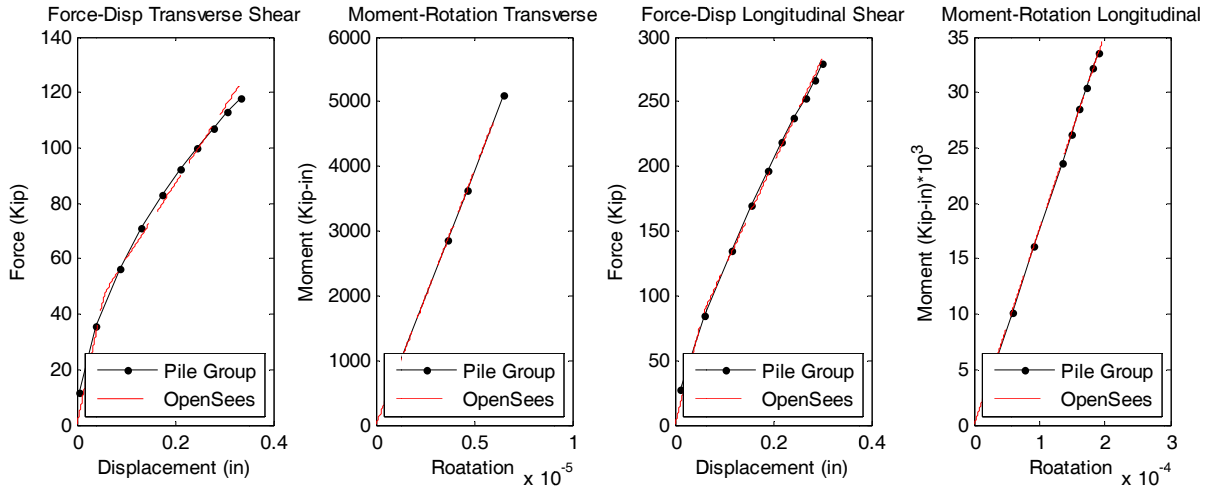

(a) Abutment foundation (b) Intermediate pier foundation

Figure 2.26 Flexible foundation boundary condition model based on soft soil substrate

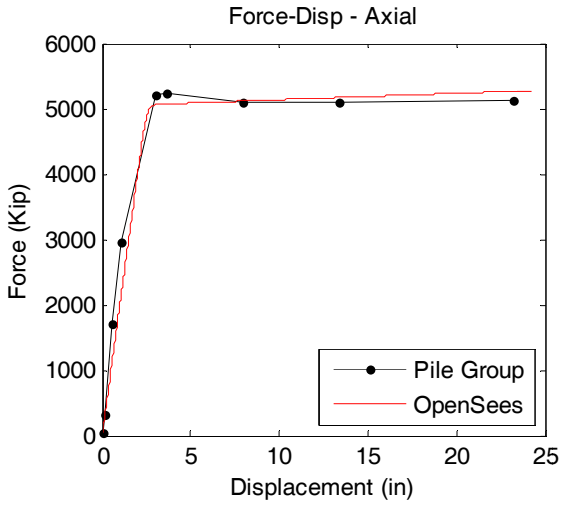

Figure 2.27 Expected axial behavior for the abutment foundation

2.6 Abutment backwalls

Abutment backwalls are placed a short distance away from each end of the bridge deck, allowing for an expansion joint gap, and are expected to be important components for the bridge with respect to its seismic behavior. When subject to longitudinal movement, the bridge is relatively flexible, and as soon as the 5 cm (2 in.) gap is closed, the superstructure can contact the backwall and then experience nonlinear behavior from not only the structural concrete backwall but also the soil backfill behind it. The most important backwall to deck interaction details are shown schematically in Figure 2.28. Some recent research has shown that backwalls can have a substantial effect on bridge response (P. Wilson and Elgamal 2010), and design recommendations (AASHTO 2009) allow the contribution of a sacrificial backwall in seismic design. The backwall can experience loading from seismic loads in both the longitudinal and transverse directions, since twisting about the vertical axis of the superstructure can cause corners of the deck and backwall to interact.

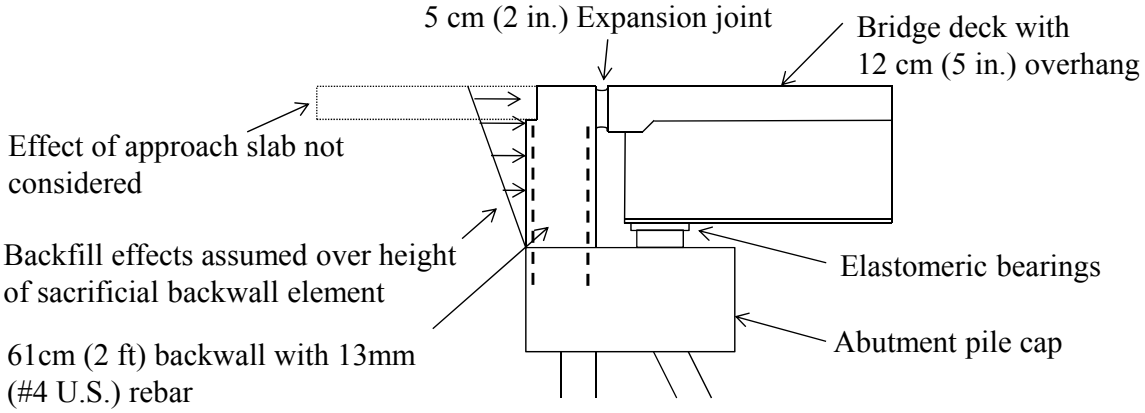

Figure 2.28 Typical detail for backwalls

Modern design recommendations consider the backwall to be sacrificial, such that any longitudinal force contribution is only from the soil backfill. Several cases are investigated for potential failure in the backwall components, and it is noted that although the backwalls may be considered sacrificial, it is likely that they have a substantial force capacity. Although this would be beneficial in reducing longitudinal bridge deck movement, it is likely to cause large base shears in the abutments which can result in significant damage to the foundation elements. Typical bridges in Illinois have two rows of 13 mm (#4 US) vertical reinforcement in the

backwall spaced at 25 cm (12 in.) along the bridge width, and embedded at 5 cm (2 in.) clear cover from the backwall faces.

Each of the different bridge cases has a slightly different backwall detail, since the backwall height is larger for the longer bridges where deeper beams are used. For the short steel deck bridge structure the backwall has a contact with the deck at a distance of 91 cm (36 in.) from the top of the abutment pile cap. A cold joint is assumed to exist at the interface between the backwall element and the abutment pile cap. Using shear friction calculations, the shear capacity of the backwall is shown to be 2200 kN (495 kips) for the 12.8m (42 ft) long backwall element. Neglecting reinforcement in compression and modeling the backwall as a cantilever concrete column loaded at the top (deck interaction location) the moment capacity of the wall governs the strength of the element. The 12.8m (42 ft) long backwall has a moment capacity of 1220 kN-m (1370 kip-ft), which corresponds to a deck pounding load of 1340 kN (300 kips), significantly lower than the shear capacity. The different superstructure models each have the same rotational plastic hinge capacity at the bottom of the back wall, while the backfill stiffness and strength depend on the back wall height.

Figure 2.29 shows the backwall structural element modeled using a rigid link connected to a bilinear zero-length element simulating the flexural stiffness and capacity of a concrete wall. The nonlinear soil behavior is defined per (Shamsabadi, Rollins, and Kapuskar 2007) and modeled using the OpenSees hyperbolic gap material, assuming that the backfill is a compacted, dense sand with an ultimate passive resistance of 160 kN per meter (10.8 kips per ft) of backwall, similar to what can be expected for typical Illinois bridges. The backwall / backfill system produces the force-displacement behavior shown in Figure 2.30 , when the prototype bridge is subjected to cyclic loading in the longitudinal direction.

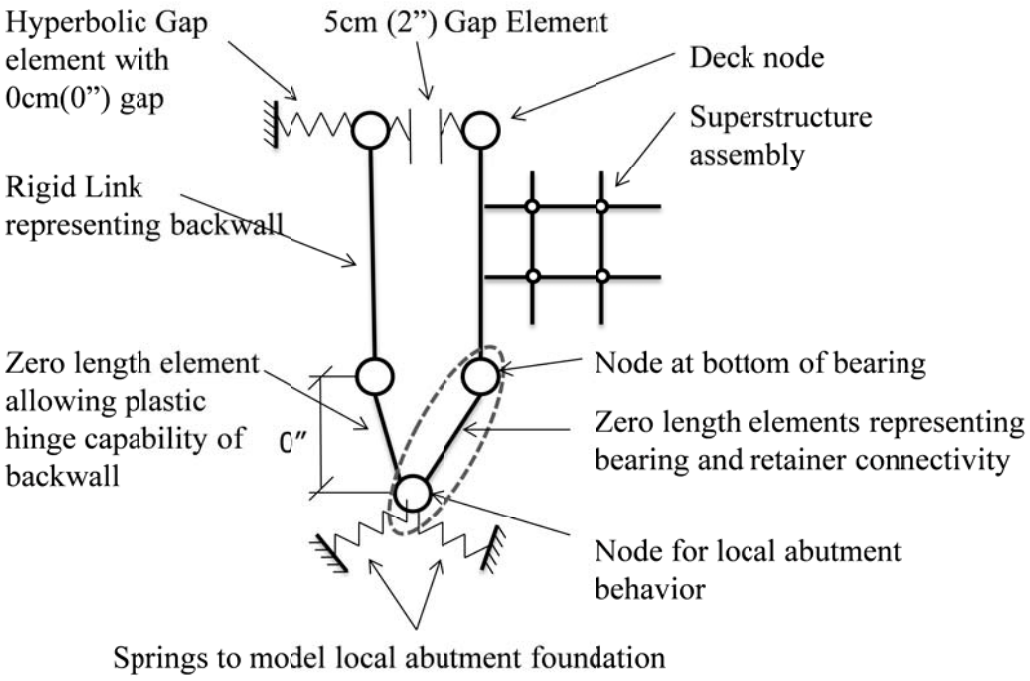

Figure 2.29 Modeling scheme of backwall and abutment elements

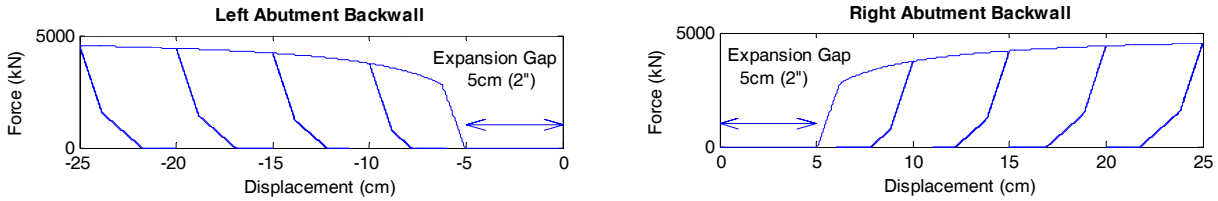

Figure 2.30 Force displacement behavior of the two abutments for a cyclic analysis of the backwall

CHAPTER 3

COMPUTATIONAL MODELING OF NONLINEAR BEARING COMPONENTS

The current design procedure from the Illinois Department of Transportation Bridge Manual (IDOT 2009), has several requirements for the design of different bearings which can be used on a typical bridge. For the bridges in the parametric study, the most important components are the Type I and Type II elastomeric bearings, the low-profile fixed steel bearings (used at only one intermediate substructure) and the side retainers. This chapter describes design recommendations for each component; it outlines the new elements formulated for modeling each behavior, and provides observations, calibrations and validations with available experimental data. For in-depth details on the formulation of the new elements the reader can reference Appendix A, or the source codes made available on the OpenSees repository (OpenSees various authors 2011).

The first stage of this research project, which will be documented extensively elsewhere, has investigated the various bearings and has provided data to be used for model calibration and validation (Steelman et al. 2011). Bearing tests were conducted in the Newmark Structural Engineering Laboratory (NSEL) at the University of Illinois at Urbana-Champaign. Two 100 kip actuators, which are attached to a steel reaction frame as shown in Figure 3.1, were used to apply a vertical load simulating the girder dead load from a bridge. A 220 kip actuator, which was attached to concrete abutments anchored to the strong floor, was used to apply a horizontal load on a loading beam attached to the bearing specimen, and thus to simulate seismic loads and displacements. This actuator has a stroke of +/- 15 in. and a maximum velocity approaching 4 in./sec, which allowed the testing apparatus to capture the PTFE friction response when subjected to high strain-rate loading. The loading beam was limited to unidirectional motion and only this unidirectional data was available for model validation and calibration.

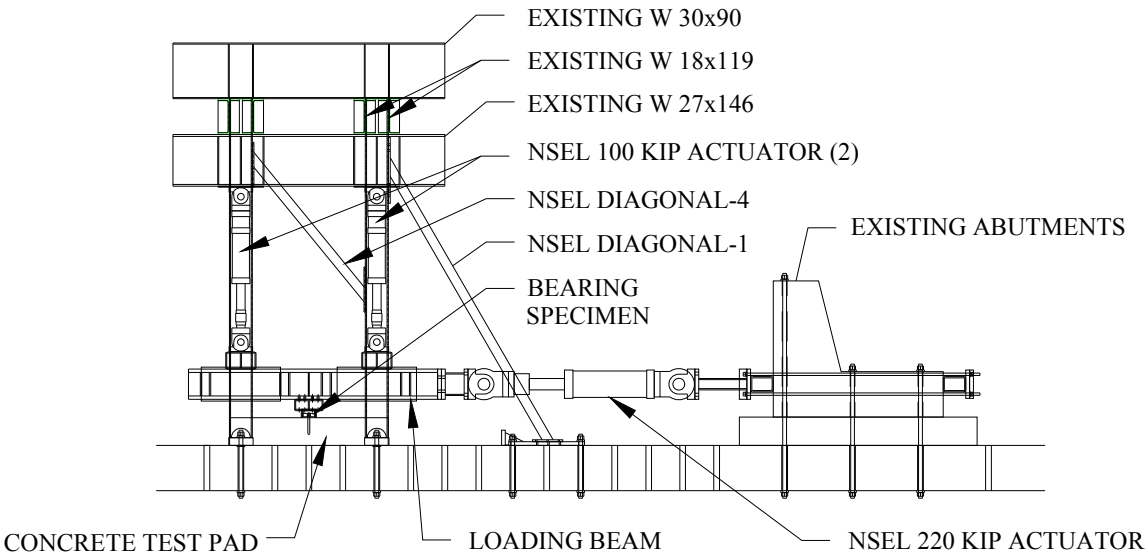

Figure 3.1. Elevation view of test frame setup

3.1 Sliding bearings model

The isolation bearings are divided into different categories depending on the deck expansion distance required. The Type I bearings shall be limited to expansion lengths of 23 m (75 ft) or less for the 15 cm (6 in.) wide and 61 m (200 ft) or less for the 38 cm (15 in.) wide bearings. The Type II assemblies allow up to 45.7 m (150 ft) of expansion length for the 15 cm (6 in.) wide bearing and 122 m (400 ft) for the 38 cm (15 in.) wide bearings.

The design of the bearings is governed by four main parameters:

1. Dead load reaction.
2. Dead load plus live load reaction.
    a. Impact not included.
3. Expansion length.
    a. Distance from fixed bearing to expansion bearing.
4. Percent slope due to nonparallel surfaces.
    a. Dead load rotation.
    b. Camber of prestressed beams.
    c. Profile grade of beam.

For the purpose of this project only the first three parameters listed above are considered; skewed and curved bridges are not studied in much detail and the slope design recommendations

are not considered. The basic design can be completed by choosing a bearing from Figures 3.7.4-21 and 3.7.4-22 from the IDOT design manual (IDOT 2009) that fits all of the following requirements:

- The total effective rubber thickness (*ERT*) of the elastomer shall be a least 2 times the total movement for the Type I bearing, where the *ERT* is defined as the summation of the individual layers of rubber including the top and bottom layers.
- For the Type II bearing, the ERT need only be equal to the total movement, due to the use of the Teflon and stainless steel sliding surfaces.
- The width of the bearing parallel to the direction of movement shall be at least 3 times the total effective rubber thickness.
- The stress due to dead load shall be between 1.38 and 3.4 MPa (200 and 500 psi)
- The stress due to dead load plus live load without impact shall be between 1.38 and 5.5 MPa (200 and 800 psi).

Alternatively a designer can choose bearings based on Figures 3.7.4-19 to 3.7.4-19 which simplify the calculations above. The bearings are designed for all the prototype bridges and the chosen bearings are shown in Chapter 5.

3.1.1 Computational implementation of sliding bearings model

To accurately capture three-dimensional bridge behavior in a numerical simulation, the bearing element models must be capable of properly representing movement in any arbitrary direction in plan. As a result, a bearing model that is defined by uncoupled behavior in two orthogonal directions would not be fully suitable, and would likely result in underestimating system displacements and overestimating forces, as has been shown in previous research (Mosqueda, Whittaker, and Fenves 2004). Past models (Constantinou, Mokha, and Reinhorn 1990) are available that were created to capture the bi-directional sliding behavior of a stainless steel-to-PTFE surface, and that can exhibit coulomb friction sliding as well as the higher initial friction break-off force that is common for slip initiation at this material interface. When either in a pre-slip or sliding configuration, this model returns a force opposing the direction of incremental displacement (model velocity) and essentially resists sliding. This is conceptually appropriate for PTFE bearings, and the model has been successfully validated with experimental data. Constantinou et al. 1990 have also shown that the break-off coefficient of friction is often insignificant for PTFE bearings, since the kinetic coefficient of friction for these bearings can

exceed the static coefficient when the model is experiencing high velocities, as is common with earthquakes.

Further study by (Nagarajaiah, Reinhorn, and Constantinou 1991) has extended the above formulation for coulomb friction (removing initial break-off due to its insignificance for PTFE bearings), leading to models applicable for simulating the response of friction pendulum sliding systems. Using new solution algorithms, the authors successfully implemented their model in three-dimensional space and, by accounting for axial force influence, were able to show an accurate prediction for a scaled shake table experiment. These friction sliding models have been adapted in many modern analysis programs, and have been the baseline for sliding bearing research in recent years.

The models from previous research, though applicable for modeling typical PTFE sliding, are not particularly well-suited for the bearings used in this research program. First, since the formulations described above are force-based, using model velocity to switch between static and sliding behavior, they are more appropriate for capturing only the sliding response, rather than the entire bearing deformation behavior. Furthermore, although initial friction break-off force has been explored for PTFE bearings Constantinou et al. 1990, some recent experimental cases (Steelman et al. 2011) have shown that not only the initial, but also the post-slip, friction break-off force (i.e., the break-off force that occurs following sliding and subsequent unloading/reloading) can exceed sliding force magnitudes at the elastomer-to-concrete interface, which cannot be readily captured using existing models. Finally, current models cannot capture any additional capacity that may be of importance to overall bearing behavior. A bi-directional displacement-based formulation is capable of overcoming all these issues, and is therefore implemented in OpenSees to model the complex nonlinear behavior of the bearings, including elastomer shearing, sliding at elastomeric and PTFE interfaces, and plastic deformation and failure of fixed bearings. These bearing models have been formulated based on types of behavior noted from previous studies in the literature (M. Constantinou, Mokha, and Reinhorn 1990; Higashino et al. 2003), and also on the ongoing laboratory testing of bearings that comprises another facet of this current project (Steelman et al. 2011).

The behavior for translation in the local x and z directions is defined using the force-displacement scheme shown in Figure 3.2. The combined force (P_{MODEL}) is the resultant of the transverse and longitudinal forces (P_{X_1} and P_{Z_1}, respectively). Early in the response history,

bearing stiffness is defined as $E_{INITIAL}$, and the bearing has a combined strength equal to the initial static friction break-off strength (P_{SI}) plus an added initial strength ($P_{INITIAL}$). P_{SI} is simply determined as the axial load on the bearing multiplied by the initial static coefficient of friction (μ_{SI}), while $P_{INITIAL}$ is a user-defined variable to account for additional break-off strength, such as of anchor bolts that need to fracture for a bearing to begin sliding. When the model displacement of the bearing reaches $\Delta_{INITIAL\_BREAK}$, the element exceeds the combined initial break-off force, so it then begins sliding (and is in a kinetic configuration).

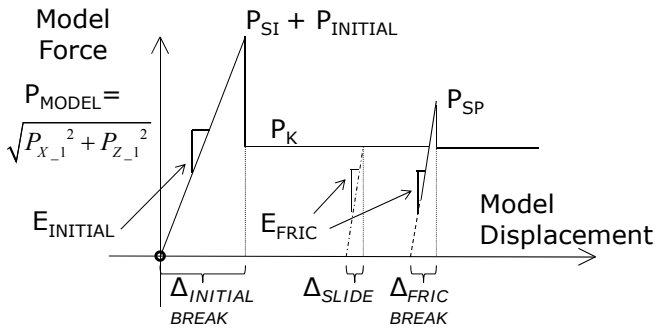

Figure 3.2. Bi-directional force-displacement model for combined *x* and *z* element translation

Once the bearing is in a kinetic state, the model stiffnesses in the *x* and *z* directions are each assigned a small positive value ($E_{INITIAL}$/100,000), and the combined bi-directional force is equal to P_K, which is the axial force on the bearing multiplied by the kinetic coefficient of friction (μ_K). For every sequential step after the bearing has begun sliding, the state of the bearing must be determined – whether it remains in the kinetic configuration and continues to slide, or if it enters a post-slip static configuration. To check for continued sliding, a kinematic hardening type of surface is used, as shown in Figure 3.3, where the stressed position of the top of the bearing in the previous converged state is located at (Δ_{X_0}, Δ_{Z_0}). The next converged state is estimated to be at (Δ_{X_1}, Δ_{Z_1}), which is oriented at an angle θ_1 from the previous state. The bearing location in the *x* and *z* directions are traced using the plastic deformations ($\Delta_{P\_X\_0}$, $\Delta_{P\_Z\_0}$), which specify the location the bearing would return to if the horizontal force went to zero. The top of bearing deformation for the previous converged state is oriented at θ_0 from ($\Delta_{P\_X\_0}$, $\Delta_{P\_Z\_0}$) towards (Δ_{X_0}, Δ_{Z_0}). The bearing continues sliding if either Equation 3.1 or 3.3

is satisfied, and if it does, the plastic deformations are updated based on Equations 3.4 and 3.5 to trace the path of the bottom of the bearing.

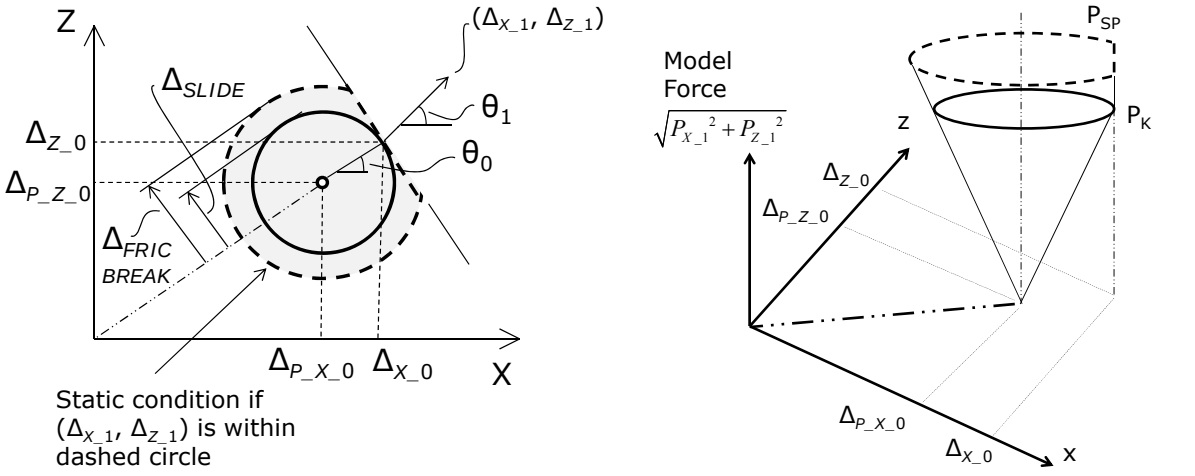

(a) bi-directional displacement representation

(b) three-dimensional force-displacement representation

Figure 3.3. Schematic representation governing continued sliding

$$\Delta_{COMB} > \Delta_{FRIC\_BREAK} \tag{3.1}$$

where

$$\Delta_{COMB} = \sqrt{(\Delta_{X\_1} - \Delta_{P\_X\_0})^2 + (\Delta_{Z\_1} - \Delta_{P\_Z\_0})^2} \tag{3.2}$$

$$|\theta_0 - \theta_1| < \frac{\pi}{2} \tag{3.3}$$

$$\Delta_{P\_X\_1} = \Delta_{X\_1} - \Delta_{SLIDE} * \frac{(\Delta_{X\_1} - \Delta_{P\_X\_0})}{\Delta_{COMB}} \tag{3.4}$$

$$\Delta_{P\_Z\_1} = \Delta_{Z\_1} - \Delta_{SLIDE} * \frac{(\Delta_{Z\_1} - \Delta_{P\_Z\_0})}{\Delta_{COMB}} \tag{3.5}$$

The model continues to simulate sliding behavior so long as the direction of movement does not change. If the movement reverses direction, then the model enters a post-slip static configuration. Once in a static configuration, the bearing stiffness becomes E_{FRIC}, and the bearing remains stationary until the force exceeds the post-slip static friction break-off force

(P_{SP}), defined as the axial force multiplied by the post-slip static coefficient of friction (μ_{SP}). The stiffness matrix used for the model is 12x12 (necessary for three-dimensional simulation), but only eight terms pertinent to the orthogonal x and z displacements actually change values between $E_{INITIAL}$, $E_{INITIAL}$/100,000, and E_{FRIC} depending on the model configuration. The combined model force (P_{MODEL}) returned by the element is distributed in the orthogonal directions per Equation 3.6 and is equivalent to P_K if the model is sliding, or to $\Delta_{COMB} * E_{INITIAL}$ or $\Delta_{COMB} * E_{FRIC}$ if the model is in one of the static conditions.

$$\left\{P_{X\_1}, P_{Z\_1}\right\}^T = \frac{P_{MODEL}}{\sqrt{(\Delta_{X\_1} - \Delta_{P\_X\_1}) + (\Delta_{Z\_1} - \Delta_{P\_Z\_1})}} \left\{(\Delta_{X\_1} - \Delta_{P\_X\_0}), (\Delta_{Z\_1} - \Delta_{P\_Z\_0})\right\}^T \quad 3.6$$

3.1.2 Experimental observations of Type I bearings

To verify that this model can realistically approximate the actual stick-slip friction behavior of various bearings, it has been used to simulate several representative experiments. Comparisons of numerical simulations with experimental results from (Steelman et al. 2011) are shown in Figure 3.4 . The bearings in Figure 3.4 (a), (b), and (c) had vertical loads of 187 kN (42 kips) which corresponds to the design stress of the imposed vertical loads of 187 kN (42 kips), and they are the Type I elastomeric bearings used by IDOT. Overall, the bearing element model can capture these physical behaviors quite well, accounting for different vertical loads on the bearings as well as variations in the coefficient of friction. The model is also adaptable to many different scenarios, such as cases with a high post-slip static break-off force or where the post-slip break off force is the same as the kinetic force.

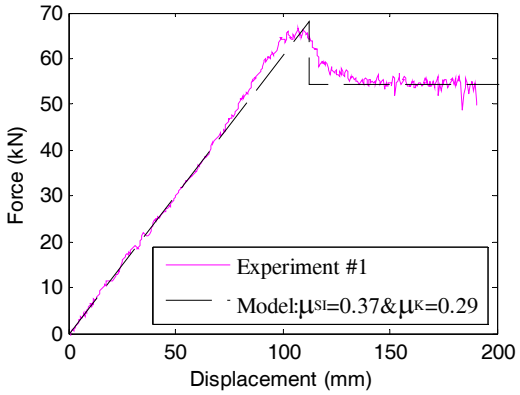

(a) force-displacement relations from monotonic longitudinal loading of Type I 7-c bearing

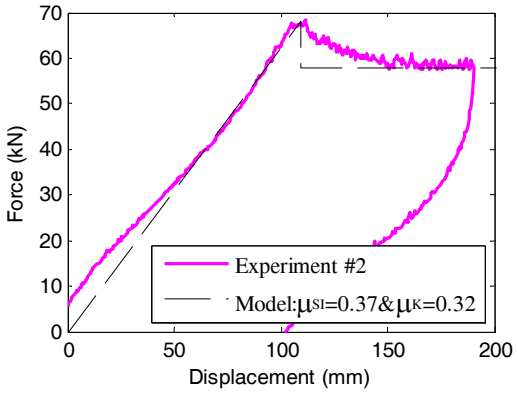

(b) force-displacement relations from monotonic longitudinal loading of Type I 7-c bearing

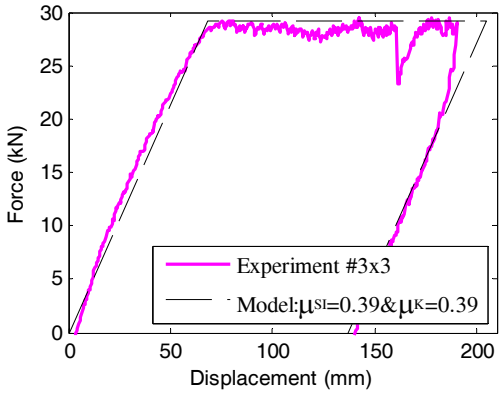

(c) force-displacement relations from monotonic longitudinal loading of Type I 7-c bearings that does not exhibit friction break off

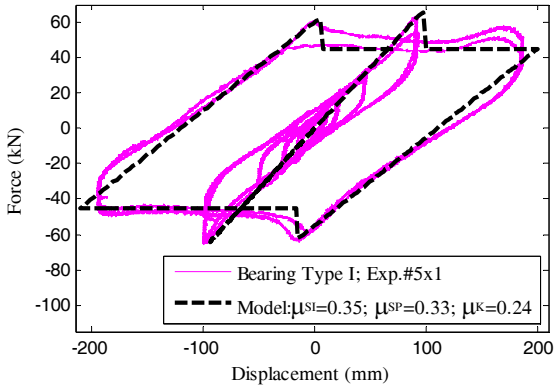

(d) force-displacement relations from cyclic longitudinal loading of Type I 7-c bearings that exhibits initial and post-slip friction break off

Figure 3.4. Demonstration of the zero-length bi-directional element and best fit to several noteworthy experiments of Type I bearings

The bi-directional element model capable of simulating bearing nonlinearities is placed in the prototype bridge model as shown in Figure 2.1, with the specific bearing behaviors defined based on preliminary experimental findings (Steelman et al. 2011). Type I bearings are used for the prototype bridge, designed based on recommendations from the IDOT bridge manual (IDOT 2009). Type I 9-b bearings with a plan area of 700 cm^2 (108 in.^{2}), and an effective rubber thickness (ERT) of 6.7 cm (2.6 in.), were used at the abutments (where design was governed by temperature expansion requirements). The ERT is the total thickness of the bearing minus that of

the steel shims. Type I 11-a bearings with a plan area of 1140 cm^2 (176 $in.^2$), and an ERT of 5 cm (2 in.), are used at the first intermediate pier (where the dead + live load combination governed the bearing size). Based on the experimental results, coefficient of friction values of $\mu_{SI} = 0.45$, $\mu_K = 0.30$, and $\mu_{SP} = 0.35$ have been used for the Type I bearings. The shear stiffness of the elastomeric bearings is calculated as:

$$K = \frac{G * A}{ERT} \tag{3.7}$$

Where:

G=Shear modulus of bearings

A= Bearing area

ERT = Effective rubber thickness

A shear modulus of 585 kPa (85 psi) was used for all elastomeric bearings based on the experimental results (Steelman et al. 2011).

3.1.3 Experimental observations of Type II bearings

The same model as defined earlier is also applicable for the Type II bearings when they remain within a particular displacement range. These bearings also showed reliable sliding behavior, however at large top plate displacements these bearings became nonlinear and unstable, requiring increasingly larger forces to re-center the bearing (Figure 3.5 (a) and (b)). This instability is believed to rapidly move the bearing into an unseated configuration, where the model as shown in Figure 3.2 will become invalid. This response is considered to be unacceptable for a quasi-isolated bridge and is addressed in further detail in Chapter 6. Figure 3.5 (a) and (b) show slow cyclic pushovers of the Type II behavior for a 7-c bearing subject to a vertical load of 187 kN (42 kips). Figure 3.5 (c) shows the same bearing subjected to a fast loading 7.5 cm/sec (3 in. /sec), and thereby the coefficient of friction is higher. Finally Figure 3.5 (d) has a validation with experimental data presented by (M. Constantinou, Mokha, and Reinhorn 1990), where a flat PTFE bearing pad was tested with an axial compression load of 350 kN (78.5 kips). Based on the experimental results, coefficient of friction values of $\mu_{SI} = 0.16$, $\mu_K = 0.15 = \mu_{SP} = 0.15$ have been used for the Type II bearings and the stiffness is again calculated per Equation 3.7.

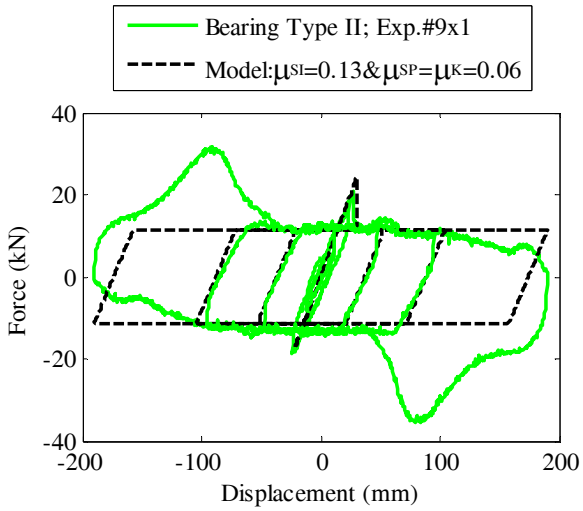

(a) force-displacement relation from longitudinal cyclic loading of a Type II bearing

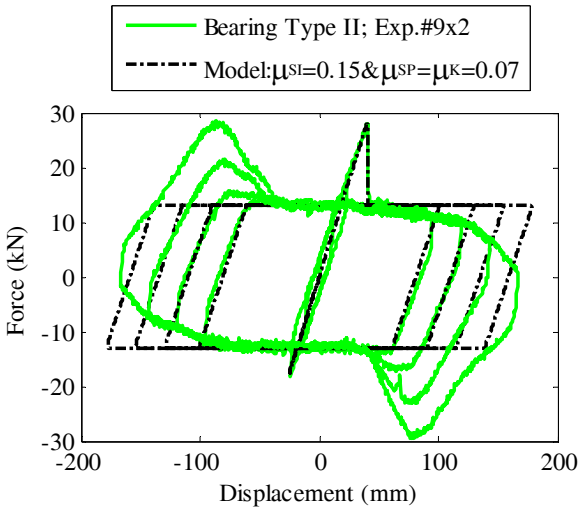

(b) force-displacement relation from Teflon bearings

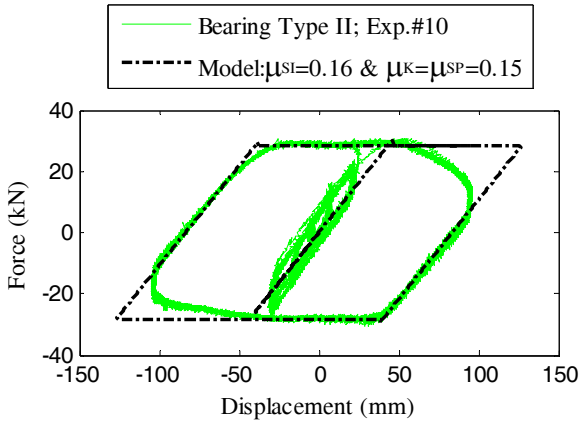

(c) force-displacement relation from longitudinal cyclic loading of a Type II bearing

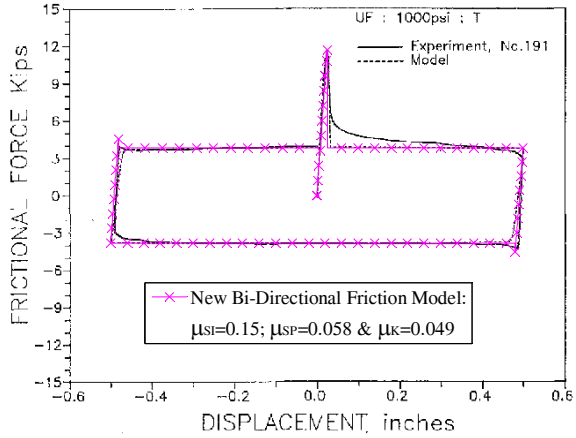

(d) force-displacement relation from Teflon bearings (M. Constantinou, Mokha, and Reinhorn 1990)

Figure 3.5. Demonstration of the zero-length bi-directional element and best fit to several noteworthy experiments of Teflon bearings

3.1.4 Bearing models subjected to dynamic excitation

The bi-directional bearing model was also verified with experimental data from Mokha et al.(1993) where PTFE bearings were subjected to dynamic bi-directional motion. Figure 3.6

shows the bi-directional displacement protocol that was used to test the Teflon bearing with elliptic excitation. The protocol was simulated with the bi-directional bearing element presented earlier and the model was found to provide a good estimate of the bearing behavior.

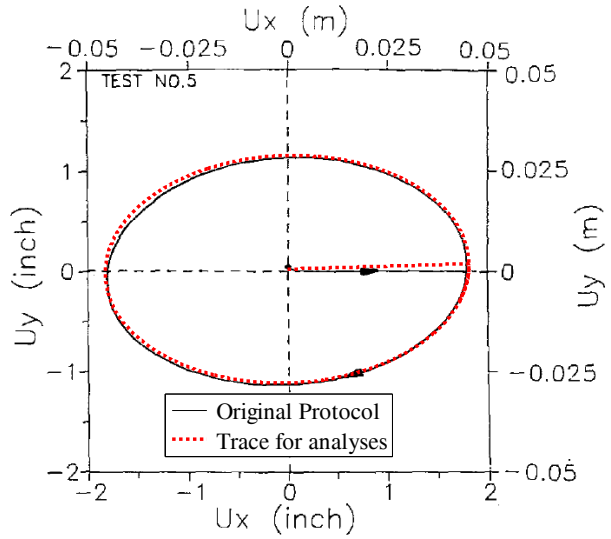

Figure 3.6. Displacement protocol for elliptic time variable excitation (Mokha et al. 1993)

Figures 3.7 and 3.8, show the force-displacement behaviors of the bearing element in the x and y directions respectively. Test # 2 from the experimental program was used for the model verification.

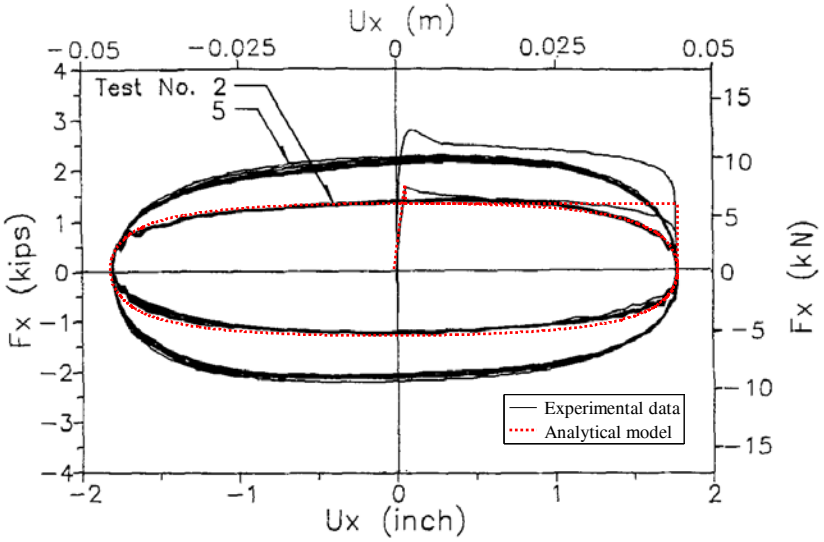

Figure 3.7. Bearing model and experimental force-displacement results (Mokha et al. 1993) in the x direction from elliptic time variable excitation

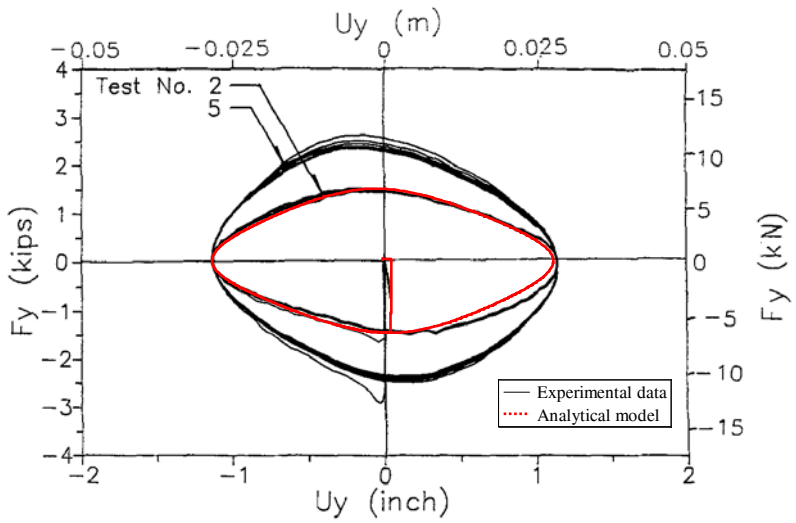

Figure 3.8. Bearing model and experimental force-displacement results (Mokha et al. 1993) in the y direction from elliptic time variable excitation

The experiments presented by (Mokha et al. 1993) also include bearings tested to time dependent earthquake motions from the 1985 Mexico City earthquake recorded at the SCT building. These include both uni-directional experiments, as well as bi-directional tests where two distinct ground motions are applied simultaneously in two orthogonal directions. Due to limitations of the shake table used, the velocity of the experiment was reduced by a factor of two and the displacement was reduced by a factor of four. The experimental results with analytical approximations for the uni-directional excitations are shown in Figures 3.9 and 3.10, and Figures 3.11 and 3.12 show the result for coupled bi-directional motion. In general it can be noted that the bearing model performs well for the time dependent analyses and it captures bidirectional interaction effectively. The velocity dependence effects appear to have little influence on the overall friction behavior even for the ground motion that is scaled down in velocity. This can be attributed to the fact that earthquake ground motions typically have higher velocities than the threshold at which the velocity dependence of Teflon bearings have a significant influence.

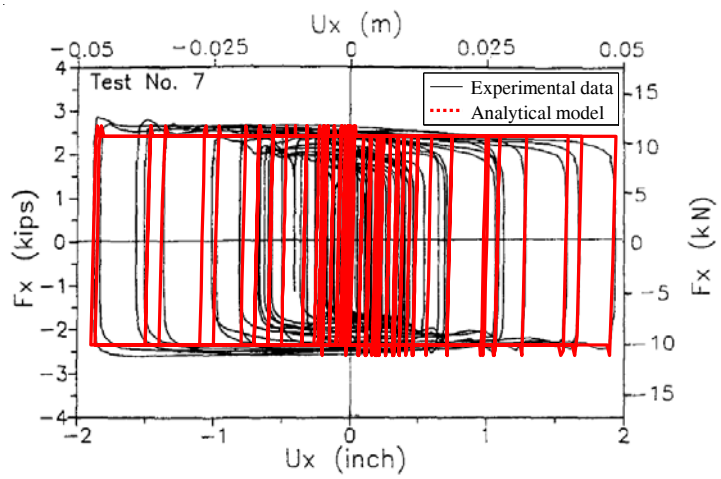

Figure 3.9. Bearing model and experimental force-displacement results (Mokha et al. 1993) in the x direction where only the Ux excitation from the Mexico City ground motion record was applied

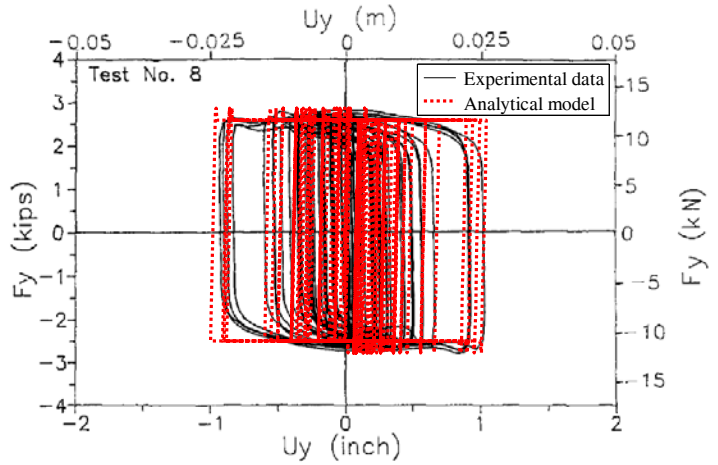

Figure 3.10. Bearing model and experimental force-displacement results (Mokha et al. 1993) in the y direction where only the Uy excitation from the Mexico City ground motion record was applied

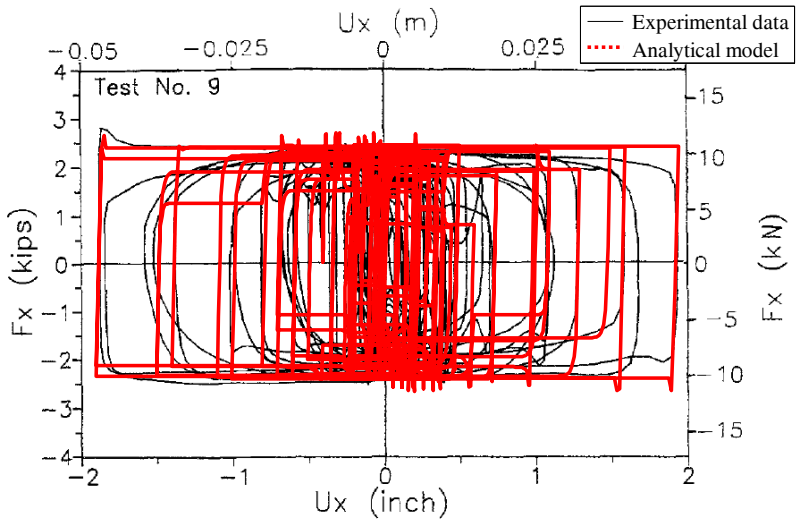

Figure 3.11. Bearing model and experimental force-displacement results (Mokha et al. 1993) in the x direction where both the Ux and Uy excitations from the Mexico City ground motion record were applied

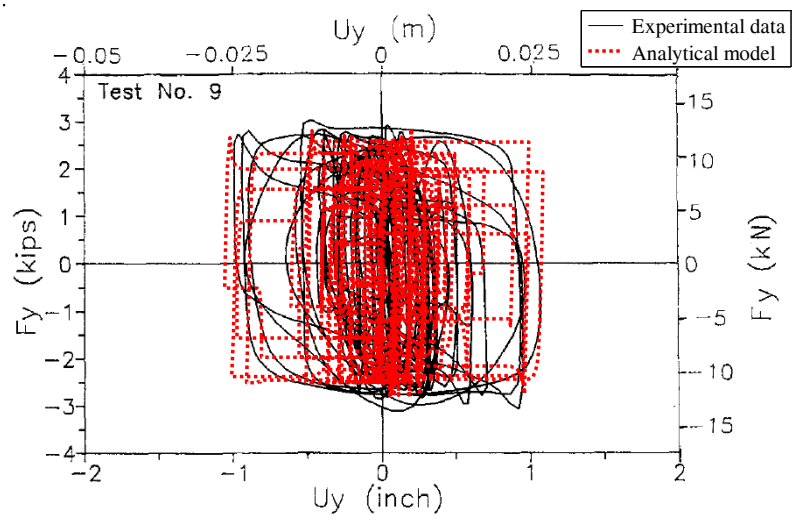

Figure 3.12. Bearing model and experimental force-displacement results (Mokha et al. 1993) in the y direction where both the Ux and Uy excitations from the Mexico City ground motion record were applied

3.2 Low-profile fixed bearing /anchor bolt model

Low-profile steel bearings shown in Figure 3.13 are installed at one of the intermediate substructures to prevent global movements of the bridge deck due to serviceability-level loads.

These bearings are normally placed on a 3.2 mm (0.125 in.) elastomeric neoprene leveling pad and are attached to the substructure using anchor bolts.

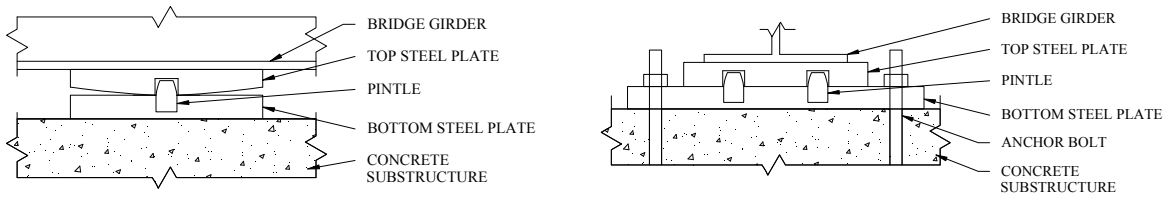

(a)Transverse view (b) Longitudinal view

Figure 3.13. Elevation views of low-profile fixed bearings investigated in this research

The current design procedure from the Illinois Department of Transportation Bridge Manual (IDOT 2009), states that the connection of the superstructure to the substructure for bridges in Seismic Performance Zone 1 (LRFD) or Seismic Performance Category A (LFD) shall be designed to withstand the total horizontal forces equal to 20% of the dead load reactions of the superstructure (R-Factor = 1.0) regardless of the specified design earthquake return period, 1000 or 500 yrs. This approach is used for the design of the pintles and anchor bolts for the fixed bearings, as well as the retainers discussed in Section 3.3.

IDOT provides a simple method for nominally designing the anchor bolts by considering shear as the only failure mode. For this approach, the number of anchor bolts required along each beam line is given by the following equation.

$$N = \frac{C_{il} * (DL)}{P_{COMPONENT}} \tag{3.8}$$

Where:

N = number of connecting components (anchor bolts or pintles) required for the given bearing under consideration

DL = superstructure dead load at the given bearing under consideration

C_{il} = 0.2 (20%) for SPZ 1 to 4 (LRFD) and SPC A to D (LFD)

$P_{COMPONENT}$ = the allowable shear force per anchor bolt (P_{FIXED_AB}) or pintle (P_{PINTLE}) for seismic loadings

The anchor bolt capacity (P_{FIXED_AB}) can then be calculated as:

$$P_{FIXED\_AB} = \varphi 0.48 A_b F_u \tag{3.9}$$

with φ = 0.75. A_b is the nominal bolt diameter, and F_u is the specified material ultimate stress. Note that the factor of 0.48 in Equation 3.9 is the product of 0.8 and 0.6. The 0.8 is placed to account for the reduced area of the bolt from the thread cut-out, and the 0.6 is used to reduce the strength based on the expected shear failure mechanism. The steel pintles are designed using essentially the same equations except the pintle capacity (P_{PINTLE}) is calculated as

$$P_{PINTLE} = \varphi 0.6 A_b F_y \tag{3.10}$$

with φ = 1.0 and F_y is the specified material yield strength of the material. Furthermore, the pintles are limited to a minimum diameter of 32 mm (1.25 in.). The minimum pintle size specification typically results in bearings where the anchor bolts are smaller than the pintles and this is expected to cause the anchor bolts to be the more critical component that will fail first in an earthquake.

3.2.1 Computational implementation of low-profile fixed bearing / anchor bolt model

The nonlinear elasto-plastic deformation of the pintles and anchor bolts, as well as the friction between the bearing components and substructure are expected to be an important consideration for this element. Currently there is only a small amount of research available that has investigated low-profile bearings or other components that may exhibit similar behaviors. A new bi-directional element has been created to simulate the elasto-plastic yielding and fracture of steel components, and can be coupled with the friction element shown in section 3.1 of this thesis, to capture all important bearing behaviors. A schematic of the model in Figure 3.14 shows a peak-oriented model based on (Ibarra, Medina, and Krawinkler 2005) with variable pinching that follows a pre-defined elasto-plastic envelope, and is capable of fracturing at a predefined displacement. For initial loading this model uses an elasto-plastic loading curve such that when a force threshold is reached yielding occurs and the model stiffness is reduced. When the model displacement changes direction and unloading begins, the model uses the initial stiffness to calculate forces, until a force of zero is reached. A circular isotropic engagement surface is

implemented such that as the model cycles, the engagement surface expands and the model force increases.

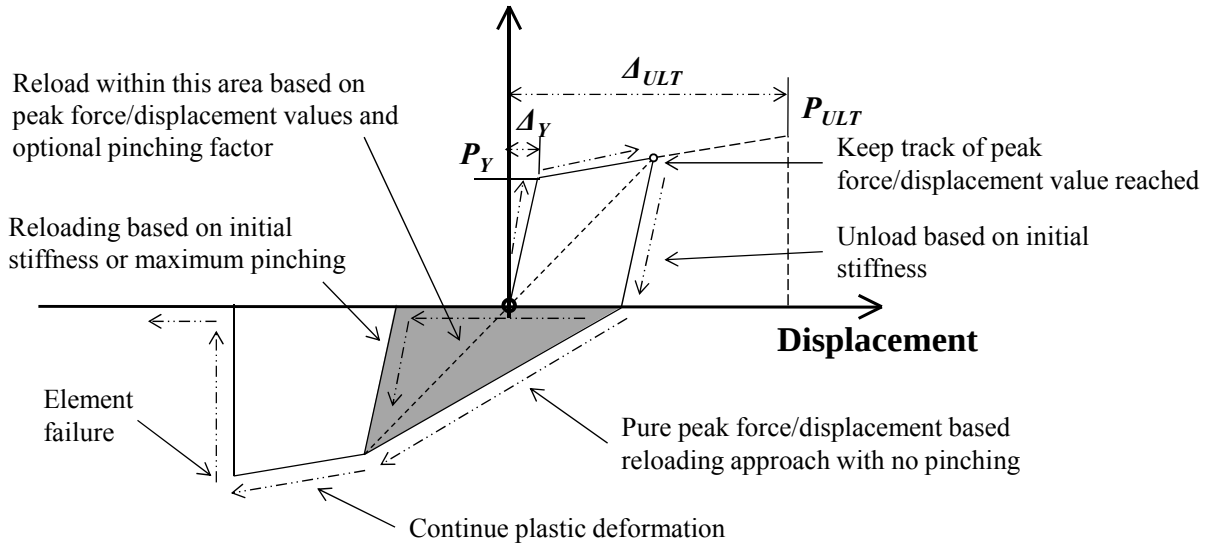

Figure 3.14. Bi-directional peak based force-displacement model for combined x and z element translation

Figure 3.14 shows that four variables are necessary to define the envelope for the fixed bearing model, namely, the yield and ultimate displacements of the model, Δ_Y and Δ_{ULT} respectively, and also the yield and ultimate forces for the model P_Y and P_{ULT} respectively. Additionally the user specifies a pinching factor that influences the reloading behavior. The model has been formulated in bi-directional space such that it couples the force - displacement behavior in the x and z directions. Figure 3.15 – Figure 3.16 show cyclic behavior of the model in bi-directional space when different pinching factors are used. The model is capable of altering the behavior from a pure peak oriented model to a fully pinched hysteresis. Note that although the same elasto-plastic envelope with strain hardening is used for initial loading, the reloading behavior of each model is significantly different. The specified displacement in the z direction is half of that used in the x direction.

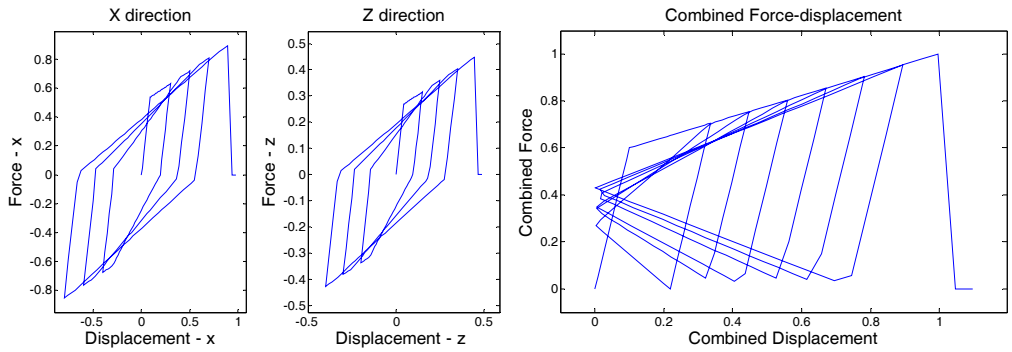

Figure 3.15. General behavior of model with pinching factor of 0.01

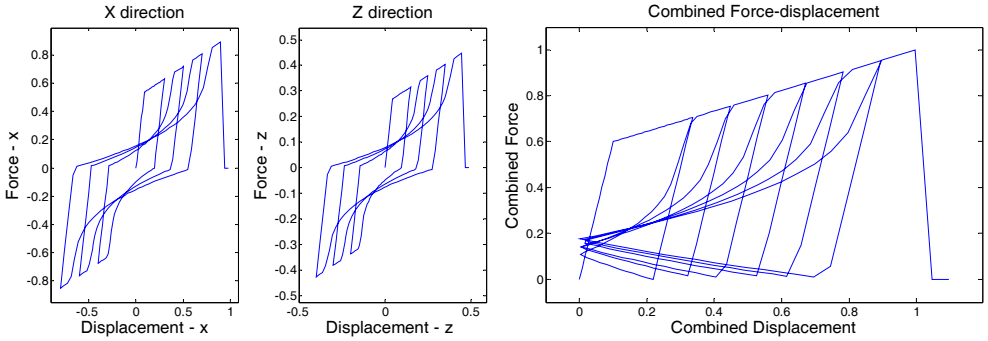

Figure 3.16. General behavior of model with pinching factor of 1

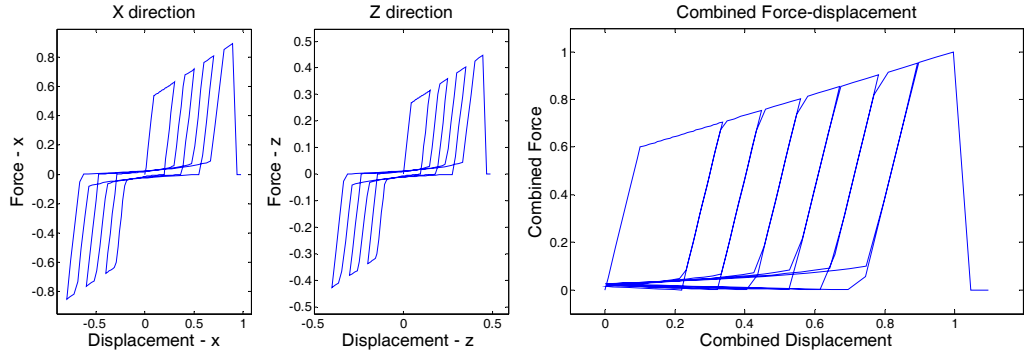

Figure 3.17. General behavior of model with pinching factor of 10

3.2.2 Observations on past experiments of fixed bearing and anchor bolts

Although no bi-directional research has been carried out for such behaviors, the model is implemented in bi-directional space. The elements expected to yield and fracture (anchor bolts and pintles) are circular so they are expected to produce the same response regardless of the direction of loading. Previous research on steel bearings (Mander et al. 1996) has shown similar response for loading in the transverse and longitudinal directions of such components. It is

therefore expected that the bi-directional coupled response would be similar regardless of the loading direction, and the circular engagement surface would be a valid modeling approach.

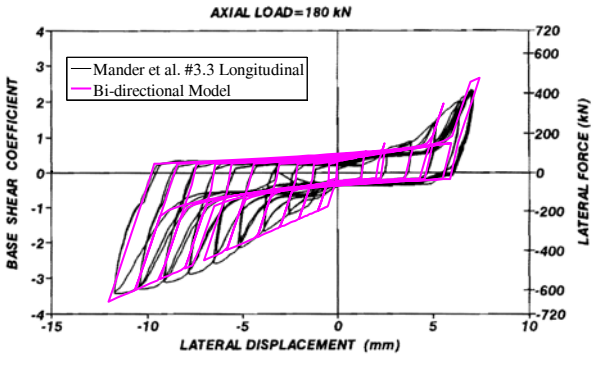

(a) P_{FACTOR}=3; P_Y=140kN; P_{ULT}=630kN; Δ_Y=0.5mm; Δ_{ULT}=12mm; μ_K=0.2

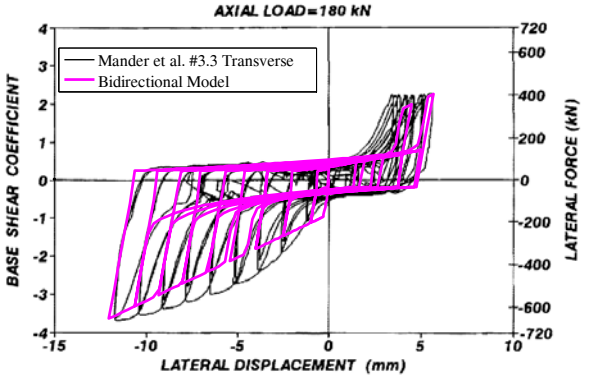

(b) P_{FACTOR}=3; P_Y=140kN; P_{ULT}=630kN; Δ_Y=0.3mm; Δ_{ULT}= 12mm; μ_K=0.2

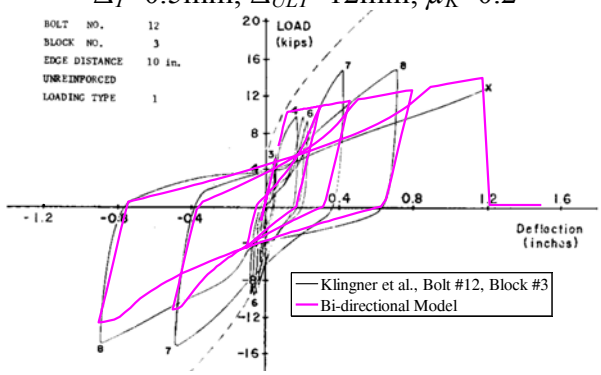

(c) P_{FACTOR}=0.3; P_Y=35.6kN; P_{ULT}=49kN; Δ_Y=3mm; Δ_{ULT}=30.5mm

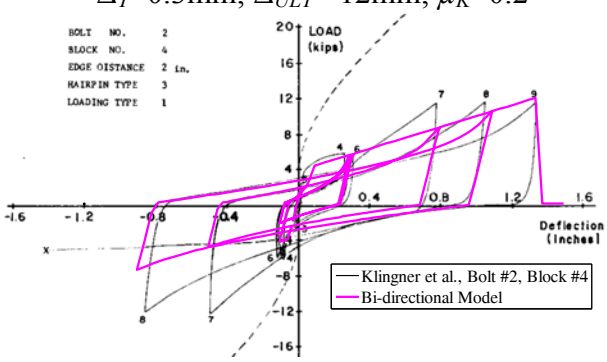

(d) P_{FACTOR}=0.3; P_Y=18kN; P_{ULT}=53kN; Δ_Y=1.3mm; Δ_{ULT}=34mm

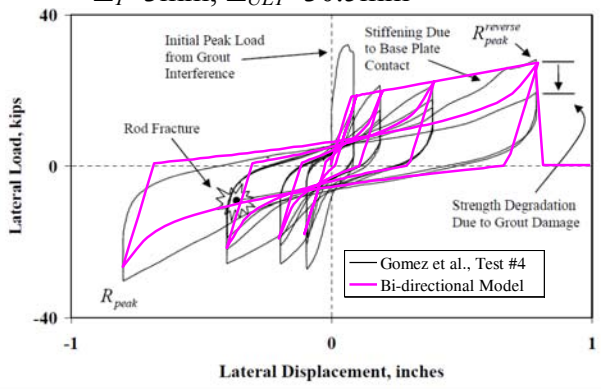

(e) P_{FACTOR}=0.8; P_Y=80kN; P_{ULT}=120kN; Δ_Y=2mm; Δ_{ULT}=20.4mm

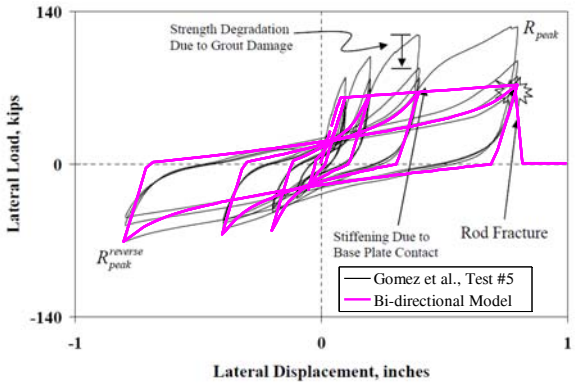

(f) P_{FACTOR}=0.5; P_Y=267kN; P_{ULT}=320kN; Δ_Y=2mm; Δ_{ULT}=20.4mm

Figure 3.18. Demonstration of the zero-length bi-directional fixed bearing element and best fit to several noteworthy experiments

The model was used to simulate experiments that are believed to have similar hysteretic behaviors to what would be expected from the low-profile steel bearings used for a quasi-isolation system. (Mander et al. 1996) tested low-profile steel bearings, and constrained deformation and fracture to the pintle components by using large over strength anchoring elements. The behavior was matched with the new bi-directional model as shown in Figure 3.18 (a) and (b), where the friction was implemented in parallel with the anchor bolt element. Figure 3.18 (c) and (d), show the model used to simulate cyclic shear tests of individual anchor bolts embed in concrete (Klinger, Mendoca, and Malik 1982), and Figure 3.18 (e) and (f), shows a simulation of the shear loading of a steel base plate that is attached to a base with grout and four anchor bolts (Gomez et al. 2009). The elements tested in past research tend to provide a similar range of shear strength capacities that can be estimated based on the size of the connecting element, the material strength and modern design equations.

As part of Stage 1 of this project, several preliminary models of the fixed bearings were created using Abaqus (Abaqus FEA 2010). The models include material and geometric nonlinearity, as well as contact interactions between elements ranging from hard contact with friction-slip behavior to mechanical or chemical perfect bond. Damage evolution models available in Abaqus/Explicit have also been included to define ranges of material strength degradation, and in so doing to mimic the global effect of crack formation and material fracture. Steel elements were modeled with an elastic-plastic hardening effect, and subsequent softening was modeled using damage evolution (i.e., due to tension and/or shear fracture). The Abaqus models capture the behavior of concrete subjected to both compressive crushing and tension cracking as a result of force interactions with the embedded anchor bolts, as well as an epoxy layer at the interface of the embedded steel anchor and concrete. A piecewise linear approximation of the Popovics (Popovics 1973) pre- and post-peak compression and the Collins-Mitchell (Collins and Mitchell 1991) tension stiffening models were used to simulate concrete behavior.

Figure 3.19 below shows a visualization of the von Mises stress contours obtained from preliminary Abaqus analyses of the low-profile fixed bearings. The simulation employs three distinct components: top plate, pintle, and bottom plate. The top plate was moved laterally in displacement control. Hard contact with friction is modeled at all interfaces, and a damage evolution model was used to represent material rupture behavior in the pintle. Note that in

Figure 3.19 (a) a large amount of shear is carried from the top plate through the pintle and into the bottom plate, whereas in Figure 3.19 (b) the pintle elements have degraded and shear is transferred primarily through friction between the two plates.

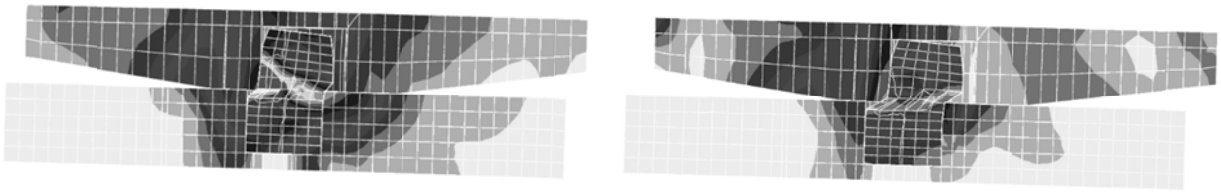

(a) Incipient pintle shear failure (b) After shear failure

Figure 3.19. Shear failure at low-profile fixed bearings

Table 3.1 presents a summary of the available experimental data, as well as the preliminary model results from the Abaqus analyses. Yield and ultimate displacement values Δ_Y and Δ_{ULT} respectively, are recorded and averaged for the different experiments. The yield and ultimate force variables used for the modeling P_Y and P_{ULT}, are compared to values predicted from a typical design equation as defined per

$$P_{ULT\_PREDICTED} = A_{b\_REAL} * F_u \tag{3.11}$$

where the area of the element (A_{b_REAL}) was adjusted based on the existence of bolt threads if any. It was noted, that by using a factor of 0.6 times the predicted ultimate behavior would provide a reasonable approximation of the experimental data. This also corresponds well with the regular design equation for bolts in shear:

$$P_{FIXED\_EXPECTED} = \varphi 0.6 * 0.8 A_b F_u \tag{3.12}$$

Equation 3.12 gives reasonable approximations for the capacities of the elements in previous research. This equation uses the factor 0.8 to account for the reduction of anchor bolt area (A_b) where the nominal diameter is used, and the factor of 0.6 reduces the capacity, assuming a pure shear failure is to occur in the critical components. The slip surface between the steel bearings, felt pad and concrete substructure has not yet been studied as part of this project. Prior research (Gomez et al. 2009; Mander et al. 1996) recommends coefficients of friction of between $\mu_K = 0.20$, and $\mu_K = 0.60$. For this project nominal coefficients were approximated to be $\mu_{SP} = \mu_K = \mu_{SI} = 0.40$ for the friction model coupled with the low-profile bearing code system.

Table 3.1 Summary of experimental and model capacities for various anchor bolt and pintle sizes

Data Source	Experiment/analysis data						Data used to create best fit model approximation								Data for behavior approximations				
	# of pintles /anchorbolts	Nominal diameter (in.)	Pintle/anchor bolt area ($in.^2$)	Nominal Area (As) ($in.^2$)	Material Yield Strength (ksi)	Material Strength (F_u) (ksi)	Yield Displacement (in.)	Yield Strength (kip)	Ultimate Displacement (in.)	Ultimate Strength (kip)	Pinching Factor	Vertical Force (kip)	Friction Force (kip)	Coefficient of Friction	$P_{y\_predicted}$= As*Fy (kip)	$P_{ult\_predicted}$ =As*Fut (kip)	Yield /Diameter	Ultimate/Diameter	$P_y/P_{y\_predicted}$	$P_{ult}/P_{ult\_predicted}$
Klingner et al. - ancor bolts	1	0.75	0.442	0.353	36	61.3	0.2	12	1.2	24.1	N/A	N/A	N/A	N/A	12.7	21.7	0.27	1.60	0.94	1.11
	1	0.75	0.442	0.353	36	61.3	0.12	8	1.2	11	0.3	N/A	N/A	N/A	12.7	21.7	0.16	1.60	0.63	0.51
	1	0.75	0.442	0.353	36	61.3	0.05	4	1.3	12	0.3	N/A	N/A	N/A	12.7	21.7	0.07	1.73	0.31	0.55
	1	0.75	0.442	0.353	36	61.3	0.05	4	1.6	14	0.3	N/A	N/A	N/A	12.7	21.7	0.07	2.13	0.31	0.65
															Average		**0.14**	**1.77**	**0.55**	**0.71**
Mander et al. - pintles	2	1.5	1.767	1.767	36	60	0.02	31.5	0.47	142	3	40.5	8.1	0.2	127.2	212.1	0.01	0.31	0.25	0.67
	2	1.5	1.767	1.767	36	60	0.01	31.5	0.47	142	3	40.5	8.1	0.2	127.2	212.1	0.01	0.31	0.25	0.67
															Average		**0.01**	**0.31**	**0.25**	**0.67**
Gomez et al. - base plates	4	0.75	0.442	0.353	66.8	96.4	0.08	18	0.8	27	0.8	N/A	N/A	N/A	94.4	136.3	0.11	1.07	0.19	0.20
	4	1.25	1.227	0.982	54.4	75	0.08	60	0.8	72	0.5	N/A	N/A	N/A	213.6	294.5	0.06	0.64	0.28	0.24
															Average		**0.09**	**0.85**	**0.24**	**0.22**
Abaqus - Pintle	2	1.25	1.227	1.227	36	58	0.25	27.45	0.53	33.9		40.5	9.1	0.22	88.4	142.4	0.20	0.42	0.31	0.24
Abaqus - Anchor bolts	2	0.75	0.442	0.353	36	70	0.14	11.4	0.4	14.9		40.5	3.4	0.08	25.4	49.5	0.19	0.53	0.45	0.30
															All data average		**0.11**	**1.02**	**0.40**	**0.60**

Without more experimental data it is expected that the proposed nonlinear model with capacity per Equation 3.13 with $\varphi = 1$ and $F_u = 415$ MPa (60 ksi), provides a reasonable estimate for the ultimate capacity of the low-profile bearings. Equation 3.13, with $\varphi = 1$ and $F_y = 250$ MPa (36 ksi) substituted for F_u, were used to estimate the yield capacity of the bearing. Values of $\Delta_Y = 0.1 d_b$ and $\Delta_{ULT} = 1.0 d_b$ were used to estimate the yield and ultimate displacements based

on the anchor bolt diameter (d_b). A detailed formulation of the model is available in Appendix A, and is believed to be easily adaptable to match future experimental data of fixed bearing components.

3.3 Retainer model

The design procedure for the retainers is the same as that for fixed bearings shown in Equation 3.8, where the anchor bolts are designed to provide a capacity of 0.2 times the reaction dead load. IDOT recommends that the individual retainer capacity can be estimated by:

$$P_{RET} = \varphi 0.48 A_b F_u \tag{3.13}$$

where $\varphi = 0.75$.

Assuming that one retainer with only a single anchor bolt (N=1) will be used at the side of a bearing, one can determine the necessary bolt size for the retainers at each bearing. Furthermore at this phase the height of the elastomeric bearing, and the thickness of the top plate of the bearing have already been calculated. The retainer height is proportioned to be at least 1/2" higher than the bearing top plate, and the other retainer dimensions are based on the size of the anchor bolt selected as shown in Figure 3. 20 and Table 3.2.

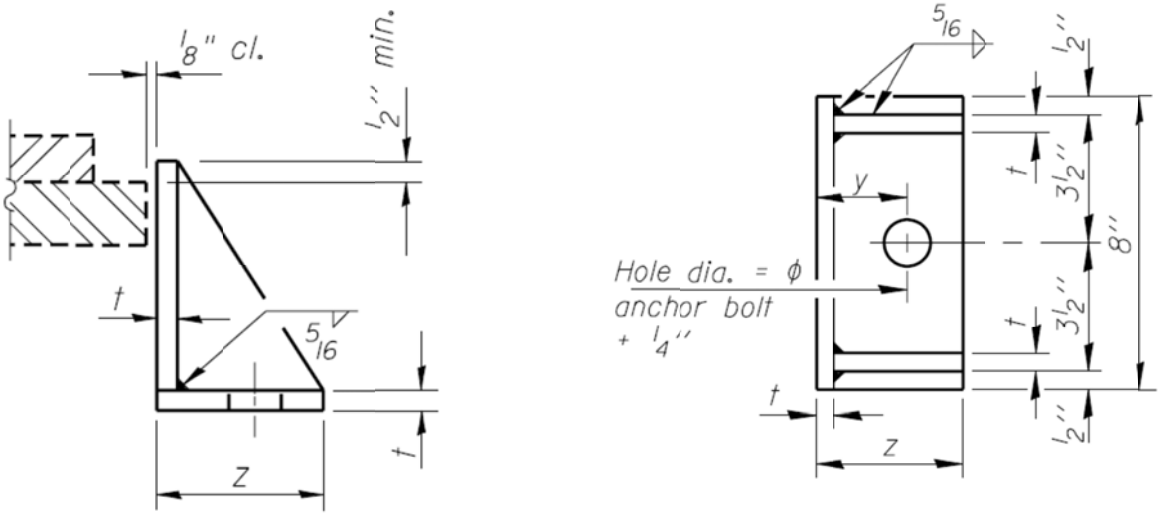

Figure 3. 20– Side retainer details and dimensions (IDOT 2009)

Table 3.2 Standard retainer dimensions

Bolt ϕ	y	z	t
5/8"	1 3/4"	3 1/16"	1/2"
3/4"	1 7/8"	3 3/8"	1/2"
1"	2 1/8"	4"	1/2"
1 1/4"	2 3/8"	4 3/4"	1/2"
1 1/2"	2 3/4"	5 1/2"	5/8"
2"	3 1/4"	6 3/8"	5/8"
2 1/2"	3 3/4"	8 1/8"	5/8"

3.3.1 Computational implementation of retainer model

The retainer force-displacement behavior is modeled using a zero-length element, as shown schematically in Figure 2.2. For the formulation in OpenSees, the user defines the following: a *gap* between the top plate and the retainer, the yield strength of the retainer (P_Y) and corresponding displacement (Δ_Y); and the ultimate strength of the retainer (P_{ULT}) and corresponding displacement (Δ_{ULT}). After the gap is closed, the model enters an elastic loading/unloading state where the element stiffness is E_E. When the yield strength is exceeded, the element experiences plastic deformation and exhibits strain hardening with a stiffness of E_P. Subsequent unloading and reloading of the element follows the initial model stiffness (E_E). When the model reaches its ultimate strength, the retainer stiffness becomes inactive (the element returns a stiffness of E_E/100,000) and its force goes to zero (representing anchor bolt fracture). A retainer model is placed in the transverse direction on each side of the elastomeric bearings, and the two retainers behave independently (as is the case in a real bridge structure). This retainer model is capable of simulating experimental behavior for different anchor bolt sizes, as indicated in Figure 3.22 (Steelman et al. 2011).

For the prototype bridge, retainers are placed at each elastomeric bearing, with anchor bolt and retainer sizes chosen based on design recommendations from the IDOT bridge manual (IDOT 2009) – 16 mm (0.625 in.) diameter anchor bolts for the abutments, and 25 mm (1.0 in.) anchor bolts at the pier with elastomeric bearings. The ultimate retainer assembly capacities (P_{ULT}) are calculated based on the threaded anchor bolt area and ultimate material strength, assuming a tensile failure condition (as was observed during testing). This results in estimated

individual retainer capacities at the abutments of 218 kN (49 kips), corresponding to 71% of the dead load at each bearing, and retainer capacities of 340 kN (76.6 kips) at the intermediate pier, corresponding to 66% of the dead load at those bearings.

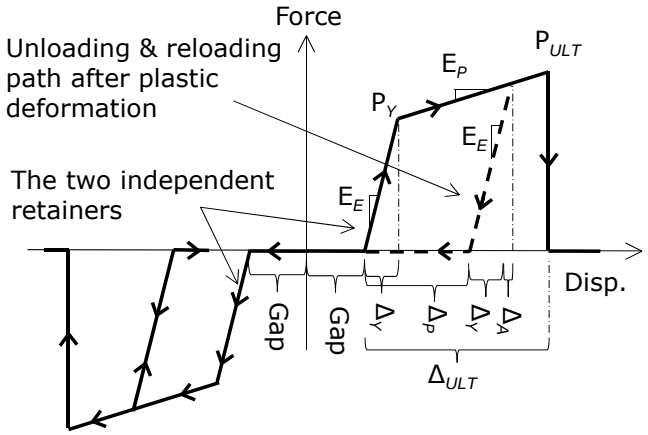

Figure 3. 21 Force-displacement behavior of the element capable of simulating a pair of individual retainers

3.3.2 Experimental observations of retainers

The experimental testing of the retainer bearings is presented in more depth by (Steelman et al. 2011). In the testing of the smaller anchor bolt and retainer assemblies (19 mm (0.75 in.) anchor bolt, Tests 6 and 7), visible damage was limited to the threaded anchor bolt and the concrete near the embedded anchor. For the larger anchor bolt and retainer assemblies (32 mm(1.25 in.) anchor bolt, Tests 11 and 12), concrete crushing was evident at the toe of the retainer, and plastic deformation was seen in the bottom plate of the retainer before a failure occurred in the anchor bolt. The horizontal force-displacement relationships from the experiments are shown in Figure 3.22 and are simulated using the nonlinear model presented earlier. The plots include the *gap*, yield strength of the retainer (P_Y), the yield displacement (Δ_Y), the ultimate strength of the retainer (P_{ULT}), and the ultimate displacement (Δ_{ULT}) used to capture the experimental curve. Note that these variables are defined to obtain the best possible fit of the data, without taking into account any material properties or failure characteristics from the experiment.

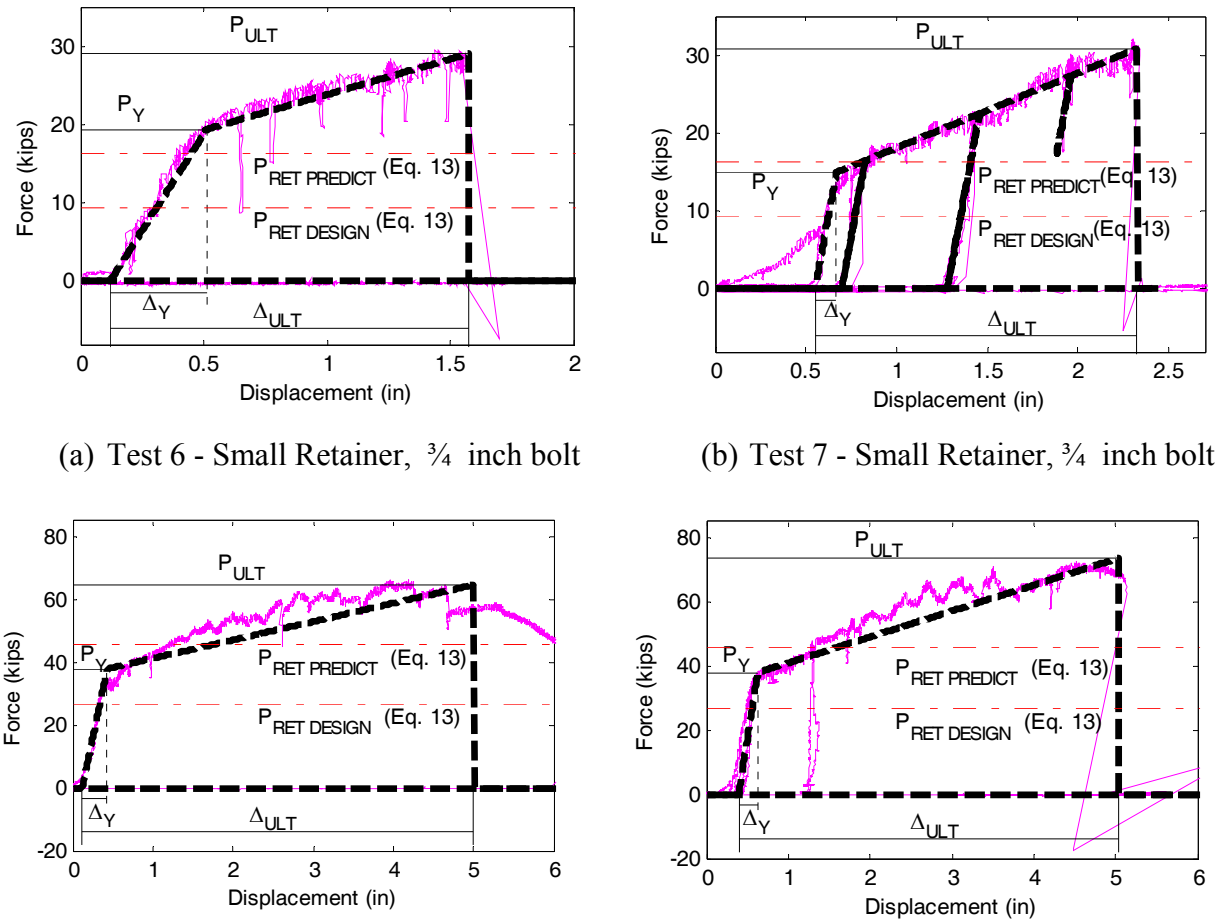

(a) Test 6 - Small Retainer, ¾ inch bolt

(b) Test 7 - Small Retainer, ¾ inch bolt

(c) Test 11 - Large Retainer, 1¼ inch bolt

(d) Test 12 - Large Retainer, 1¼ inch bolt

Figure 3.22 Force-displacement results from experimental tests on retainers (light & solid line) validated with material model (dark & dashed line)

Along with the force-displacement relation for each test, Figure 3.22 also shows the initial design strength (P_{RET_DESIGN})for each assembly calculated per Equation 3.13, assuming that the anchor material has an ultimate strength F_u of 60ksi, as specified for the ASTM F1554, Grade 36 material. Random tension testing of three anchor samples however indicated that the material was likely rejected Grade 55 material. Ultimate strengths obtained from the three tension test specimens were 84.7, 73.9, and 73.5 ksi, giving an average of 77.4ksi, which results in a $\Omega = F_{u\_Design}/F_{u\_Actual} = 77.4 / 60 = 1.3$ factor of overstrength just from the material capacity. A prediction of the actual retainer assembly strength is also calculated per Equation 3.13, but F_u = 77.4 ksi, is used to account for the material overstrength, and a φ factor of 1.0 is used. The predicted actual strength, $P_{RET\_PREDICT}$ is also shown in Figure 3.22, as well as in Table 3.3.

In typical construction the retainers are placed such that there is a 3.2 mm (1/8 in.) gap between the bearing top plate and the retainer. The experiments were conducted, without this 3.2 mm (1/8 in.) gap, such that the top plate was flush against the retainer at the beginning of a test, however, there is an additional distance that the top plate needs to travel before a significant increase in force is recorded. This distance can be termed as the engagement gap, and it exists because the oversized bolt hole in the retainer leaves space between the anchor bolt and the edge of the retainer hole. The engagement gap, as well as other relevant experimental data, is shown in Table 3.3.

Table 3.3 Design and experimental data for the tested retainers

Design Data	**Test 6**	**Test 7**	**Test 11**	**Test 12**
Bolt Diameter (in)	0.75	0.75	1.25	1.25
Bolt Area (in^2)	0.442	0.442	1.227	1.227
P_u (design) (kips)	60	60	60	60
P_{RET_DESIGN} (Eq.3.13 F_u=60) (kips)	9.5	9.5	26.5	26.5
P_u (coupon) (kips)	77.37	77.37	77.37	77.37
$P_{RET\_PREDICT}$ (Eq.3.13 F_u=77.4) (kips)	16.4	16.4	45.6	45.6

Experimental Data	**Test 6**	**Test 7**	**Test 11**	**Test 12**	**Average**	**Std.Dev.**
Engagement gap (in)	0.12	0.55	0.12	0.39	0.30	0.21
Δ_Y (in)	0.39	0.12	0.31	0.24		
Δ_{ULT} (in)	1.46	1.77	4.88	4.65		
P_Y (kips)	19.6	15.1	38.2	38.2		
P_{ULT} (kips)	29.2	31.0	65.2	74.2		

Normalized relations	**Test 6**	**Test 7**	**Test 11**	**Test 12**	**Average**	**Std.Dev.**
E_E (ksi)	49.68	127.52	121.34	161.78	115.08	47.09
E_P (ksi)	9.09	9.65	5.91	8.16	8.20	1.65
F_{ULT}/F_Y	1.49	2.06	1.71	1.94	1.80	0.25
$\mu=\Delta_{ULT}/\Delta_Y$	3.70	15.00	15.50	19.67	13.47	6.84

Capacity Comparison	**Test 6**	**Test 7**	**Test 11**	**Test 12**	**Average**	**Std.Dev.**
P_{ULT}/P_{RET_DESIGN}	3.06	3.25	2.46	2.80	2.89	0.34
$P_{RET\_PREDICT}$ (Eq.3.14 F_u=1.3*60) (kips)	27.57	27.57	76.58	76.58	N/A	N/A
$P_{ULT}/P_{RET\_PREDICT}$ (Eq. 3.14)(kips)	1.06	1.13	0.85	0.97	1.00	0.12

3.3.3 Validation and calibration of retainer model

For future calibration of the computational retainer models it would be best to develop an improved estimate of the ultimate retainer capacity. Equation 3.13 from before can be modified to better account for the failure mechanism and anchor material capacity.

$$P_{RET} = \varphi 0.8 A_b F_u \tag{3.14}$$

where:

- instead of using φ = 0.75 as before, φ = 1.0 will be used.
- instead of using a reduction factor 0.48 that includes the effect of a shear failure mechanism, only a factor of 0.8 will be used to account for the reduced area of the bolt
- A_b will be the nominal bolt diameter and
- F_u will be the ultimate stress of the material. An overstrength factor may be used to increase this value if the ultimate stress of the supplied material is expected to be significantly higher than stated in design codes, (i.e. $F_{u\_Actual} = \Omega * F_{u\_Design}$)

Using Equation 3.14, with an overstrength of 1.3 for the ultimate stress of the material, one can calculate an improved estimate of the retainer capacity. Note that the this equation provides a reasonable procedure for determining the capacity as can be seen from the last row of Table 3.3 where the P_{ULT} /$P_{RET\_PREDICTED}$ (Eq. 14, F_u=1.3*60) ratio compares the experimental results to Equation 3.14, and gives values near unity for all experiments.

To allow for the computational modeling of various retainers and anchor bolt sizes, it is necessary to define five variables, a *gap*, P_Y, Δ_Y, P_{ULT} and Δ_{ULT}. The ultimate capacity of the assembly P_{ULT} can be calculated based on the area of the anchor bolt by using Equation 3.14, and using the ratio of P_{ULT}/P_Y = 1.80, one can also determine the yield strength of the retainer. Furthermore at this phase it would be suitable to try to keep the same stiffness properties for the assemblies, and by using E_E=115.08 (ksi), E_P=8.2 (ksi) one can determine the yield and ultimate displacements Δ_Y and Δ_{ULT}. Finally the gap should be specified as the initial gap left at construction plus the average engagement gap: *gap* = 0.125+0.30 = 0.425(in). Keeping these values constant, along with calculating a value for P_{ULT}, provide sufficient information to inform the model. The model was calibrated for 3/4 inch and 1.25 inch anchor bolts as described above,

and per the values listed in Table 3.3 a value of 0.3 was assumed to specify the engagement gap, and the calibrated models were plotted against the experimental data in Figure 3.23. Note that there is a good fit to the experimental data, when the only input variable specified for the model is the anchor bolt diameter and material strength.

Table 3.4 New model definitions for various bolt sizes

Bolt Diameter (in)	**0.63**	**0.75**	**1**	**1.25**	**1.5**	**2**	**2.5**
Bolt Area (in^2)	0.31	0.44	0.79	1.23	1.77	3.14	4.91
F_u	60	60	60	60	60	60	60
P_{RET} Eq.3.14 (kips)	14.7	21.2	37.7	58.9	84.8	150.8	235.6
P_Y (kips)	8.2	11.8	20.9	32.7	47.1	83.8	130.9
Δ_Y (in)	0.07	0.10	0.18	0.28	0.41	0.73	1.14
Δ_{ULT} (in)	0.87	1.25	2.23	3.48	5.01	8.90	13.91

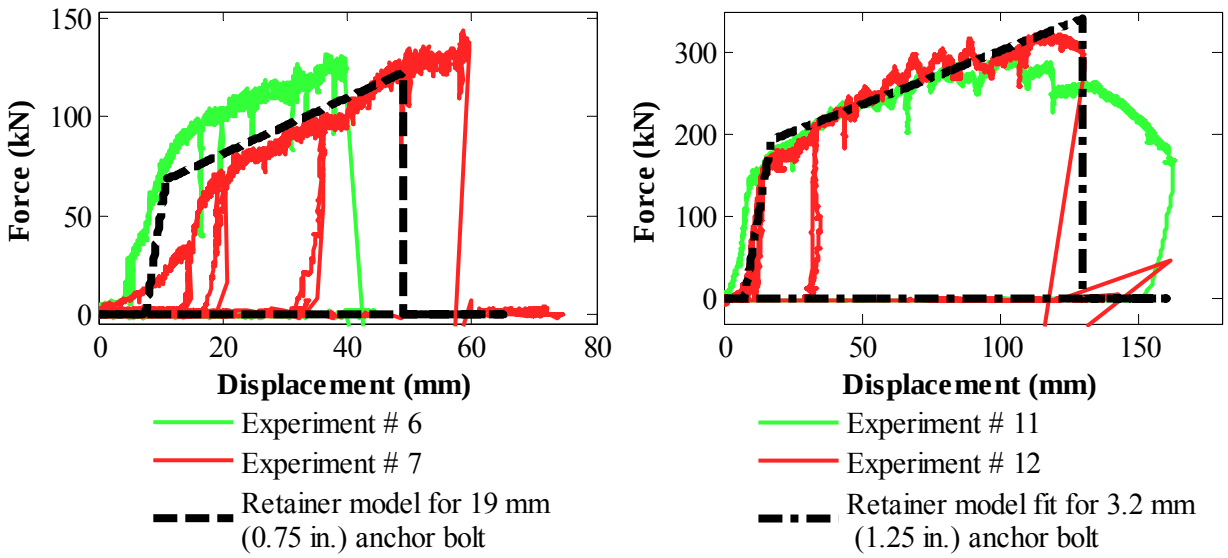

(a) Experimental and model pushover behavior of retainers with 19 mm (0.75 in) anchor bolts

(b) Experimental and model pushover behavior of retainers with 32 mm (1.25 in) anchor bolts

Figure 3.23 Independently calibrated model with experimental data

CHAPTER 4

STATIC PUSHOVER ANALYSES OF PROTOTYPE BRIDGE SYSTEM

This chapter presents monotonic static pushover analyses for the prototype bridge in the longitudinal and transverse directions of the bridge deck. These analyses were used to demonstrate the localized behaviors of the prototype bridge model defined in Chapter 2 and exercise the bearing models presented in Chapter 3. Although the bridge model has the capability to simulate nonlinear foundations, the prototype bridge was used for these analyses, thereby assuming rock foundations, such that the abutment and pier bases were fully fixed. This allows the behavior of the bearings, retainers, and substructures to specifically be studied in more detail. Sections 4.1 and 4.2 show longitudinal and transverse pushover analyses of the prototype system. For the prototype bridge, retainers are placed at each elastomeric bearing, with anchor bolt and retainer sizes chosen based on design recommendations from the IDOT bridge manual. This resulted in 16 mm (0.625 in.) diameter anchor bolts for the abutments, and 25 mm (1.0 in.) anchor bolts at the pier with elastomeric bearings. The ultimate retainer assembly capacities (P_{RET}) used for the transverse analyses in section 4.2 of this chapter are calculated based on the procedures in Chapter 3 with an added material over strength of 1.3. This resulted in estimated individual retainer capacities at the abutments of 85 kN (19 kips), corresponding to 71% of the dead load at each bearing, and retainer capacities of 113 kN (25 kips) at the intermediate pier, corresponding to 66% of the dead load at those bearings. It is important to note that over strength is not used in any other chapters of this thesis. Section 4.3 presents transverse pushovers for an alternative calibrated design where these retainers have the exact capacity of 0.2 times the bearing dead load, and both pushover analyses are later compared to a case where all bearings are assumed to be linear elastic and infinitely stiff (Section 4.4). In addition to showing the system behavior, the pushover analyses also point out important patterns in sequence of damage, which are further investigated in Chapters 6 and 7.

To perform the static pushover analyses of the structure, only vertical dead loads were assumed to be active on the structure at the time of analysis. This is most appropriate for capturing the reality of bridges in southern Illinois where heavy traffic congestion is rare.

Corotational transformations were used for the model such that geometric nonlinearities are captured. Lateral loads were applied proportionally to the mass distribution of the structure, and a node at the center of the bridge deck was used to monitor the system displacement for control of the algorithm. Displacement of this control node is subsequently called the model displacement for the remainder of this chapter. A load control integrator was used to apply incremental lateral loads on the structure and an adaptive algorithm technique with an ample number of iterations (50) was used to obtain convergence for the highly nonlinear system. The adaptive technique used a Newton Raphson solution for the general analysis until a case of high nonlinearity and no convergence was reached. At this point, the technique would attempt a Newton Raphson method with a Line Search Algorithm, a Modified Newton Raphson Algorithm, and would then change the analysis step size to reach a convergent solution.

4.1 Longitudinal pushover analysis – prototype design

Figure 4.1 shows the longitudinal analysis of the prototype bridge structure, where the system experienced softening at a displacement of 40 mm (1.6 in.), exhibited a plateau where displacement increased with little increase in force, and then gained significant strength and stiffness at a system displacement of 50 mm (2 in.). The following key events in the longitudinal pushover analysis are indicated in Figure 4.1, with the associated progression of damage discussed below:

A. Yielding of column base longitudinal reinforcement and plastic deformation of Pier 2,
B. Friction slip of the four inside bearings at each abutment (bearings that primarily carry girder and deck loads),
C. Friction slip of the two outside bearings at each abutment (bearings that carry parapet loads in addition to girder and deck loads),
D. Deck-backwall interaction and subsequent softening due to nonlinear backfill deformation,

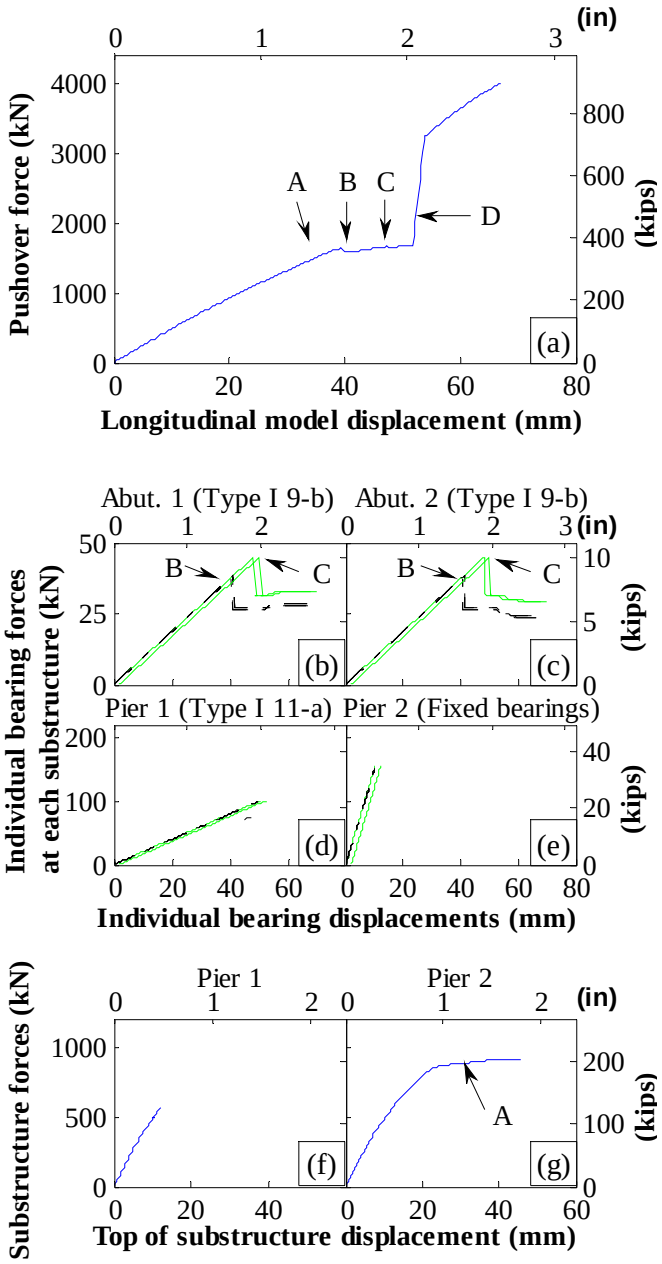

Figure 4.1 Longitudinal pushover analysis of prototype bridge

Figure 4.1 shows that the bearing slip force is related to the vertical load at each individual bearing. For example, the interior bearings at the abutments (Figure 4.1 (b) and (c)) carry the least dead load and slipped at the lowest horizontal force magnitude, while the elastomeric bearings at Pier 1 (Figure 4.1 (d)) did not slip at all for this particular analysis since they are carrying a large vertical load, and the pier allows some elastic deformation. Relative stiffness of the bearings also has an effect on the global structural performance. For example, the

fixed-bearings, which have a high stiffness and large capacity, transferred significant forces during the analysis and thereby caused some yielding and plastic deformation at Pier 2. Conversely, the elastomeric bearings at Pier 1 are much more flexible and provided sufficient deformation capacity so the forces were kept relatively low (and that substructure remained essentially elastic). Since this behavior does not necessarily satisfy the ideal quasi-isolation goal where substructures are protected from damage, one aim of Stage 3 of the research project is to develop strategies for mitigating the force imbalance between piers 1 and 2. A better approach would be to size the bolts or pintles to fail before the substructure yielded. Finally, system behavior of a quasi-isolated bridge in the longitudinal direction is significantly dependent on the backwall stiffness and strength. As shown here, a typical backwall with compacted backfill has the potential to double the force capacity of the system, and to limit longitudinal displacements to only several inches.

The longitudinal behavior of the prototype bridge compares favorably with overall trends observed in other similar pushover studies. For example, in a parametric study of existing older (non-quasi-isolated) Illinois bridges, (Bignell, LaFave, and Hawkins 2005) showed that for longitudinal pushover analyses of regular bridges (2 to 4 span superstructures with wall and pier substructures) the first events to occur would typically be flexural yielding at the intermediate substructures, where steel bearings were used. Subsequently, bearing failures – such as overturning of rocker bearings at the abutments – were frequently noted to occur, followed by expansion joint gap closure and a capacity increase due to the backwalls. In summary, response in the longitudinal direction of both the prototype bridge and the structures studied by (Bignell, LaFave, and Hawkins 2005) are significantly dependent on the substructure elements; Bignell et al. also noted that bridge skew can have a significant influence on the progression of damage, as well as on the total force capacity of a bridge structure.

4.2 Transverse pushover analysis – prototype design

As shown in Figure 4.2 (a), during the transverse pushover analysis the system experienced initial stiffening up to 30 mm (1.2 in.) of displacement as various elements were first engaged. At later model displacements between 30 and 40 mm (1.2 and 1.6 in.), the system experienced sharp drops in force capacity due to the failure of critical components. The

following key events in the transverse pushover analysis are indicated in Figure 4.2, with the associated progression of damage discussed below:

A. Contact of bearing top plates with retainers at Abutment 1,
B. Break-off of anchor bolts at low-profile fixed bearings and subsequent sliding,
C. Failure of retainers and subsequent friction slip of bearings at Abutment 2,
D. Rotation of deck about Pier 1, with reverse movement of bearings at Abutment 1,
E. Friction slip of bearing P1-6 at Pier 1 (see Figure 4.3 (e) for key bearing locations), and contact of retainers at Abutment 1 in the reverse direction,
F. Friction slip of bearing P1-1 at Pier 1.

Plan views of the bridge system and primary resisting forces for each of the states listed above are shown in Figure 4.3. At the beginning of the analysis, the system translated in the direction of the applied forces and slightly rotated clockwise about Pier 2, where the relatively stiff fixed bearings were located (states A-B). Due to their high stiffness, the low-profile fixed bearings were the first to exceed peak capacity and begin sliding (states B-C). This caused the superstructure to rotate in the counter-clockwise direction, thus redistributing forces among different components and causing the retainers to break off and the Type I bearings to slide at Abutment 2. At states D-E, the system lost most stiffness and began rotating about Pier 1 (where the retainers had additional capacity). As the system continued rotating, the retainers in the reverse direction of Abutment 1 were engaged and the system softened since the bearings at Pier 2 slipped and began sliding.

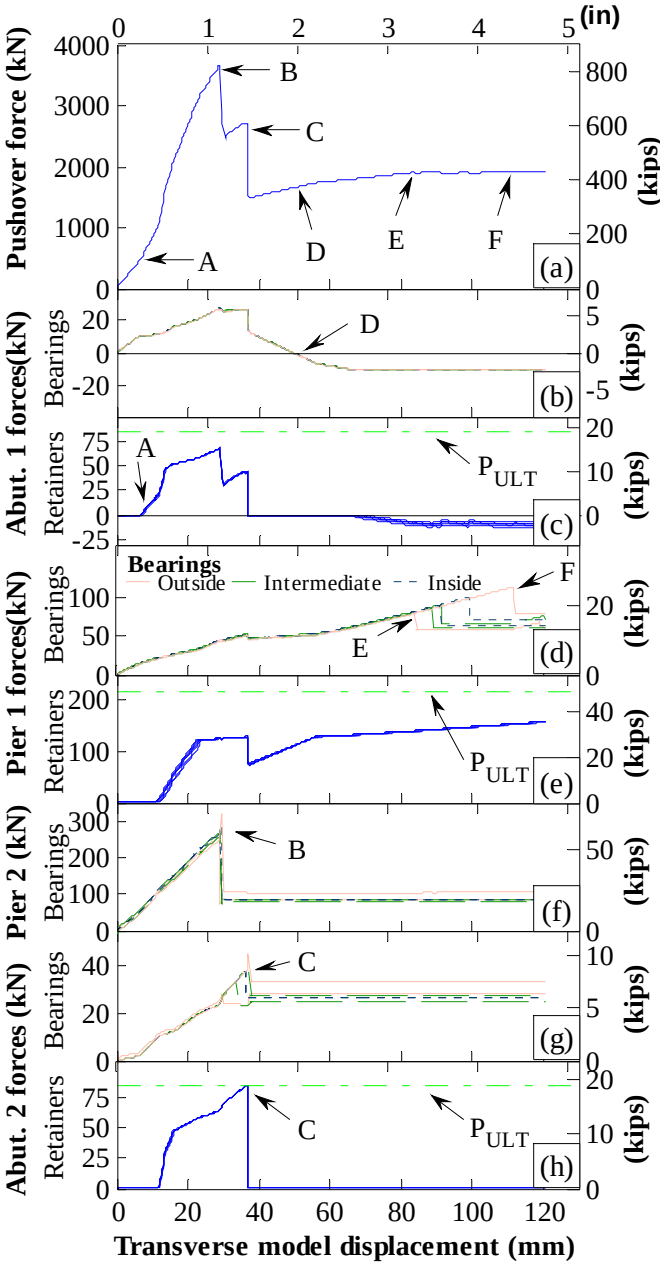

Figure 4.2 Transverse pushover analysis of prototype bridge

In this analysis, the piers did not experience significant nonlinear behavior since they were loaded in double curvature, and due to their relatively short length and large diameter they were stronger than other components in the bridge system. However, the piers will not always exhibit linear behavior in the transverse direction since their strength could place them at a different point in the damage hierarchy for taller bridges or where smaller columns are used.

Rotation of the bridge deck can also potentially lead to interaction with the backwall at the corners of the superstructure, if there is a large inequality in the bearing stiffness at different substructures.

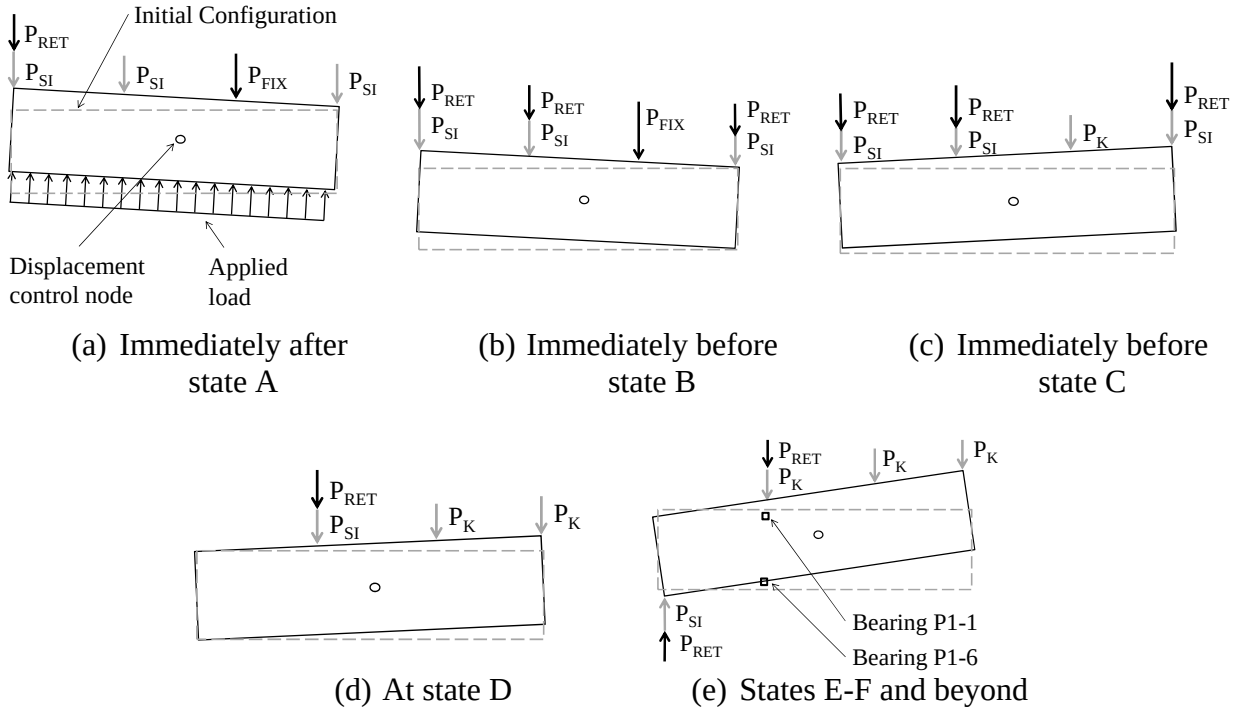

Figure 4.3 Bridge plan views schematically describing movement and resisting forces (transverse pushover analysis)

After state C, when the retainers at Abutment 2 break off, the superstructure rotates significantly and the bi-directional behavior of the bearings becomes quite important when considering global bridge response. Failure of bearings P1-1 and P1-6 occurred due to a combination of transverse and longitudinal deformations, which arose from the superstructure rotating in plan. Figure 4.4 shows that the break-off force at bearing P1-1, 125 kN (28.1 kips), is the resultant of the transverse and longitudinal forces, 115 kN (25.6 kips) and 51 kN (11.5 kips). Furthermore, Figure 4.4 (c) shows that the bearing model accounts for the change in vertical loads due to the superstructure overturning effect from the pushover analysis. At the beginning of the analysis, bearings P1-1 and P1-6 had higher vertical loads than the other bearings since they carry the parapet dead load, but later P1-6 slipped before P1-1 due to the change in vertical load (states E and F, respectively).

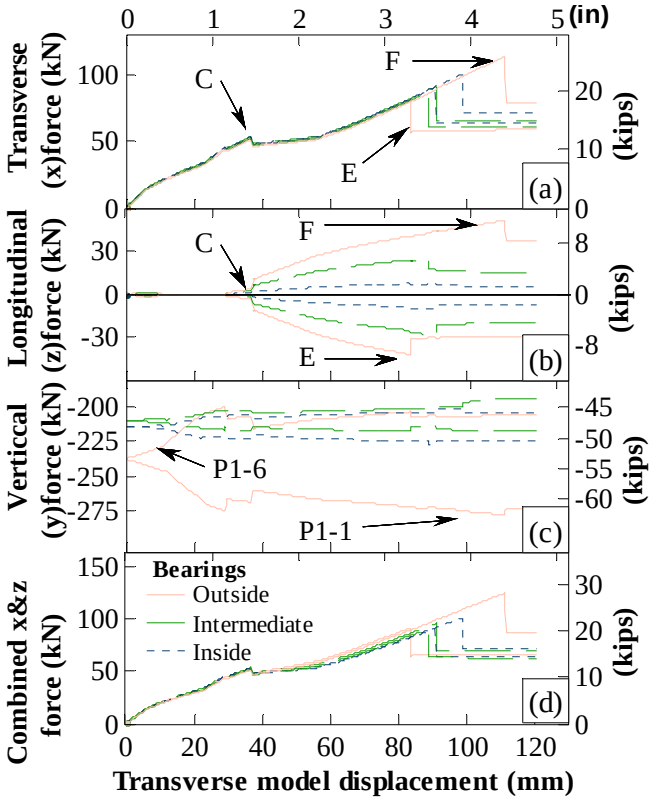

Figure 4.4 Bearing forces at Pier 1 for transverse pushover analysis of prototype bridge

The transverse analyses also indicate the importance of the transfer of force between different vertical components of the bridge. Since most of the mass of the bridge is concentrated at the concrete deck, forces would typically travel down through the diaphragm elements and bridge girders into the bearing components, after that they would be transferred to the top of the substructure, and would be carried down through the substructure elements into the foundation. The diaphragm element stiffness is modeled in the prototype bride, but they are assumed to remain linear elastic so nonlinearities are not explicitly modeled. It is possible that lateral forces are large enough to cause yielding and possibly buckling in the diaphragm elements, so these forces will be compared to the diaphragm capacities at a later stage of this project. The maximum diaphragm forces are typically close to the combination of the bearing sliding force and the retainer fracture force.

4.3 Transverse pushover analysis – calibrated quasi-isolated design

As noted above, the retainer capacity in the prototype design, based on current IDOT design procedures, was 0.71 times the dead load at an individual bearing for the abutments, and 0.66 times the bearing dead load at Pier 1. An indication of the performance of a more calibrated (or alternative) design for the quasi-isolated bridge prototype could be one where the retainer capacities are more limited, for example to only 0.2 times the dead load at an individual bearing. This would correspond to 25 kN (5.6 kips) and 66 kN (14.8 kips) for the abutment and pier retainer capacities, respectively. Such a configuration would provide adequate strength for service loading, but would reduce the overall force transferred to the substructure in the event of an earthquake. A transverse pushover analysis was completed for this calibrated design, with the results shown in Figure 4.5. Some of the key events from the transverse pushover analysis of this calibrated design (using the same letter notations as before) are noted in Figure 4.5, while additional events that have not been discussed previously are:

G. Failure of retainers and subsequent sliding of the bearings at Abutment 1,
H. Failure of retainers at the Pier 1 substructure,
I. Stick-slip behavior of elastomeric and fixed bearings due to redistribution of forces through the system.

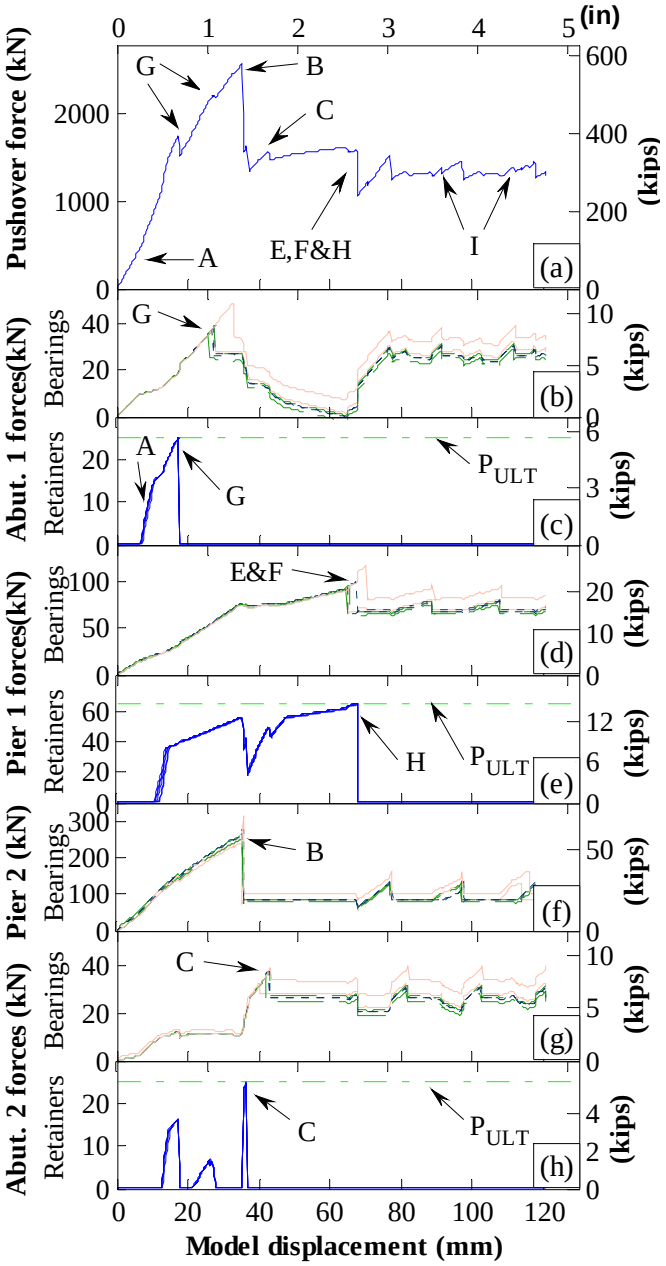

Figure 4.5 Transverse pushover of calibrated bridge design

For this analysis the retainers at all substructures failed and the bridge experienced much less rotation than in the analysis shown in Section 4.2. The total system force capacity was reduced from 3700 kN (830 kips) to 2600 kN (580 kips), allowing the structure to begin sliding at a lower force. After all retainers fail, the superstructure does not rotate much in plan, and after a global displacement of 70 mm (2.7 in.) the bearings begin sticking and slipping at various times through the analysis. This is caused by force redistribution to different sections of the

superstructure, which leads to differential (and sometimes reverse) movements in the bearings.

4.4 Transverse pushover analysis – fixed condition at all bearings

To further characterize the absolute and relative performance of the quasi-isolation system, the pushover analyses shown in Sections 4.2 and 4.3 above can also be compared to a case where the bearings are modeled as directly attached to the superstructure and substructure and simply exhibiting linear elastic behavior (with no failure or slip), as shown in Figure 4.6 (a). This case leads to very large forces for only a small transverse movement of the bridge. At a model displacement of 28 mm (1.1 in.), which corresponds to the displacement at peak force for the prototype bridge transverse pushover, the fixed condition case produced a force of 15300 kN (3440 kips). This corresponds to roughly four times the maximum force observed in the prototype bridge design and six times the maximum force in the calibrated design. For even larger displacements, the maximum transverse force for the quasi-isolated systems remained at a plateau of around 1600 kN (360 kips), while the fixed condition pushover force continued increasing. Since the piers were still modeled as fiber sections and the bearings were not allowed to deform and slip for the fixed condition analysis, this case resulted in significant yielding and plastic deformation of the two multi-column piers. Pier force-displacement diagrams for the three analyses are shown in Figure 4.6 (b) and (c). By implementing retainers with lower capacity, the calibrated design case limited the shear force in Pier 1 to 930 kN (205 kips), while the same pier reached a maximum force of 1350 kN (305 kips) for the original prototype design. For both quasi-isolated analyses, Pier 2 reached a maximum force of 1535 kN (345 kips), which corresponds to the combined break-off force for the fixed bearings at that substructure. Stage 3 of the research project is investigating other bridge variations with calibrated designs that should provide the desired quasi-isolation behavior.

Results of the transverse pushover analyses are similar to some previous parametric studies carried out for existing older wall pier bridges in southern Illinois. Those analyses, performed by (Bignell, LaFave, and Hawkins 2005), typically employed steel bearings and included model nonlinearities in the substructure and foundation elements. In many of those parametric transverse analyses, significant total force drops occurred due to failures of the bearings at abutments and at intermediate piers, rather than due to failures in the substructure and

foundation elements. This failure progression is similar to that intended for quasi-isolated bridges, where bearings would reliably permit controlled fusing and would limit the force transferred to substructures. Pushover curves from the earlier parametric pushover analyses, look similar to the quasi-isolated analyses experiencing large (and sometimes multiple) force reductions at global displacements of 25-60 mm (1.0-2.4 in.).

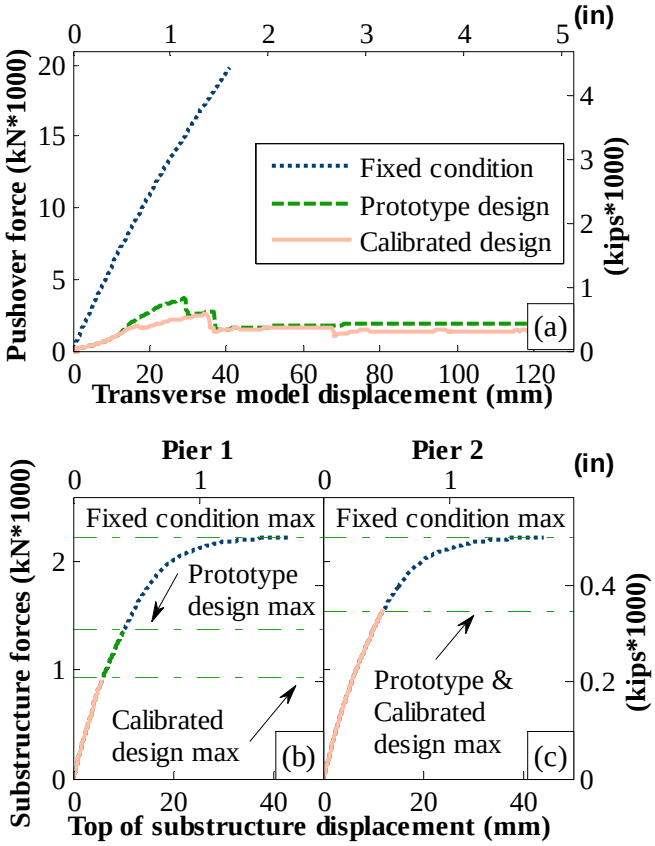

Figure 4.6 Comparison of transverse pushover analyses

4.5 Summary of localized behaviors and pushover analyses

When a prototype bridge system is subjected to monotonically increasing longitudinal loading, flexural yielding occurs at the concrete pier with the low-profile fixed bearings, followed by slip of the elastomeric bearings at the abutments, and then finally the backwall deforms when the superstructure closes the expansion joint gap. The abutment backwall provides significant force capacity to the system, and limits longitudinal deformations of the structure. It was noted that the outside bearings which carry higher loads from the added weight of the parapet experience friction break-break off at a later stage than the inside bearings, but this

did not cause a significant influence on the overall pushover curve. The influence of the backwall component should be taken into account during seismic analysis and design since it can limit the level of force transferred to the substructure and could provide savings for the substructures of the bridge. The fixed bearing ultimate capacity should be studied in further detail, since that component can be designed to break-off at lower forces and thereby prevent yielding of the piers and nonlinearity in the foundations. This is the intended behavior for bridges designed by the IDOT procedure.

When the bridge system was subjected to transverse loading, the superstructure rotates due to the relative stiffness of the bearings and retainers that are engaged. Fixed bearings fail first and begin sliding, followed by failure of the retainers and subsequent sliding of the bearings at the other substructures. Bi-directional behavior of the bearings is important for cases where superstructure twisting in plan may occur. It was noted that in this scenario the overturning effects, the bi-directional coupling and varying force distribution can cause significant differential in bearing break-off forces. The capacity of the retainers and low-profile fixed bearing assemblies have a significant influence on forces transferred between the superstructure and substructure of the bridge. A pushover analysis that only incorporates the stiffness of the bridge deck and piers (but not the stiffness and capacity of the bearings) significantly overestimates the system forces.

In general it was noted that these pushover analyses presented valuable information about localized behaviors, the sequence of damage and peak shears that can be expected in a typical bridge. The analyses point out critical elements such as pier 2 in the longitudinal direction, and also highlight the benefit of the backwalls in the longitudinal direction. The inelastic pushover analyses give a much better idea of the behavior than the case where the bearings are considered elastic, but none of the analyses presented in this chapter give a good representation of what system displacements are to be expected from an earthquake. The parametric incremental dynamic analyses discussed in Chapters 5-7 provide comprehensive results on what the expected seismic performance of quasi-isolated bridges would be in the central U.S.

CHAPTER 5

OVERVIEW OF PARAMETRIC STUDY

The broader goal of this study is to better understand the seismic performance of bridges that have the potential to reach what would be considered a quasi-isolated response. The matrix of parametric variations (Table 2.1) was developed to capture a range of bridge structures that are considered typical for the state of Illinois. Parameters varied include the superstructure type and length, the substructure type, the substructure height, the foundation stiffness, and the isolation bearing types. Based on drawings of existing bridges and collaboration with the IDOT technical review panel, the selected bridges were considered to be characteristic for the Southern Illinois region. The seismic hazard for this region was also a focus of this study, since the quasi isolation system is considered best suited for regions with high-risk, low recurrence earthquakes. Therefore the various bridges were studied for earthquake ground shaking inputs particular to the New Madrid Seismic Zone (NMSZ). The seismic hazard was scaled to investigate different earthquake intensities, and two sets of ground motions were used to capture the hazard for locations with different soil types. This chapter gives an outline of the parametric variations and seismic hazards considered for the study.

5.1 Parametric variations and naming conventions

Bridge model variations are named with a series of letters and numbers to provide a nomenclature for the parameters used in the study. The first two letters of the model name indicate the superstructure type, (Ss-Steel short; Sl-Steel long; Cs-Concrete short). The third letter and the following two numbers designate the intermediate substructure type (C-Column pier; W-Wall pier) and height in feet (15 ft - 4.5 m; 40 ft - 12.2 m). The next letter and number indicate the bearing type used (T1-Type I IDOT bearing; T2-Type II IDOT bearing), and the final letter indicates the soil conditions modeled (F-Fixed/rock; S- Flexible foundation boundary condition). Based on these definitions, the prototype bridge can be denoted as SsC15T1F, whereas SlW40T2S would indicate a bridge with a long steel superstructure, supported on 12.2

m (40 ft) wall piers with flexible foundation boundary conditions and Type II IDOT bearings. Later in this study, the symbols 'X', 'x', and '#' are used to designate all the variations of a particular parameter. Bridge variations defined using this nomenclature result in forty-eight distinct bridges that are studied in this research. Details on the various parameters used are available in Table 5.1, and two sample meshes of the finite element bridge models created with OpenSees (McKenna, Mazzoni, and Fenves 2006) are shown in Figure 5.1.

Table 5.1 Specifications for various bridge parameters

Superstructure Information	Steel Short (Ss)	Steel Long (Sl)	Concrete Short (Cs)
Girder size	W27x84 U.S.	W40x183 U.S.	91.4cm (36 in.) PPC I-Girder
Span lengths	15.2 - 15.2 - 15.2 m (50 - 50 - 50 ft)	24.4 - 36.6 - 24.4 m (80 - 120 - 80 ft)	18.3 - 18.3 - 18.3 m (60 - 60 - 60 ft)
Superstructure weight	96 kN/m (6.6 kip/ft)	105 kN/m (7.2 kip/ft)	124 kN/m (8.45 kip/ft)
Abutment Bearing Information			
Type I	9-b	15-e	9-c
Plan dims.	23x30 cm (9x12 in.)	38x61 cm (15x24 in.)	23x30 cm (9x12 in.)
Effective Rubber Thickness (ERT)	6.7 cm (2.6 in.)	13.3 cm (5.25 in.)	7.6 cm (3 in.)
Type II	7-b	9-b	9-a
Plan dims.	18x30 cm (7x12 in.)	23x30 cm (9x12 in.)	23x30 cm (9x12 in.)
Effective Rubber Thickness (ERT)	3.8 cm (1.5 in.)	6.7 cm (2.6 in.)	4.8 cm (1.9 in.)
Ret. anchor bolt dia.	1.6 cm (0.625 in.)	1.9 cm (0.75 in.)	1.9 cm (0.75 in.)
$P_{RET\_EXPECTED}$	65 kN (15 kips)	94 kN (21 kips)	94 kN (21 kips)
Pier Bearing Information			
Type I	11-a	15-b	13-a
Plan dims.	28x41 cm^2 (11x16 in.)	38x61 cm (15x24 in.)	33x51 cm (13x20 in.)
Effective Rubber Thickness (ERT)	6.7 cm (2.6 in.)	13.3 cm (5.25 in.)	7.6 cm (3 in.)
Type II	11-a	15-a	13-a
Plan dims.	28x41 cm^2 (11x16 in.)	38x61 cm (15x24 in.)	33x51 cm (13x20 in.)
Effective Rubber Thickness (ERT)	5.1 cm (2 in.)	7.6 cm (3 in.)	4.8 cm (1.9 in.)
Ret. anchor bolt dia.	2.5 cm (1.0 in.)	3.8 cm (1.5 in.)	3.2 cm (1.25 in.)
$P_{RET\_EXPECTED}$	170 kN (38 kips)	377 kN (85 kips)	262 kN (59 kips)
Fixed bearing	9x11	9x13	9x19
Plan dims.	23x28 cm (9x11 in.)	23x33 cm (9x13 in.)	23x48 cm (9x19 in.)
Anchor bolt dia.	1.9 cm (0.75 in.)	3.2 cm (1.25 in.)	2.5 cm (1.0 in.)
$P_{FIXED\_EXPECTED}$	113 kN (25 kips)	315 kN (71 kips)	200 kN (45 kips)

Multi-Column Pier Substructure Information						
Column clear height	4.5 m (15 ft)	12.2 m (40 ft)	4.5 m (15 ft)	12.2 m (40 ft)	4.5 m (15 ft)	12.2 m (40 ft)
Column diameter	91 cm (36 in)	91 cm (36 in)	91 cm (36 in)	91 cm (36 in)	91 cm (36 in)	91 cm (36 in)
Reinf. Ratio	1.07%	1.07%	1.46%	1.46%	1.46%	1.46%
Wall Pier Substructure Information						
Wall clear height	4.5 m (15 ft)	12.2 m (40 ft)	4.5 m (15 ft)	12.2 m (40 ft)	4.5 m (15 ft)	12.2 m (40 ft)
Wall width	10.7 m (35 ft)	10.7 m (35 ft)	10.7 m (35 ft)	10.7 m (35 ft)	10.7 m (35 ft)	10.7 m (35 ft)
Wall thickness	91 cm (36 in.)	91 cm (36 in.)	91 cm (36 in.)	91 cm (36 in.)	91 cm (36 in.)	91 cm (36 in.)
Reinf. Ratio	0.15%	0.15%	0.15%	0.19%	0.15%	0.19%

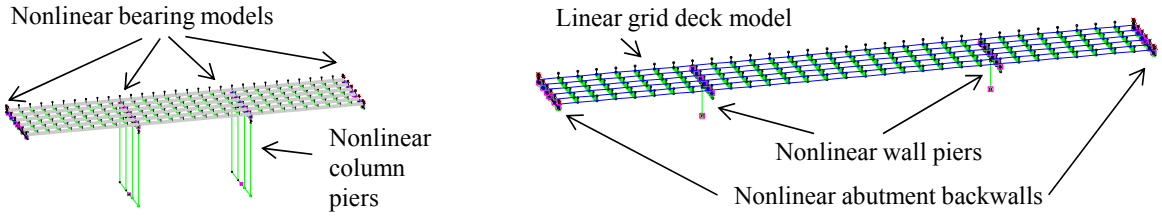

(a) Bridge CsS40T1F (b) Bridge SlW15T1F

Figure 5.1 Sample finite element meshes for two prototype bridges

5.2 Earthquake simulation for parametric study

Numerical models for seismic analyses have over time progressed from simplified linear approximations of stiffness and force to more advanced nonlinear systems where components capable of cracking, yielding, sliding and buckling can be modeled individually. Currently, the most advanced type of analysis is one where all nonlinear behaviors are explicitly simulated, the numerical model is subjected to transient dynamic excitation, and a structure's behavior and characteristics are observed and updated at every time step as nonlinearity appears throughout the model. This type of analysis, however, makes the results highly dependent on the particular ground motion selected for analysis. To ascertain the validity of these analyses, researchers use multi-record incremental dynamic analysis (IDA) with several ground motions and vary the motion intensity by a scale factor to provide a comprehensive representation of bridge behavior (Vamvatsikos and Cornell 2002). The bridges in this parametric study are subjected to response history analyses with different ground motions to assess effects from the nature of the hazard, the intensity of earthquake excitation, and the different directions of shaking. Damping in the model occurs both from hysteretic damping due to the nonlinear behaviors of the elements, and also from stiffness and mass proportional viscous damping, that is added explicitly and is estimated to be 5%.

5.2.1. Seismic hazard quantification

There are numerous properties of the applied ground motion that affect the response of a structure to a given earthquake. These include, but are not necessarily limited to, the magnitude

of the earthquake, the source mechanism, the distance from the epicenter to the bridge site, the attenuation of the seismic motions with distance, and the soil type at the bridge site. These factors vary greatly for different locations in the United States, and much research (Tavakoli, Pezeshk, and Cox 2010; Wen and Wu 2001), has gone into understanding, quantifying, and simulating earthquakes in the Mid-America region, where a relatively high seismic risk exists, but the hazard is not particularly well understood. For a given epicentral distance and earthquake magnitude, the soil type at the site is the main factor that then governs the amplitude and frequency content of strong ground motion. This is accounted for in the seismic design provisions given by AASHTO (2009), where the design response spectrum varies based on one of the seven recognized soil types, all of which may be found in Illinois.

Based on studies of the NMSZ, researchers have developed various synthetic records that are capable of modeling characteristics of the Mississippi embayment. Wu and Wen (1999) performed studies and generated ground motions for rock and soil sites in Mid-America, focusing specifically on Memphis, TN, St. Louis, MO, and Carbondale, IL. Ten synthetic ground motion acceleration records were developed for each combination of site location, site condition (rock versus soil), and return period (475 years and 2475 years). Acceleration spectra, assuming 5% damping, were generated for bedrock excitation as well as for a Carbondale site based on boring log data; however, it was deemed that although these ground records were interesting, it would be necessary to generate new 1000 year return period records, and the records would have to be evaluated for both a general soft soil condition as well as some type of typical stiff soil condition.

Additional work has been performed by Fernandez and Rix (2008) to provide characteristic synthetic free-field surface ground motions for several locations throughout the Upper Mississippi Embayment. Figure 5.2 identifies locations with available ground motions that include the effects of inelastic soil response for deep soil conditions. Suites of surface ground acceleration records were generated at each site identified on the map, with ten records produced for each of 475, 975, and 2475 year return period events. From these ground motions, two sets of 10 synthetic records can provide realistic hazard approximations for a 7% in 75 year risk (1000 year recurrence) event for southern Illinois locations with rock (Cape Girardeau, MO - CG records) and stiff soils (Paducah, KY - Pa records). The acceleration, velocity, and

displacement spectra for the ground motions provided by Fernandez and Rix (2008) at these two locations are shown in Figure 5.3 throughFigure 5.5.

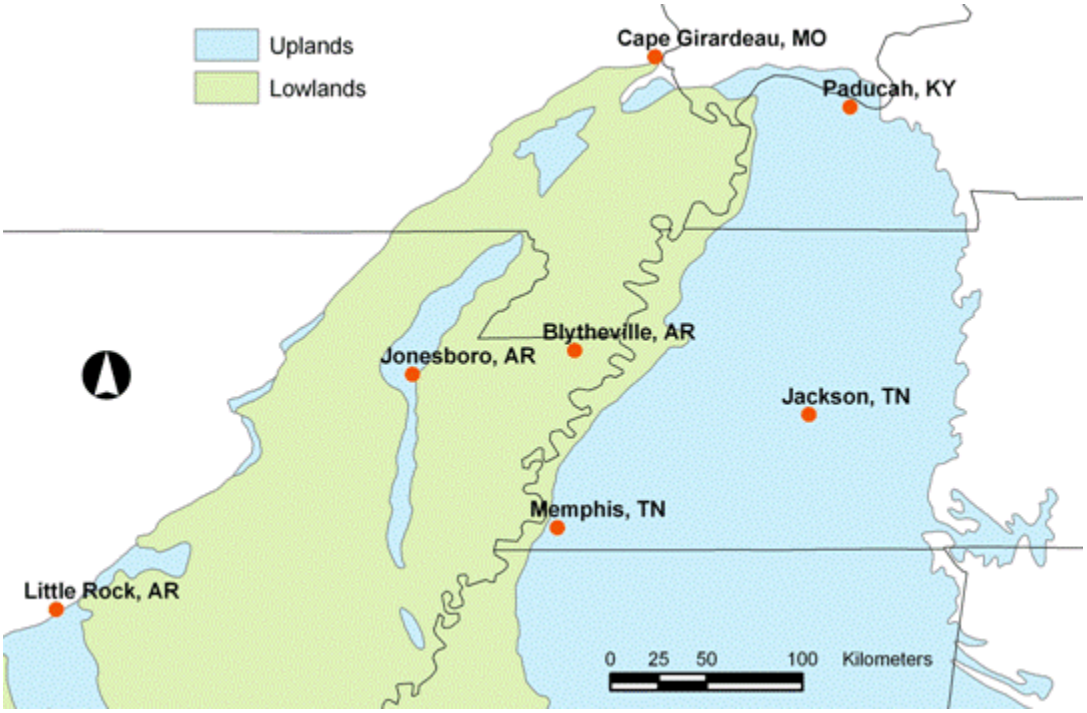

Figure 5.2 Cities for which Fernandez and Rix (2008) provide suites of synthetic ground motion records

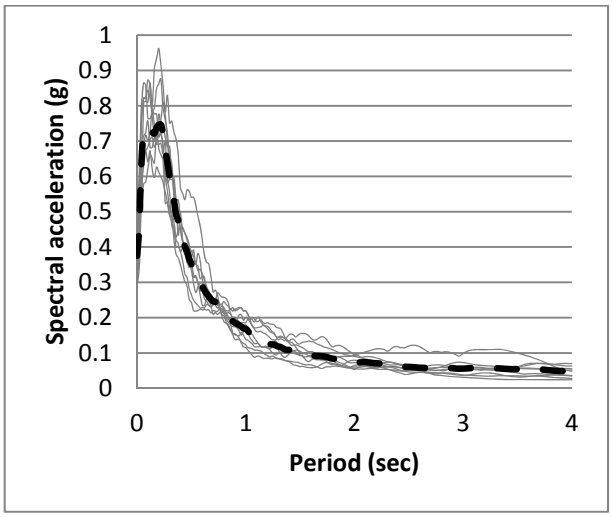

(a) Acceleration spectra for Cape Girardeau

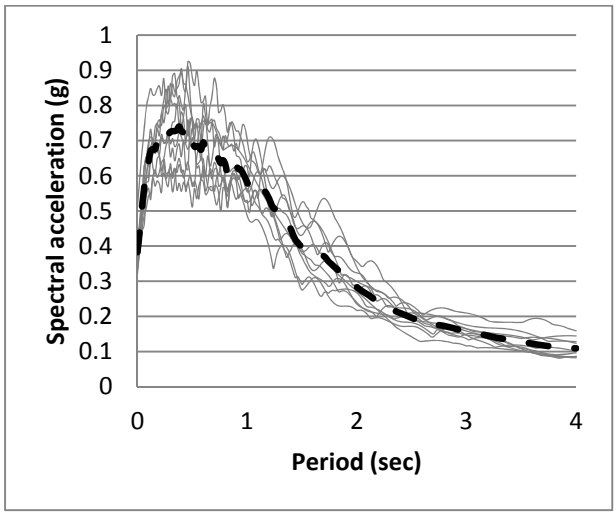

(b) Acceleration spectra for Paducah

Figure 5.3 Acceleration spectra for synthetic ground records

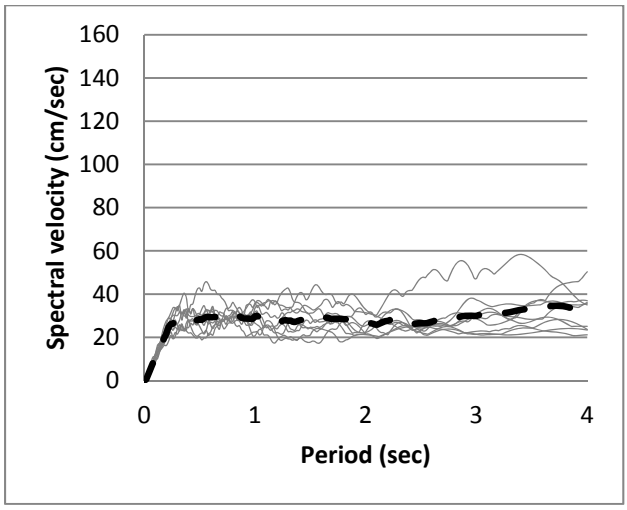

(a) Velocity spectra for Cape Girardeau

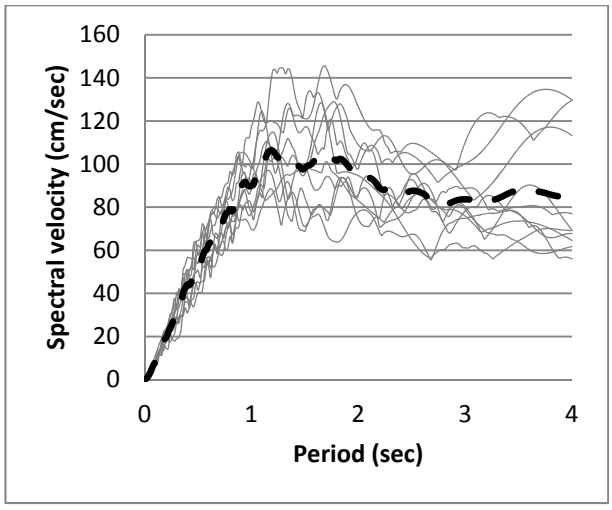

(b) Velocity spectra for Paducah

Figure 5.4 Velocity spectra for synthetic ground records

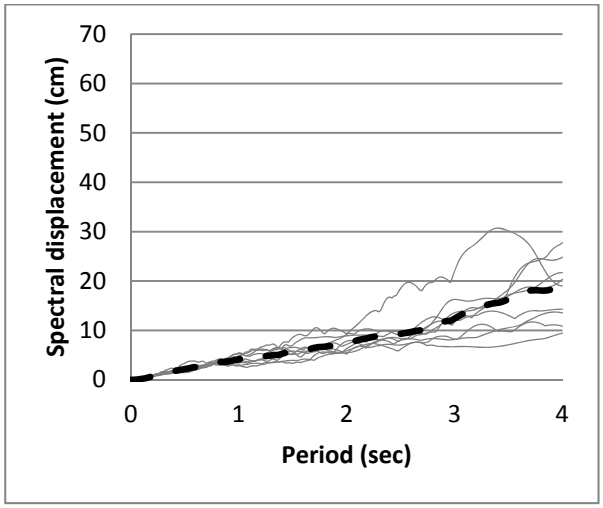

(a) Displacement spectra for Cape Girardeau

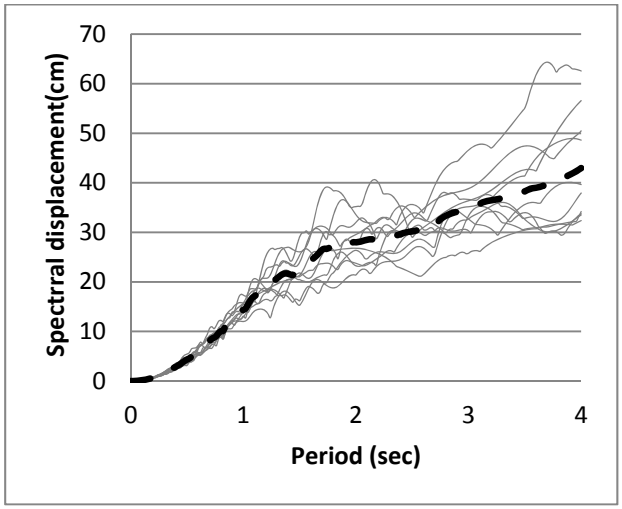

(b) Displacement spectra for Paducah

Figure 5.5 Displacement spectra for synthetic ground records

5.2.2. Scaling of ground motions

An important consideration as to how ground motions are applied for analysis also deals with the baseline hazard to which the bridge is subjected. Previous research suggests that before modeling, all ground motions should be normalized to some measure of intensity, such as the Peak Ground Acceleration (PGA), Peak Ground Velocity (PGV), or spectral acceleration at the

first-mode period of the structure ($S_a(T_1)$) (Vamvatsikos and Cornell 2002). The parametric suite contains bridges with elastic first-mode natural periods varying from 0.2 seconds to over 1 second, and periods increase greatly as nonlinearities appear during analysis. A modal analysis for the parametric variations in this study was performed as part of this project by Meléndez Gimeno (2011). Therefore it was decided to normalize the motions based on a technique used in the SAC Joint Venture (Somerville et al. 1997), where a single scale factor is used to minimize the weighted sum of the squared error between the average spectrum and the target design spectrum. Weighting factors of 0.1, 0.3, 0.3, and 0.3, for periods of 0.2, 1, 2, and 4 seconds, respectively, can be used to provide an approximation over a range of periods. Equation (5.1) shows the calculation for least-squares fit, based on an assumption of lognormally distributed ground shaking hazard at each period:

$$SF = \prod_{i=1}^{N} \left[\frac{S_{ai}^{t}}{S_{ai}^{EQ}} \right]^{w_i} \tag{5.1}$$

where $\mathbf{S_{ai}^{t}}$ is the design spectral acceleration at period i, $\mathbf{S_{ai}^{EQ}}$ is the synthetic ground record average spectral acceleration at period i, $\mathbf{w_i}$ is the weighting factor for period i, and Π denotes the product of a sequence across the different periods being matched. This procedure is particularly well-suited for research applications since it places more emphasis on scaling a ground motion for periods of 1, 2, and 4 seconds, with less emphasis on matching the spectral acceleration for low period excitation, where ground motions can be more significantly variable.

This methodology was used to fit the synthetic ground motions to a 1000 year recurrence design spectra hazard for Cairo, Illinois, which is derived by AASHTO (2008). The rock CG records are normalized to Soil Class B hazard and the stiff soils Pa records are normalized to the Soil Class D hazard at the location. Figure 5.6 shows the existing ground motion spectra normalized to the respective design spectra, and these ground motions constitute the baseline hazard used in this research.

The ground motions as shown in Figure 5.6 are considered to be at a Scale Factor (SF) of 1.0, and are linearly scaled up and down to provide relative estimates of structural performance for different excitation hazards. The location of Cairo, Illinois has one of the highest hazards for the state, and a reasonably high hazard for the NMSZ. Other locations in the region would

typically have lower hazards, so as an example the design spectrum hazard in Carbondale, IL can be approximated by scaling the baseline ground motions with a factor of roughly 0.5. Also, since the IDOT design procedure is a prescriptive one that is not directly dependent on the spectral acceleration, bridges that perform adequately for the Cairo location will likely do so for any Illinois site. The current research used six distinct scale factors (0.5; 0.75; 1.0 = design; 1.25; 1.5; and 1.75) that encompassed different hazard levels.

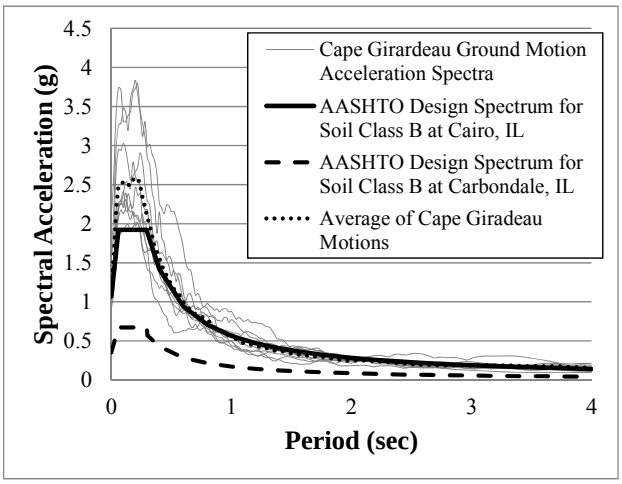

(a) Acceleration spectra for Cape Girardeau normalized to Cairo Soil Class B Hazard (rock)

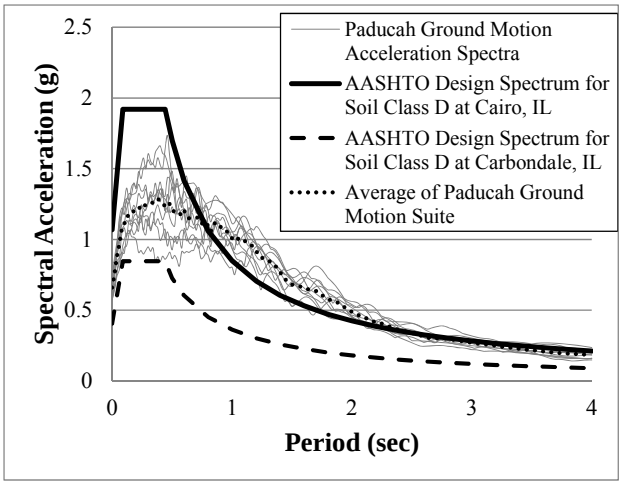

(b) Acceleration spectra for Paducah normalized to Cairo Soil Class D Hazard (stiff soil)

Figure 5.6 Spectral acceleration of synthetic ground records normalized to the Cairo, Illinois design hazard

The spectral acceleration of actual earthquake events increases logarithmically for higher magnitude risks, and so the linear scaling used herein does not perfectly simulate higher risks. However, the maximum considered earthquake (MCE) hazard (2% in 50 year risk) for the Cairo location can be approximated to be between the 1.5 and 1.75 linearly scaled ground motions. The scaled ground motions are shown along with the ASCE 7-05 MCE Spectrum in Figure 5.7.

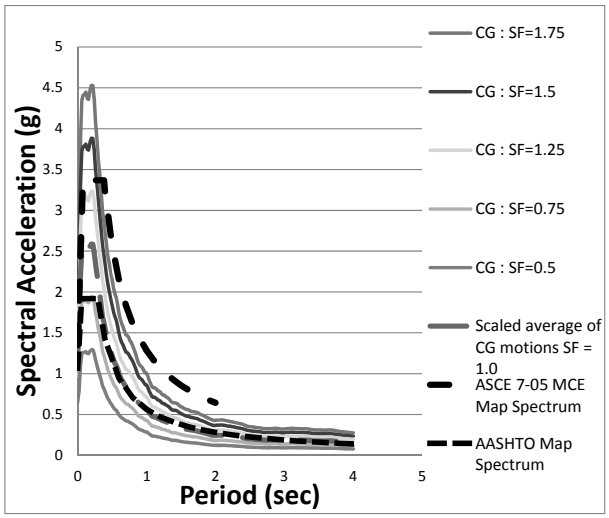

(a) Scaled Cape Girardeau ground motion averages

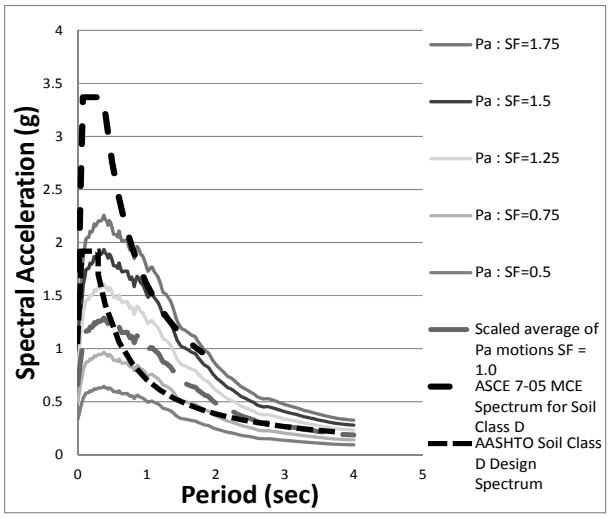

(b) Scaled Paducah ground motion averages

Figure 5.7 Scaled ground motion averages compared to design spectra

5.2.3. Vertical acceleration effects

The effects of vertical accelerations can be a significant concern for bridges since they can alter the force distribution, perhaps even causing failure in reinforced concrete piers (Kim, Holub, and Elnashai 2011), and can also cause large variations in the normal force experienced by bearings / isolators. Furthermore, since vertical accelerations are typically of high frequency content, they can coincide with the vertical natural period of the bridge and cause increased vertical oscillation.

The current research, however, does not include the effects of vertical acceleration, for several compelling reasons. (a) This project is aimed at bridges in southern Illinois, a region of roughly 200 x 400 km (125 x 250 miles) located north of the New Madrid fault zone, and since vertical accelerations attenuate quickly (Elgamal and He 2004), becoming less significant for epicentral distances greater than 30km, it is likely that high vertical acceleration would not be a typical hazard for most of the area. (b) The NMSZ is believed to be characterized by a strike-slip fault that is not expected to produce high vertical accelerations, and current research confirms that horizontal-to-vertical component (H/V) spectral ratios are relatively high, with values between 2 and 4 in the low-frequency range ($f \leq 5$ Hz) (Zandieh and Pezeshk 2011; Tavakoli, Pezeshk, and Cox 2010). (c) Contrary to general speculation, some recent research has shown that vertical acceleration may have negligible effects on sliding-isolation systems (Mosqueda,

Whittaker, and Fenves 2004; Iemura, Jain, and Taghikhany 2004). (d) In many of the parametric bridge cases, the response is primarily influenced by the presence of retainers, fixed bearings and backwalls, rather than behavior in the bearing isolators or piers that could be more affected by vertical acceleration.

5.2.4. Directionality effects

Current design provisions (AASHTO 2009) recommend that when carrying out calculations in one of a bridge's orthogonal directions, in addition to applying the full demand in the direction of interest, the designer should also add 30% of the absolute value of the demand in the perpendicular direction to account for the directional uncertainty of earthquake motion. Some recent research (Mackie, Cronin, and Nielson 2011), has used nonlinear MDOF analyses of symmetric multi-span highway bridges with no skew, within a stochastic framework, to show that the incidence angle is typically negligible in the bridge response. Other work (Bisadi and Head 2010), however, has shown that there may be significant variance caused by the incidence angle. Only uni-directional ground motions are available for the region, and therefore the current research focused primarily on orthogonal applications of the ground shaking. Sample studies were carried out with non-orthogonal (45° incident angle) excitation, for the SsC15T2S, SlW15T1F and the CsC40T1S bridge variations. As will be shown in the Chapters 6 and 7, although non-orthogonal excitation may alter bridge response and vary the sequence of damage, maximum bridge response typically occurs from unidirectional application of orthogonal ground motions. The design scenario where 30% of the ground motion is applied in a perpendicular direction is also discarded as it is also believed to provide little if any additional information than the pure orthogonal cases.

CHAPTER 6

DYNAMIC ANALYSES OF QUASI-ISOLATED SYSTEMS

Transient dynamic analyses have been performed for each bridge configuration with all twenty ground motions (scaled independently). Stiffness and mass proportional damping of 5% is used in the mode and additional damping occurs from hysteretic behavior of the nonlinear elements. Each model experiences a unique nonlinear response for each ground motion, and different limit states are reached in every individual analysis. Force and displacement data has been recorded for each nonlinear component of the bridge at every time step of the ground motion. Looking at individual components leads to a comprehensive, but complex, overview of the bridge's performance, so the data has also been simplified for separate systems. For example, at every substructure all bearing forces are summed and represented against an average of the bearing displacements. The bridge SsC40T1S was chosen to show a sample dynamic behavior since this bridge experiences several interesting nonlinearities, and also results in a sequence of damage that is discouraged per the IDOT ERS. All raw data from the analyses is presented in Appendix B.

6.1 Limit states encountered in dynamic analyses of bridges

A list of limit states that can be expected for a typical bridge in both the longitudinal and transverse directions is shown in Table 6.1. Nonlinear limit states include sliding and failure in the bearing components, as well as yielding of the backwalls and piers. These can be observed from hysteretic force-displacement curves of the various elements, as will be shown in Figure 6.2 and Figure 6.6. Un-seating of the bearing elements can occur if the bearings slide off of the piers or abutments. This is not explicitly modeled, and therefore these limit states were determined based on maximum acceptable displacements. Type I bearings were experimentally shown to be reliable, and the model defined in Section 3.1 was considered to be valid, as long as there was sufficient contact between the bearing and the concrete substructure. Pier caps and

abutment seats were considered to be dimensioned based on the IDOT Bridge Manual (IDOT 2009).

For the 1000 year event, the required support width, *N*, in inches, is calculated as:

$$N = \left[3.94 + 0.0204L + 0.084H + 1.087\sqrt{H}\sqrt{1+\left(2\frac{B}{L}\right)^2} \right] \frac{1+1.25F_vS_1}{\cos\alpha} \quad (6.1)$$

Where:

L= Typical length between expansion joints (ft)

H= Height of tallest substructure unit between expansion joints, including units at the joints (ft)

B = Out-to-out width of the superstructure (ft)

α = Skew angle (°)

F_vS_1= One second period spectral response coefficient modified for Site Class

B/L = Not to be taken greater than 3/8

This equation was used to design the appropriate seat width for each bridge structure for the Cairo Seismic Hazard. Type I bearing unseating was assumed to occur when any part of the bearing moved off of the designed substructure seat, as is shown in Figure 6.1 (a). At this phase, although the structure may not have collapsed, the bearing model would not capture the response accurately, and it is likely that the system will move into a more unstable configuration. As was presented in Chapter 3, Type II bearings were tested to displacements large enough to where the top plate was not in full contact with the bottom plate. Since highly nonlinear and unstable behaviors were observed for these bearings when the contact area decreased, unseating was assumed to occur when the contact distance (smallest dimension of rectangular contact area) became less than 7.5 cm (3 in.) as is shown in Figure 6.1 (b). For example Type II 7-b bearings, used at the abutments of short steel (Ss) structures, are assumed to begin unseating at a longitudinal displacement of 10.5 cm (4 in). Unseating of the bearings can cause extensive damage to the superstructure, substructure and diaphragm elements, or lead to a local or global collapse of the girders. Also, after unseating occurs, the validity of the computational models becomes somewhat questionable and the system is considered to have reached a critical limit state. Although this unseating is not considered unacceptable based on current IDOT ERS

philosophy, it is expected that future revisions of the IDOT bridge manual will aim to prevent this limit state as it is expected to lead to span loss in the bridge.

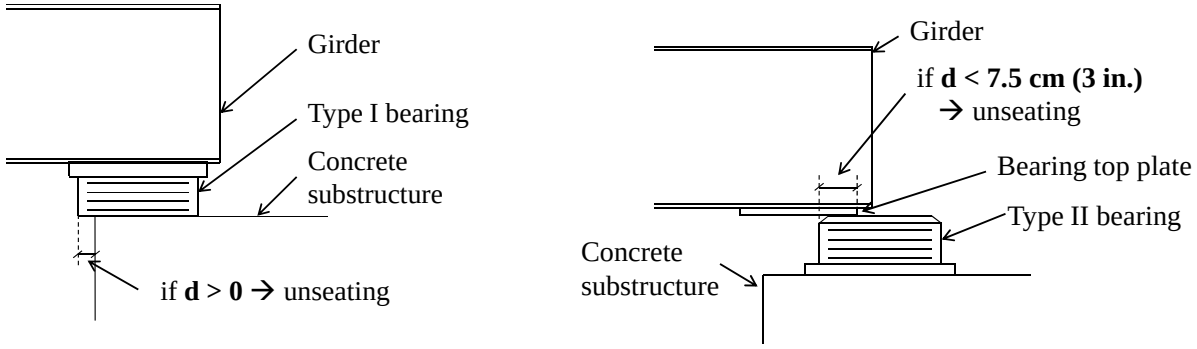

(a) Type I bearing unseating condition (b) Type II bearing unseating condition

Figure 6.1 Schematic representation of bearing unseating condition

Table 6.1 Typical limit states observed in bridge prototypes

Acceptable for quasi-isolation	**Acceptable as Level 3 fusing for quasi-isolation**
EA - Elastomeric bearings slide at abutment	P1 - Pier 1 yields
EP - Elastomeric bearing slides at Pier 1	P2 - Pier 2 yields
RA - Retainer failure at abutment	
RP - Retainer failure at Pier 1	**Discouraged for quasi-isolation**
Fb - Fixed (low-profile) bearing failure	UA - Unseating of bearing at abutment
Bw - Backwall yielding	UP - Unseating of bearing at pier

Although a nonlinear model was used to simulate the behavior of the flexible foundation boundary condition, no significant nonlinearity was encountered in the foundation elements, and limit states were not encountered for the foundation systems. Maximum foundation shear displacements were observed for the long superstructure bridge with wall pier substructures and remained below 20 cm (8 in.) for the design level earthquake. Even at MCE loading, the largest foundation deformations were less than 25 cm (10 in.), and the elements remained essentially elastic. The nonlinear curves used for modeling of the flexible foundation condition are discussed in Chapter 2, and by inspection it can be seen that the foundations only go a little bit into the non-linear range. Since steel H-pile foundations were used both at the abutment and at the piers, the performance of these systems is likely better than for some other types of foundations used in Illinois, so base shear data from this study can be used to determine if other foundation systems may be applicable for carrying quasi-isolated bridges.

When subjecting a bridge to transverse excitation, the limit states of bearings sliding and retainers failing are technically considered as independent events; however, by inspection of the results, it was noted that the retainers had a much larger influence on global behavior than did the bearings. The retainer capacity was the primary factor controlling the force transferred between superstructure and substructure, and until the retainers had failed, the system movement and relative bearing displacements remained essentially zero. Therefore, when considering limit states for transverse analyses, only the RA and RP limit states are indicated hereafter, indicating simultaneous occurrence of also the EA and EP limit states, respectively.

6.2 Longitudinal dynamic behavior of quasi-isolated bridge systems

Longitudinal hysteretic behavior of the bearings, backwalls, and piers of the SsC15T2S bridge are shown in Figure 6.2. The bridge was subjected to pure longitudinal ground shaking from one of the stiff soil (Pa) ground motions with scale factors of 0.5 and 1.5. The relative pier displacement is calculated by taking the top of the pier displacement, subtracting the foundation shear deformation as well as the base rotation times the pier height, and thereby giving a force displacement behavior which is comparable for different foundations and different pier heights. In Figure 6.2 the maximum recorded forces and relative displacements are shown with an X and a square respectively. Relative displacements of the bearings indicate the magnitude of movement at the sliding interface such that the elastic bearing deformation is removed (i.e. when the bearing force is zero).

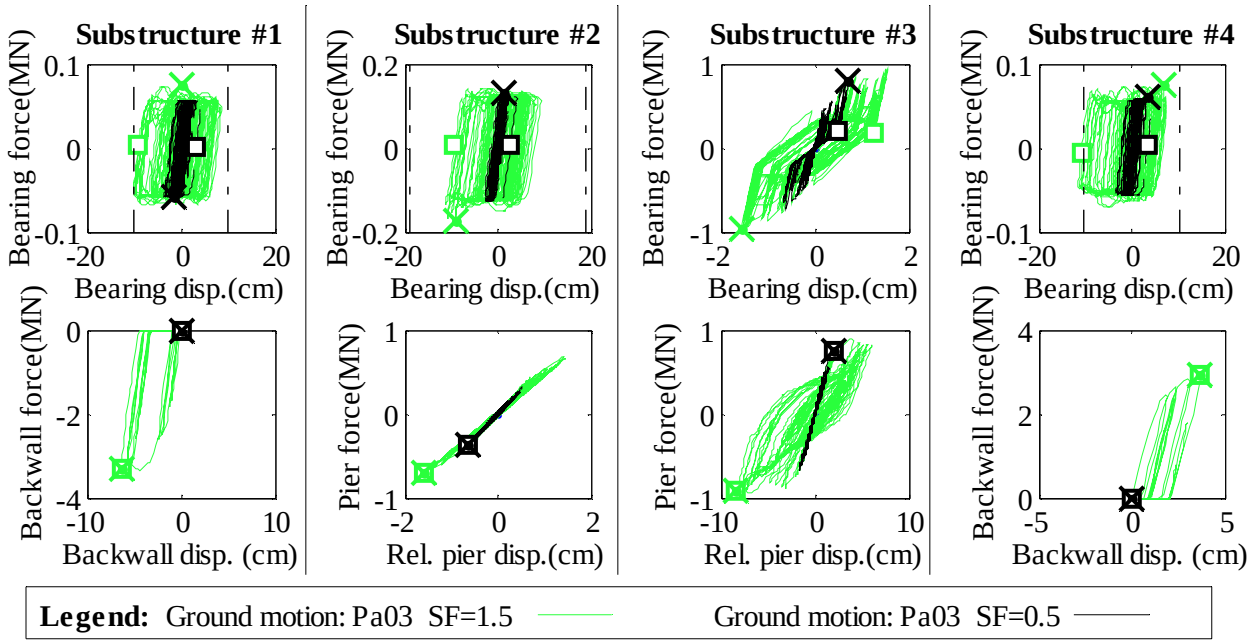

Figure 6.2 Longitudinal dynamic behavior of the SsC15T2S bridge subjected to pure longitudinal excitation. Maximum response indicated with a square for relative displacement and an X for force

Figure 6.2 shows the occurrence of several interesting nonlinear behaviors for the typical longitudinal analyses. The ground motion applied at SF = 0.5 results in only elastic deformation of the column piers, and there is no contact with the backwalls. However, when the SF = 1.5 motion is applied, column Pier 2 experiences yielding, the backwall is engaged and experiences nonlinear deformation, and the bearings slide much more, coming close to unseating at Substructure #4 (where the UA limit state is indicated by the vertical dash-dot lines).

Results similar to those presented above are available for all components for each individual analysis. To capture the bridge behavior for the entire suite of ground motions and for varying earthquake intensity, the indicated maximum values from the plots above are transferred onto Figure 6.3, where the force and displacement response are plotted against the earthquake scale factor, resulting in an IDA curve for the bridge response. The plots use a circle to show the average response to the suite of ten Paducah ground motions applied at a certain scale factor, and horizontal lines are used to indicate the range of standard deviations for the data set. The squares and Xs, indicating the maximum displacements and forces specific to the analyses carried out with the Pa 03 ground motion (at SF = 1.5 and SF = 0.5), have also been transferred onto Figure 6.3

The IDA curves in Figure 6.3 also show the incremental behavior for the SsC15T2S bridge, subjected to non-orthogonal shaking at a 45° incident angle. It can be seen that the non-orthogonal analysis causes the fixed bearing component to fracture and slide (toward experiencing a displacement of about 10 cm (4 in.) at SF = 1.75), while the pure longitudinal case causes only minor elasto-plastic deformation. For the non-orthogonal shaking, the coupled longitudinal and transverse forces exceed the bearing capacity, while in the pure longitudinal case Pier 2 experienced yielding before the fixed bearing fractures, as can be observed from the Substructure #3 forces shown in Figure 6.2. Finally these IDA plots show that, with the exception of the Substructure #3 fixed bearing displacements, all other force and displacement response is greater for the pure longitudinal excitation. The non-orthogonal shaking case is also compared to pure transverse excitation in Section 6.3.

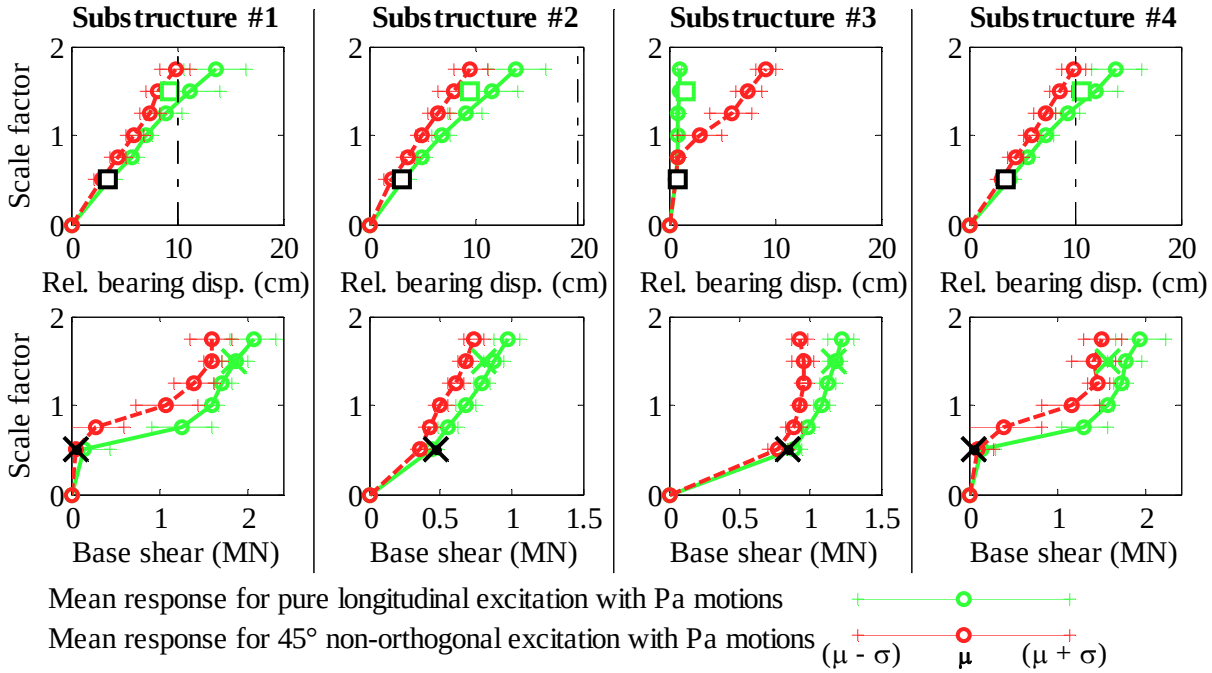

Figure 6.3 Maximum absolute longitudinal response of SsC15T2S bridge for incremental hazard

The IDA plots are useful in determining the overall system behavior and the sequence of damage as different limit states occur in different analyses. For instance, in Figure 6.3 one can see that the base shear at the abutments corresponds to backwall interaction that begins to appear at SF = 0.75, but the forces are lower than shown in Figure 6.2 since compacted backfill absorbs

a larger part of the seismic demands. The base shear for Substructure #3 is limited to roughly 1.2 MN (270 kips) due to yielding of the column pier at that substructure. The sequence of damage for the SsC15T2S bridge subjected to Pa (stiff soil) ground motions is shown in Figure 6.4 (a) and (c). The SsC15T1S bridge experiences yielding of Pier 2 before the design level earthquake, and also unseating at the abutment when the SF = 1.5 incremental hazard is reached. Both of these limit states are discouraged for a properly quasi-isolated system.

A preferred longitudinal sequence of damage for the quasi-isolated system would begin with "inexpensive" limit states (bearings sliding, EA and EP) for small earthquakes, followed by relatively easy to repair limit states (Fb and Bw) for design level earthquakes, and finally would permit damage to substructure elements (P1 and P2) so long as there is no unseating of the bearings. For the IDOT ERS, an underlying requirement is that there is no substructure yielding or unseating for scale factors of 1.0 or less. Figure 6.4 (b) shows a schematic of a sample acceptable sequence of damage, which is also plotted with square markers in part (c) of that figure. Note that the sequence of damage does not need to follow any particular pattern of damage, as long as limit states do not enter the dark (orange in color) shading indicated in Figure 6.4 (c).

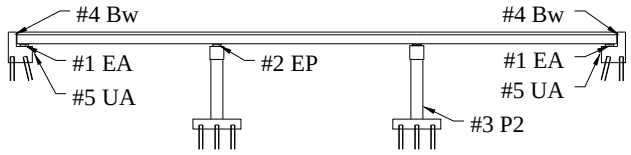

(a) Sequence of damage for SsC15T2F bridge

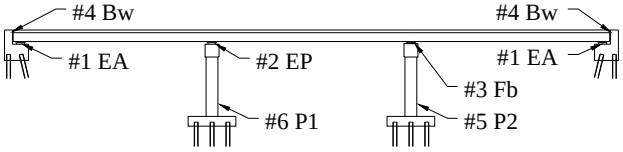

(b) A sample sequence of acceptable damage

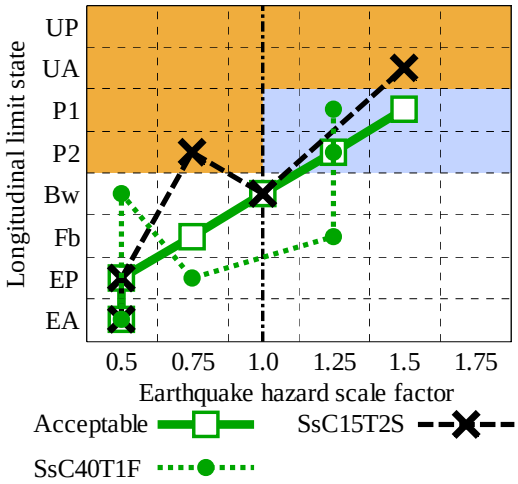

(c) Sequence of damage plot

Figure 6.4 Sequence of damage representation for incremental longitudinal hazard

A sample of an acceptable longitudinal sequence of damage is the bridge variation SsC40T1F. Figure 6.5 shows the IDA plots for the relative bearing and pier displacements for

that bridge when subjected to the Pa and the CG ground motion suites. The tall pier system is relatively flexible and has a high period of vibration, so the overall system displacement (and bearing displacement at the abutments grows essentially linearly with the increase in excitation intensity. Since the piers are flexible no yielding occurs at lower scale factors and fusing of the bearings at the intermediate substructures occurs later than for the short bridge variant. The IDA curves and hysteretic data, show that after a scale factor of about 1.25, the bearings at the intermediate substructure bearings have fused, and the pier displacements increase more than the overall system (deck) displacement. This occurs because the backwalls limit the deck's longitudinal displacement while the piers oscillate greatly from excitation of their self-weight. The sequence of damage for the SsC40T1F structure, as shown in Figure 6.4 is acceptable, since no unseating occurs and pier damage occurs only after the design earthquake. Finally, comparing the response of the bridge subjected to CG vs. Pa motions, it is clear that the excitation from the stiff, Class D soils, is larger and this makes sense since the structural period of this bridge is initially high and increases as damage occurs through the system.

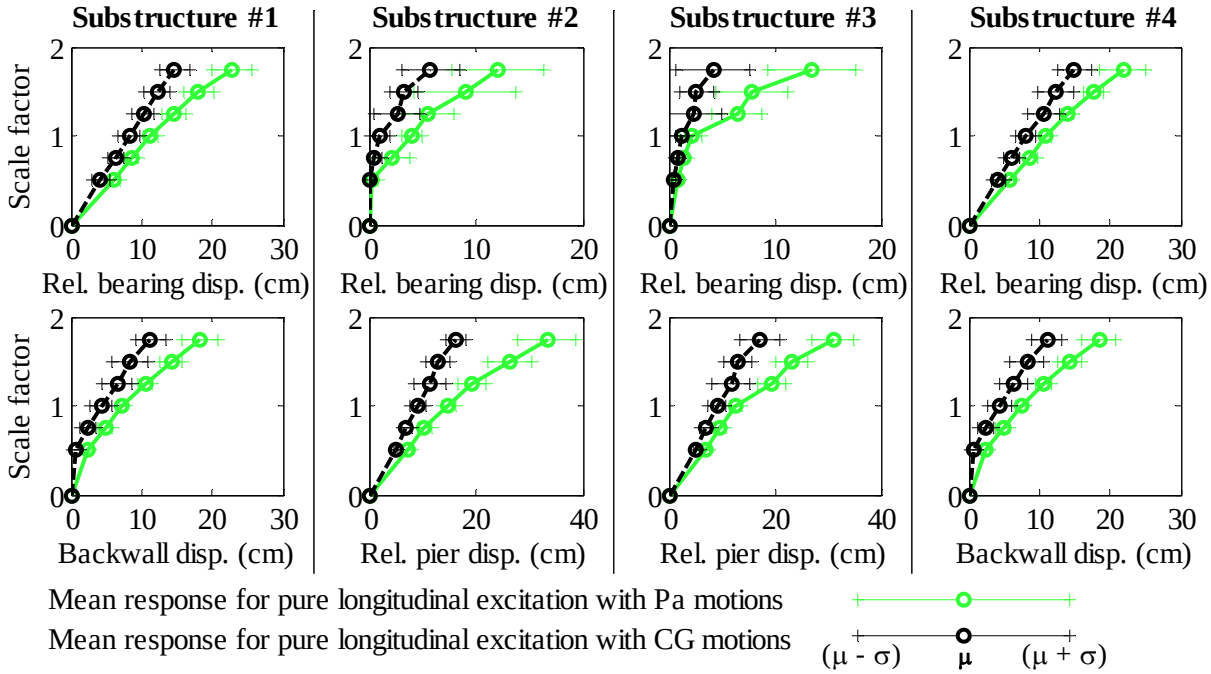

Figure 6.5 Maximum absolute longitudinal response of SsC40T1F bridge for incremental hazard

6.3 Transverse dynamic behavior of quasi-isolated bridge systems

Figure 6.6 shows hysteretic behavior of the retainers, bearings, and foundations of the SsC15T2S bridge when subjected to pure transverse excitation from one of the stiff soil (Pa) ground motions with scale factors of 0.5 and 1.5. From the force-displacement plots, it can be seen that the bearings begin to slide primarily after the retainers have failed, and one can also observe some nonlinear behavior in the foundations for the higher earthquake loads.

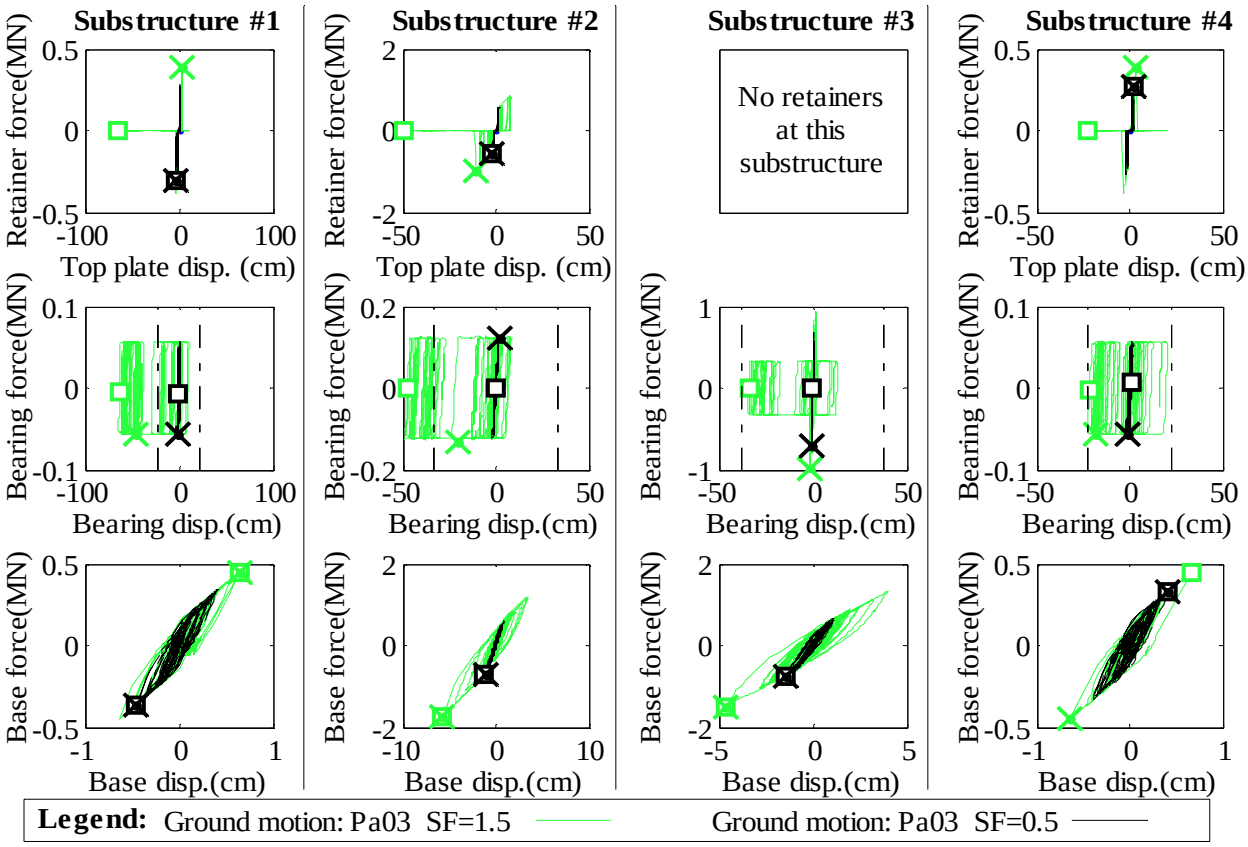

Figure 6.6 Transverse dynamic behavior of the SsC15T2S bridge subjected to pure transverse excitation. Maximum response indicated with a square for relative displacement and a cross for force

In Figure 6.7 the maximum absolute response values are again transferred onto IDA curves that show the response mean and standard deviation of the SsC15T2S bridge for pure transverse and non-orthogonal excitation. The base shear plots at the abutments correspond well to the maximum retainer and bearing sliding forces recorded earlier, while the base shears at the piers tend to increase even after bearing and retainer failure. This is because the mass of the piers

can cause additional seismic force for higher levels of ground acceleration. The abutment retainers fail and permit sliding at a hazard level of roughly SF = 0.75; the low-profile fixed bearings start to fail at a scale factors of 1.25, while the Pier 1 retainers fuse last at SF = 1.5. After the fuse components have failed, the displacements begin to increase significantly, resulting in abutment and pier bearings unseating at SF = 1.5. The pure transverse excitation again causes much larger base shears and displacements than the non-orthogonal excitation. This behavior can be explained since the bridge investigated with non-orthogonal excitation takes advantage of multiple lateral systems, including the side retainers and strong axis of the pier substructures, for the transverse force component, and the abutment backwall for the longitudinal force component.

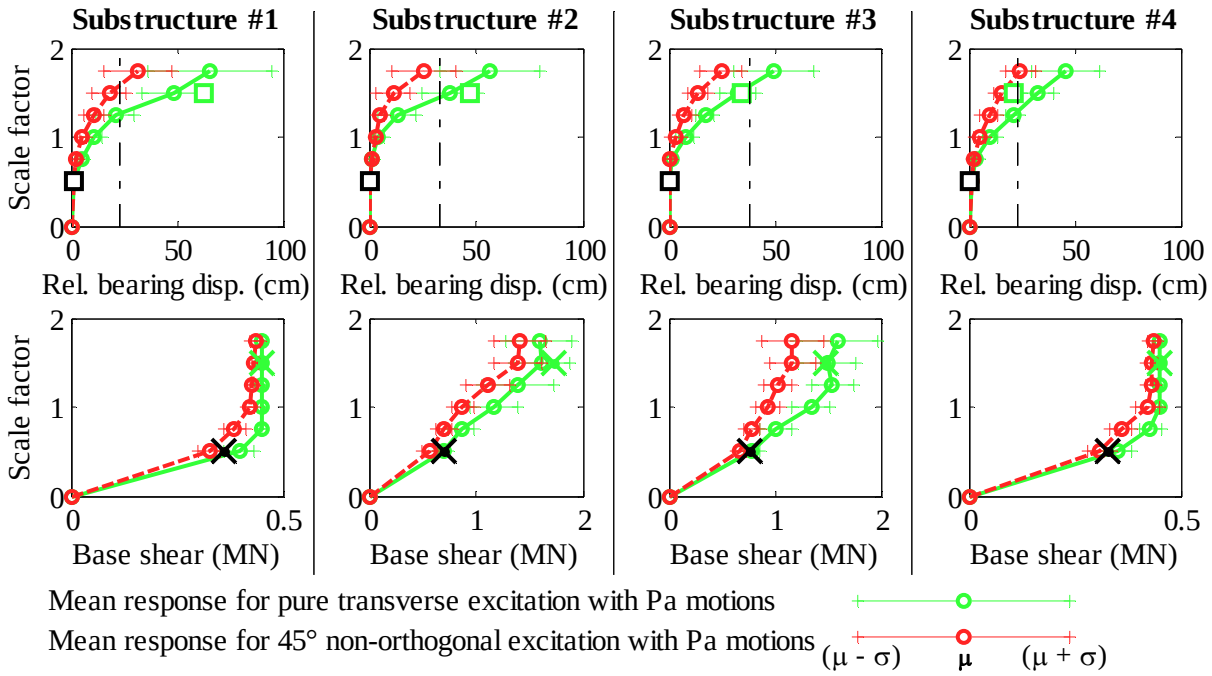

Figure 6.7 Maximum absolute transverse response of SsC15T1S bridge for incremental hazard

The transverse sequence of damage for the SsC15T2S structure, as shown in Figure 6.8, follows an acceptable level of fusing with the exception of the unseating behavior at close to the MCE hazard. An acceptable sequence of damage for the system permits retainer damage (RA and RP), and fixed bearing damage (Fb), as well as column pier yielding (P1 and P2) for larger

than design level earthquakes. An acceptable damage sequence is shown in Figure 6.8 (b), and is plotted with squares in part (c) of the same figure.

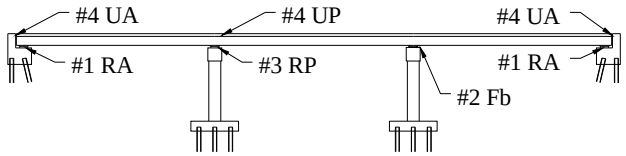

(a) Sequence of damage for SsC15T2F bridge

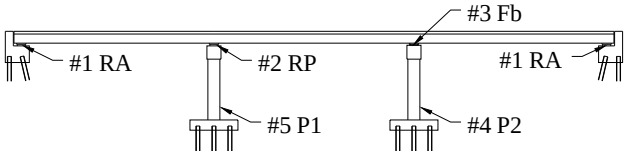

(b) A sample sequence of acceptable damage

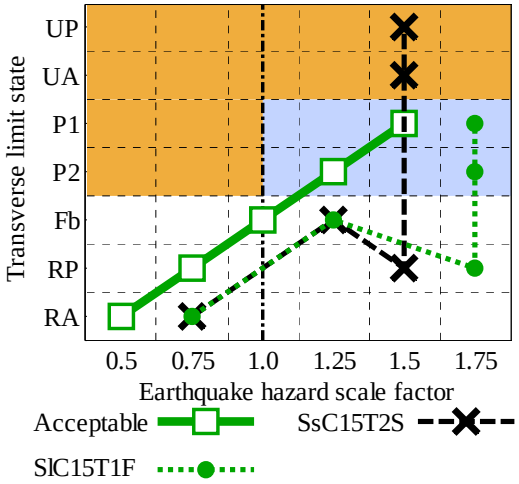

(c) Sequence of damage plot

Figure 6.8 Sequence of damage representation for incremental transverse hazard

The SlC15T1F bridge also has an acceptable sequence of damage for transverse excitation as is shown in Figure 6.8 (c). The IDA curves that characterize the bridge behavior are shown in Figure 6.9. The bearing displacement plots show that although the transverse displacements are high (36 cm (14 in.)), no unseating occurs. For this bridge all bearing components fuse, thereby permitting quasi-isolation of the structure. Despite the full fusing, intermediate pier damage is noted to occur at a high scale factors. The yielding in the piers occurs sue to the self-weight of the piers and the large forces from the long (Sl) superstructure.

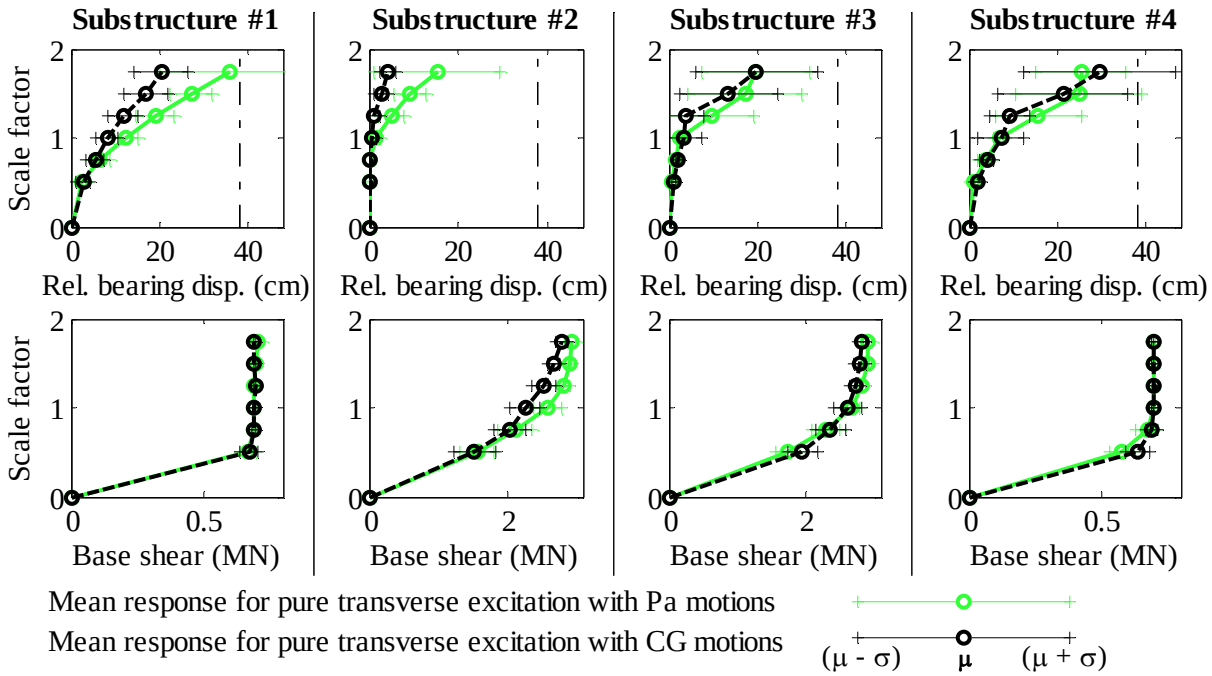

Figure 6.9 Maximum absolute transverse response of SlC15T1F bridge for incremental hazard

CHAPTER 7

RESULTS OF PARAMETRIC STUDY

Results from the entire parametric space were compared based on the peak recorded displacements, the normalized abutment and intermediate substructure base shears, and the observed sequence of damage. Peak recorded displacement values for a specific bridge and scale factor were taken as the average maximum bearing displacement for an entire suite of records. The maximum base shears were normalized by dividing the base shear by the vertical force at the substructure foundation before beginning the seismic analysis. Finally the sequence of damage was evaluated based on the methodology presented in Chapter 6 where Figure 6.3 and 6.6 were used to schematically represent limit states as they occur in the longitudinal and transverse directions. Appendix B presents the raw results from the parametric study and Appendix C presents post-processed data which is more convenient for the system evaluation. Section 7.1 presents comparison of the response of the different bridges and sections 7.2 - 7.4 present insight to the performance of the quasi isolated systems.

7.1 Data synthesis and evaluation

7.1.1 System displacements

Table 7.1 presents the average maximum displacements for various groups of bridges, for different directions and for different ground motions of excitation. The nomenclature used to identify the bridge variations is described in detail in Chapter 5. Two letters are used to indicate the superstructure type, (Ss-Steel short; Sl-Steel long; Cs-Concrete short), another letter and the two numbers designate the intermediate substructure type (C-Column pier; W-Wall pier) and height in feet (15 ft - 4.5 m; 40 ft - 12.2 m). Furthermore a letter and number indicate the bearing type used (T1-Type I IDOT bearing; T2-Type II IDOT bearing) and a final letter indicates the soil conditions modeled (F-Fixed/rock; S-flexible boundary conditions). Thereby in Table 7.1 the value listed under C, Longitudinal Stiff Soil (Pa) (12.9 cm), presents the average maximum displacement for all 24 bridge variations that have multi-column piers. Comparisons between systems are also presented, for example from the (40'-15')/40' cell in the first section,

we can note that out of the entire parametric space, bridges with tall piers experience 50% more displacement when subjected to longitudinal excitation from Stiff Soil Pa ground motions. Finally at the bottom of Table 7.1 there is a comparison between system response from the CG and Pa Ground motions. There we can observe that bridges with higher periods (Sl, 40' or S soil) typically experience larger amplification of response from the Stiff Soil excitation than those with shorter periods. Comparisons considered to be of interest are indicated with a gray background and are discussed in more detail in sections 7.2 – 7.4 of this chapter.

Table 7.1 Average maximum displacements at SF = 1.0 for different groups of bridge systems, and comparison of results

Longitudinal Stiff Soil (Pa) (cm)

Ss	Sl	Cs
10.4	17.0	12.7

C	W	(W-C)/W
12.9	13.8	0.06

15'	40'	(40'-15')/40'
8.9	17.9	0.50

T1	T2	(T2-T1)/T2
12.1	14.7	0.17

F	S	(S-F)/S
12.7	14.1	0.10

Transverse Stiff Soil (Pa) (cm)

Ss	Sl	Cs
15.0	22.1	17.5

C	W	(W-C)/W
19.5	16.8	-0.16

15'	40'	(40'-15')/40'
12.6	23.7	0.47

T1	T2	(T2-T1)/T2
15.5	20.9	0.26

F	S	(S-F)/S
14.1	22.3	0.37

Longitudinal Rock (CG) (cm)

Ss	Sl	Cs
6.9	9.6	7.6

C	W	(W-C)/W
8.2	7.9	-0.03

15'	40'	(40'-15')/40'
6.3	9.8	0.36

T1	T2	(T2-T1)/T2
7.1	8.9	0.20

F	S	(S-F)/S
8.0	8.0	0.00

Transverse Rock (CG) (cm)

Ss	Sl	Cs
10.2	11.3	9.5

C	W	(W-C)/W
10.5	10.1	-0.04

15'	40'	(40'-15')/40'
9.4	11.3	0.17

T1	T2	(T2-T1)/T2
8.5	12.2	0.31

F	S	(S-F)/S
10.3	10.4	0.01

All longitudinal displacements average

10.25

All transverse displacements average

13.64

Ratio (Pa-CG)/Pa

Ss	Sl	Cs
0.33	0.44	0.40

C	W
0.37	0.43

15'	40'
0.30	0.45

T1	T2
0.41	0.39

F	S
0.37	0.43

Ratio (Pa-CG)/Pa

Ss	Sl	Cs
0.32	0.49	0.46

C	W
0.46	0.40

15'	40'
0.26	0.52

T1	T2
0.45	0.41

F	S
0.27	0.53

Table 7.2 Average maximum displacements at SF = 1.75 for different groups of bridge systems, and comparison of results

Longitudinal Stiff Soil (Pa) (cm)

Ss	Sl	Cs
22.8	34.5	26.8

C	W	(W-C)/W
26.7	29.4	0.09

15'	40'	(40'-15')/40'
19.5	36.6	0.47

T1	T2	(T2-T1)/T2
26.2	29.9	0.12

F	S	(S-F)/S
25.9	30.2	0.14

Transverse Stiff Soil (Pa) (cm)

Ss	Sl	Cs
60.8	66.6	59.7

C	W	(W-C)/W
52.6	72.2	0.27

15'	40'	(40'-15')/40'
59.6	65.2	0.09

T1	T2	(T2-T1)/T2
52.1	72.7	0.28

F	S	(S-F)/S
51.9	72.9	0.29

Longitudinal Rock (CG) (cm)

Ss	Sl	Cs
13.3	19.2	15.2

C	W	(W-C)/W
16.1	15.7	-0.02

15'	40'	(40'-15')/40'
12.1	19.7	0.38

T1	T2	(T2-T1)/T2
14.5	17.3	0.16

F	S	(S-F)/S
15.3	16.5	0.07

Transverse Rock (CG) (cm)

Ss	Sl	Cs
31.3	29.1	27.0

C	W	(W-C)/W
25.0	33.3	0.25

15'	40'	(40'-15')/40'
28.8	29.4	0.02

T1	T2	(T2-T1)/T2
23.7	34.6	0.31

F	S	(S-F)/S
26.9	31.3	0.14

All longitudinal displacements average

21.01

All transverse displacements average

43.76

Ratio (Pa-CG)/Pa

Ss	Sl	Cs
0.42	0.44	0.43

C	W
0.40	0.47

15'	40'
0.38	0.46

T1	T2
0.45	0.42

F	S
0.41	0.45

Ratio (Pa-CG)/Pa

Ss	Sl	Cs
0.48	0.56	0.55

C	W
0.52	0.54

15'	40'
0.52	0.55

T1	T2
0.55	0.52

F	S
0.48	0.57

7.1.2 System base shears

Base shears are compared in a manner similar to displacements; global observations on the response are presented in Sections 7.2 – 7.4.

Table 7.3 Average maximum pier base shears at SF = 1.0 for different groups of bridge systems, and comparison of results

Longitudinal Stiff Soil (Pa)

Pier 1	Pier 2

Ss		Sl		Cs	
0.31	0.376	0.254	0.292	0.208	0.246

C		W		(W-C)/W	
0.24	0.303	0.283	0.334	0.154	0.093

15'		40'		(40'-15')/40'	
0.3	0.414	0.219	0.222	-0.39	-0.87

T1		T2		(T2-T1)/T2	
0.27	0.32	0.248	0.317	-0.11	-0.01

F		S		(S-F)/S	
0.24	0.288	0.287	0.349	0.18	0.175

Transverse Stiff Soil (Pa)

Pier 1	Pier 2

Ss		Sl		Cs	
0.51	0.543	0.5	0.56	0.46	0.54

C		W		(W-C)/W	
0.45	0.483	0.54	0.62	0.17	0.22

15'		40'		(40'-15')/40'	
0.56	0.628	0.44	0.48	-0.27	-0.32

T1		T2		(T2-T1)/T2	
0.52	0.551	0.48	0.55	-0.07	0.00

F		S		(S-F)/S	
0.51	0.532	0.49	0.57	-0.04	0.07

Longitudinal Rock (CG)

Pier 1	Pier 2

Ss		Sl		Cs	
0.39	0.383	0.288	0.3	0.23	0.24

C		W		(W-C)/W	
0.26	0.293	0.351	0.345	0.255	0.152

15'		40'		(40'-15')/40'	
0.35	0.377	0.261	0.261	-0.35	-0.44

T1		T2		(T2-T1)/T2	
0.31	0.321	0.30	0.316	-0.04	-0.02

F		S		(S-F)/S	
0.29	0.30	0.323	0.341	0.10	0.129

Transverse Rock (CG)

Pier 1	Pier 2

Ss		Sl		Cs	
0.47	0.515	0.42	0.48	0.36	0.43

C		W		(W-C)/W	
0.38	0.42	0.48	0.54	0.21	0.22

15'		40'		(40'-15')/40'	
0.48	0.55	0.38	0.41	-0.24	-0.35

T1		T2		(T2-T1)/T2	
0.44	0.48	0.42	0.48	-0.05	-0.01

F		S		(S-F)/S	
0.51	0.55	0.35	0.41	-0.47	-0.34

Ratio (Pa-CG)/Pa

Ss		Sl		Cs	
-0.27	-0.02	-0.13	-0.03	-0.09	0.01

C		W	
-0.09	0.03	-0.24	-0.03

15'		40'	
-0.16	0.09	-0.19	-0.18

T1		T2	
-0.14	-0.01	-0.21	0.00

F		S	
-0.23	-0.03	-0.13	0.02

Ratio (Pa-CG)/Pa

Ss		Sl		Cs	
0.08	0.05	0.15	0.14	0.21	0.20

C		W	
0.17	0.12	0.12	0.13

15'		40'	
0.15	0.12	0.13	0.14

T1		T2	
0.15	0.12	0.13	0.13

F		S	
0.00	-0.04	0.29	0.28

Table 7.4 Average maximum abutment base shears at SF = 1.0 for different groups of bridge systems, and comparison of results

Longitudinal Stiff Soil (Pa)

Abut 1	Abut 2

Ss		Sl		Cs	
2.70	2.62	2.482	2.408	2.213	2.131

C		W		(W-C)/W	
2.24	2.15	2.182	2.112	-0.03	-0.02

15'		40'		(40'-15')/40'	
1.88	1.86	2.538	2.4	0.26	0.22

T1		T2		(T2-T1)/T2	
2.18	2.11	2.241	2.15	0.03	0.02

F		S		(S-F)/S	
2.37	2.26	2.048	2.009	-0.16	-0.12

Transverse Stiff Soil (Pa)

Abut 1	Abut 2

Ss		Sl		Cs	
0.71	0.71	0.84	0.84	0.97	0.97

C		W		(W-C)/W	
0.79	0.80	0.79	0.79	0	-0.01

15'		40'		(40'-15')/40'	
0.79	0.79	0.79	0.79	0.00	0.00

T1		T2		(T2-T1)/T2	
0.84	0.84	0.75	0.75	-0.12	-0.12

F		S		(S-F)/S	
0.79	0.79	0.79	0.80	0.00	0.01

Longitudinal Rock (CG)

Abut 1	Abut 2

Ss		Sl		Cs	
2.27	2.24	2.081	2.042	1.72	1.71

C		W		(W-C)/W	
1.81	1.80	1.761	1.753	-0.03	-0.03

15'		40'		(40'-15')/40'	
1.70	1.68	1.877	1.868	0.10	0.10

T1		T2		(T2-T1)/T2	
1.80	1.80	1.77	1.753	-0.02	-0.03

F		S		(S-F)/S	
1.87	1.83	1.705	1.724	-0.10	-0.06

Transverse Rock (CG)

Abut 1	Abut 2

Ss		Sl		Cs	
0.71	0.71	0.84	0.84	0.97	0.96

C		W		(W-C)/W	
0.79	0.79	0.79	0.79	0.00	0.00

15'		40'		(40'-15')/40'	
0.79	0.79	0.79	0.79	0.00	0.00

T1		T2		(T2-T1)/T2	
0.83	0.83	0.75	0.75	-0.11	-0.11

F		S		(S-F)/S	
0.79	0.79	0.79	0.79	0.00	0

Ratio (Pa-CG)/Pa

Ss		Sl		Cs	
0.16	0.15	0.16	0.15	0.22	0.20

C		W	
0.19	0.17	0.19	0.17

15'		40'	
0.10	0.10	0.26	0.22

T1		T2	
0.17	0.15	0.21	0.18

F		S	
0.21	0.19	0.17	0.14

Ratio (Pa-CG)/Pa

Ss		Sl		Cs	
0.00	0.00	0.00	0.00	0.00	0.00

C		W	
0.00	0.00	0.00	0.00

15'		40'	
0.00	0.00	0.00	0.00

T1		T2	
0.00	0.00	0.00	0.00

F		S	
0.00	0.00	0.00	0.00

The abutment base shears in Table 7.4 include all force transferred at the abutment foundations, including the backwall force, but not the backfill contribution. Since these are normalized based on abutment vertical loads which are relatively low, they result in relatively high factors. We can note that the longitudinal abutment base shears correspond to the backwall capacities, and the transverse shears correspond to the retainer and bearing capacities.

7.1.3 Sequence of damage

The sequence of damage for each structure was evaluated based on the procedures presented in Chapter 6. Since incremental hazard is applied it is important to evaluate the performance of the structure at design level earthquakes, as well as at MCE level earthquakes, and it is preferred that the sequence of damage follows the acceptable patterns as were presented in Figures 6.3 and 6.6. Table 7.5 – 7.8 present the sequence of damage for each bridge when subjected to a different direction and type of excitation. These tables are used to find similarities in damage patterns between groups of bridges. For example by inspection we note that only bridges with tall column piers and short superstructures (Ss and Cs) experience acceptable sequence of damage in the longitudinal direction, while all other bridges experience yielding of Pier 2. To further aid in the visualization of unseating behaviors, Tables 7.9 – 7.12 are presented to show the scale factor at which unseating was first noted for the given bridge variations.

Table 7.5 Limit state occurrence for all bridges subject to incremental longitudinal Pa motion excitation

			Steel short (Ss) superstructure		Steel long (Sl) superstructure		Precast Concrete (Cs) superstructure	
			Short 4.5 m (15 ft)	Tall 12.2 m (40 ft)	Short 4.5 m (15 ft)	Tall 12.2 m (40 ft)	Short 4.5 m (15 ft)	Tall 12.2 m (40 ft)
Column pier substructure	Type I Bearings	Fixed Fdn.	EP|**P2**|Bw|(1)	|Bw|(1)|P2|EP|P1|Fb|	|Bw|**P2**|EP|(1)|P1|	|Bw|**P2**|**P1**|(1)|	|Bw|**P2**|EP|(1)|	|Bw|EP|(1)|P2|P1|
		Flex. Fdn.	EP|**P2**|Bw|(1)	|Bw|(1)|P2|P1|EP|Fb|	|Bw|**P2**|EP|(1)|P1|	|Bw|**P2**|**P1**|(1)|	|Bw|EP|**P2**|(1)|	|Bw|EP|(1)|P2|P1|
	Type II Bearings	Fixed Fdn.	EP|**P2**|Bw|(1)|Fb|**UA**|	|Bw|**UA**|(1)|P2|P1|Fb|UP	|EP|Bw|**P2**|(1)|**UA**	|Bw|EP|**P2**|**P1**|**UA**|(1)|	EP|Bw|**P2**|(1)|**UA**	|Bw|EP|**UA**|(1)|P2|P1|
		Flex. Fdn.	|EP|**P2**|Bw|(1)|**UA**|	|Bw|**P2**|**UA**|(1)|P1|Fb|	|EP|Bw|**P2**|(1)|**UA**	|Bw|UA|EP|**P2**|**P1**|(1)|	EP|Bw|**P2**|(1)|**UA**	|Bw|EP|**UA**|(1)|P2|P1|
Wall pier substructure	Type I Bearings	Fixed Fdn.	EP|**P2**|Fb|Bw|(1)|P1|	Bw|EP|**P2**|**P1**|Fb(1)	**P2**|Bw|EP|(1)|P1|	|Bw|**P2**|**P1**|(1)|EP|	|**P2**|EP|Bw|**P1**|(1)	|Bw|**P2**|**P1**|(1)|EP|Fb|
		Flex. Fdn.	EP|**P2**|Bw|(1)|P1|Fb|	Bw|EP|**P2**|**P1**|Fb(1)	|Bw|**P2**|(1)|P1|EP	|Bw|**P2**|**P1**|(1)|EP|	|**P2**|EP|Bw|(1)|P1|	|Bw|**P2**|**P1**|(1)|EP|Fb|
	Type II Bearings	Fixed Fdn.	EP|**P2**|Fb|Bw|(1)|**UA**|	Bw|EP|**P2**|**P1**|Fb|**UA**|(1)|**UP**	**P2**|EP|Bw|(1)|**UA**	|Bw|**P2**|**P1**|**UA**|(1)|EP|	|**P2**|EP|Bw|(1)|**UA**|	|Bw|**P2**|**P1**|**UA**|(1)|EP|Fb|
		Flex. Fdn.	EP|**P2**|Fb|Bw|(1)|**UA**|	Bw|EP|Fb|**P2**|**P1**|**UA**|**UP**|(1)	EP|Bw|**P2**|(1)|**UA**	|Bw|**P2**|**P1**|**UA**|(1)|EP|	|**P2**|EP|Bw|(1)|**UA**|	|Bw|**P2**|**P1**|**UA**|(1)|EP|Fb|

Notes:
- (1) indicates the state of the structure at the design level hazard (SF=1). Limit states to left of the marker occur at lower, or at the design level earthquake and limit states on the right occur at higher intensities.
- If a limit state is not indicated then it did not occur for the mean response at hazard levels up to SF=1.75.
- Limit states that are bolded occur earlier in the sequence of damage than is intended by the IDOT ERS

Table 7.6 Limit state occurrence for all bridges subject to incremental longitudinal CG motion excitation

			Steel short (Ss) superstructure		Steel long (Sl) superstructure		Precast Concrete (Cs) superstructure	
			Short 4.5 m (15 ft)	Tall 12.2 m (40 ft)	Short 4.5 m (15 ft)	Tall 12.2 m (40 ft)	Short 4.5 m (15 ft)	Tall 12.2 m (40 ft)
Column pier substructure	Type I Bearings	Fixed Fdn.	|EP|**P2**|Bw|(1)	|Bw|(1)|P2|P1|EP	|Bw|**P2**|(1)|EP|P1|	|Bw|(1)|P2|P1|	|Bw|**P2**|EP|(1)|	|Bw|(1)|P2|P1|
		Flex. Fdn.	|EP|**P2**|Bw|(1)	|Bw|(1)|P2|P1|EP|Fb|	|Bw|**P2**|(1)|EP|P1|	|Bw|(1)|P2|P1|	|Bw|EP|**P2**|(1)|	|Bw|(1)|P2|P1|
	Type II Bearings	Fixed Fdn.	|EP|**P2**|Bw|(1)|Fb|**UA**|	|Bw|(1)|**UA**|P2|P1|Fb|	|EP|Bw|**P2**|(1)	|Bw|EP|(1)|P2|P1|**UA**|	|Bw|EP|**P2**|(1)	|Bw|EP|(1)|**UA**|P2|P1|
		Flex. Fdn.	|EP|**P2**|Bw|(1)|**UA**|	|Bw|(1)**UA**|P1||P2|Fb|	|EP|Bw|**P2**|(1)	|Bw|EP|(1)|**UA**|P2|P1|	|Bw|EP|**P2**|(1)	|Bw|EP|**UA**|(1)|P2|P1|
Wall pier substructure	Type I Bearings	Fixed Fdn.	EP|**P2**|Fb|Bw|**P1**|(1)	Bw|**P2**|**P1**|(1)|EP|Fb|	**P2**|Bw|EP|(1)|P1|	|Bw|**P2**|**P1**|(1)|	|**P2**|EP|Bw|(1)|P1|	|Bw|**P2**|**P1**|(1)|
		Flex. Fdn.	EP|**P2**|Bw|Fb|(1)|P1|	Bw|**P2**|**P1**|(1)|EP|Fb|	|Bw|**P2**|(1)|P1|EP	|Bw|**P2**|**P1**|(1)|	|**P2**|EP|Bw|(1)|P1|	|Bw|**P2**|**P1**|(1)|
	Type II Bearings	Fixed Fdn.	EP|**P2**|Fb|Bw|(1)|P1|**UA**|	Bw|**P2**|**P1**|(1)|EP|Fb|**UA**|	**P2**|EP|Bw|(1)	|Bw|**P2**|**P1**|(1)|**UA**|	|**P2**|EP|Bw|(1)|	|Bw|**P2**|**P1**|(1)|**UA**
		Flex. Fdn.	EP|**P2**|Fb|Bw|(1)|P1|**UA**|	Bw|EP|Fb|**P2**|**P1**|(1)|**UA**|	EP|Bw|**P2**|(1)|**UA**	|Bw|**P2**|**P1**|(1)|**UA**|	|**P2**|EP|Bw|(1)|	|Bw|**P2**|**P1**|(1)|**UA**

Notes:
- (1) indicates the state of the structure at the design level hazard (SF=1). Limit states to left of the marker occur at lower, or at the design level earthquake and limit states on the right occur at higher intensities.
- If a limit state is not indicated then it did not occur for the mean response at hazard levels up to SF=1.75.
- Limit states that are bolded occur earlier in the sequence of damage than is intended by the IDOT ERS

Table 7.7 Limit state occurrence for all bridges subject to incremental transverse Pa motion excitation

			Steel short (Ss) superstructure		Steel long (Sl) superstructure		Precast Concrete (Cs) superstructure	
			Short 4.5 m (15 ft)	Tall 12.2 m (40 ft)	Short 4.5 m (15 ft)	Tall 12.2 m (40 ft)	Short 4.5 m (15 ft)	Tall 12.2 m (40 ft)
Column pier substructure	Type I Bearings	Fixed Fdn.	RA|Fb|(1)|EP|RP|	RA|**P2**|**P1**|(1)|	RA|(1)|Fb|P2|P1	RA|**P2**|**P1**|(1)|**UA**	RA|Fb|(1)|EP|RP|**UP**	RA|EP|**P2**|**P1**|(1)|
		Flex. Fdn.	RA|Fb|(1)|EP|RP|**UA**|**UP**	RA|**P2**|**P1**|(1)|	RA|(1)|P1|P2|Fb|**UA**	RA|**P2**|**P1**|(1)|	RA|Fb|(1)|EP||RP|**UP**	RA|EP|(1)|P2|P1|
	Type II Bearings	Fixed Fdn.	Fb|RA|(1)|EP|RP|**UA**|**UP**	RA|**P2**|**P1**|**UA**|(1)|RP	RA|(1)|P2|Fb|**UA**	RA|**P2**|**P1**|**UA**|(1)|	RA|Fb|(1)|EP|**UA**|**UP**|RP	RA|EP|**P2**|**P1**|**UA**(1)|
		Flex. Fdn.	RA|Fb|(1)|EP|RP|**UA**|**UP**	RA|**P2**|**P1**|**UA**|(1)|RP	RA|(1)|P2|Fb|**UA**	RA|**UA**|**P2**|**P1**|(1)|	RA|(1)EP|Fb|**UA**|RP|**UP**|	RA|EP|P2|**P1**|**UA**(1)|
Wall pier substructure	Type I Bearings	Fixed Fdn.	RA|Fb|EP|RP|(1)	RA|EP|Fb|(1)	RA|Fb|(1)|EP|RP|**UA**	RA|(1)|EP|Fb|RP|	RA|EP|Fb|(1)|RP|**UP**|	RA|Fb|EP|(1)
		Flex. Fdn.	RA|Fb|(1)|EP|RP|**UA**|**UP**|	RA|EP|Fb|(1)|**UA**|**UP**|	RA|Fb|(1)|EP|**UA**|RP|**UP**	RA|(1)|Fb|EP|**UA**|RP|**UP**	RA|EP|Fb|EP(1)|RP|**UA**|**UP**|	RA|Fb|EP|(1)|**UA**|**UP**|
	Type II Bearings	Fixed Fdn.	RA|EP|Fb|(1)|**UA**|RP|**UP**|	RA|EP|Fb|(1)|**UA**|**UP**|	RA|(1)|Fb|EP|**UA**|RP|**UP**	RA|**UA**|Fb|(1)|EP|RP	RA|EP|Fb|EP(1)|RP|**UA**|**UP**|	RA|EP|Fb|(1)|RP|**UA**|**UP**|
		Flex. Fdn.	RA|EP|Fb|(1)|**UA**|RP|**UP**|	RA|EP|Fb**UA**|(1)|**UP**|	RA|(1)|Fb|EP|**UA**|RP|**UP**	RA|Fb|**UA**|(1)|EP|RP|	RA|EP|Fb|EP(1)|RP|**UA**|**UP**|	RA|EP|Fb|(1)|RP|**UA**|**UP**|

Notes:
- (1) indicates the state of the structure at the design level hazard (SF=1). Limit states to left of the marker occur at lower, or at the design level earthquake and limit states on the right occur at higher intensities.
- If a limit state is not indicated then it did not occur for the mean response at hazard levels up to SF=1.75.
- Limit states that are bolded occur earlier in the sequence of damage than is intended by the IDOT ERS

Table 7.8 Limit state occurrence for all bridges subject to incremental transverse CG motion excitation

			Steel short (Ss) superstructure		Steel long (Sl) superstructure		Precast Concrete (Cs) superstructure	
			Short 4.5 m (15 ft)	Tall 12.2 m (40 ft)	Short 4.5 m (15 ft)	Tall 12.2 m (40 ft)	Short 4.5 m (15 ft)	Tall 12.2 m (40 ft)
Column pier substructure	Type I Bearings	Fixed Fdn.	RA|Fb|(1)|EP|RP|	RA|(1)|P2|	RA|(1)|Fb|P2|P1	RA|**P2**|**P1**|(1)	RA|Fb|(1)|EP|	RA|EP|(1)|P2|P1|
		Flex. Fdn.	RA|Fb|(1)	RA|(1)|P2|	RA|(1)	RA|(1)|P2|P1|	RA|Fb|(1)|EP|	RA|EP|(1)|P2|P1|
	Type II Bearings	Fixed Fdn.	RA|Fb|(1)|**UA**	|RA|(1)|P2|P1|RP|**UA**|	RA|(1)|P2|Fb|**UA**|	RA|(1)|P2|P1|**UA**|	RA|Fb|(1)|EP|**UA**	RA|EP|(1)|P2|P1|**UA**|
		Flex. Fdn.	RA|Fb|(1)|RP|**UA**|	|RA|(1)|P2|P1|RP|**UA**|	RA|(1)|P2|Fb|**UA**|	RA|(1)|P2|P1|**UA**|	RA|(1)|Fb|EP|**UA**	RA|EP|(1)|P2|P1|**UA**|
Wall pier substructure	Type I Bearings	Fixed Fdn.	RA|Fb|EP|RP|(1)	RA|EP|Fb(1)	RA|Fb|(1)|EP|RP	RA|(1)|EP|Fb|	RA|EP|Fb|(1)|RP|	RA|Fb|EP|(1)
		Flex. Fdn.	RA|Fb|(1)|EP|RP|	RA|EP|Fb(1)	RA|(1)|EP|Fb|	RA|(1)|EP|Fb|	RA|EP|Fb|EP(1)|RP|	RA|(1)|EP|Fb|
	Type II Bearings	Fixed Fdn.	RA|EP|Fb|(1)|RP|**UA**|	RA|EP|Fb|(1)|**UA**|**UP**|	RA|(1)|EP|Fb|**UA**	RA|Fb|(1)|EP|RP|**UA**	RA|EP|Fb|EP(1)|**UA**|RP|	RA|EP|(1)Fb|**UA**|
		Flex. Fdn.	RA|EP|Fb|(1)|**UA**|RP|**UP**|	RA|EP|Fb|(1)|**UA**|**UP**|	RA|(1)|EP|Fb|**UA**	RA|Fb|(1)**UA**|EP|RP|	RA|EP|Fb|EP(1)|**UA**|RP|	RA|EP|(1)Fb|**UA**|RP

Notes:
- (1) indicates the state of the structure at the design level hazard (SF=1). Limit states to left of the marker occur at lower, or at the design level earthquake and limit states on the right occur at higher intensities.
- If a limit state is not indicated then it did not occur for the mean response at hazard levels up to SF=1.75.
- Limit states that are bolded occur earlier in the sequence of damage than is intended by the IDOT ERS

Table 7.9 Scale factor of bearing unseating due to longitudinal Pa motion excitation

			Steel short (Ss) superstructure		Steel long (Sl) superstructure		Concrete (Cs) superstructure	
			4.5 m (15 ft)	12.2 m (40 ft)	4.5 m (15 ft)	12.2 m (40 ft)	4.5 m (15 ft)	12.2 m (40 ft)
Column pier substructure	Type I Bearings	Fixed Fdn.	NA	NA	NA	NA	NA	NA
		Flex. Fdn.	NA	NA	NA	NA	NA	NA
	Type II Bearings	Fixed Fdn.	**1.5**	**0.75**	**1.25**	**1**	**1.5**	**1**
		Flex. Fdn.	**1.5**	**1**	**1.25**	**0.75**	**1.5**	**1**
Wall pier substructure	Type I Bearings	Fixed Fdn.	NA	NA	NA	NA	NA	NA
		Flex. Fdn.	NA	NA	NA	NA	NA	NA
	Type II Bearings	Fixed Fdn.	**1.5**	**1**	**1.5**	**0.75**	**1.5**	**1**
		Flex. Fdn.	**1.5**	**1**	**1.25**	**0.75**	**1.5**	**1**

Table 7.10 Scale factor of bearing unseating due to longitudinal CG motion excitation

			Steel short (Ss) superstructure		Steel long (Sl) superstructure		Concrete (Cs) superstructure	
			4.5 m (15 ft)	12.2 m (40 ft)	4.5 m (15 ft)	12.2 m (40 ft)	4.5 m (15 ft)	12.2 m (40 ft)
Column pier substructure	Type I Bearings	Fixed Fdn.	NA	NA	NA	NA	NA	NA
		Flex. Fdn.	NA	NA	NA	NA	NA	NA
	Type II Bearings	Fixed Fdn.	**1.75**	**1.25**	NA	**1.25**	NA	**1**
		Flex. Fdn.	**1.75**	**1.25**	NA	**1.25**	NA	**1**
Wall pier substructure	Type I Bearings	Fixed Fdn.	NA	NA	NA	NA	NA	NA
		Flex. Fdn.	NA	NA	NA	NA	NA	NA
	Type II Bearings	Fixed Fdn.	**1.75**	**1.25**	NA	**1.25**	NA	**1.75**
		Flex. Fdn.	**1.75**	**1.5**	**1.75**	**1.25**	NA	**1.75**

Table 7.11 Scale factor of bearing unseating due to transverse Pa motion excitation

			Steel short (Ss) superstructure		Steel long (Sl) superstructure		Concrete (Cs) superstructure	
			4.5 m (15 ft)	12.2 m (40 ft)	4.5 m (15 ft)	12.2 m (40 ft)	4.5 m (15 ft)	12.2 m (40 ft)
Column pier substructure	Type I Bearings	Fixed Fdn.	NA	NA	NA	1.75	1.75	NA
		Flex. Fdn.	1.75	NA	1.75	NA	1.75	NA
	Type II Bearings	Fixed Fdn.	1.5	1	1.5	0.75	1.25	1.5
		Flex. Fdn.	1.5	1	1.25	0.75	1.25	1.75
Wall pier substructure	Type I Bearings	Fixed Fdn.	NA	NA	1.75	NA	1.75	NA
		Flex. Fdn.	1.75	1.75	1.75	1.5	1.75	1.75
	Type II Bearings	Fixed Fdn.	1.5	1.5	1.5	0.75	1.5	1.5
		Flex. Fdn.	1.25	1	1	1	1.25	1.25

Table 7.12 Scale factor of bearing unseating due to transverse CG motion excitation

			Steel short (Ss) superstructure		Steel long (Sl) superstructure		Concrete (Cs) superstructure	
			4.5 m (15 ft)	12.2 m (40 ft)	4.5 m (15 ft)	12.2 m (40 ft)	4.5 m (15 ft)	12.2 m (40 ft)
Column pier substructure	Type I Bearings	Fixed Fdn.	NA	NA	NA	NA	NA	NA
		Flex. Fdn.	NA	NA	NA	NA	NA	NA
	Type II Bearings	Fixed Fdn.	1.5	1.75	1.5	1.75	1.25	1.75
		Flex. Fdn.	1.5	1.75	1.75	1.75	1.75	1.75
Wall pier substructure	Type I Bearings	Fixed Fdn.	NA	NA	NA	NA	NA	NA
		Flex. Fdn.	NA	NA	NA	NA	NA	NA
	Type II Bearings	Fixed Fdn.	1.5	1.5	1.75	1.25	1.5	1.5
		Flex. Fdn.	1.5	1.25	1.75	1.5	1.5	1.5

7.2 General observations on earthquake hazard application

Based on the data provided in Section 7.1, as well as further information from appendices B and C, the following observations were developed for the parametric study.

7.2.1 Non-orthogonal (45° incident angle) application of ground motions.

Non-orthogonal seismic excitation was found to be as-critical or less critical than uni-directional ground motion application for the quasi-isolated system studied in this paper. The SsC15T2S, SlW15T1F and the CsC40T1S bridge variations were studied with uni-directional and non-orthogonal excitation, and it was determined that the mean bridge response was less for non-orthogonal ground motion application. As can be observed from the SsC15T2S results presented in Chapter 6 as well as the non-orthogonal result comparisons in Appendix C, the non-orthogonal excitation can often alter the sequence of damage, i.e. cause bearing failure or pier yielding, before it would occur in one of the orthogonal directions, but the peak displacements and base shears would still be recorded for cases where pure orthogonal excitation is applied. This behavior can be explained since the bridge tested with non-orthogonal excitation takes advantage of multiple lateral systems including the side retainers and strong axis of the pier substructures for the transverse force component, and the abutment backwall for the longitudinal force component.

7.2.2 Effect of ground motion type (rock CG motions vs. stiff soils Pa motions).

Excitation from Pa (stiff soil) ground motions typically resulted in higher displacement and base shear response than the CG (rock) ground motions, and this can be attributed to the relatively long period of the structures which are more susceptible to low frequency excitation. Results for the entire parametric space subject to longitudinal excitation with Pa motions at the design level earthquake hazard, resulted in 35% higher displacements, a 7% decrease in intermediate substructure base shears, and a 17% increase in the abutment backwall forces. For transverse excitation, the Pa motions resulted in 31% higher displacements, 15% higher base shears at the intermediate substructures, and the abutment base shears remained equivalent since they were limited by the retainer and bearing sliding force capacity for both types of excitation. The increase in base shear and displacements was more significant in structures with longer

periods (i.e. Sl vs. Ss superstructure, tall vs. short substructures and flexible vs. fixed base) which were again more susceptible to higher period excitation. By general observation of damage patterns in the entire parametric space it was noted that the Pa and CG motions produce approximately the same sequence of damage, but the Pa motions normally result in higher limit states being reached at lower hazard levels. For example in the longitudinal direction 35% more bridges experienced unseating when subject to the Pa than the CG motions.

7.3 Comparison of bridge systems in parametric study

7.3.1 Effect of isolation bearings (Type I vs. Type II).

Type II bearings typically result in slight reduction (7%) of Pier 1 base shears, slight reduction (11%) of transverse abutment base shears, and significantly higher displacements (19% longitudinal and 28% transverse). Due to the higher displacement, as well as the different unseating criteria used for Type II bearings, those systems tend to unseat at much lower hazard levels than bridges with Type I bearings. When subjected to stiff soil (Pa) longitudinal excitation, all bridges with tall substructures and Type II bearings (XxX40T2X) (twelve out of twenty-four Type II configurations) unseated at hazard levels at or lower than the design level earthquake (SF = 1.0), and almost all Type II bearing systems had unseated for SF = 1.75 for both the CG and Pa ground motions. In the transverse direction similar behavior was observed for the Type II bridges, with eight out of twenty-four Type II cases unseating before SF = 1 for the Pa motions, and all twenty-four bridges experiencing unseating by SF = 1.75 for both Pa and CG motions.

Type I bearing systems on the other hand performed much better, with no unseating recorded for longitudinal excitation level lower than the design level. For transverse excitation with Pa (stiff soil) ground motions, one out of twenty-four bridges unseated at a scale factor of SF = 1.5 and an additional twelve bridge variants unseated at SF =1.75. The bridges that had unseated were primarily bridges with flexible foundation boundary conditions. No transverse, unseating was recorded for Type I bearing systems for the CG (rock) ground motions so these bridges are considered vulnerable only for high seismic hazards conditions. Comparison of Type I and Type II bearing behavior can be observed from Figure 7.1.

7.3.2 *Effect of substructure type (multi-column pier vs. wall pier) and superstructure height (4.5 m (15 ft) vs. 12.2 m (40 ft)).*

For longitudinal analyses most wall and multicolumn pier bridges follow a similar sequence of damage where Pier 2 was damaged at low earthquake scale factors. Tall column pier structures with short steel and concrete superstructures (SsC40 and CsC40) were an exception since these bridges did not experience any column damage until after the design level earthquake was reached, after which both Piers 1 and 2 exhibit yielding. Tall wall pier structures (XxW40) and long steel bridges with tall column piers (SlC40) were not as flexible and yielding occurred in both the isolated and non-isolated substructures, Piers 1 and 2 respectively. For short substructure bridge variants, Pier 1 was isolated and protected from damage up to the design level earthquake, after which some of the piers with Type I bearings (namely SlC and XxW variants) were noted to experience yielding.

For transverse excitation, short multi-column pier substructures (XxC15) and all wall substructures (XxW##) were typically strong enough that the fixed bearings and Pier 1 retainers failed thereby allowing for effective quasi isolation. One exception was the long steel bridges (Sl) where some pier yielding was noted at high hazard levels for the short column pier variants. When subject to transverse excitation most tall multi-column pier substructures (XxC40) yield before reaching the design level earthquake, and the Pier 1 retainers and low-profile fixed bearings remain essentially elastic even at high levels of seismic design.

Bridges with tall pier substructures on average experienced maximum deformations that were 43% and 32% larger than their short pier equivalents for longitudinal and transverse excitation, respectively. These higher displacements often resulted in unseating failures as was noted in section 7.3.1. The tall pier substructures experienced lower normalized base shears than short pier bridges by 39% for longitudinal and 30% for transverse excitation. The difference in base shears can be attributed to the fact that the base shears were capped by the lateral yield capacity of the substructures which were lower for the taller piers. Backwall forces, however, increased by 22% for the taller bridge variations. The normalized intermediate substructure base shear of the wall pier bridges were 7% higher in the longitudinal and 12 % higher in the transverse directions, which can again be attributed to the yield capacity of the different systems. The displacement response and the abutment forces of the column and wall pier systems did not vary significantly.

7.3.3 Effect of superstructures type (Steel short / Steel long / Concrete short).

As is discussed in section 5.2.2 the long steel (Sl) superstructures often experienced pier yielding earlier than the other superstructures. This can be attributed to the higher axial load at the substructures, as well as the higher fuse capacities which are designed as a factor of the dead load. System displacements increased with superstructure length, and the short steel (Ss) superstructure generally had slightly higher normalized base shears. This is primarily because the substructure mass was higher when compared to the superstructure.

7.3.4 Effect of foundation boundary condition stiffness (fixed vs. flexible).

Bridge cases with flexible foundation conditions experienced 5% higher longitudinal displacements and 19% higher transverse displacements than brides with fixed foundations. The base shears were noted to be of similar magnitudes for the two foundation cases. Since the flexible foundations could accommodate some displacement, their presence often times altered the sequence of damage such that piers and fixed bearings experienced lower forces and were thereby damaged at higher scale factors of excitation, or were not damaged at all. Due to the higher displacement demands, flexible variations were somewhat more prone to unseating, typically reaching the UA or UP limit state at a scale factor of about 0.25 lower that what was observed for fixed foundation cases.

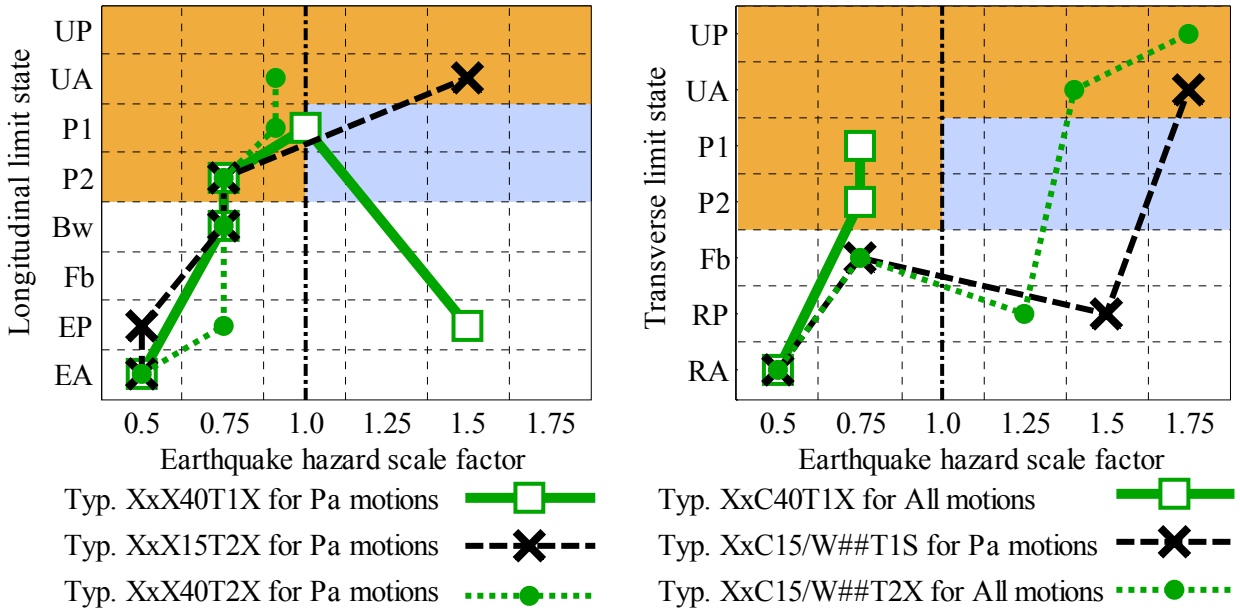

(a) General trends in longitudinal system damage

(b) General trends in transverse system damage

Legend of limit states

UP - Unseating of bearing at pier	Fb - Fixed (low-profile) bearing failure	RA - Retainer failure at abutment
UA - Unseating of bearing at abutment	Bw - Backwall yielding	RP - Retainer failure at Pier 1
P2 - Pier 2 yields	EA - Elastomeric bearings slide at abutment	
P1 - Pier 1 yields	EP - Elastomeric bearing slides at Pier 1	

Figure 7.1 General trends of system damage for some typical bridge cases

7.4 Other observations on bridge performance

The global bridge behavior is noted to be highly dependent on the capacity and the nonlinear behavior of the superstructure to substructure connecting elements. A sensitivity study will be carried out as part of this project to quantify the influence of these components on the quasi-isolated response. The study will vary the capacity of the backwalls, fixed bearings, and retainers, and is aimed at producing improved designs that would provide acceptable quasi-isolated bridge response. Based on the current results it is believed that the abutment backwalls have a significant potential contribution in limiting the longitudinal bridge displacements.

When looking at the results of the study, it should be noted that the ground motions were initially normalized to design spectra of Cairo, IL which is about the highest hazard for Illinois and the NMSZ in general. Bridges with quasi-isolation systems farther away from the seismic zone and at lower hazard levels are expected to perform better than those shown in this study.

The results from this research tend to be similar to other studies on bridges in the NMSZ. When studying fragilities of wall pier bridge in Illinois, Bignell and LaFave (2010) found that overall, bridge systems in the region are expected to experience only moderate damage for MCE level hazard, which is similar to the conclusions herein. Similarly they noted that pier properties were important in the general bridge response, but in contrast to the study presented in this paper they found that bearings (steel roller, low-profile fixed and elastomeric in some cases) had little influence in the bridge fragility. A different study of simply supported multispan bridges by Nielson and DesRoches (2007), showed that at MCE level earthquakes, significant vulnerabilities exist at the piers, abutments and in the unseating of girders. The study found that longitudinal and transverse displacement demands were of the same order, whereas the IDA results shown herein indicate that for continuous bridges transverse deformations tend to be much greater than longitudinal especially at higher degree of excitation.

CHAPTER 8

CONCLUSIONS

This thesis describes the development of numerical models for full bridge systems which capture all important aspects of nonlinear behavior and allow for evaluation of quasi-isolation as a seismic design philosophy. The work is part of an effort to refine the Illinois Department of Transportation (IDOT) earthquake resisting system for certain classes of bridges, where the quasi-isolation approach aims to maintain essentially elastic seismic behavior in the bridge substructure and superstructure for design level earthquakes while constraining damage to specific fusing mechanisms implemented at the interface between the two. The system utilizes low-profile fixed steel bearings at one intermediate substructure and steel reinforced elastomeric bearings that allow for thermal movement at all other substructures. The elastomeric bearings include (i) IDOT Type I bearings, where the elastomer is placed directly on the concrete substructure (vulcanized to only a top steel plate); and (ii) IDOT Type II bearings, which consist of a bottom steel plate anchored to the substructure, the elastomeric bearing, a middle plate vulcanized to the elastomer and coated on the top side with polytetrafluoroethylene (PTFE), and a top plate with a stainless steel mating surface carrying the girder load directly onto the PTFE surface. A formulation is provided for modeling these bearings that exhibit bi-directional friction stick-slip behavior, and the model is shown to be capable of representing experimental data. The low-profile steel bearings are placed to limit movements from serviceability loads on the bridge and include two steel plates connected with pintles, where the bottom plate is connected to the substructure with anchor bolts. A second bi-directional model is presented that can capture the yielding behavior of the fixed bearing components in three dimensional space. L-shaped steel retainer brackets are placed on the side of the elastomeric bearings to limit transverse movement, and are modeled using a bilinear element with an initial gap that can capture failure of the component at a specified displacement. In the case of larger seismic events the bearing components are intended to “fuse” and experience nonlinear behavior that can allow for passive isolation of the structure.

The thesis also describes modeling of the substructures, foundations, and abutment backwalls, where nonlinear behavior can influence the global behavior of a bridge. The behavior of a prototype bridge is presented through pushover analyses, and local behavior of the components are investigated. The second part of the thesis includes a parametric study that varies the bridge superstructure, substructure, foundation stiffness and quasi-isolation bearings. Bridge response was studied using incremental dynamic analyses with realistic ground motions suites for the New Madrid Seismic Zone (NMSZ), which were normalized to the design hazard at Cairo, IL (1000 year ≈ 7% in 50 year recurrence event). The suites were scaled up and down to obtain realistic behavior results for different intensity of earthquake hazard. The hazard from the maximum considered earthquake (MCE) (2500 year ≈ 2% in 50 years recurrence event) was estimated to be equal to the design level earthquake scaled by a factor of about 1.75. Performance was evaluated based on system displacements, base shears and the sequence of damage, giving insight to the global behavior of the structure at different hazard levels.

8.1 Observations from the computational study

The static pushover and dynamic parametric analyses point to the following conclusions:

- From the current parametric study, only a few bridge variants were noted to unseat for design level earthquakes, indicating that most structures in Illinois would not experience catastrophic damage during their typical design life. Since a high hazard level was used to scale the ground motions, unseating and span loss are not likely for regions of with moderate seismic risk.
- Bridges with Type II IDOT bearings were shown to be more prone to unseating, as the area of the bearing surface proved to often be insufficient given the magnitude of the displacement demand. Unseating of the bearings is an unstable and unpredictable behavior leading to large displacements, potential damage to deck and diaphragm elements and possible local or global collapse. Tall structures with Type II bearings experienced longitudinal unseating before design level earthquakes, and nearly all bridges with those bearings experienced both transverse and longitudinal unseating for MCE level hazards.

- Bridges with Type I bearings showed reliable behavior in preventing system collapse. No unseating was noted for longitudinal excitation of these bridges, and unseating of the bearings was only observed at MCE hazard earthquakes at regions with stiff (Class D) soil types.
- The sequence of damage of most bridge structures indicates yielding of piers with fixed bearings for small earthquakes, and potential unseating of some bridges for large seismic events, which are both discouraged for quasi-isolation. This research indicates that some calibration of fuse component capacities and revision of seat width equations can improve the sequence of damage for many bridge systems. Equations currently used in the IDOT Bridge manual should be modified to address these issues.
- Displacements in the longitudinal direction are generally much lower than in the transverse direction due to the influence of the backwall elements. For design level earthquakes transverse displacements were roughly 25% higher than the longitudinal, and the transverse displacements increased faster as the intensity of the earthquake increased. This can be explained since after the retainers and fixed bearings have failed, there is no active restraint of the system in the transverse direction.
- The capacity of the retainers and low-profile fixed bearing assemblies were noted to have a significant influence on forces transferred between the superstructure and substructure of the bridge. The fixed bearing capacity is much higher than the column yield limits, so the longitudinal sequence of damage is not as intended for quasi-isolation. The retainers at the abutments currently have a low capacity and can be adjusted to carry larger transverse forces at those substructures.
- Bridge displacement response was noted to be significantly larger for systems with tall pier substructures, flexible foundation boundary condition types and Type II bearings.
- Ground motions simulating stiff (Class D) soils typically resulted in larger force and displacement demands than rock (Class B) ground motions of similar intensity. The stiff soil ground motions also resulted in more limit states being reached at lower hazard intensities.

8.2 Preliminary recommendations for calibration of the quasi-isolation system

Based on the conclusions provided, the following updates to the IDOT Bridge Design Manual would improve the quasi-isolation system:

- Increase size of bearing surface for Type II bearings. This could be done by using a larger top stainless steel plate or larger bearings in general. Increasing the contact area would provide greater travel capacity and prevent unseating. This would be particularly beneficial for the longitudinal direction of excitation.
- Calibrate the strength of fixed bearing anchor bolts and pintles such that they fail at loads just higher than service loads (wind and small seismic events). Retainer strength, which is usually governed by the anchor bolt strength, should also be calibrated for the same objective. A capacity based design should be performed for piers in both directions so that fusing occurs in the bearing components before the substructure is damaged. This may also be accomplished in some cases by using more stringent constraints on the material properties used in the anchor bolts and pintles, for example by not allowing higher strength anchor bolt material to be reclassified as A36.
- Backwalls were shown to have a significant influence in reducing longitudinal displacements, so it may be beneficial to reformulate seat width equations such that different longitudinal and transverse seat widths are proportional to the expected displacements. For design level earthquakes, transverse displacements were 25% higher, so a design ration of 3-to-4 for longitudinal to transverse seat width could be appropriate. If the abutment foundations have redundant capacity, backwalls can be designed to be stronger and to limit longitudinal displacements even more than was shown in this study.
- Provide procedures and encourage designers to consider the backwall contribution for seismic design. This can allow for significant cost savings in substructure material which would otherwise be required to limit longitudinal response.

8.3 Further research needs

Additional research needs have been identified through this project and are organized in three distinct disciplines. The topics listed in Section 8.3.1 will be carried out as part of the ongoing research at the University of Illinois.

8.3.1 Suggestions for improvements to quasi-isolated systems to be performed as the next stage of this project

- Conduct sensitivity study on the superstructure to substructure connecting elements that will determine which components are most critical and will seek improved system behavior. Some investigations should include trying to use lower capacity fixed bearing components and retainers, thereby permitting improved system behavior based on current IDOT ERS goals. Different capacity backwalls should also be investigated to better understand the influence of these components.
- Determine if system geometry can be altered to improve the quasi-isolation response. This may include changing bearings used, using different retainer capacities and not using fixed bearings.
- Update seat width equations to accommodate required seismic displacements without unseating.
- Calibrate design equations and methods to better incorporate quasi-isolation into the design procedures. This would include adjustment of fixed bearing and retainer equations to allow for a preferred sequence of damage in the system.

8.3.2 Improvements to element models for bearing components

- The experiments presented for validation include only individual retainer and bearing tests. Retainer and bearings may have more complex behavior when tested together. The models may need to be updated to incorporate any interaction behaviors between the two components.
- The low-profile fixed bearings are built in displacement space, with a circular engagement surface, and are based on idealistic approximations of the bearing behavior. There is insufficient bi-directional data to validate these models effectively, so additional

experimental and advanced should modeling be performed to study the detailed behavior of these elements. With more information, the model behavior may be modified and calibrated differently than presented in this work.

8.3.3 Further study of global behavior of quasi-isolated systems

- This work considers only three-span bridges where the fixed bearings are on the second pier and there is no skew. Although quasi isolation may be effective for many different bridge variations, skew effects should be studied in more detail as they can influence the bridge behavior significantly. Integral abutment bridges should also be studied.
- The current research has shown that the quasi-isolation methodology works especially well with the Type I bearing systems for the fixed foundations and the pile group foundations with soft soils. Different foundation (single row piles or spread footing foundation) systems may produce a significantly different response so the applicability of quasi-isolation may not be as beneficial. More research on the quasi-isolation system is performed with different foundation types that may be much more flexible than the flexible boundary conditions considered in this research.
- The cost of the quasi-isolation system is believed to be significantly less than that of a classical isolation system since a complex design and high-cost components are not necessary. The system is also promising for mitigating seismic effects for a variety of bridges. A cost-benefit analysis that compares quasi-isolation systems to classical isolation systems and to fixed bearing systems should be performed to determine the feasibility and benefits of quasi-isolation.
- The quasi-isolation design methodology has the potential be adapted to more locations than the NMSZ, so investigation with various hazards should be performed to see if these systems may be suitable for other locations.

REFERENCES

AASHTO. 2008. *AASHTO Seismic Design Paramaters CD*.

AASHTO. 2009. *Guide specifications for LRFD seismic bridge design with interims*. Washington, D.C.: American Association of State Highway and Transportation Officials (AASHTO).

AASHTO. 2010. *Guide specifications for seismic isolation design - Third Edition*. Washington, D.C.: American Association of State Highway and Transportation Officials (AASHTO).

Abaqus FEA. 2010. *Abaqus FEA*. Vélizy-Villacoublay, France: SIMULIA website, Dassault Systèmes. http://www.simulia.com/products/abaqus_fea.html.

Abo-Shadi, Nagi A., M Saiidi, and David H. Sanders. 1999. *Seismic Response of Bridge Pier Walls in the Weak Direction*. Center for Civil Engineering Earthquake Research Department of Civil Engineering/258: University of Nevada, Reno, April.

ACI 318. 2008. Building Code Requirement s for Structural Concrete (ACI 318-08) and Commentary. American Concrete Institute, June.

Ang, Beng Ghee, M. J. Nigel Priestley, and T. Paulay. 1989. "Seismic Shear Strength of Circular Reinforced Concrete Columns." *ACI Structural Journal* 86 (1) (January 1): 45-59.

Aviram, Ady, Kevin R. Mackie, and Bozidar Stojadinovic. 2008. *Guidelines for Nonlinear Analysis of Bridge Structures in California*. Berkeley, CA: University of California Berkeley, August.

Barth, Karl E., and Haiyong Wu. 2006. "Efficient nonlinear finite element modeling of slab on steel stringer bridges." *Finite Elements in Analysis and Design* 42 (14-15) (October): 1304-1313. doi:10.1016/j.finel.2006.06.004.

Berry, Michael P., Dawn E. Lehman, and Laura N. Lowes. 2008. "Lumped-Plasticity Models for Performance Simulation of Bridge Columns." *ACI Structural Journal* 105 (3) (May 1): 270-279.

Bignell, John L., James M. LaFave, and Neil M. Hawkins. 2005. "Seismic vulnerability assessment of wall pier supported highway bridges using nonlinear pushover analyses." *Engineering Structures* 27 (14) (August 24): 2044-2063. doi:10.1016/j.engstruct.2005.06.015.

Bignell, John, and James LaFave. 2010. “Analytical fragility analysis of southern Illinois wall pier supported highway bridges.” *Earthquake Engineering & Structural Dynamics* 39 (7) (June 1): 709-729. doi:10.1002/eqe.966.

Bisadi, V., and M. Head. 2010. Orthogonal Effects in Nonlinear Analysis of Bridges Subjected to Multicomponent Earthquake Excitation. In , 20-20. ASCE. doi:10.1061/41130(369)20. http://ascelibrary.org/proceedings/resource/2/ascecp/369/41130/20_1.

Boulanger, Ross W., Christina J. Curras, Bruce L. Kutter, Daniel W. Wilson, and Abbas Abghari. 1999. “Seismic Soil-Pile-Structure Interaction Experiments and Analyses.” *Journal of Geotechnical and Geoenvironmental Engineering* 125 (9): 750-759. doi:10.1061/(ASCE)1090-0241(1999)125:9(750).

Buckle, Ian G. 1990. “Seismic Isolation: History, Application, and Performance—A World View.” *Earthquake Spectra* 6 (2): 161-201. doi:10.1193/1.1585564.

Chai, Yuk Hon, M. J. Nigel Priestley, and Frieder Seible. 1991. “Seismic Retrofit of Circular Bridge Columns for Enhanced Flexural Performance.” *ACI Structural Journal* 88 (5) (September 1): 572-584.

Chang, Ching-Jen, and Donald W. White. 2008. “An assessment of modeling strategies for composite curved steel I-girder bridges.” *Engineering Structures* 30 (11) (November): 2991-3002. doi:16/j.engstruct.2008.04.011.

Choi, Eunsoo, Reginald DesRoches, and Bryant Nielson. 2004. “Seismic fragility of typical bridges in moderate seismic zones.” *Engineering Structures* 26 (2) (January): 187-199. doi:10.1016/j.engstruct.2003.09.006.

Ciampoli, Marcello, and Paolo E Pinto. 1995. “Effects of Soil-Structure Interaction on Inelastic Seismic Response of Bridge Piers.” *Journal of Structural Engineering* 121 (5) (May 1): 806. doi:10.1061/(ASCE)0733-9445(1995)121:5(806).

Collins, Michael P., and Denis Mitchell. 1991. *Prestressed concrete structures*. Englewood Cliffs, N.J.: Prentice Hall.

Constantinou, M., A. Mokha, and A. Reinhorn. 1990. “Teflon bearings in base isolation II: Modeling.” *Journal of Structural Engineering* 116 (2): 455–474.

Elgamal, A., and L. He. 2004. “Vertical earthquake ground motion records: an overview.” *Journal of Earthquake Engineering* 8 (5): 663–697.

Ensoft Inc. 2010. *Ensoft, Inc.* Austin, Texas: http://www.ensoftinc.com/, July 4, 2010.

FEMA. 1988. *NEHRP recommended provisions for the development of seismic regulations for new buildings*. Washington, D.C.: Federal Emergency Management Agency (FEMA).

Fernandez, J. Alfredo, and Glenn J. Rix. 2008. Seismic Hazard Analysis and Probabilistic Ground Motions in the Upper Mississippi Embayment. In , 8-8. ASCE.

doi:10.1061/40975(318)8.
http://ascelibrary.org/proceedings/resource/2/ascecp/318/40975/8_1.

Filipov, Evgueni T., Joshua S. Steelman, Jerome F. Hajjar, James M. LaFave, and Larry A. Fahnestock. 2010. Bridge Bearing Fuse Systems for Regions with High-Magnitude Earthquakes at Long Recurrance Intervals. In Toronto, Ontario, Canada: EERI, July 25.

Gomez, Ivan, Amit Kavinde, Chris Smith, and Gregory Deierlein. 2009. *Shear transfer in exposed column base plates*. American Institute of Steel Construction. University of California, Davis & Stanford University, March.

Haroun, Medhat A., Gerard C. Pardoen, Robin Shepherd, Hesham A. Haggag, and Robert P. Kazanjy. 1993. *Cyclic Behavior of Bridge Pier Walls for Retrofit*. RTA. Department of Civil and Environmental Engineering: University of California, Irvine, December.

Higashino, Masahiko, Hiroki Hamaguchi, Shigeo Minewaki, and Satoru Aizawa. 2003. "Basic Characteristics and Durability of Low-Friction Sliding Bearings for Base Isolation." *Earthquake Engineering and Engineering Seismology* 4 (1): 95-105.

Ian G. Buckle, Michael C. Constantinou, Mirat Dicleli, and Hamid Ghasemi. 2006. *Seismic Isolation of Highway Bridges, MCEER Report 06-SP07*. MCEER University of Buffalo, August 29.

Ibarra, Luis F, Ricardo A Medina, and Helmut Krawinkler. 2005. "Hysteretic models that incorporate strength and stiffness deterioration." *Earthquake Engineering & Structural Dynamics* 34 (12) (October 1): 1489-1511. doi:10.1002/eqe.495.

Iemura, H., S. K. Jain, and T. Taghikhany. 2004. Effect of Vertical Acceleration on Seismic Performance of Resilient Sliding Isolation Systems in Highway Bridges. In Waseda University., December 7.

IDOT. 2009. *Bridge Manual*. Springfield, IL: Illinois Department of Transportation.

Kim, Sung Jig, Curtis J. Holub, and Amr S. Elnashai. 2011. "Analytical Assessment of the Effect of Vertical Earthquake Motion on RC Bridge Piers." *Journal of Structural Engineering* 137: 252. doi:10.1061/(ASCE)ST.1943-541X.0000306.

Klinger, R. E., J. A. Mendoca, and J. B. Malik. 1982. "Effect of Reinforcing Details on the Shear Resistance of Anchor Bolts Under Reversed Cyclic Loading." *ACI Journal* 79 (1) (January 1): 3-12.

Kowalsky, Mervyn J., M. J. Nigel Priestly, and Frieder Seible. 1999. "Shear and Flexural Behavior of Lightweight Concrete Bridge Columns in Seismic Regions." *ACI Structural Journal* 96 (1) (January 1): 136-148.

Liam Finn, W. D. 2005. "A Study of Piles during Earthquakes: Issues of Design and Analysis." *Bulletin of Earthquake Engineering* 3 (2) (January): 141-234. doi:10.1007/s10518-005-1241-3.

Mackie, Kevin R., Kyle J. Cronin, and Bryant G. Nielson. 2011. “Response Sensitivity of Highway Bridges to Randomly Oriented Multi-Component Earthquake Excitation.” *Journal of Earthquake Engineering* 15 (July): 850-876. doi:10.1080/13632469.2010.551706.

Mander, J. B., D-K. Kim, S.S. Chen, and G.J. Premus. 1996. *Response of Steel Bridge Bearings to Reversed Cyclic Loading*. Technical Report. Buffalo, NY: State University of New York at Buffalo, November 13.

McKenna, F., S. Mazzoni, and G. L Fenves. 2006. *Open System for Earthquake Engineering Simulation (OpenSees)*. University of California, Berkeley, CA.: Pacific Earthquake Engineering Research Center, http://opensees.berkeley.edu/. http://opensees.berkeley.edu/.

Meléndez Gimeno, C. 2011. “Seismic analysis for design of highway bridges in Illinois.” University of Illinois at Urbana-Champaign

Mosqueda, Gilberto, Andrew S. Whittaker, and Gregory L. Fenves. 2004. “Characterization and Modeling of Friction Pendulum Bearings Subjected to Multiple Components of Excitation.” *Journal of Structural Engineering* 130 (3) (March 1): 433-442.

Naeim, Farzad, and James M. Kelly. 1999. *Design of seismic isolated structures: from theory to practice*. John Wiley and Sons, March 11.

Nagarajaiah, Satish, Andrei M. Reinhorn, and Michalakis C. Constantinou. 1991. “Nonlinear Dynamic Analysis of 3-D–Base-Isolated Structures.” *Journal of Structural Engineering* 117 (7) (July): 2035-2054.

Nielson, Bryant G., and Reginald DesRoches. 2007. “Analytical Seismic Fragility Curves for Typical Bridges in the Central and Southeastern United States.” *Earthquake Spectra* 23: 615. doi:10.1193/1.2756815.

Nielson, Bryant G, and Reginald DesRoches. 2007. “Seismic Performance Assessment of Simply Supported and Continuous Multispan Concrete Girder Highway Bridges.” Journal of Bridge Engineering 12 (5) (September 1): 611. doi:10.1061/(ASCE)1084-0702(2007)12:5(611).

OpenSees various authors. 2011. *Open Sees Repository - http://opensees.berkeley.edu/WebSVN/listing.php?repname=OpenSees&path=%2Ftrunk%2FSRC*.

PEER. 2003. PEER Structural Performance Database for Concrete Columns. PEER. http://nisee.berkeley.edu/spd/.

PoLam, Ignatius, and Hubert Law. 2000. *Soil Structure Interaction of Bridges for Seismic Analysis*. Fountain Valley, CA: Earth Mechanics Inc., September 25.

Popovics, Sandor. 1973. “A numerical approach to the complete stress strain curve for concrete.” *Cement and concrete research* 3 (5): 583-599.

Scott, Michael H., and Gregory L. Fenves. 2006. “Plastic Hinge Integration Methods for Force-Based Beam–Column Elements.” *Journal of Structural Engineering* 132 (2): 244-252. doi:10.1061/(ASCE)0733-9445(2006)132:2(244).

Shamsabadi, Anoosh, Kyle M. Rollins, and Mike Kapuskar. 2007. “Nonlinear soil-abutment-bridge structure interaction for seismic performance-based design.” *Journal of Geotechnical and Geoenvironmental Engineering* 133 (6): 707-720.

Somerville, P., N. Smith, S. Punyamurthula, and J. Sun. 1997. *Development of ground motion time histories forphase 2 of the FEMA/SAC steel project.* SAC Joint Venture. Sacramento, CA.

Steelman, Joshua S., Larry A. Fahnestock, James M. LaFave, Jerome F. Hajjar, Evgueni T. Filipov, and Douglas A. Foutch. 2011. Seismic Response of Bearings for Quasi-Isolated Bridges – Testing and Component Modeling. In LasVegas, NV: ASCE Structural Engineering Institute, April 14.

Tavakoli, Behrooz, Shahram Pezeshk, and Randel Tom Cox. 2010. “Seismicity of the New Madrid Seismic Zone Derived from a Deep-Seated Strike-Slip Fault.” *Bulletin of the Seismological Society of America* 100 (4) (August 1): 1646-1658. doi:10.1785/0120090220.

Tobias, Daniel H., Ralph E. Anderson, Chad E. Hodel, William M. Kramer, Riyad M. Wahab, and Richard J. Chaput. 2008. “Overview of Earthquake Resisting System Design and Retrofit Strategy for Bridges in Illinois.” *Practice Periodical on Structural Design and Construction* 13 (3): 147-158.

Tongaonkar, N.P., and R.S. Jangid. 2003. “Seismic response of isolated bridges with soil–structure interaction.” *Soil Dynamics and Earthquake Engineering* 23 (4) (June 1): 287-302. doi:10.1016/S0267-7261(03)00020-4.

Vamvatsikos, Dimitrios, and C. Allin Cornell. 2002. “Incremental dynamic analysis.” *Earthquake Engineering & Structural Dynamics* 31 (3) (March 1): 491-514. doi:10.1002/eqe.141.

Wang, Yen-Po, Lap-Loi Chung, and Wei-Hsin Liao. 1998. “Seismic response analysis of bridges isolated with friction pendulum bearings.” *Earthquake Engineering & Structural Dynamics* 27 (10) (October 1): 1069-1093. doi:10.1002/(SICI)1096-9845(199810)27:10<1069::AID-EQE770>3.0.CO;2-S.

Wen, Y. K., and Chiun-Lin Wu. 2001. “Uniform Hazard Ground Motions for Mid-America Cities.” *Earthquake Spectra* 17 (2): 359 -384. doi:10.1193/1.1586179.

Wilson, P., and A. Elgamal. 2010. Bridge-abutment-backfill dynamic interaction modeling based on full scale tests. In Toronto, Ontario, Canada: EERI, July 25.

Wu, Chiun-Lin, and Y. K Wen. 1999. *Uniform Hazard Ground Motions and Response Spectra for Mid-America Cities*. December 31. http://hdl.handle.net/2142/9181.

Zandieh, Arash, and Shahram Pezeshk. 2011. “A Study of Horizontal-to-Vertical Component Spectral Ratio in the New Madrid Seismic Zone.” *Bulletin of the Seismological Society of America* 101 (1) (February 1): 287 -296. doi:10.1785/0120100120.

APPENDIX A

NONLINEAR MODEL FORMULATION

A.1 Bidirectional Bearing Elements

The OpenSees syntax for zero-length bi-directional sliding bearings model is as follows

element ZLSlidingBearing $eleTag $iNode $jNode $p_2 $r1 $r2 $r3 $p_initial $e_i $mu_si $mu_sp $mu_k $e_p $n_i

$eleTag - unique element object tag
$iNode $jNode - end nodes
$p_2 - tag associated with previously-defined UniaxialMaterial used to define vertical translation behavior of bearing
$r1,$r2,$r3 - tags associated with previously-defined UniaxialMaterial used to define rotation about local 1,2,3 axes, respectively
$p_initial - added initial bearing strength
$e_i - initial bearing stiffness
$mu_si - initial static coefficient of friction
$mu_sp - post-slip static coefficient of friction
$mu_k - kinetic coefficient of friction
$e_p - post-slip bearing stiffness
$n_i - initial vertical force on bearing

The zero length bi-directional element is defined using four uniaxial materials and a combined bi-axial material model. The user defines uniaxial materials that characterize the element behavior for translation in the local *y* direction (axial), and rotation about the local *x, y* and *z* axes. The behavior for translation in the local *x* and *z* directions is defined using the force-displacement rule based model shown in Figure A.1and described hereafter. Note that Figure A.1 is very similar to Figure 3.2 shown in Chapter 3 but contains additional information about the bearing model.

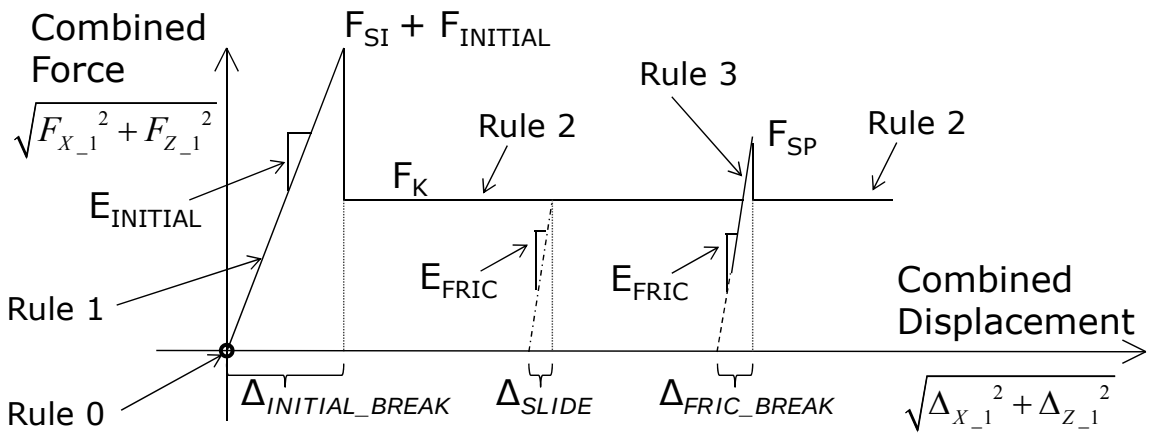

Figure A.1 Bi-directional force-displacement rule-based model for combined *x* & *z* translation in element

The initial static, kinetic, and post slip static, friction forces are defined as:

$$F_{SI} = \mu_{SI} * N_0 \quad \text{A.1}$$

$$F_K = \mu_K * N_0 \quad \text{A.2}$$

$$F_{SP} = \mu_{SP} * N_0 \quad \text{A.3}$$

where μ_{SI}, the initial static coefficient of friction, μ_K , the kinetic coefficient of friction, and μ_{SP},the post slip static coefficient of friction are user defined variables and N_0 is the axial load (*z*-direction) on the element at the preceding converged step. $E_{INITIAL}$ and E_{FRIC} are the user defined stiffness of the bearing for the initial and post slip cases. Since no axial load is typically applied before the first step of an analysis, a nominal axial load, N_0, of 0.01* $E_{INITIAL}$ is imposed to prevent a case where the static and kinetic friction forces are equal to zero. The model can have a predefined initial capacity ($F_{INITIAL}$) that is in addition to the initial friction break off force. The friction model is implemented into the OpenSees source code using C++, with a set of governing rules that determine the force and stiffness representation of the model in OpenSees. Common terms used in the formulation include Δ_{X_0} and Δ_{Z_0}, the displacements from the preceding converged step in the *x* and *z* directions respectively, and $\Delta_{P\_X\_0}$ and $\Delta_{P\_Z\_0}$, the plastic deformations from the preceding converged step in the *x* and *z* directions respectively, the plastic deformations are initially zero. Δ_{COMB} is the combined bidirectional differential displacement for

the current step as defined in Equation A.4. For the current step E_{X_1} and E_{Z_1}, are the calculated element stiffness in the *x* and *z* directions respectively, and F_{X_1} and F_{Z_1}, are the calculated element forces in the *x* and *z* directions respectively. The governing displacement values are defined as $\Delta_{INITIAL\_BREAK}$, Δ_{SLIDE} and Δ_{FRIC_BREAK} as shown in Equations A.5 through A.7.

$$\Delta_{COMB} = \sqrt{(\Delta_{X\_1} - \Delta_{P\_X\_0})^2 + (\Delta_{Z\_1} - \Delta_{P\_Z\_0})^2} \quad \text{A.4}$$

$$\Delta_{INITIAL\_BREAK} = \frac{F_{SI} + F_{INITIAL}}{E_{INITIAL}} \quad \text{A.5}$$

$$\Delta_{SLIDE} = F_K / E_{FRIC} \quad \text{A.6}$$

$$\Delta_{FRIC\_BREAK} = F_{SP} / E_{FRIC} \quad \text{A.7}$$

Rule 0 - Initial Configuration

This condition is only implemented at the start of a run, when Δ_{COMB} is equal to zero. When the model is in this initial configuration the tangent for both the x and z directions is $E_{INITIAL}$, and the force returned for the element for translation in the x and z directions is zero. The bi-directional response remains in Rule 0 until Δ_{COMB} gains a value greater than zero. When there is a non-zero bidirectional displacement and Δ_{COMB} exceeds $\Delta_{INITIAL\_BREAK}$, initial friction break-off is initiated and the model enters Rule 2, otherwise the model enters Rule 1. If the model enters Rule 2 the plastic deformations are updated as shown in Equations A.8 and A.9.

$$\Delta_{P\_X\_1} = \Delta_{X\_1} - \Delta_{SLIDE} * \frac{(\Delta_{X\_1} - \Delta_{P\_X\_0})}{\Delta_{COMB}} \quad \text{A.8}$$

$$\Delta_{P\_Z\_1} = \Delta_{Z\_1} - \Delta_{SLIDE} * \frac{(\Delta_{Z\_1} - \Delta_{P\_Z\_0})}{\Delta_{COMB}} \quad \text{A.9}$$

Rule 1 –Initial Static Configuration

For the static configuration the tangent for both the *x* and *z* directions is $E_{INITIAL}$, and the forces returned for the element for translation in the *x* and *z* directions are given by Equations A.10 and A.11 respectively.

$$F_{X\_1} = E_{INITIAL} * \Delta_{COMB} * \frac{(\Delta_{X\_1} - \Delta_{P\_X\_0})}{\Delta_{COMB}} = E_{INITIAL} * (\Delta_{X\_1} - \Delta_{P\_X\_0}) \quad \text{A.10}$$

$$F_{Z\_1} = E_{INITIAL} * (\Delta_{Z\_1} - \Delta_{P\_Z\_0}) \quad \text{A.11}$$

At this configuration since the element is static, we again check to see if Δ_{COMB} exceeds $\Delta_{INITIAL\_BREAK}$, and in the case that it does the model enters Rule2, otherwise the model remains in the current configuration. If the model enters Rule 2 the plastic deformations are updated as shown in Equations A.8 and A.9, otherwise if the model stays in Rule 1, the plastic deformations stay the same as before.

Rule 2 - Kinetic Configuration

This is the configuration at which slip has occurred, the element looses stiffness in the *x* and *z* directions, and the combined bi-directional force is equal to F_K. To allow for improved convergence, the element retains a tangent stiffness of $E_{INITIAL}/100000$ in both the *x* and *z* directions, and the forces returned are calculated using Equations A.12 and A.13 for the two directions.

$$F_{X\_1} = F_K * \frac{(\Delta_{X\_1} - \Delta_{P\_X\_1})}{\sqrt{(\Delta_{X\_1} - \Delta_{P\_X\_1})^2 + (\Delta_{Z\_1} - \Delta_{P\_Z\_1})^2}} \quad \text{A.12}$$

$$F_{Z\_1} = F_K * \frac{(\Delta_{Z\_1} - \Delta_{P\_Z\_0})}{\sqrt{(\Delta_{X\_1} - \Delta_{P\_X\_1})^2 + (\Delta_{Z\_1} - \Delta_{P\_Z\_1})^2}} \quad \text{A.13}$$

To determine whether the model remains in the kinetic configuration and continues sliding, or if it enters the post slip-static configuration a kinematic hardening type surface is used as shown in Figure 3.3. The kinetic configuration will continue if either Equation A.14 or A.15 is satisfied.

$$\Delta_{COMB} > \Delta_{FRIC\_BREAK} \quad \text{A.14}$$

$$|\theta_0 - \theta_1| < \frac{\pi}{2} \quad \text{A.15}$$

where,

$$\theta_0 = \tan^{-1}\left(\frac{\Delta_{Z\_0} - \Delta_{P\_Z\_0}}{\Delta_{X\_0} - \Delta_{P\_X\_0}}\right) \quad \text{A.16}$$

$$\theta_1 = \tan^{-1}\left(\frac{\Delta_{Z\_1} - \Delta_{Z\_0}}{\Delta_{X\_1} - \Delta_{X\_0}}\right) \quad \text{A.17}$$

If the model remains in the kinetic configuration the plastic deformations are updated as shown in Equations A.8 and A.9, otherwise the model enters post slip static case as defined in

Rule 3, and the plastic deformations remain the same as the preceding converged step.

Rule 3 – Post Slip Static Configuration

This case is similar the initial static configuration. The tangent for both the x and z directions is E_{FRIC}, and the forces returned for the element for translation in the x and z directions are given by Equations A.10 and A.11, where E_{FRIC} should be used instead of $E_{INITIAL}$. At this configuration a check is performed to see if Δ_{COMB} exceeds Δ_{SLIDE}, and in the case that it does the model enters Rule2, and begins to slide, otherwise the model remains in the static configuration. If the model enters Rule 2 the plastic deformations are updated as shown in Equations A.8 and A.9, otherwise the model remains in Rule 3, the plastic deformations stay the same as before.

A.2 Zero-Length bi-directional fixed bearing / anchorbolt element

The OpenSees syntax for zero-length bi-directional sliding bearings model is as follows

element ZLFixedBearing $eleTag $iNode $jNode $p_2 $r1 $r2 $r3 $p_y $d_y $p_ult $d_ult $PFactor

$eleTag - unique element object tag
$iNode $jNode - end nodes
$p_2 - tag associated with previously-defined UniaxialMaterial used to define vertical translation behavior of bearing
$r1,$r2,$r3 - tags associated with previously-defined UniaxialMaterial used to define rotation about local 1, 2, 3 axes, respectively
$p_y - yield strength of the bearing model
$d_y - yield displacement of the bearing model
$p_ult - ultimate strength of the bearing model
$d_ult - ultimate displacement of the bearing model
$PFactor – pinching factor for model

The user defines values for the yield and ultimate displacements of the model, Δ_Y and Δ_{ULT} respectively; and also the yield and ultimate forces for the model P_Y and P_{ULT} respectively. The engagement surface displacement, Δ_{ENG_S}, is initially defined equal to the yield displacement Δ_Y, and the engagement surface force P_{ENG_S}, is initially defined as they yield force P_Y. Based on the user defined values, the following variables are derived before a run begins:

$$E_I = \frac{P_Y}{\Delta_Y} \quad \text{A.18}$$

$$E_P = \frac{P_{ULT} - P_Y}{\Delta_{ULT} - \Delta_Y} \quad \text{A.19}$$

Common terms used in the formulation include Δ_{X_0} and Δ_{Z_0}, the displacements from the preceding converged step in the *x* and *z* directions respectively, and Δ_{X_1} and Δ_{Z_1}, the trial deformations in the current step in the *x* and *z* directions respectively, Δ_{COMB} is the combined bidirectional displacement for the current step as defined in Equation A.20. The incremental displacements in the x and z directions as well as the combined incremental displacement are calculated for each step based on Equations A.21 to A.23.

$$\Delta_{COMB} = \sqrt{(\Delta_{X\_1})^2 + (\Delta_{Z\_1})^2} \quad \text{A.20}$$

$$\Delta_{X\_INC} = \Delta_{X\_1} - \Delta_{X\_0} \quad \text{A.21}$$

$$\Delta_{Z\_INC} = \Delta_{Z\_1} - \Delta_{Z\_0} \quad \text{A.22}$$

$$\Delta_{COMB\_INC} = \sqrt{(\Delta_{X\_INC})^2 + (\Delta_{Z\_INC})^2} \quad \text{A.23}$$

A residual engagement surface, which is the location the model would reach zero force after plastic deformation, is defined for each step per Equation A.24 and unloading deformation which is the deformation the model needs to undergo to obtain zero force is calculated per Equation A.25

$$\Delta_{ENG\_S\_RES} = \Delta_{ENG\_S} - P_{ENG\_S} / E_I \quad \text{A.24}$$

$$\Delta_{UNL} = \frac{\sqrt{F_{X\_0}{}^2 + F_{Z\_0}{}^2}}{E_I} \quad \text{A.25}$$

Values for the current force vector and the loading vector are defined based on the following equations:

$$\theta_F = \tan^{-1}\left(\frac{F_{Z\_0}}{F_{X\_0}}\right) \quad \text{A.26}$$

$$\theta_L = \tan^{-1}\left(\frac{\Delta_{Z\_INC}}{\Delta_{X\_INC}}\right) \quad \text{A.27}$$

where F_{X_0} and F_{Z_0}, are the element forces from the previous time step in the x and z directions respectively.

The model is formulated in a displacement space framework and a rule based approach is used to determine the state of the model for different displacements. A set of inequalities are valid when the model's current rule is between Rule 0 and Rule 5, but once the model is switched to Rule 6, all other rules are disengaged and the bearing is considered to have failed. The algorithm tests the following conditions in the following order and assigns a rule when a condition is met:

if $\Delta_{COMB} > \Delta_{ULT}$ Rule 6 is engaged (element failure)

if $\Delta_{ENG\_S} < \Delta_{COMB} < \Delta_{ULT}$ Rule 2 is engaged (plastic deformation of element)

if $|\theta_F - \theta_L| < \frac{\pi}{2}$ Rule 1 is engaged (continued loading/reloading of element)

if $\Delta_{COMB} > \Delta_{ENG\_S\_RES}$ Rule 3 is engaged (unloading within residual engagement surface)

if $\Delta_{COMB\_INC} < \Delta_{UNL}$ Rule 4 is engaged (unloading outside of residual engagement surface)

otherwise Rule 5 is engaged where reloading begins after a zero force is obtained in the element

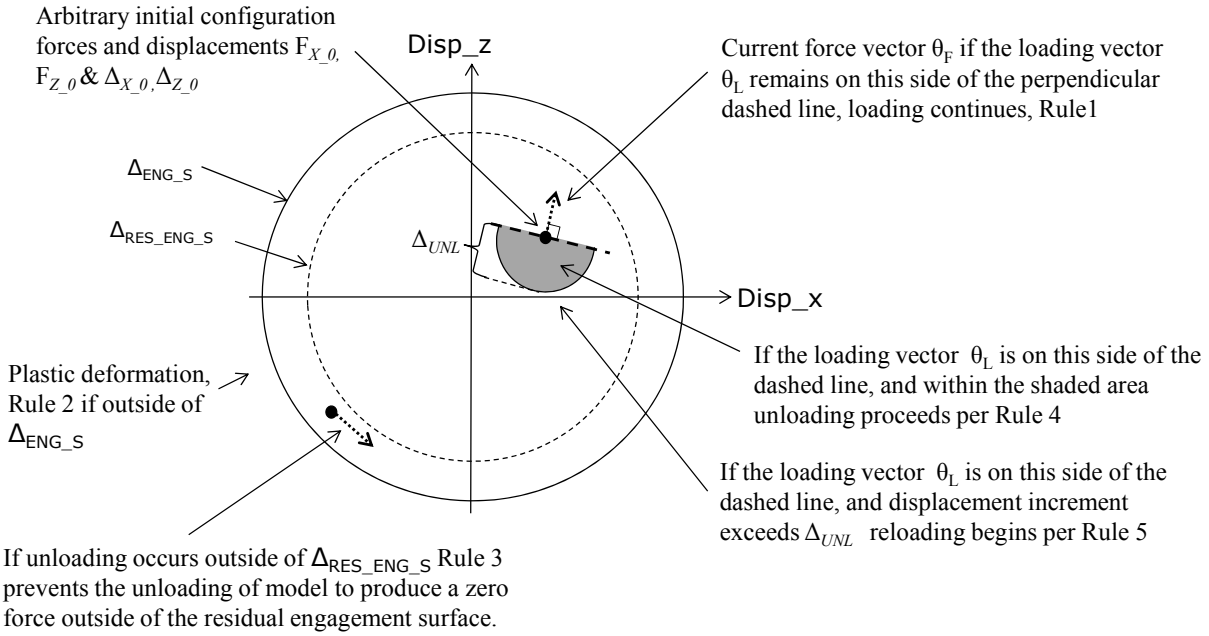

Figure A.2 Schematic representation of conditions that determine loading, unloading and reloading rules in bi-directional displacement space

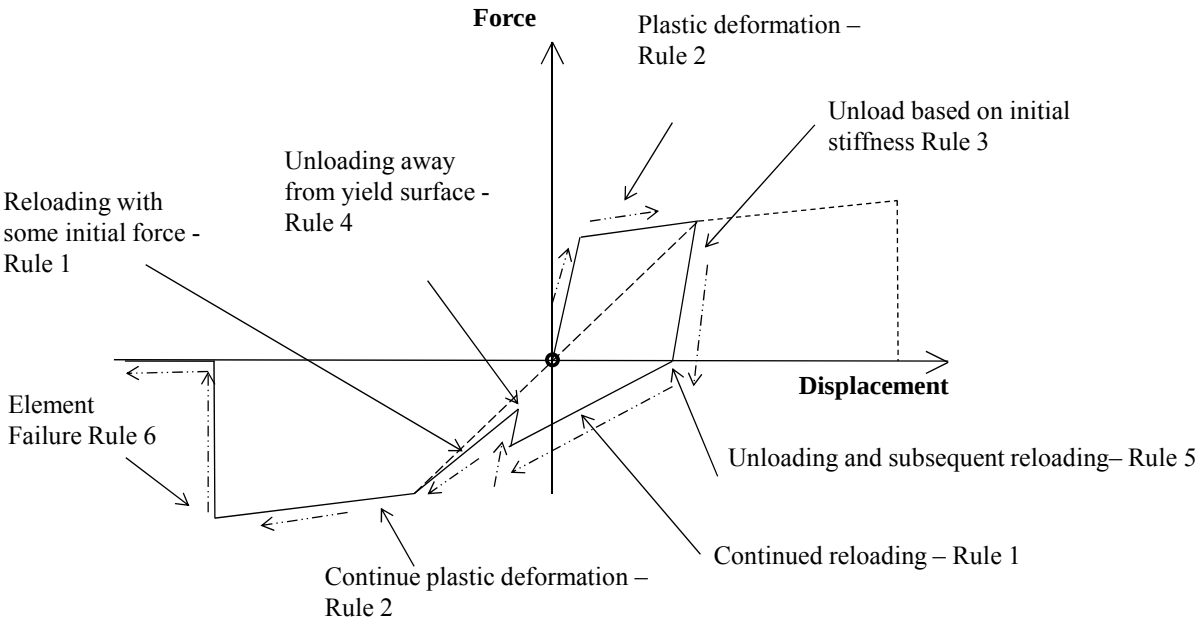

Figure A.3 Bi-directional peak based force-displacement model with rule definitions

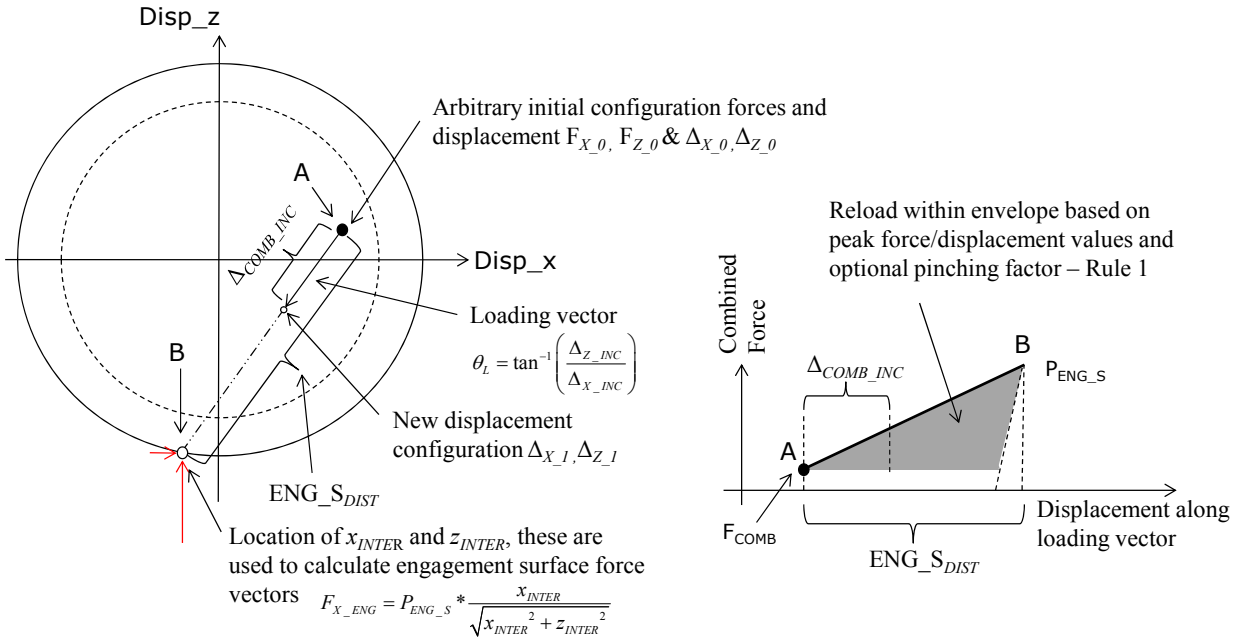

Figure A.4 Schematic representation for reloading variables used in formulation

Rule 0 - Initial configuration

The model begins the first step in Rule 0, and the model has a stiffness of E_I in both the x and z directions and the force is zero until a displacement is imposed on the model and the rule is switched.

Rule 1 –Initial or continued elastic loading

When the model enters rule 1, it means that the model has some arbitrary force in direction θ_F and the model continues loading in a direction, θ_L that is continues increasing the load on the element. Using a circular equation for the engagement surface we can calculate the point where the loading vector with the direction of θ_L intersects the engagement surface, and we can calculate an appropriate value for the increased force and the new model stiffness. If we calculate the intersection point to be at x_{INTER} and z_{INTER}, then we can use Equations A.28 through A.33 to calculate the model forces.

$$ENG\_S_{DIST} = \sqrt{(\Delta_{X\_0} - x_{INTER})^2 + (\Delta_{Z\_0} - z_{INTER})^2} \qquad \text{A.28}$$

$$F_{X\_ENG} = P_{ENG\_S} * \frac{x_{INTER}}{\sqrt{x_{INTER}^{\ 2} + z_{INTER}^{\ 2}}} \quad \text{A.29}$$

$$F_{Z\_ENG} = P_{ENG\_S} * \frac{z_{INTER}}{\sqrt{x_{INTER}^{\ 2} + z_{INTER}^{\ 2}}} \quad \text{A.30}$$

$$F_{COMB} = \sqrt{F_{X\_0}^{\ 2} + F_{Z\_0}^{\ 2}} \quad \text{A.31}$$

Force determination in x direction

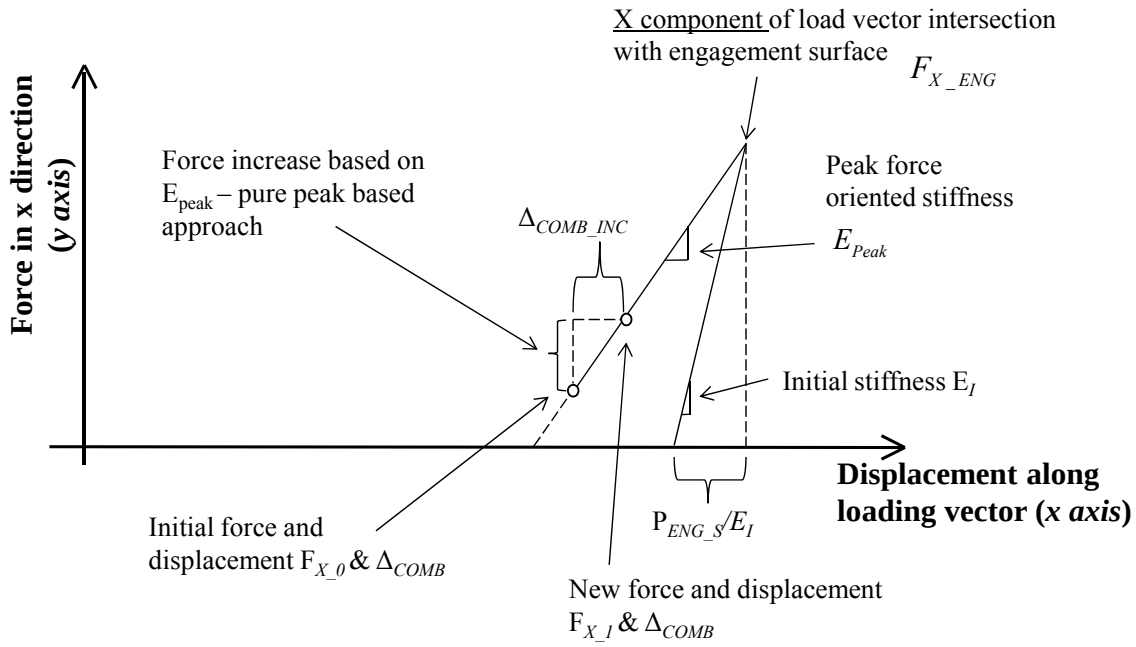

Figure A.5 Loading conditions per pure peak based approach

$$F_{X\_1} = F_{X\_0} + (F_{X\_ENG} - F_{X\_0}) * \frac{\Delta_{COMB\_INC}}{ENG\_S_{DIST}} \quad \text{A.32}$$

$$F_{Z\_1} = F_{Z\_0} + (F_{Z\_ENG} - F_{Z\_0}) * \frac{\Delta_{COMB\_INC}}{ENG\_S_{DIST}} \quad \text{A.33}$$

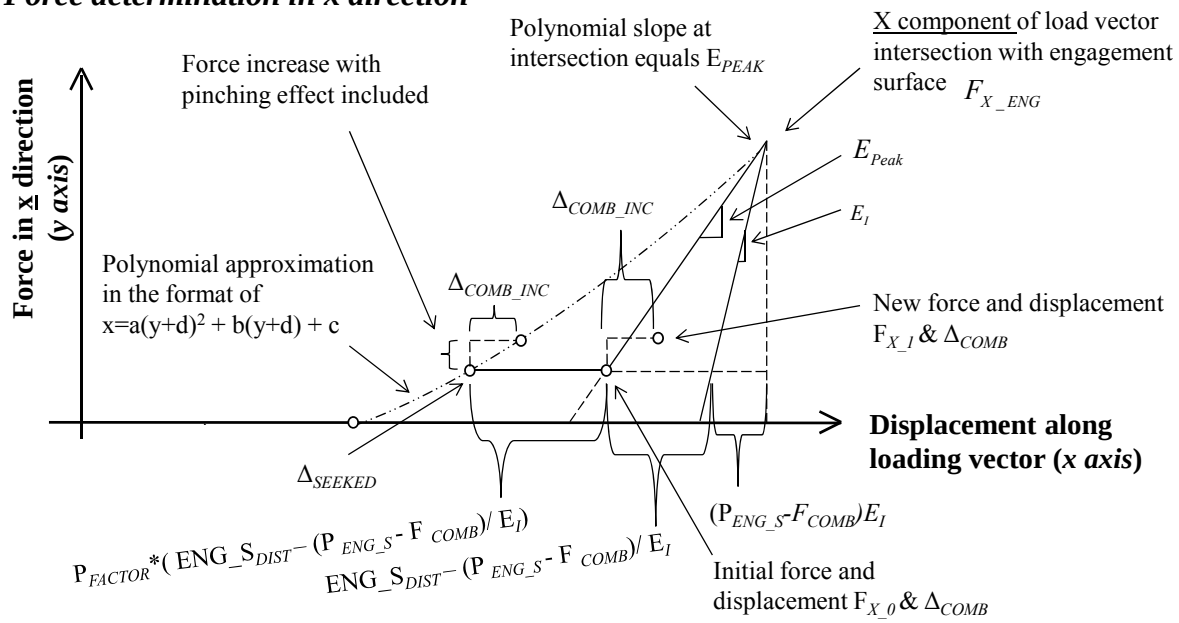

Figure A.6 Loading conditions per modified peak based approach that can be used to reduce reloading rate

In a case where pinching is implemented an alternative method using a polynomial to increment force is used. Figure A.6 shows the effect of the reduced reloading rate due to pinching.

$$F_{X\_1} = F_{X\_0} + (F_{X\_INTER} - F_{X\_0}) * \frac{\Delta_{COMB\_INC}}{P_{FACTOR} * ENG\_S_{DIST}} \quad \text{A.34}$$

$$F_{Z\_1} = F_{Z\_0} + (F_{Z\_INTER} - F_{Z\_0}) * \frac{\Delta_{COMB\_INC}}{P_{FACTOR} * ENG\_S_{DIST}} \quad \text{A.35}$$

When the model is in rule 1 and continues loading it returns stiffnesses per the following equations:

$$E_X = \frac{F_{X\_1} - F_{X\_0}}{\Delta_{X\_INC}} \quad \text{A.36}$$

$$E_Z = \frac{F_{Z\_1} - F_{Z\_0}}{\Delta_{Z\_INC}} \quad \text{A.37}$$

Rule 2 – Plastic deformation of element

This rule is engaged when the element experiences plastic deformation. The engagement surface displacement, Δ_{ENG_S}, the residual engagement surface displacement, $\Delta_{ENG\_S\_RES}$, and the engagement surface force P_{ENG_S}, are updated based on EquationsA.38, A.24 and A.39 respectively.

$$\Delta_{ENG\_S} = \Delta_{COMB} \tag{A.38}$$

$$P_{YS} = P_Y + (\Delta_{COMB} - \Delta_Y) * E_P \tag{A.39}$$

The model returns a stiffness of E_P in both the x and z directions and the model forces are determined by Equations A.40 and A.41.

$$F_{X\_1} = P_{ENG\_S} * \frac{\Delta_{X\_1}}{\Delta_{COMB}} \tag{A.40}$$

$$F_{Z\_1} = P_{ENG\_S} * \frac{\Delta_{Z\_1}}{\Delta_{COMB}} \tag{A.41}$$

Rule 3 – Unloading within residual engagement surface

This unloading occurs when the model is nearby the engagement surface, to prevent an irregular drop in force when the model is travelling tangent to the engagement surface. The model returns a force vector perpendicular to the engagement surface, pointing to the origin of the model. The model returns a stiffness of E_I in both the x and z directions and the model forces are determined by Equations A.42 and A.43.

$$F_{X\_1} = E_I * (\Delta_{COMB} - \Delta_{ENG\_S\_RES}) * \frac{\Delta_{X\_1}}{\Delta_{COMB}} \tag{A.42}$$

$$F_{Z\_1} = E_I * (\Delta_{COMB} - \Delta_{ENG\_S\_RES}) * \frac{\Delta_{Z\_1}}{\Delta_{COMB}} \tag{A.43}$$

Rule 4 – Unloading outside of residual engagement surface

This unloading occurs when the model is not within the engagement surface. The model returns a reduced force depending on the loading direction. The model returns a stiffness of E_I in both the x and z directions and the model forces are determined by Equations A.44 and A.45 .

$$F_{X\_1} = F_{X\_0} + E_I * \Delta_{X\_INC} \quad \text{A.44}$$

$$F_{Z\_1} = F_{Z\_0} + E_I * \Delta_{Z\_INC} \quad \text{A.45}$$

Rule 5– Unloading and subsequent reloading

This rule is similar to Rule 1, but makes some preliminary modifications to the initial values used. The previous step forces F_{X_0} and F_{Z_0} are set to zero, and the previous displacements to the values calculated per Equations A.46 and A.47. After this modification the forces and stiffnesses can be calculated using the same procedure outlined in Rule 1.

$$\Delta_{X\_0} = \Delta_{X\_0} - \Delta_{UNL} * \frac{\Delta_{X\_INC}}{\Delta_{COMB\_INC}} \quad \text{A.46}$$

$$\Delta_{Z\_0} = \Delta_{Z\_0} - \Delta_{UNL} * \frac{\Delta_{Z\_INC}}{\Delta_{COMB\_INC}} \quad \text{A.47}$$

Rule 6– Element Failure

When this rule is reached the model experienced fracture and has no further effect in the global analysis. The element model returns a stiffness of E_I /10000 in both the x and z directions and it returns a force of zero in both directions. The model cannot return to another rule after this.

A.3 Retainer Material

The OpenSees syntax for retainer model is:

uniaxialMaterial RetainerMaterial $matTag $gap $d_y $d_ult $p_y $ p_ult

$matTag - unique material object integer tag
$gap - gap between the bearing top plate and the retainer
$d_y – yield displacement of the retainer
$d_ult - ultimate displacement of the retainer
$p_y - yield strength of the retainer
$p_ult - ultimate strength of the retainer

As input for this material model the user defines the *gap* between the top plate and the retainer, the yield strength of the retainer (F_Y), the yield displacement (Δ_Y), the ultimate strength of the retainer (F_{ULT}), and the ultimate displacement (Δ_{ULT}). These variables are shown schematically on Figure A**.7** which is very similar to Figure 3.11 shown in Chapter 3 but contains additional information about the retainer strain hardening.

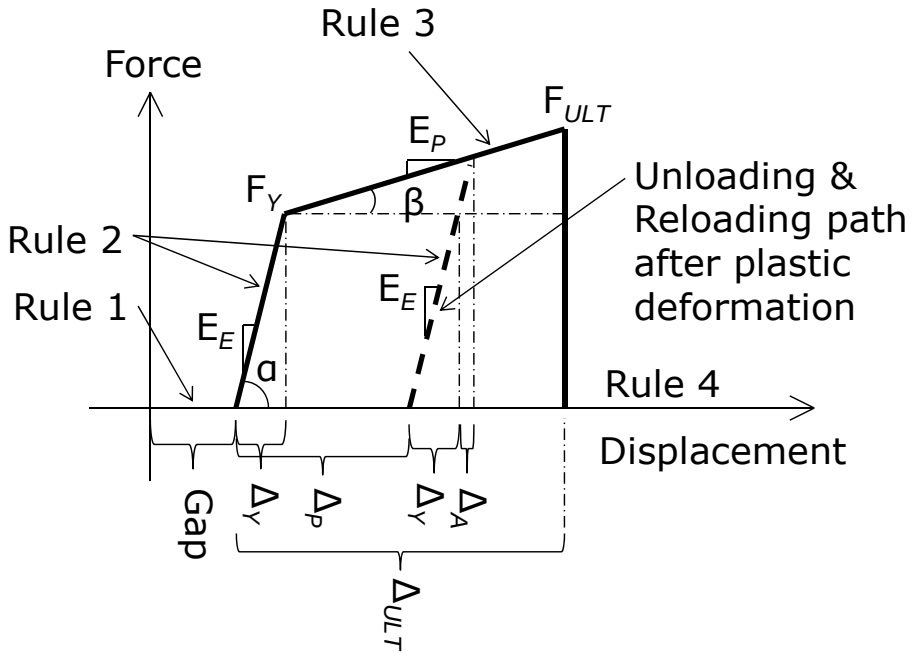

Figure A.7 Force-displacement behavior of individual retainer

Based on the user defined values, the following variables are derived:

$$E_E = \frac{F_Y}{\Delta_Y} \tag{A.48}$$

$$E_P = \frac{F_{ULT} - F_Y}{\Delta_{ULT} - \Delta_Y} \tag{A.49}$$

And also,

$$\alpha = \arctan\left(\frac{F_Y}{\Delta_Y}\right) \tag{A.50}$$

$$\beta = \arctan\left(\frac{F_{ULT} - F_Y}{\Delta_{ULT} - \Delta_Y}\right) \tag{A.51}$$

$$\Delta_{A\_0} = (\Delta_{P\_0}) * \left(\frac{\sin(\alpha) * \sin(\pi/2 + \beta)}{\sin(\alpha - \beta)}\right) \tag{A.52}$$

where Δ_{P_0} is the plastic strain in the retainer, initially equal to zero.

The model begins the first step in Rule 1, and before the failure of the retainer (Rules 1 – 3) the force-displacement behavior of the material is governed based on the following inequalities:

Rule 1 if $\Delta_{RET\_1} < (gap + \Delta_{P\_0})$,

Rule 2 if $(gap + \Delta_{P\_0}) < \Delta_{RET\_1} < (gap + \Delta_{P\_0} + \Delta_Y + \Delta_{A\_0})$,

Rule 3 if $(gap + \Delta_{P\_0} + \Delta_Y + \Delta_{A\_0}) < \Delta_{RET\_1} < (gap + \Delta_{ULT})$, and

Rule 4 if $(gap + \Delta_{ULT}) < \Delta_{RET\_1}$.

Rule 1 – No contact with retainer

Since bearing top plate is not in contact with the retainer, the material tangent is $E_E/100000$ and the force returned (F_{RET_1}) for the material is zero. The plastic deformation remains the same as specified for the last converged step.

Rule 2 – Elastic loading of retainer

The retainer is an elastic loading/unloading state, the material tangent is E_E and the force returned for the material is specified by Equation A.53. The plastic deformation remains the same as specified for the last converged step.

$$F_{RET\_1} = \left(\Delta_{RET\_1} - gap - \Delta_{P\_0}\right) * \mathrm{E}_E \tag{A.53}$$

Rule 3 – Plastic deformation of retainer

The retainer is undergoing plastic deformation. The material stiffness is E_P and the force returned for the material is specified by Equation A.54. The plastic deformation for this rule is redefined as shown in Equation A.55.

$$F_{RET\_1} = F_Y + \left(\Delta_{RET\_1} - gap - \Delta_Y\right) * \mathrm{E}_P \tag{A.54}$$

$$\Delta_{P\_1} = \Delta_{RET\_1} - gap - F_{RET\_1} / E_E \tag{A.55}$$

Rule 4 – Failure of retainer

Once this condition is reached the retainer is no longer active, the material model returns a tangent of $E_E/100000$ and a force of zero for the remainder of the analysis. It is not possible to return to any of the previous cases in the material model, even when the displacement falls under Δ_{ULT}.

APPENDIX B

RAW DATA FROM PARAMETRIC ANALYSES

This appendix contains all the results from the parametric study. Data is presented in the form of IDA curves similar to those in Chapter 6, which present maximum force and displacement results obtained from the nonlinear dynamic analyses. Since numerous ground motions are used the average of the response of the entire suite is shown as a circular marker, and values of plus and minus one standard deviation for the suite response are shown as a tick adjoined to the mean with a thin line. The mean response for the different scale factors of hazards are adjoined with a thick line.

For each bridge the response from the rock (CG) and stiff soil (Pa) ground motions are shown on the same plot with a different line color. Results from all 48 bridge variations are shown in this appendix, and are organized as shown in Table B.1. Each figure has part (a) that shows the force IDA results and part (b) that shows the displacement IDA results for each bridge variation. Figures B.49 – B.54 show the non-orthogonal results for three sample bridges. Those figures show only one set of the ground motions, and show a comparison of the non-orthogonal to the orthogonal results for each bridge.

Table B.1 Organization of raw IDA results from parametric study

Ss	C15	T1F - T1S - T2F - T2S	Figures B.1 - B.2 - B.3 - B.4
	C40	T1F - T1S - T2F - T2S	Figures B.5 - B.6 - B.7 - B.8
	W15	T1F - T1S - T2F - T2S	Figures B.9 - B.10 - B.11 - B.12
	W40	T1F - T1S - T2F - T2S	Figures B.13 - B.14 - B.15 - B.16
Sl	C15	T1F - T1S - T2F - T2S	Figures B.17 - B.18 - B.19 - B.20
	C40	T1F - T1S - T2F - T2S	Figures B.21 - B.22 - B.23 - B.24
	W15	T1F - T1S - T2F - T2S	Figures B.25 - B.26 - B.27 - B.28
	W40	T1F - T1S - T2F - T2S	Figures B.29 - B.30 - B.31 - B.32
Cs	C15	T1F - T1S - T2F - T2S	Figures B.33 - B.34 - B.35 - B.36
	C40	T1F - T1S - T2F - T2S	Figures B.37 - B.38 - B.39 - B.40
	W15	T1F - T1S - T2F - T2S	Figures B.41 - B.42 - B.43 - B.44
	W40	T1F - T1S - T2F - T2S	Figures B.45- B.46 - B.47 - B.48
SsC15T2S - Non-orthogonal			Figure B.49 (Pa), Figure B.50 (CG)
SlW15T1F - Non-orthogonal			Figure B.51 (Pa), Figure B.52 (CG)
CsC40T1S - Non-orthogonal			Figure B.53 (Pa), Figure B.54 (CG)

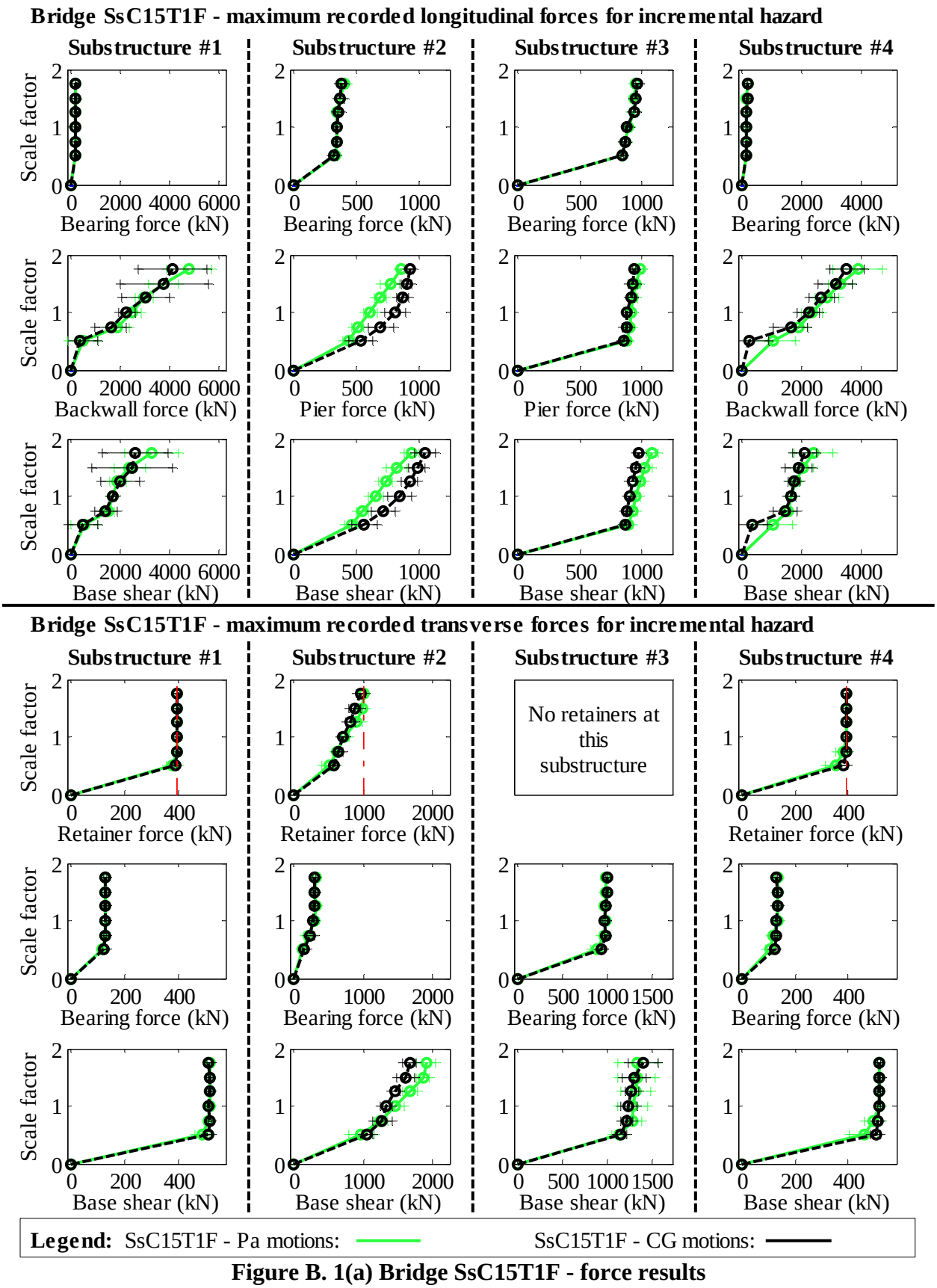

Figure B. 1(a) Bridge SsC15T1F - force results

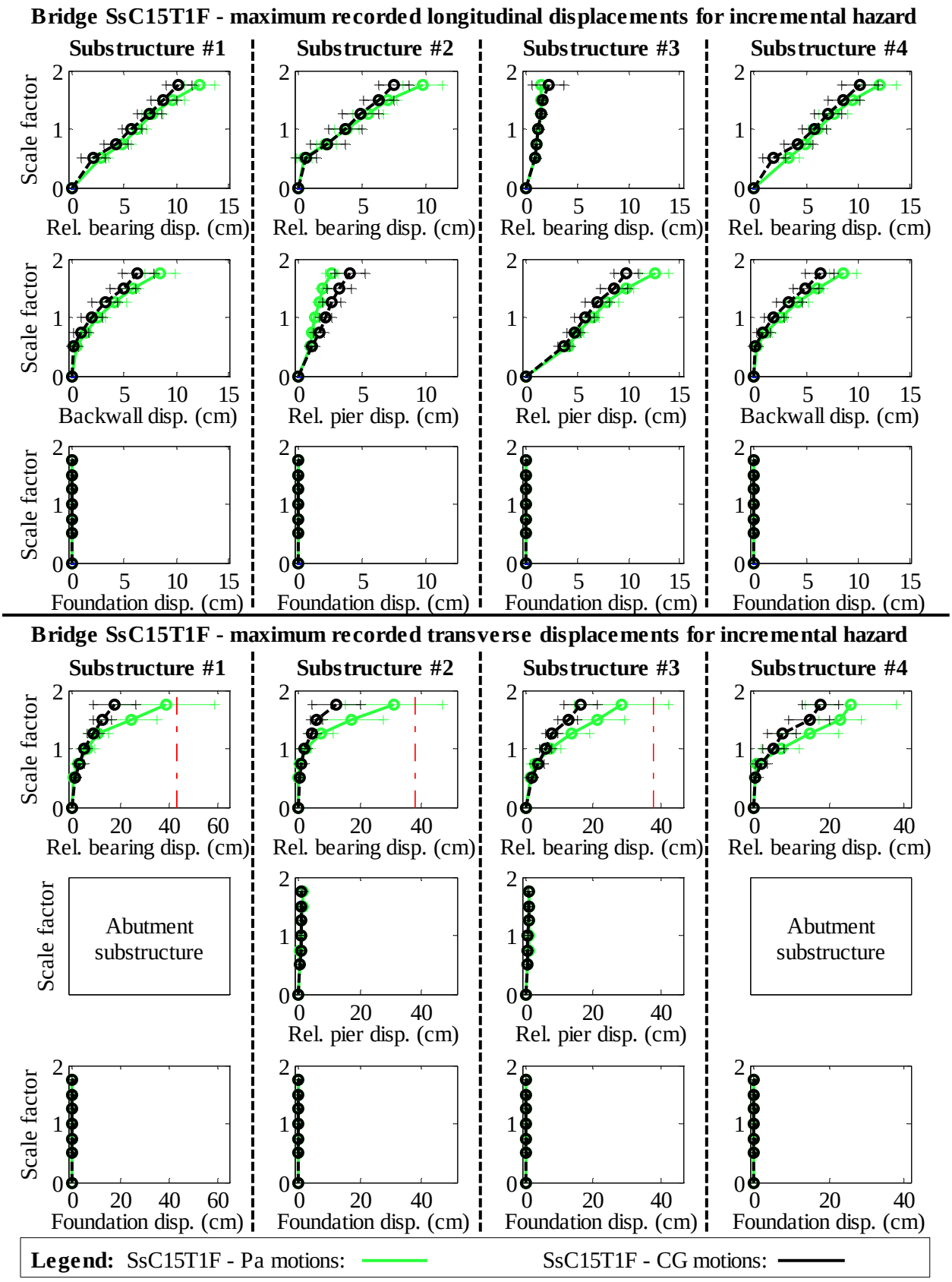

Figure B. 1(b) Bridge SsC15T1F - displacement results

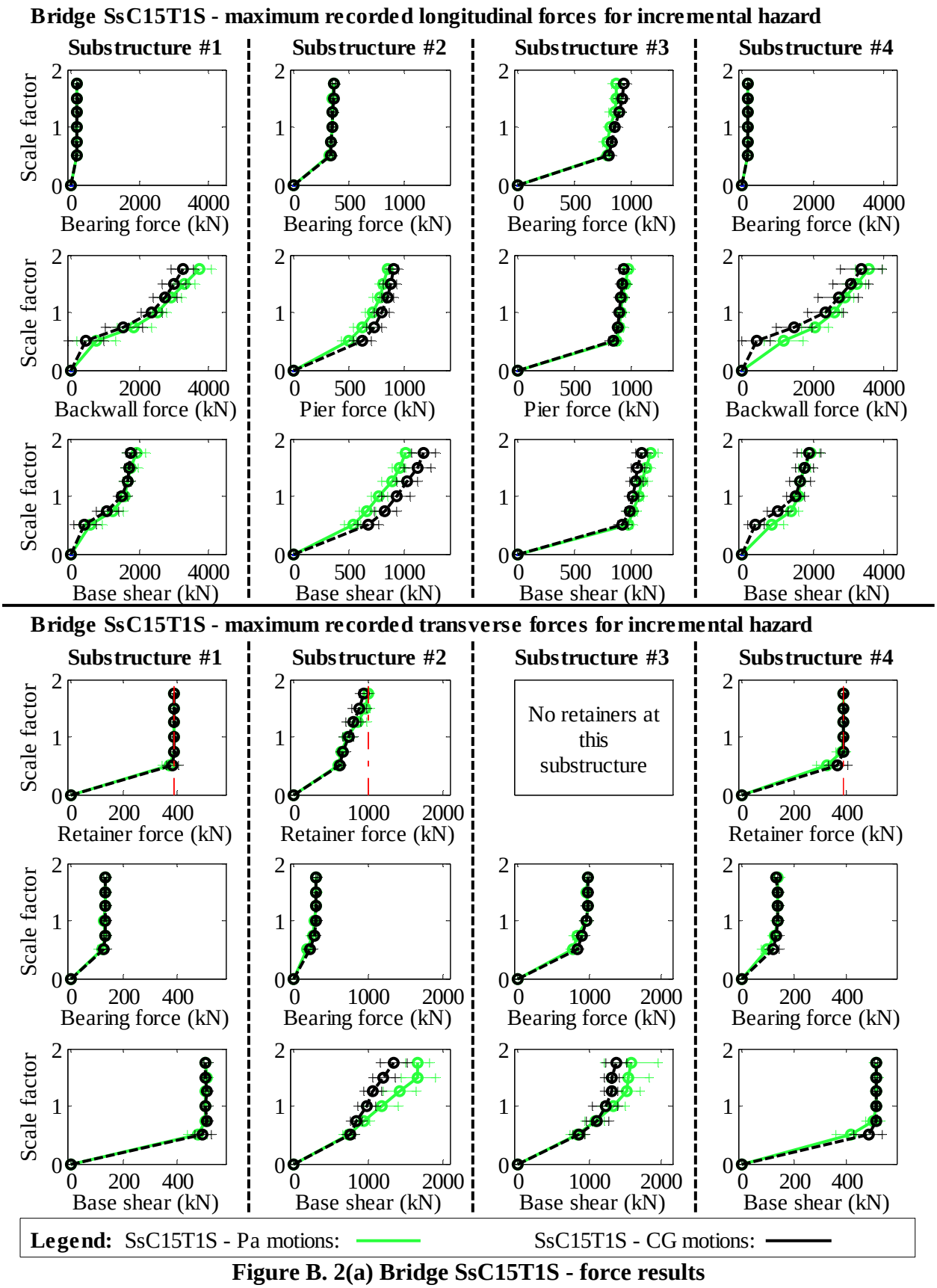

Figure B. 2(a) Bridge SsC15T1S - force results

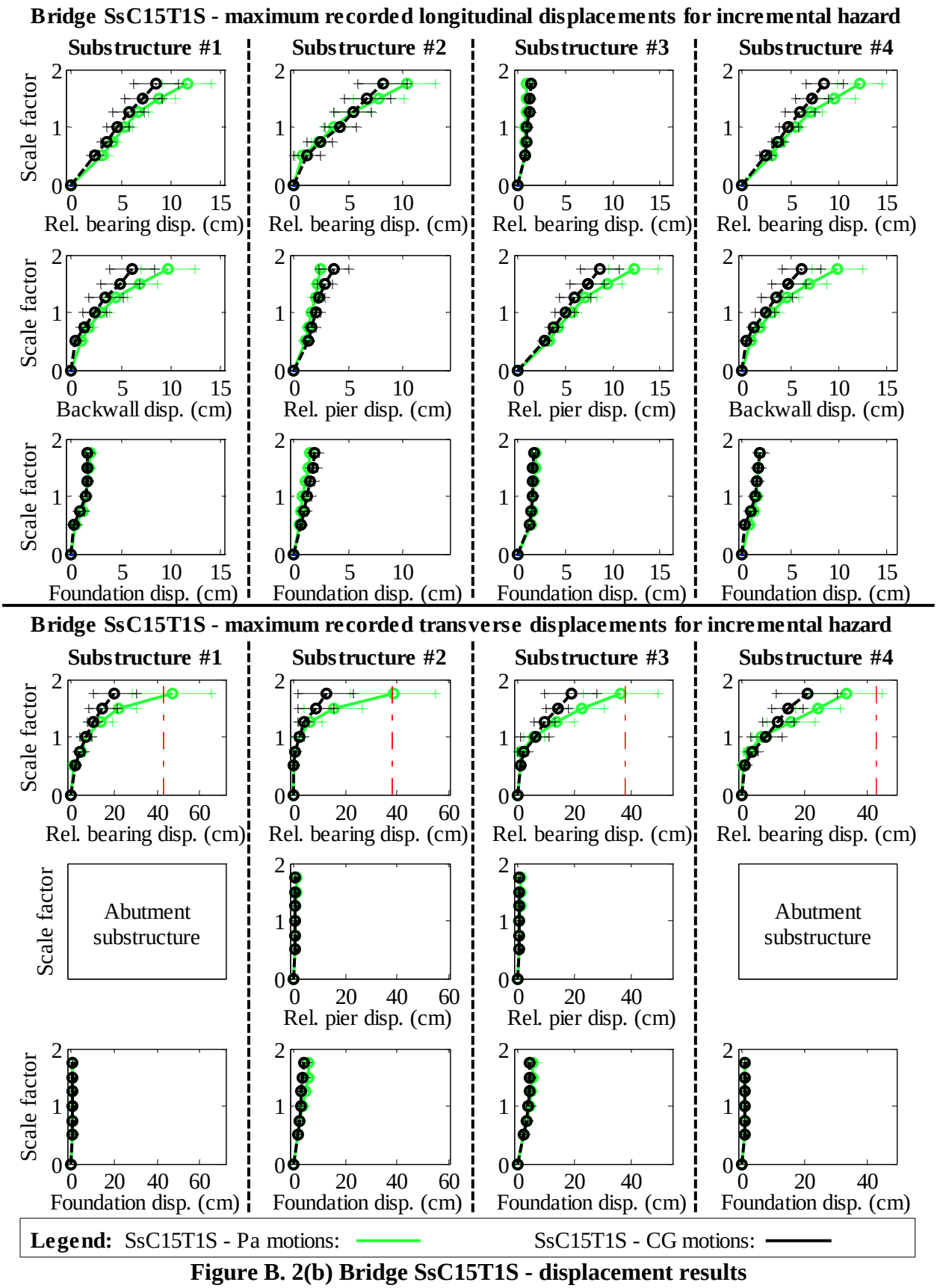

Figure B. 2(b) Bridge SsC15T1S - displacement results

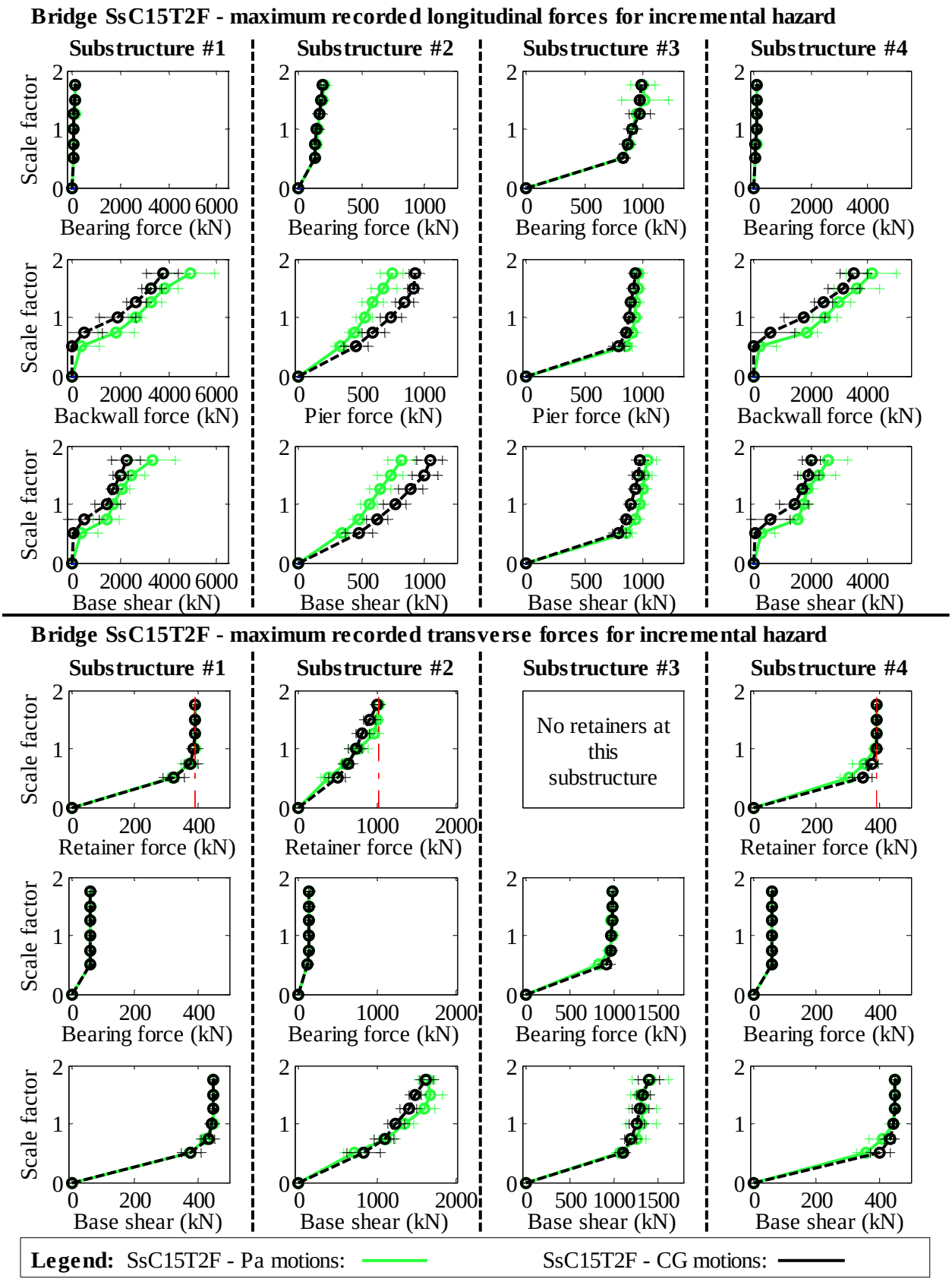

Figure B. 3(a) Bridge SsC15T2F - force results

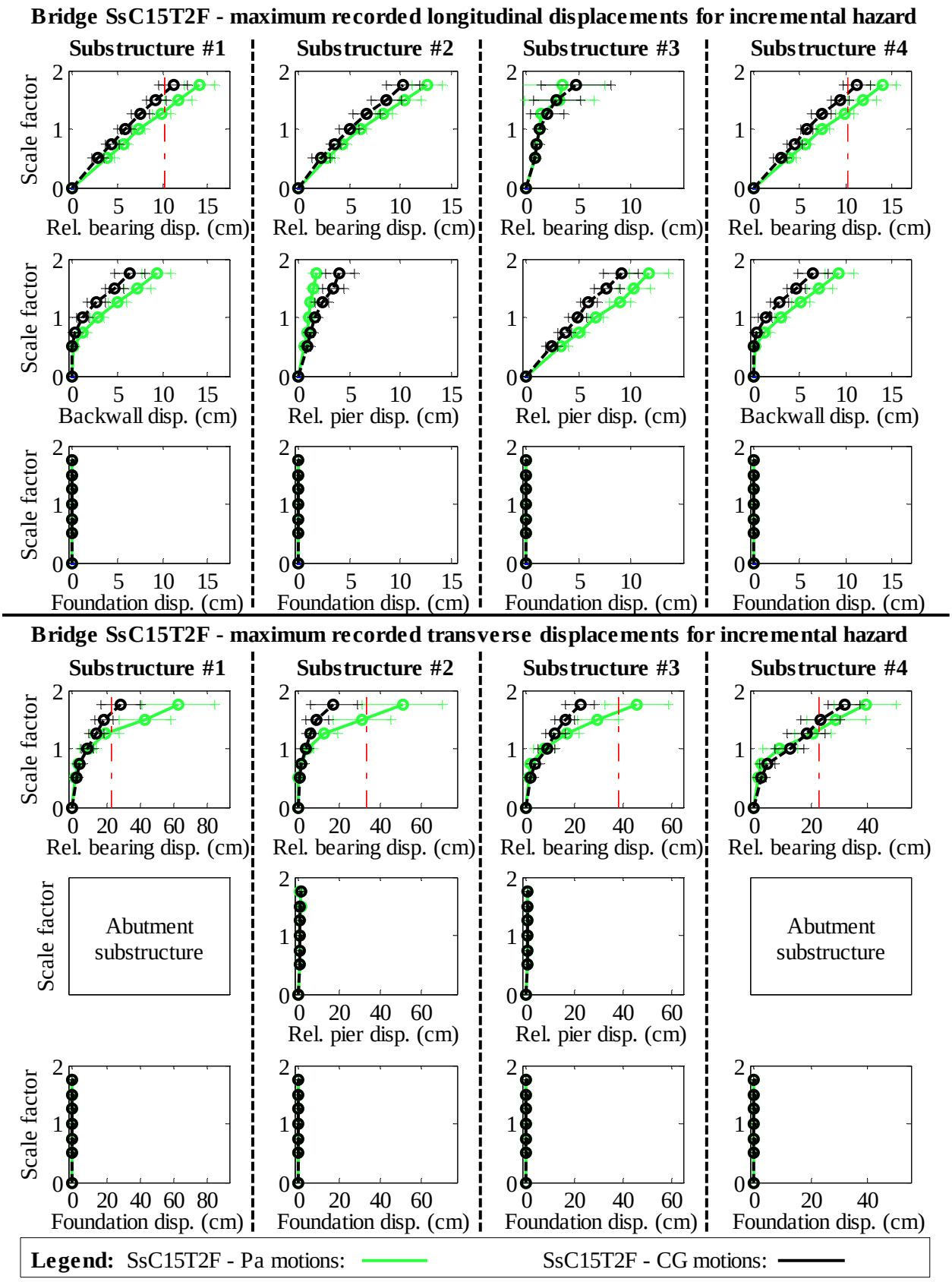

Figure B. 3(b) Bridge SsC15T2F - displacement results

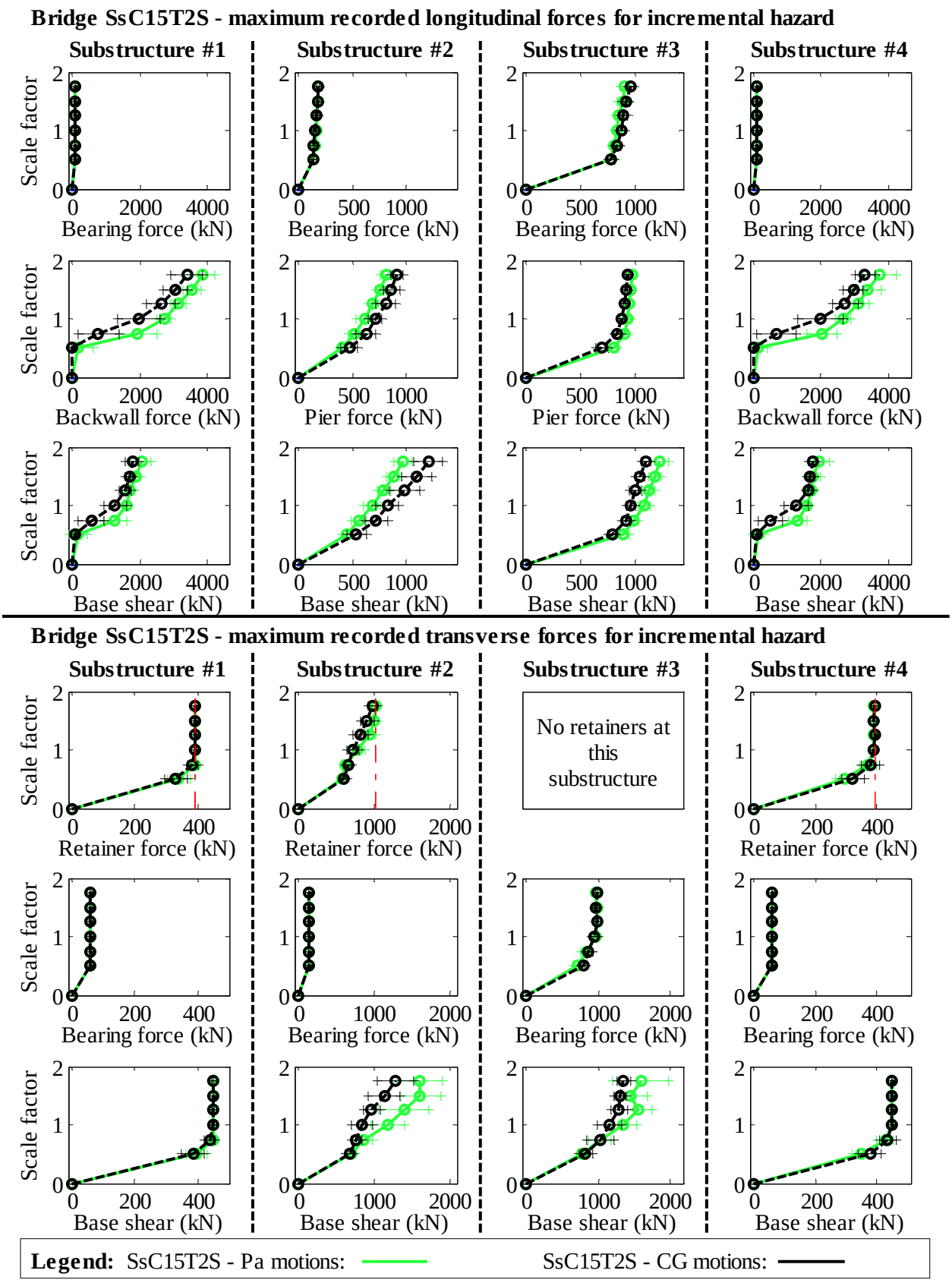

Figure B. 4(a) Bridge SsC15T2S - force results

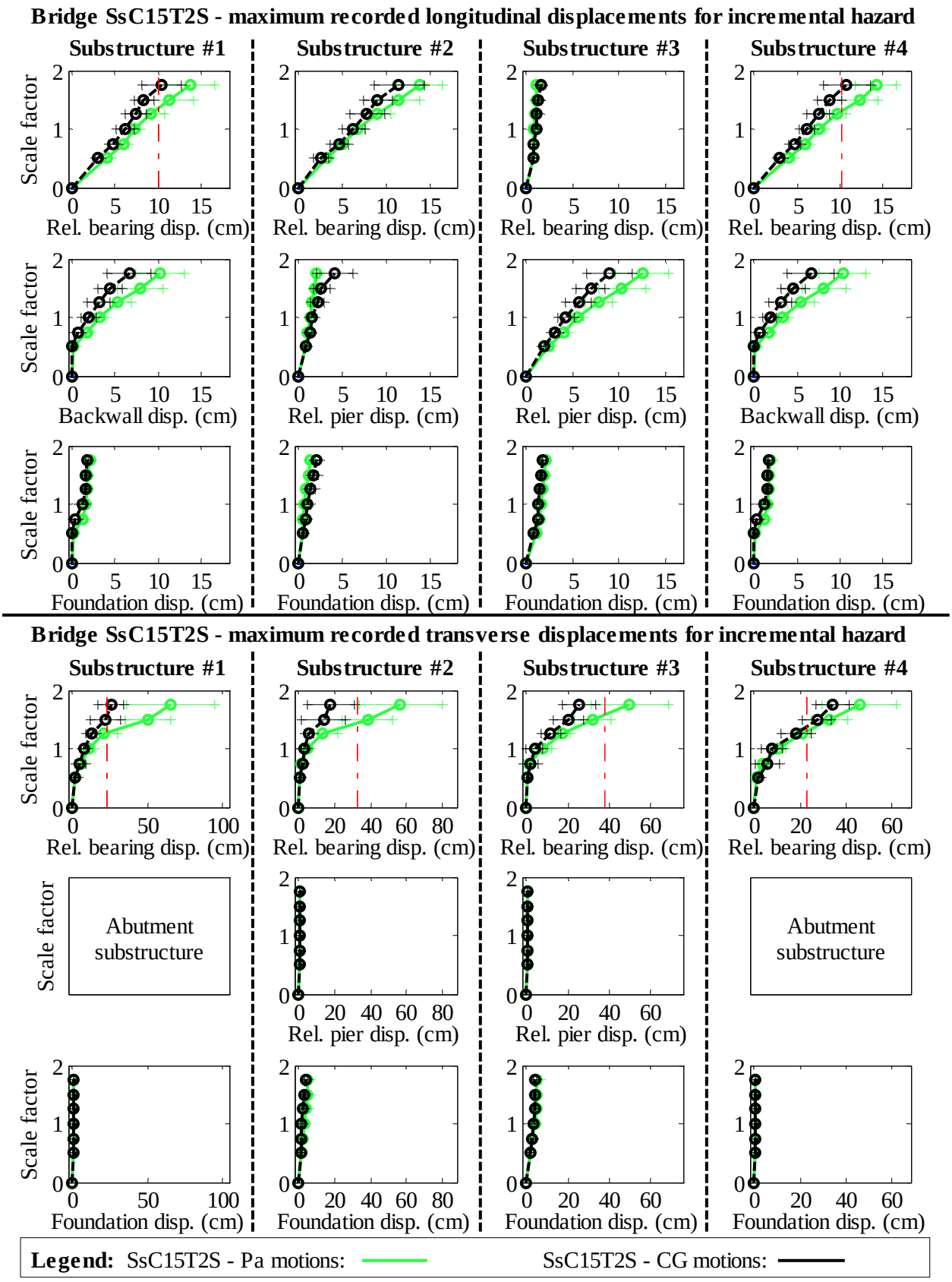

Figure B. 4(b) Bridge SsC15T2S - displacement results

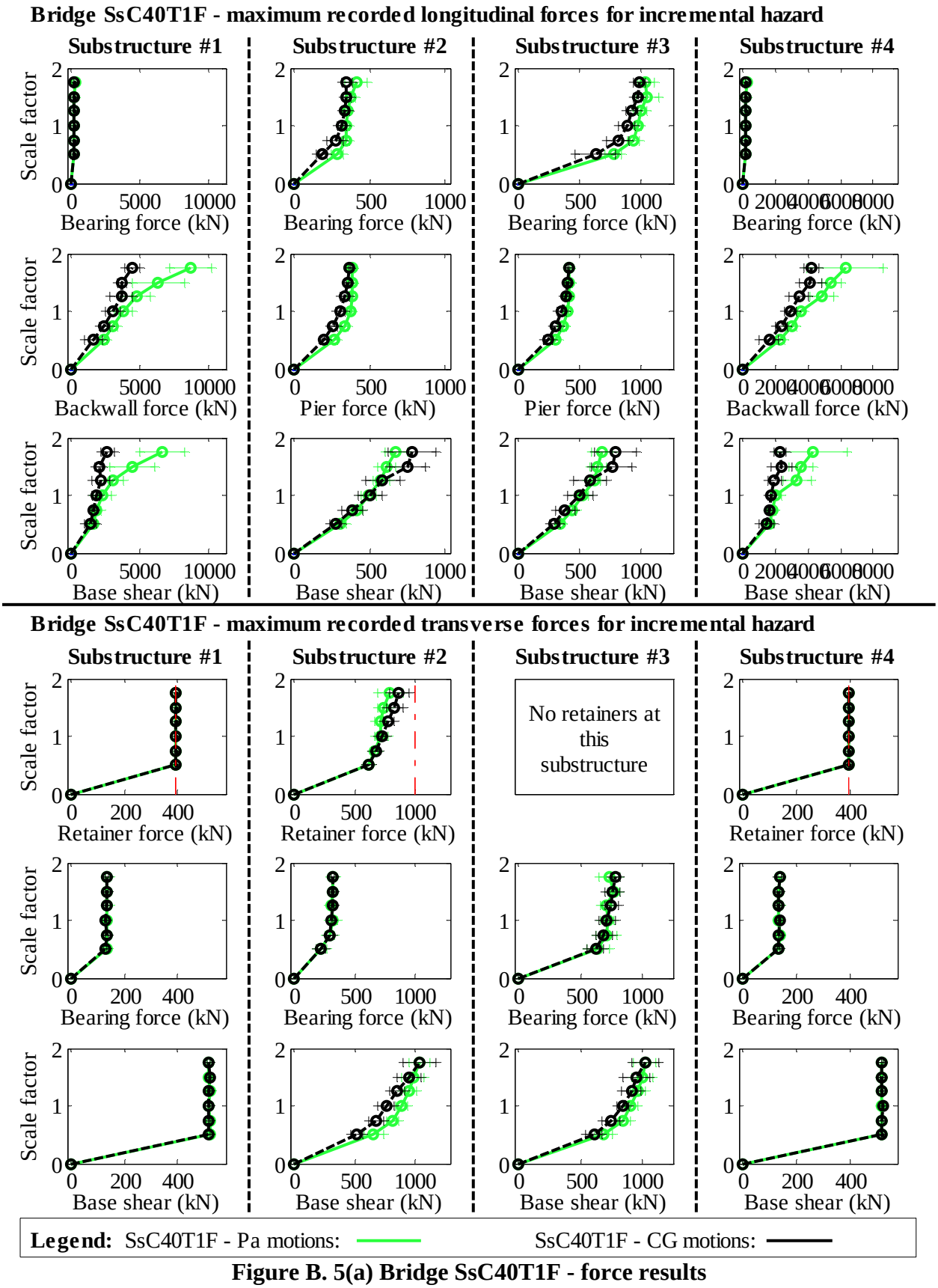

Figure B. 5(a) Bridge SsC40T1F - force results

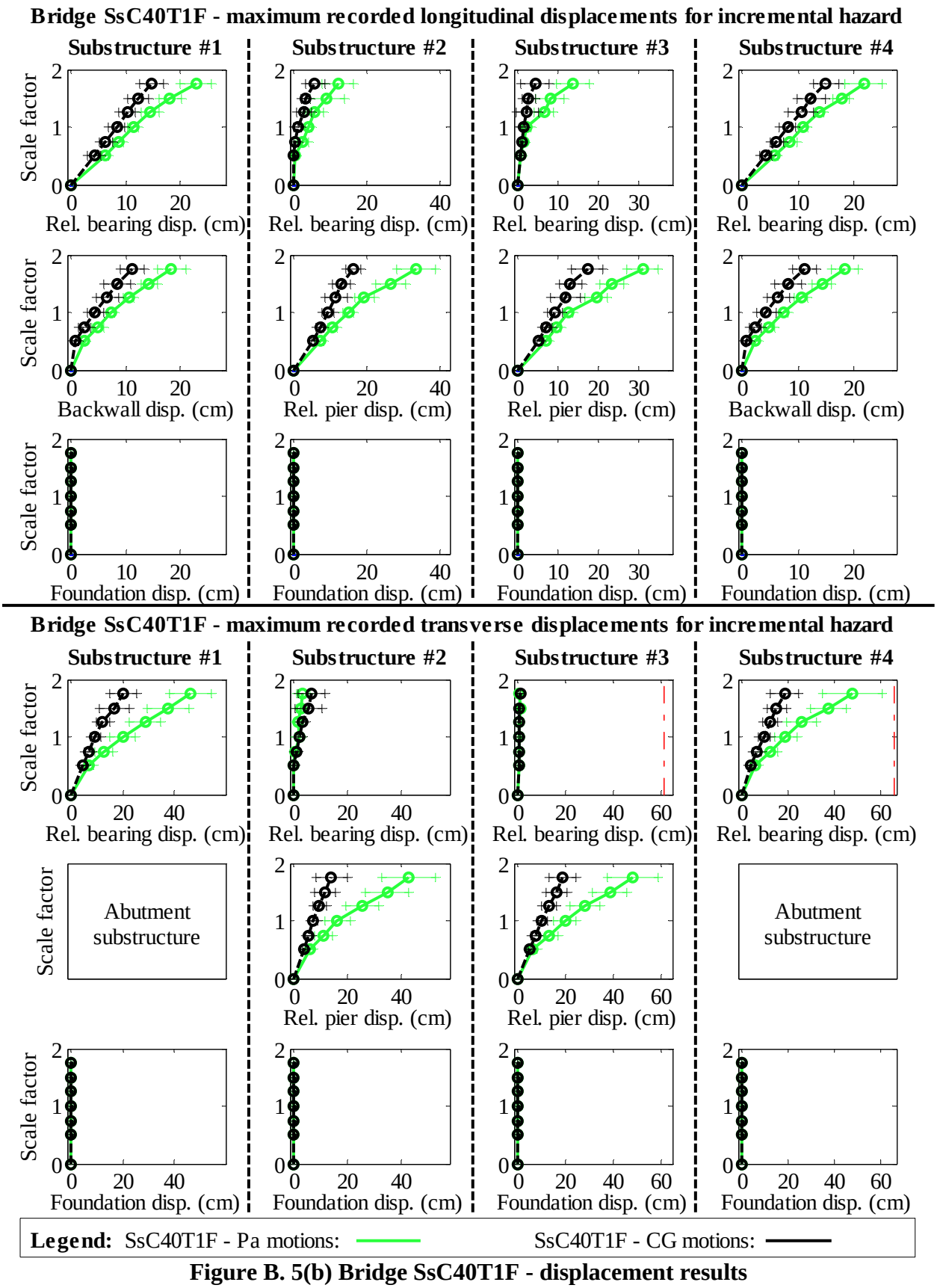

Figure B. 5(b) Bridge SsC40T1F - displacement results

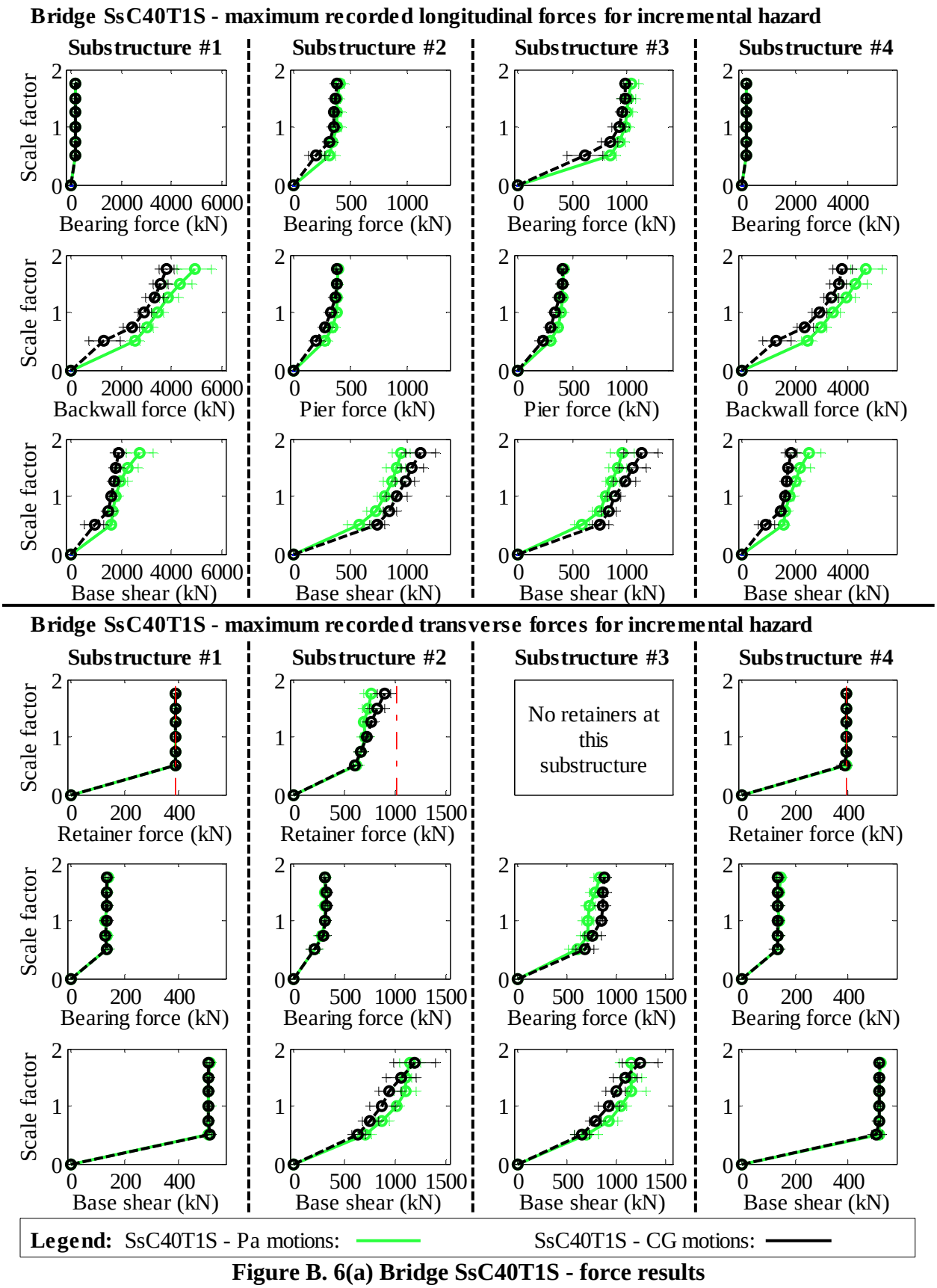

Figure B. 6(a) Bridge SsC40T1S - force results

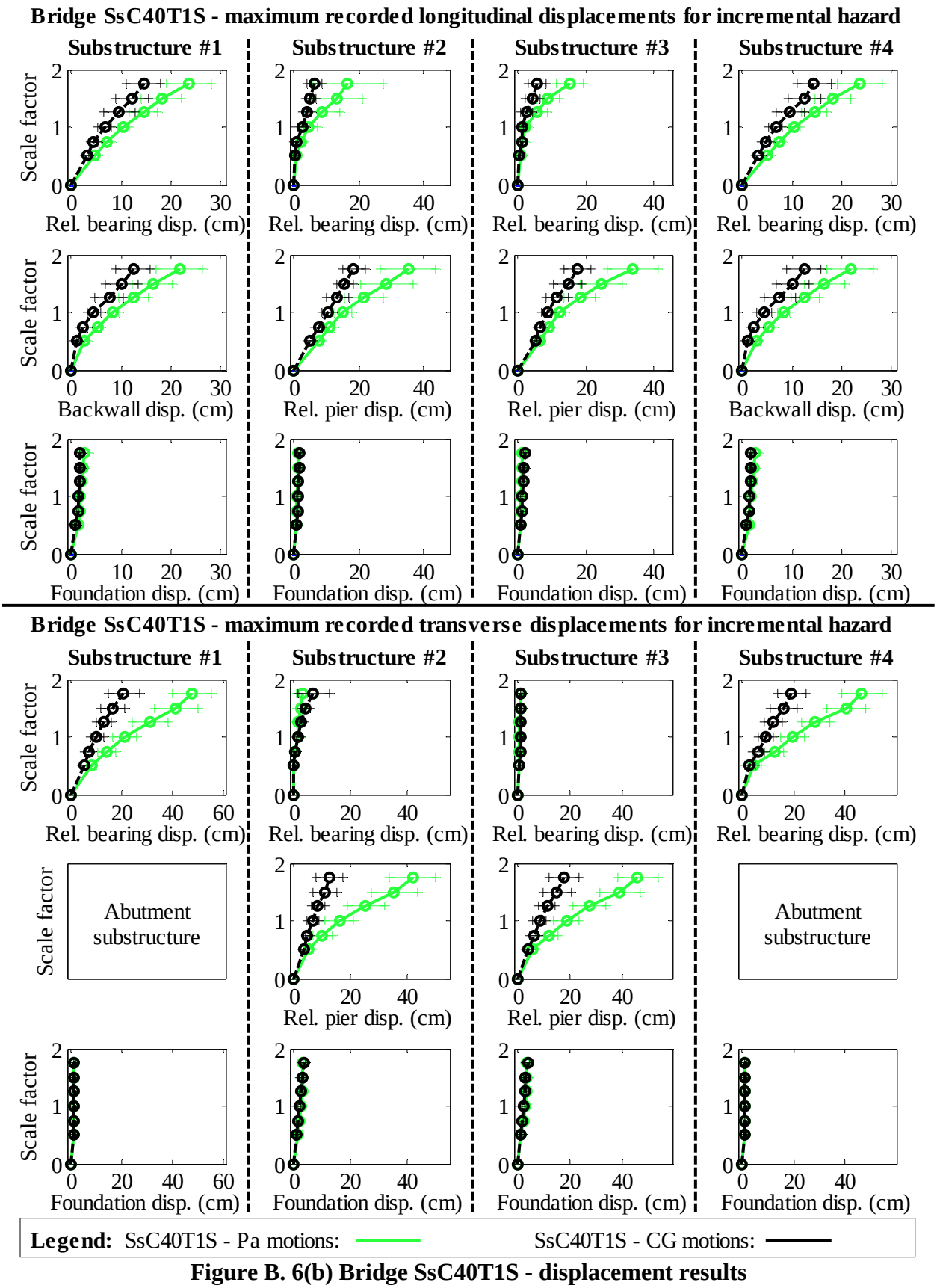

Figure B. 6(b) Bridge SsC40T1S - displacement results

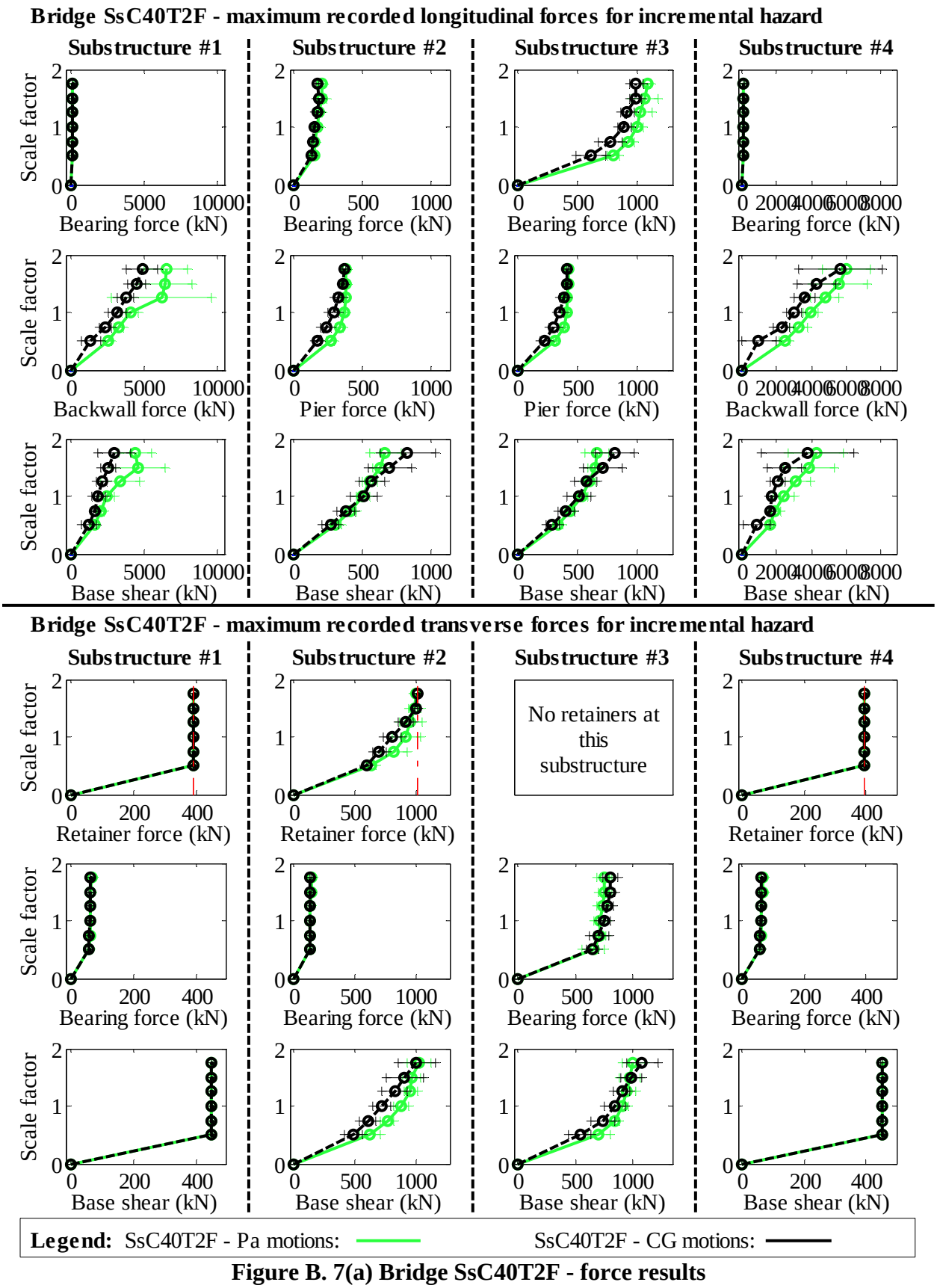

Figure B. 7(a) Bridge SsC40T2F - force results

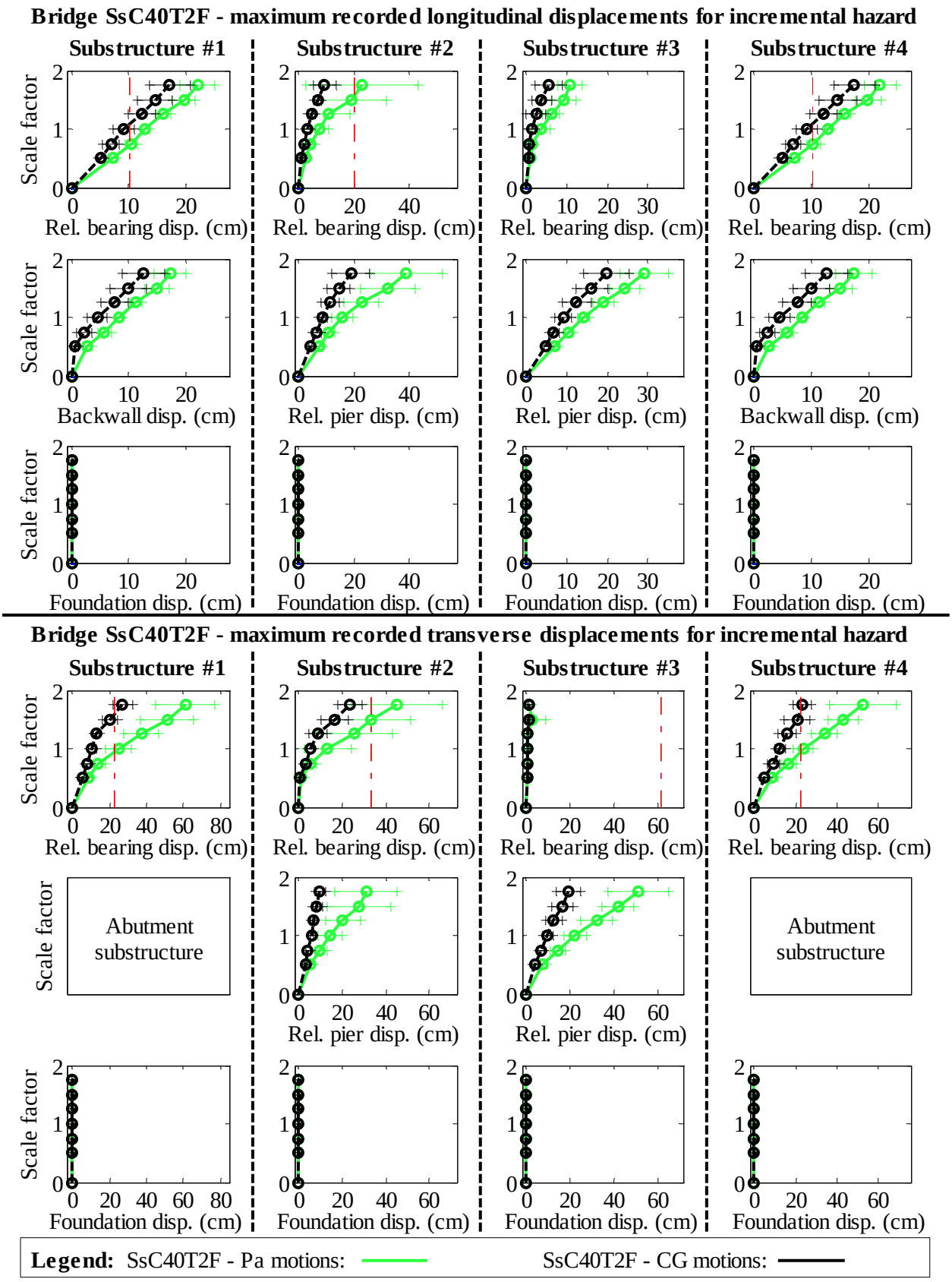

Figure B. 7(b) Bridge SsC40T2F - displacement results

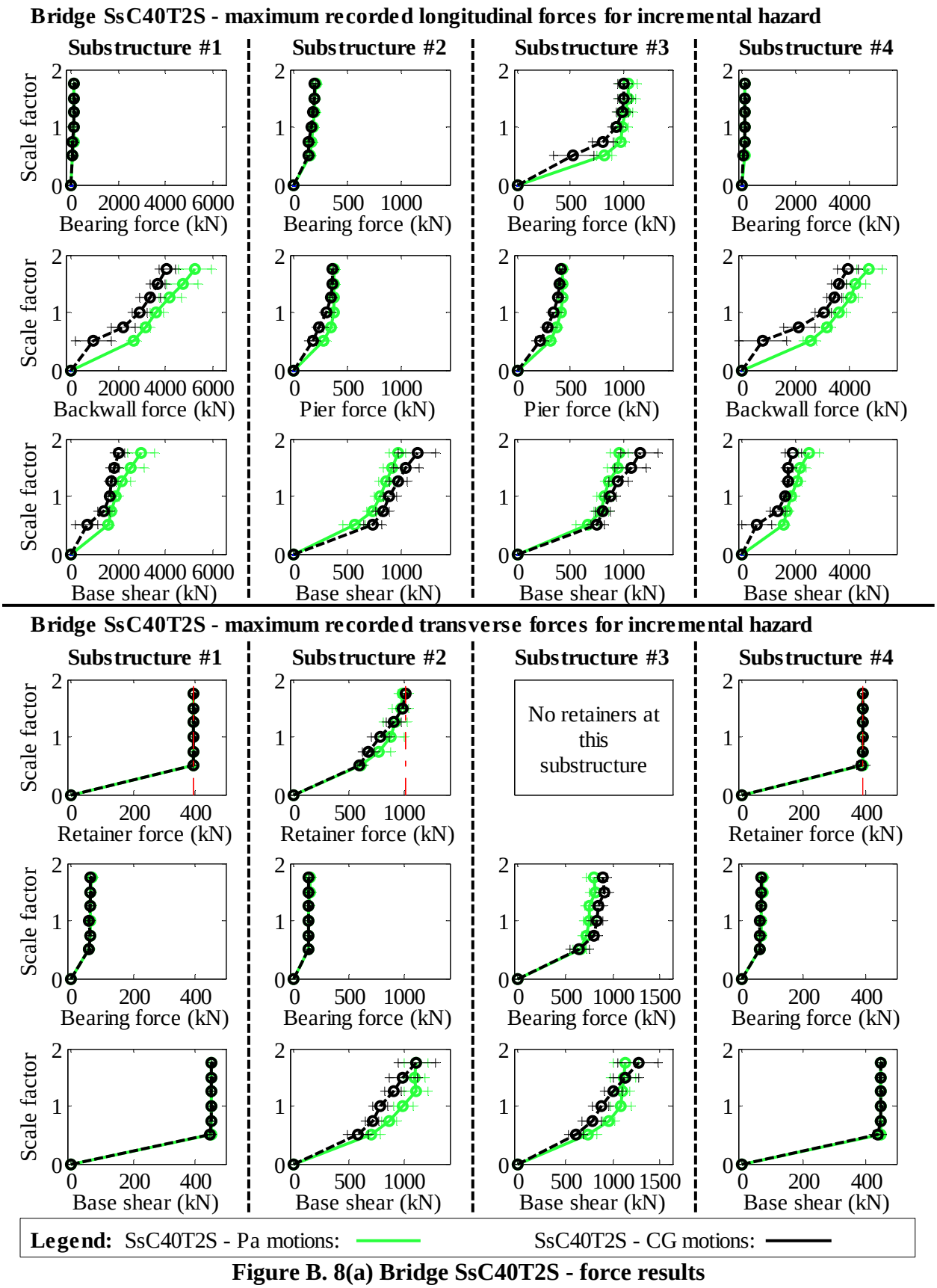

Figure B. 8(a) Bridge SsC40T2S - force results

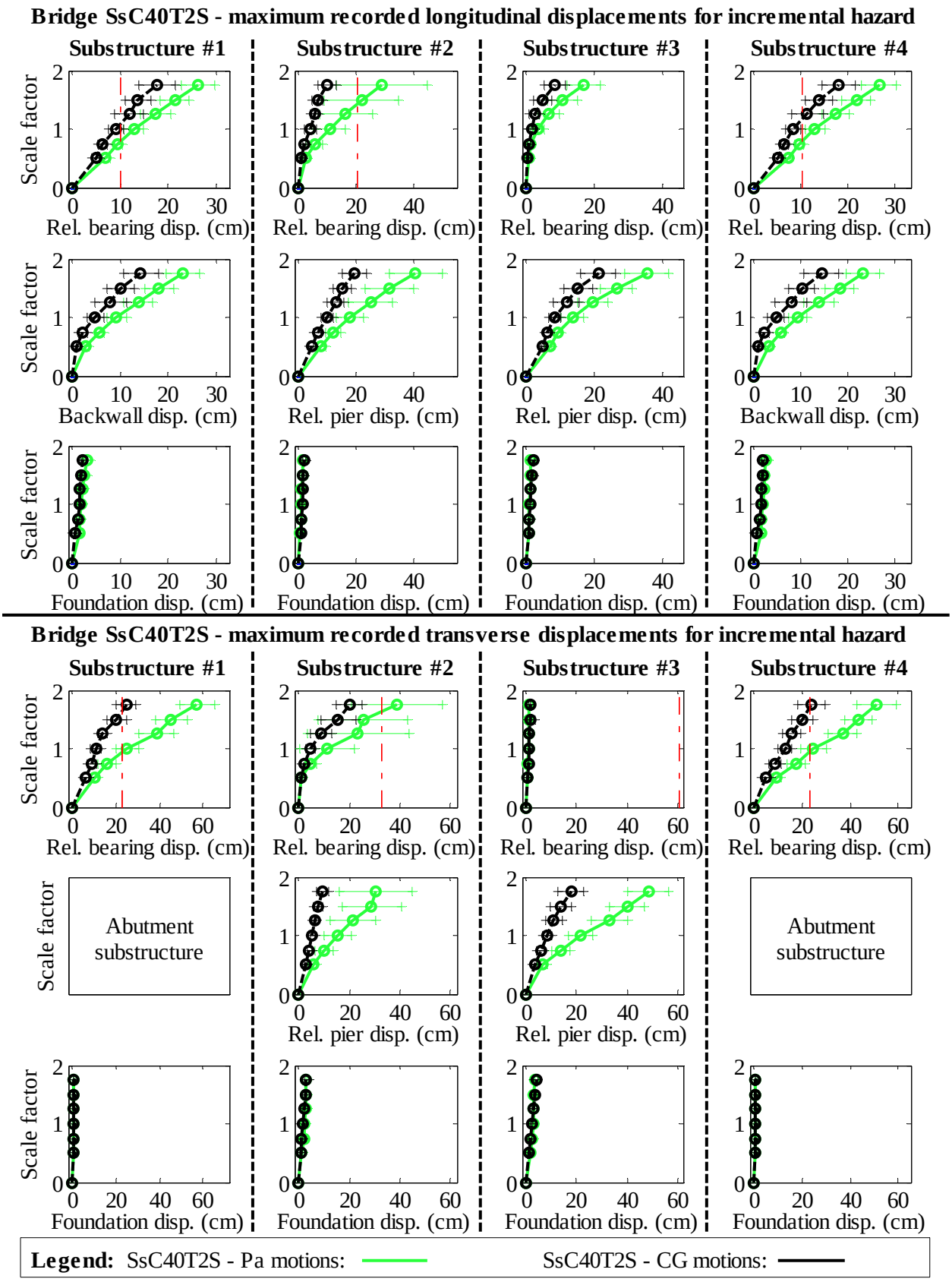

Figure B. 8(b) Bridge SsC40T2S - displacement results

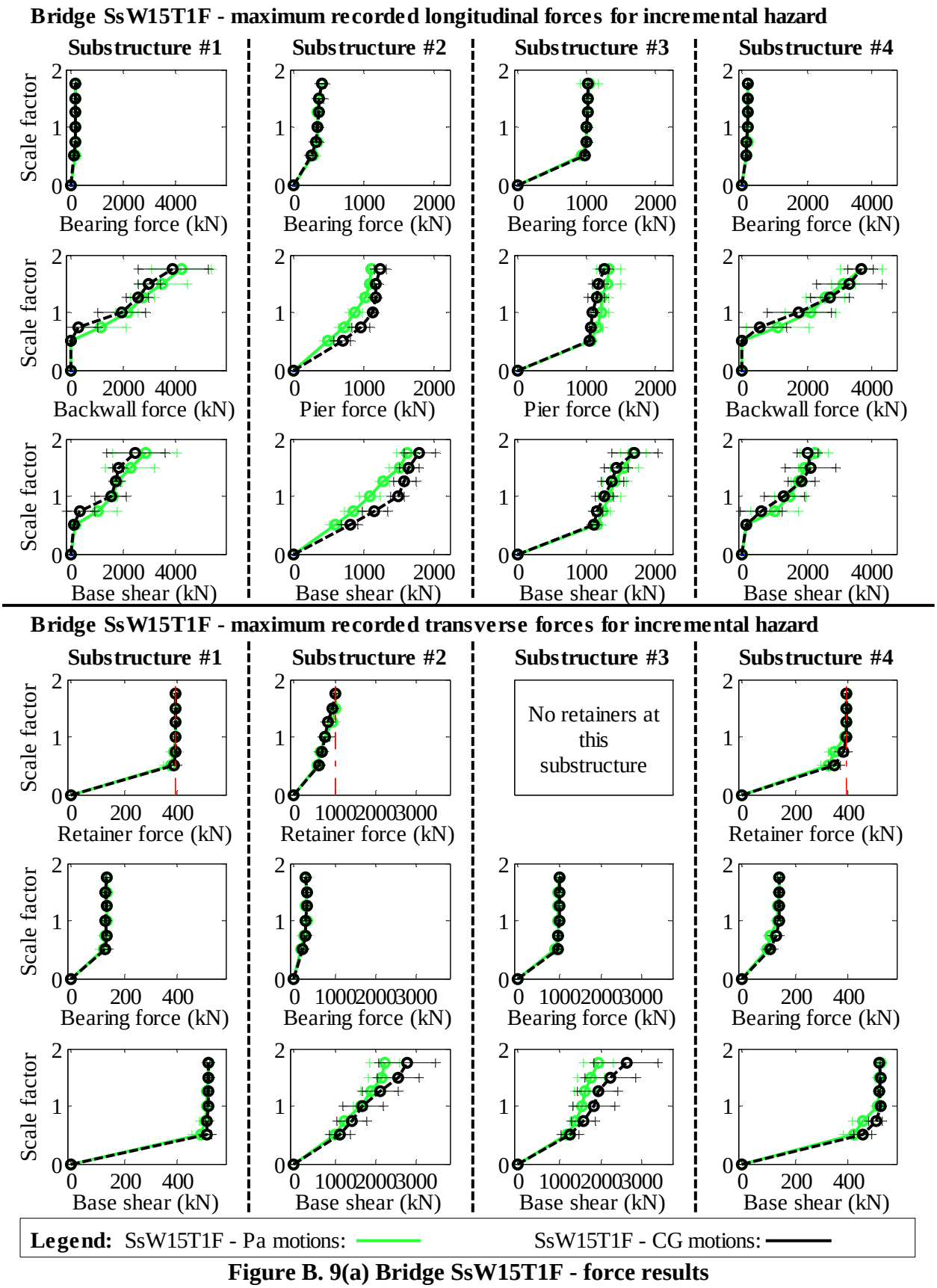

Figure B. 9(a) Bridge SsW15T1F - force results

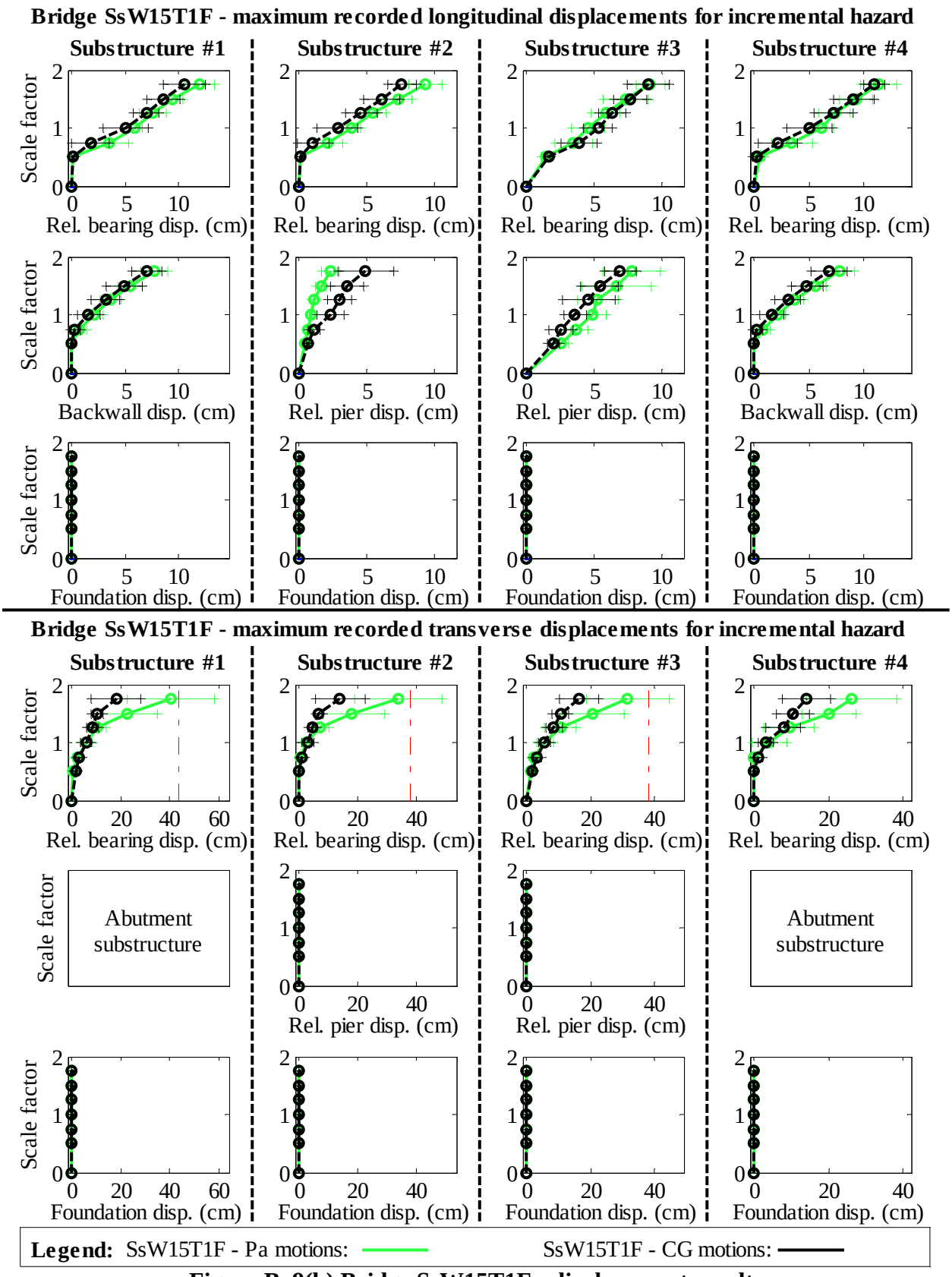

Figure B. 9(b) Bridge SsW15T1F - displacement results

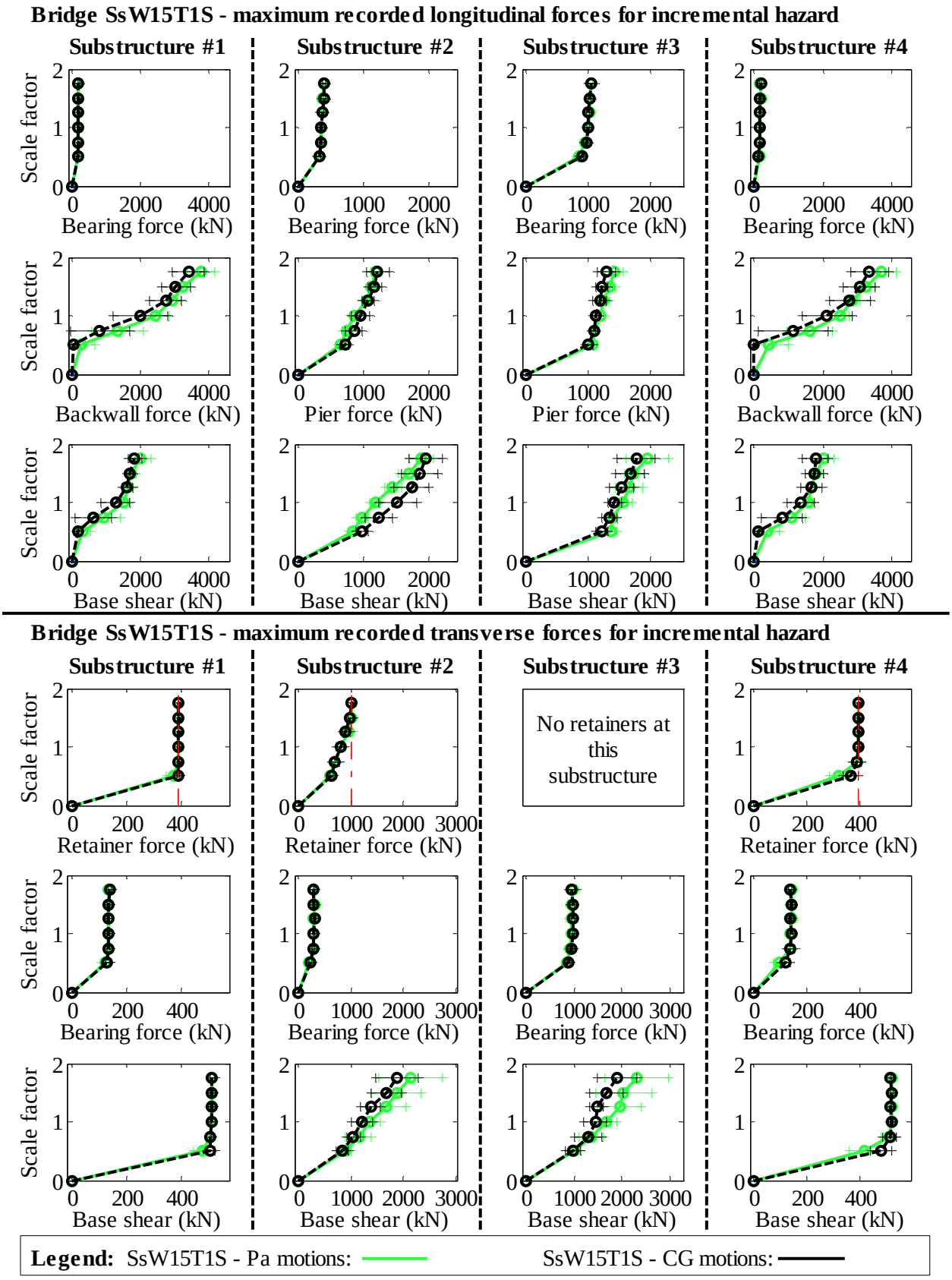

Figure B. 10(a) Bridge SsW15T1S - force results

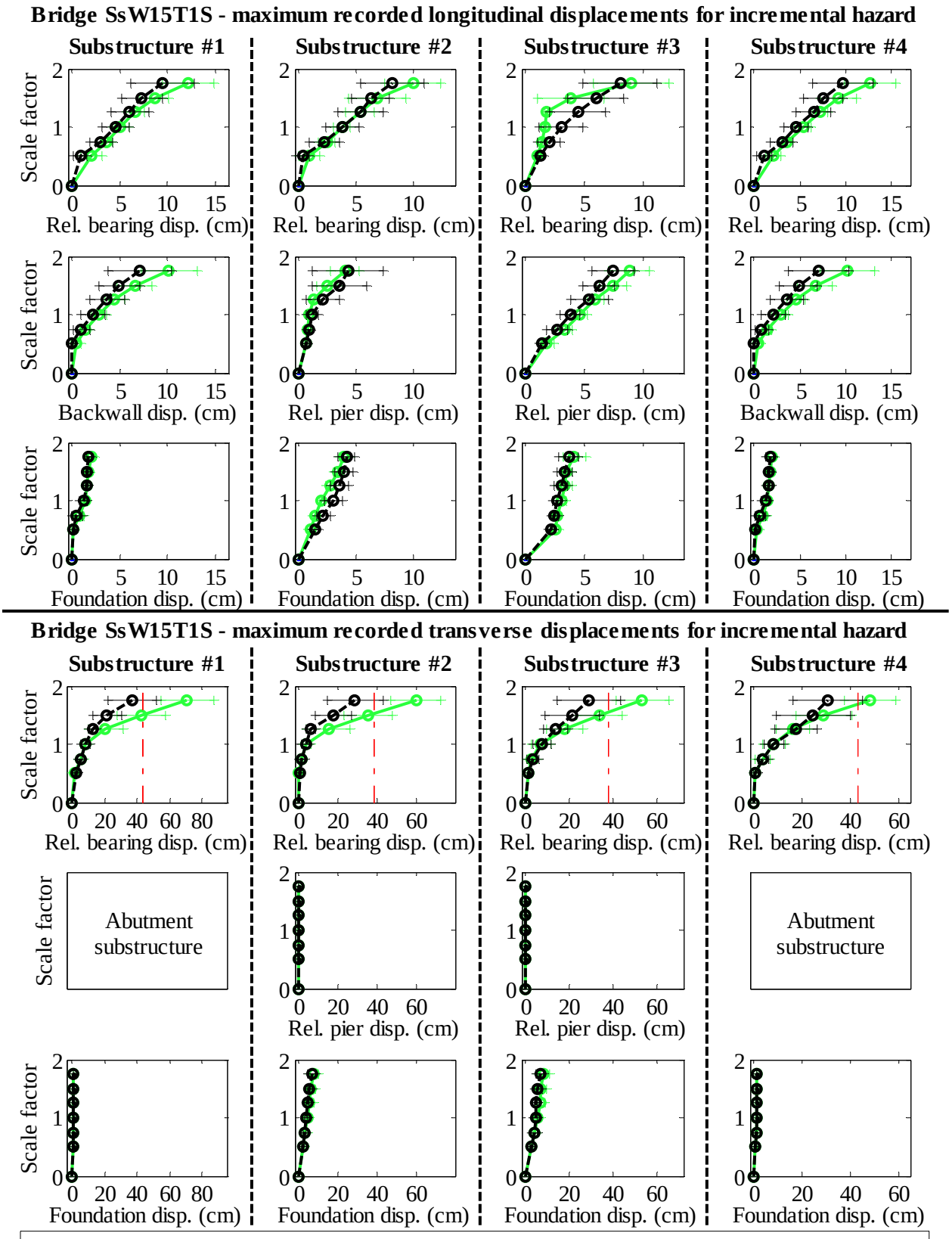

Figure B. 10(b) Bridge SsW15T1S - displacement results

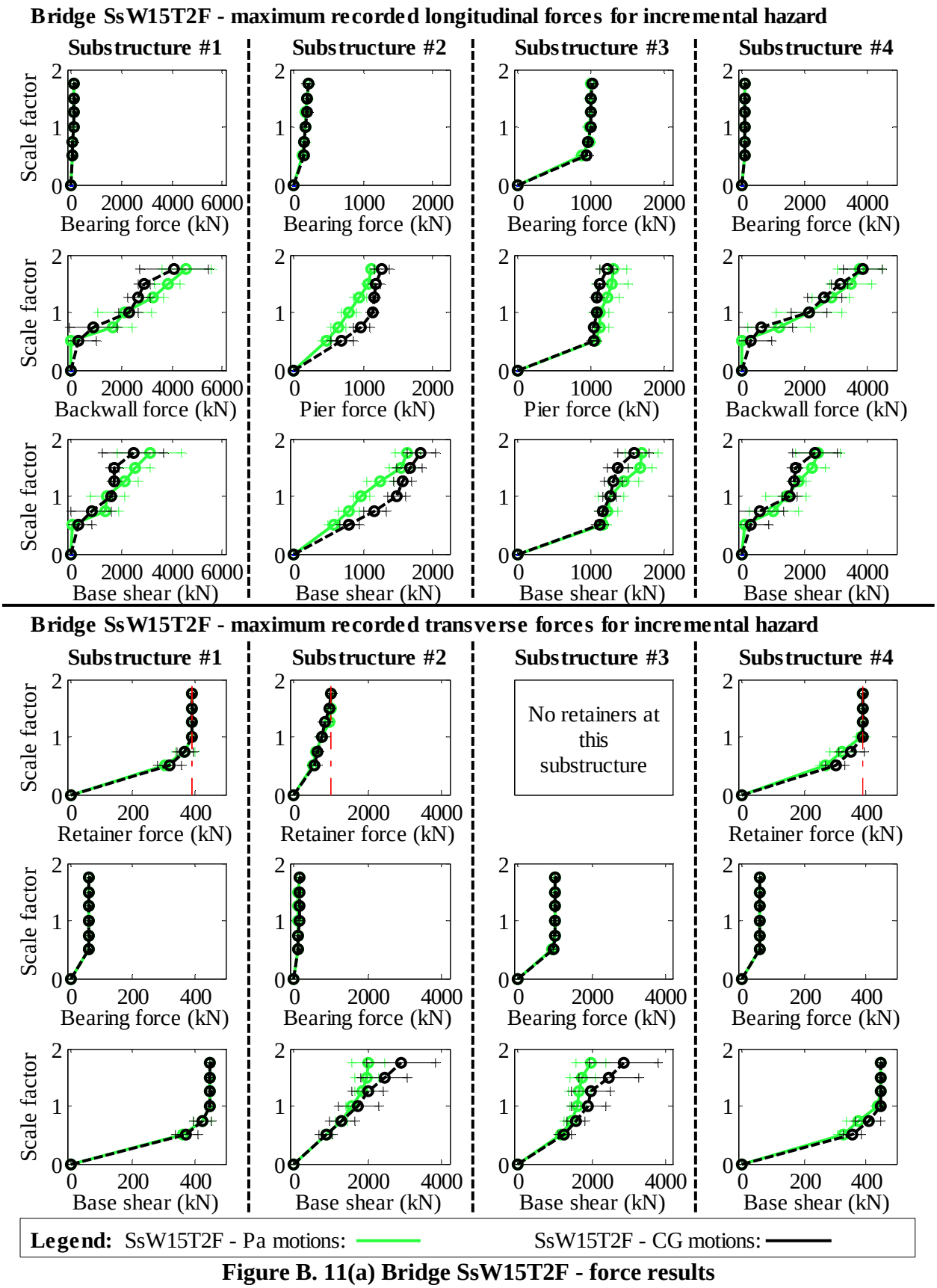

Figure B. 11(a) Bridge SsW15T2F - force results

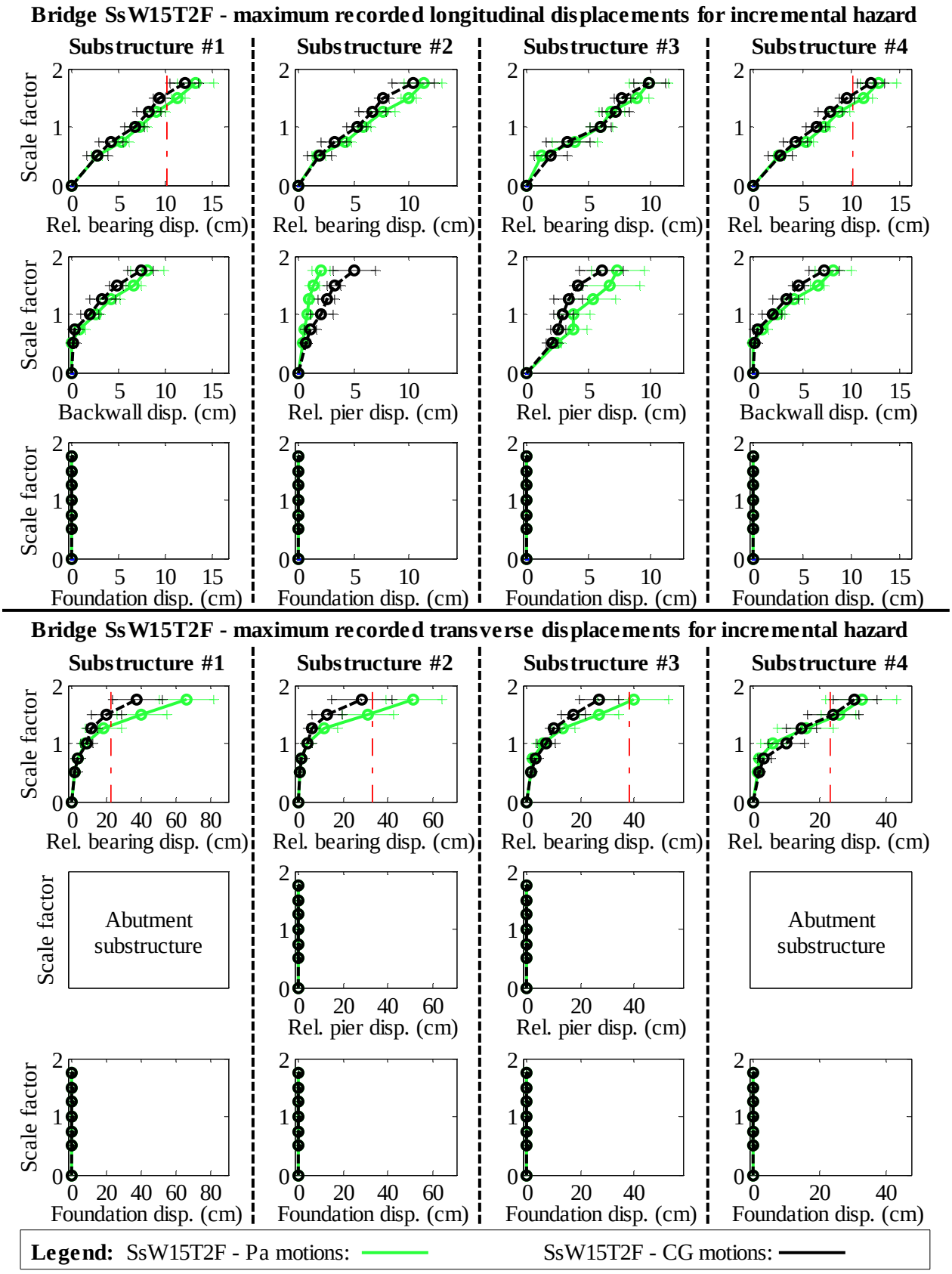

Figure B. 11(b) Bridge SsW15T2F - displacement results

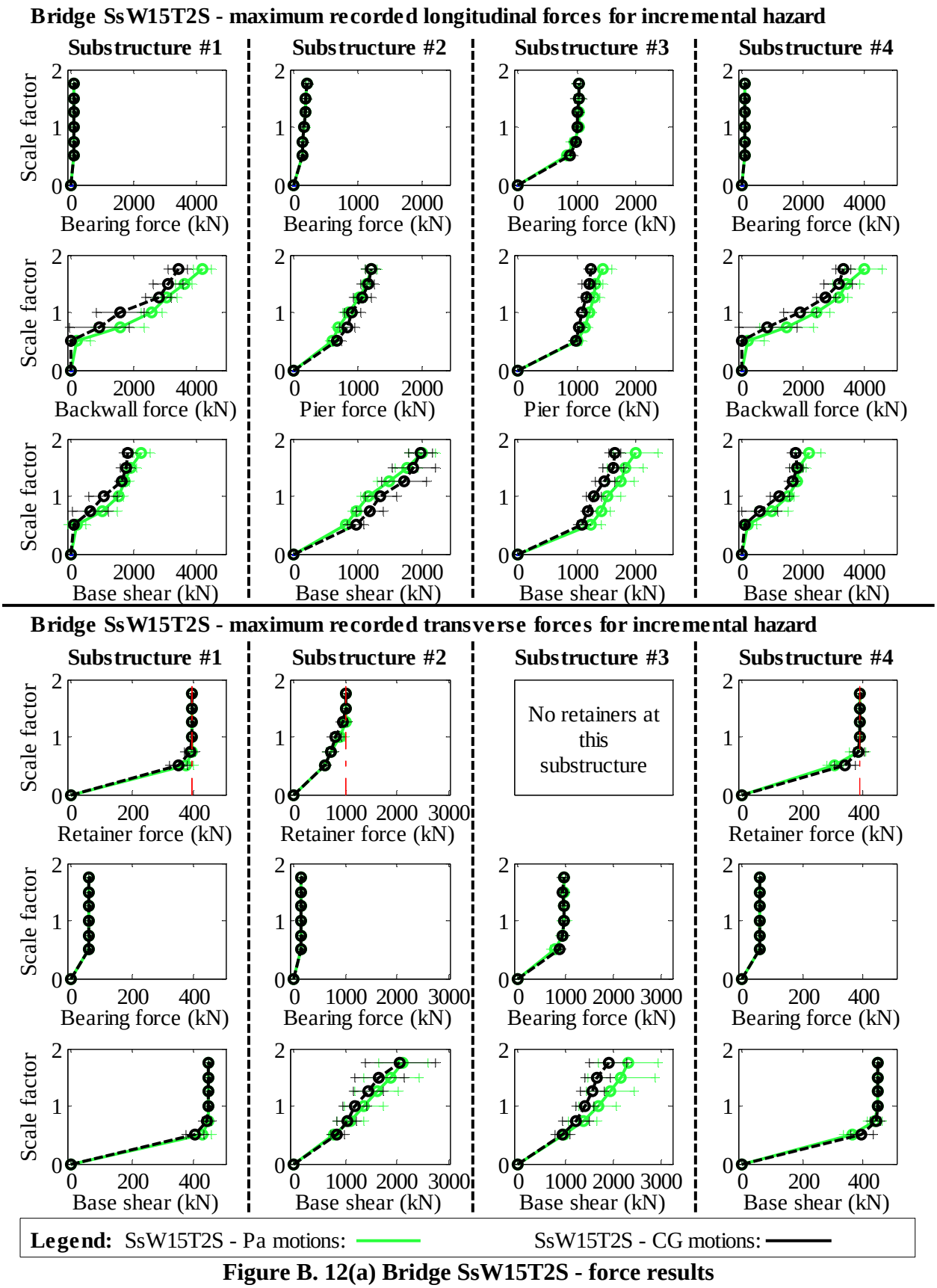

Figure B. 12(a) Bridge SsW15T2S - force results

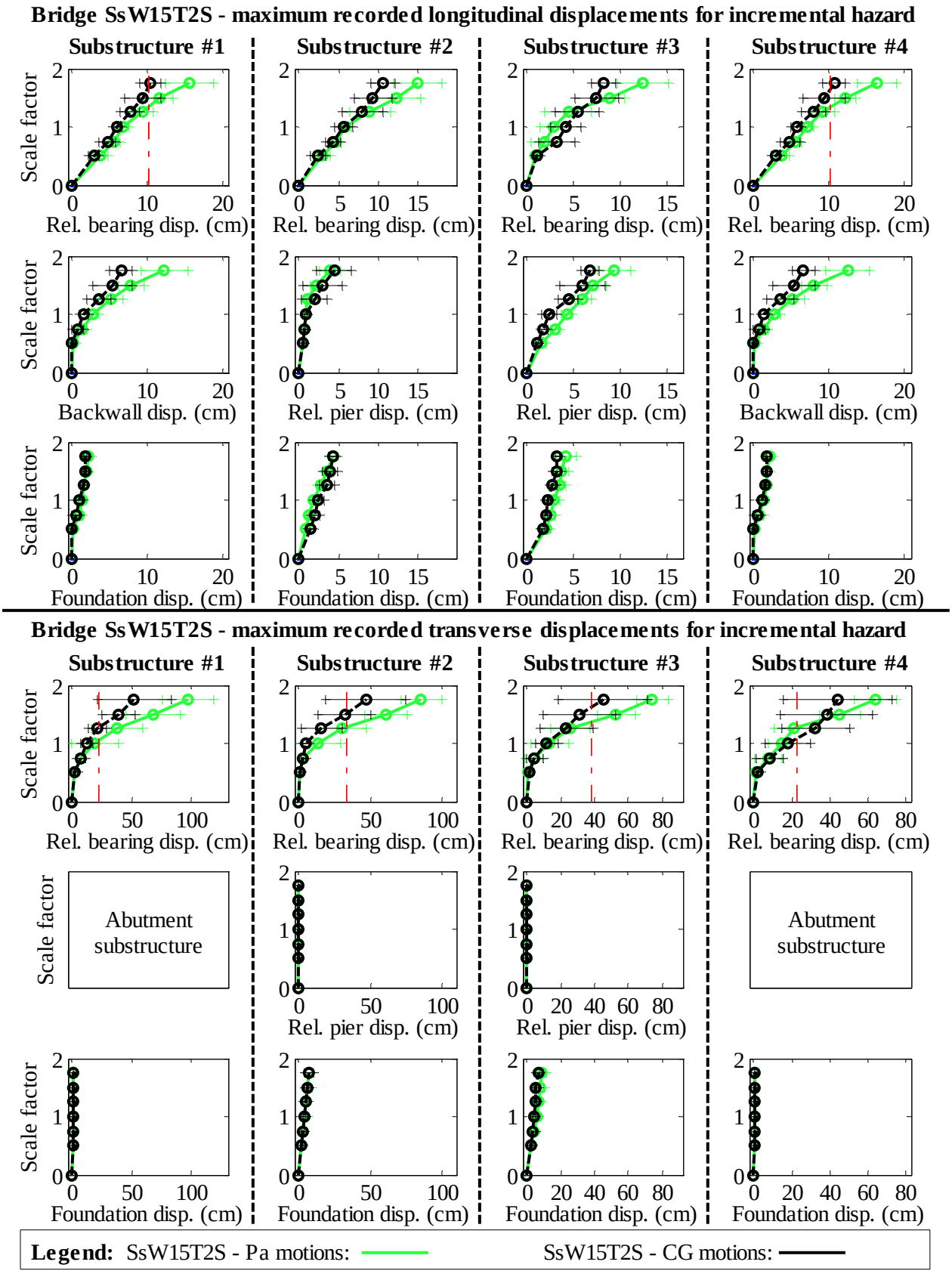

Figure B. 12(b) Bridge SsW15T2S - displacement results

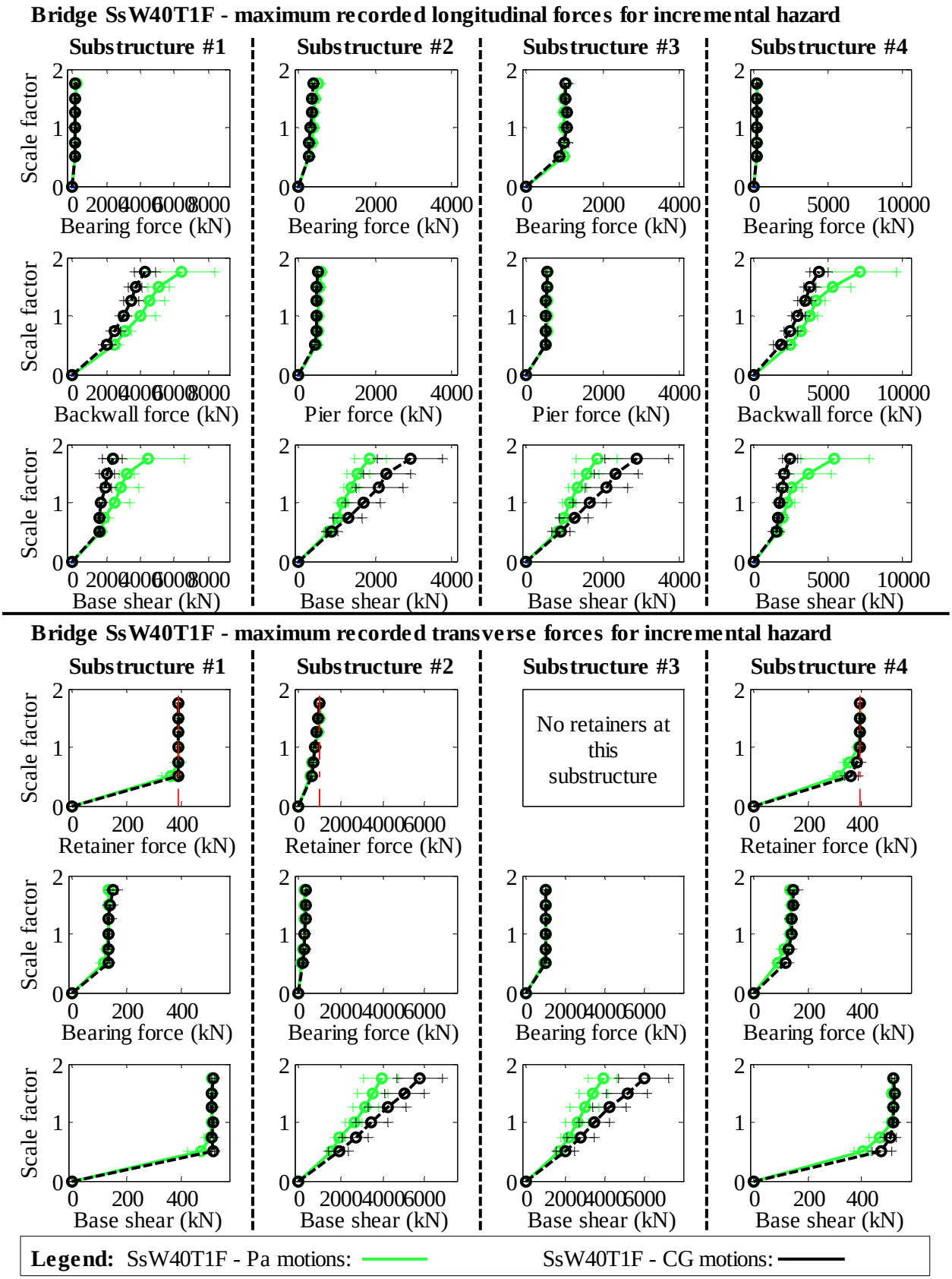

Figure B. 13(a) Bridge SsW40T1F - force results

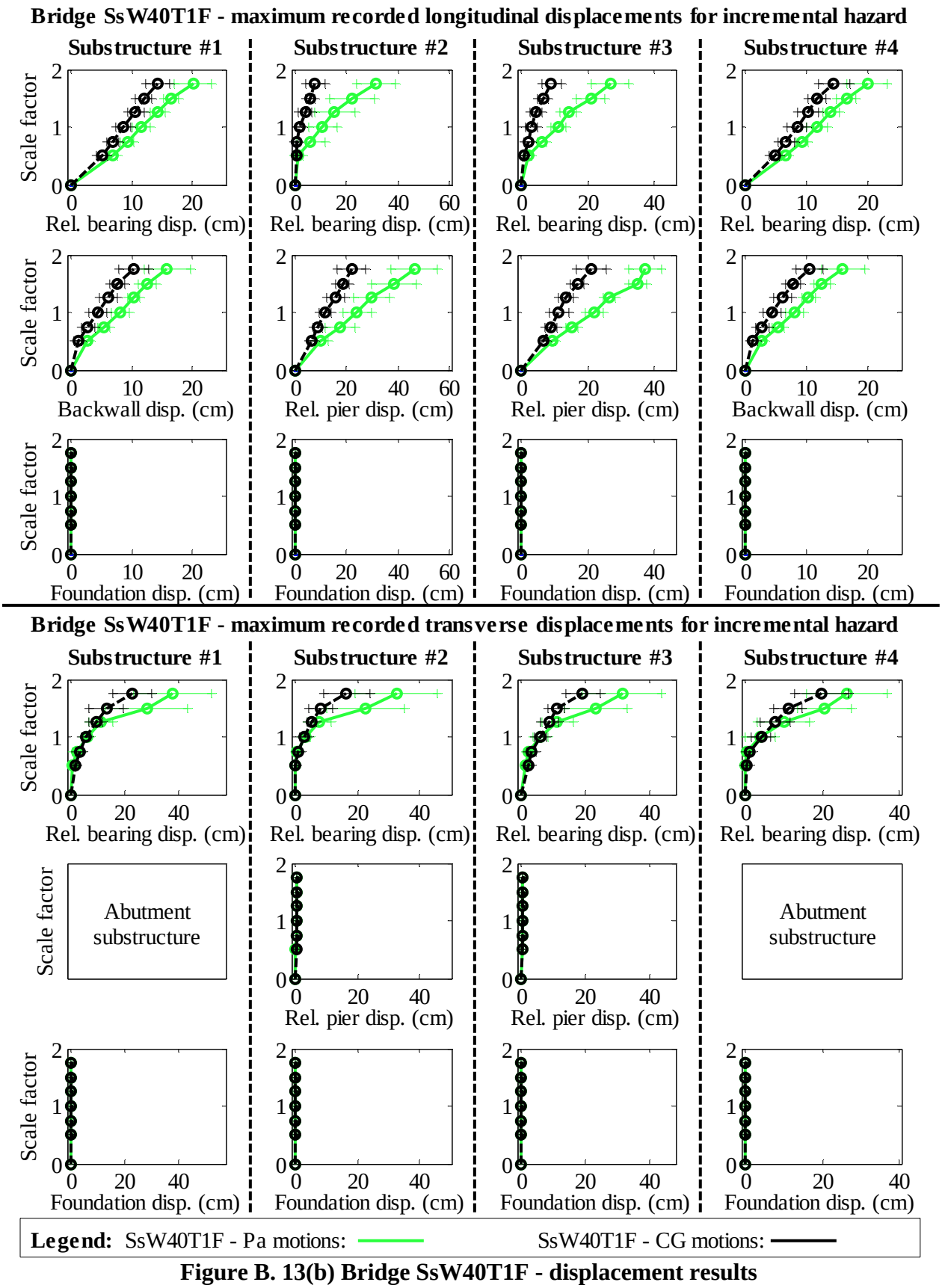

Figure B. 13(b) Bridge SsW40T1F - displacement results

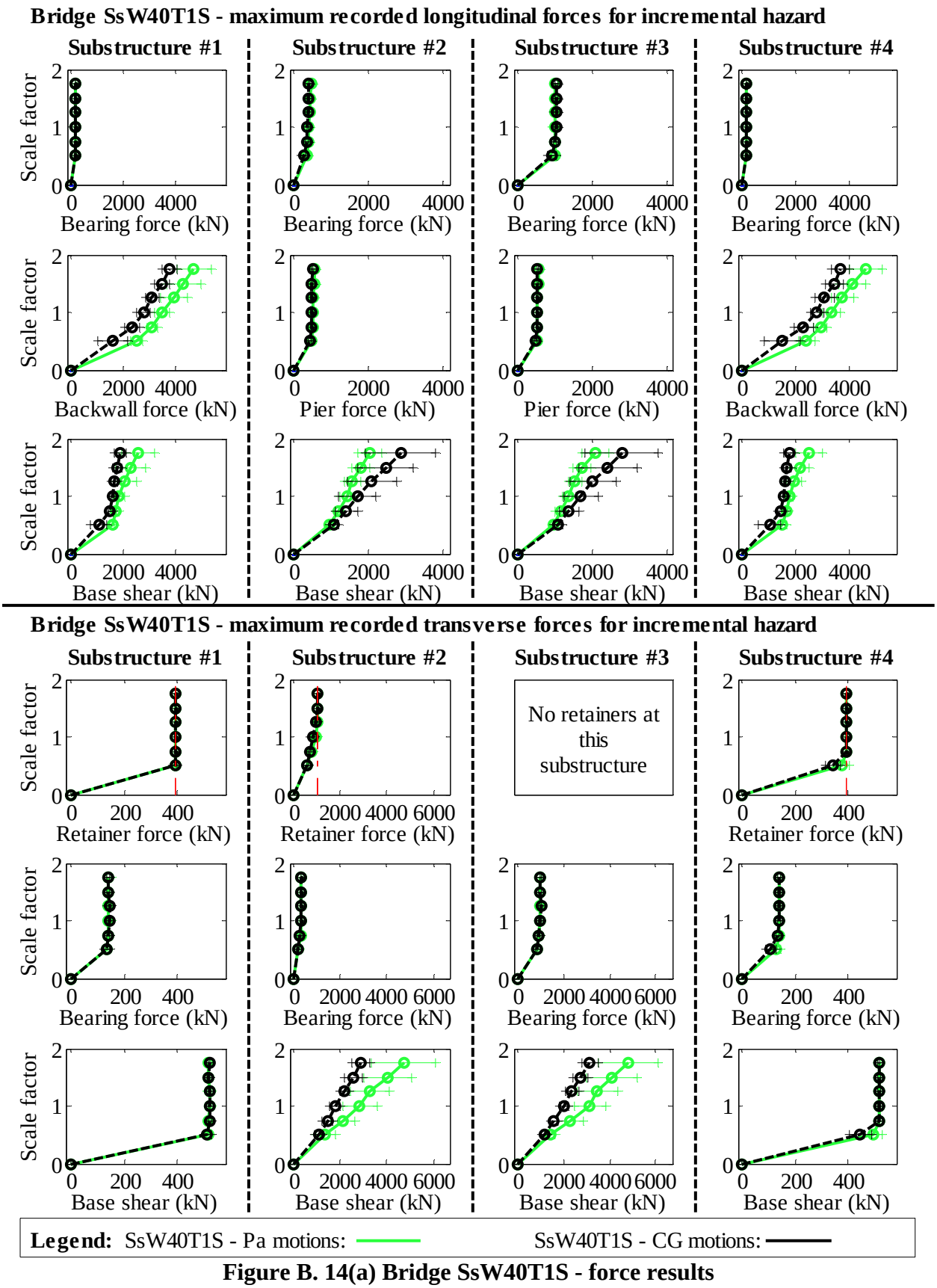

Figure B. 14(a) Bridge SsW40T1S - force results

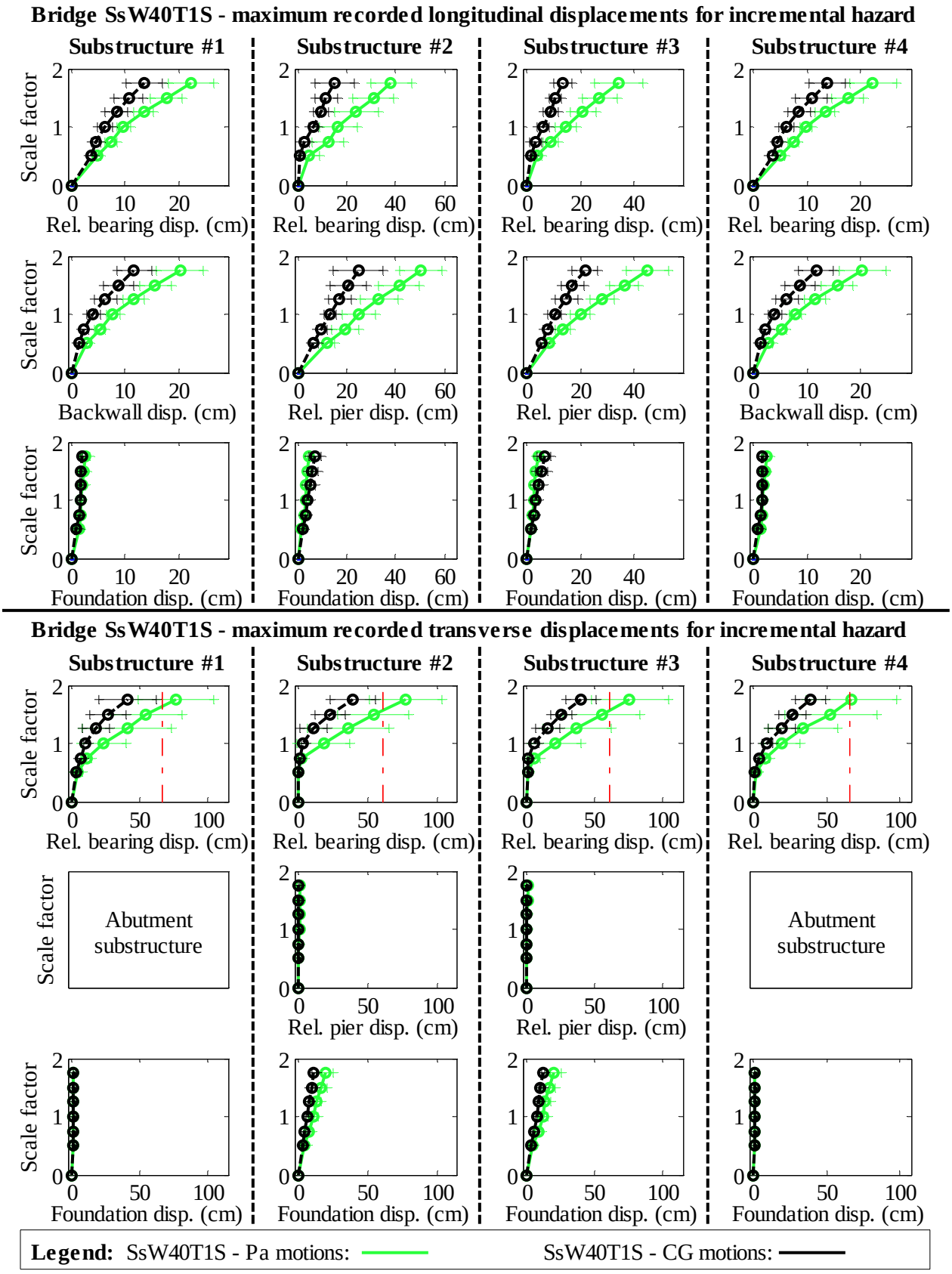

Figure B. 14(b) Bridge SsW40T1S - displacement results

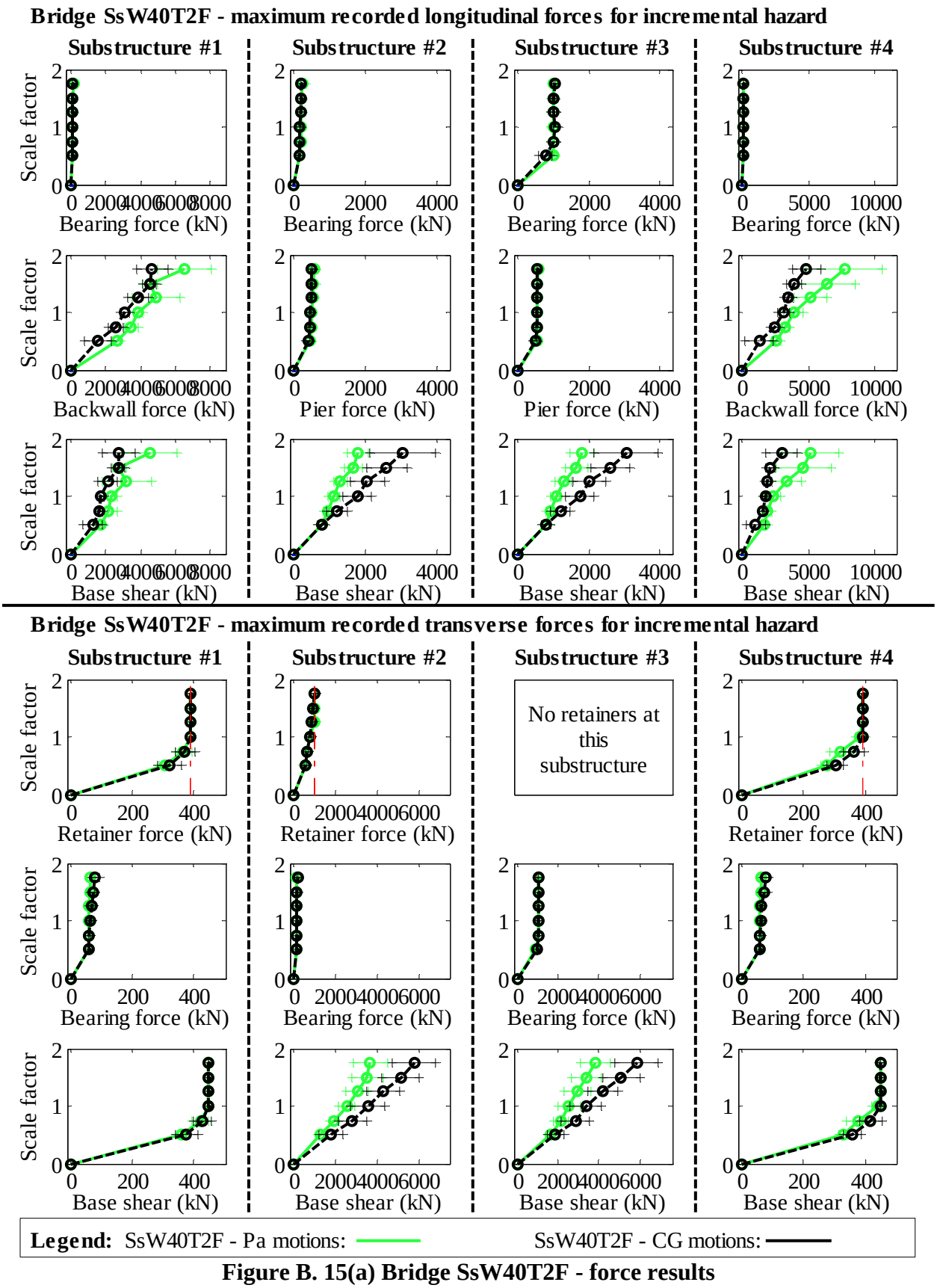

Figure B. 15(a) Bridge SsW40T2F - force results

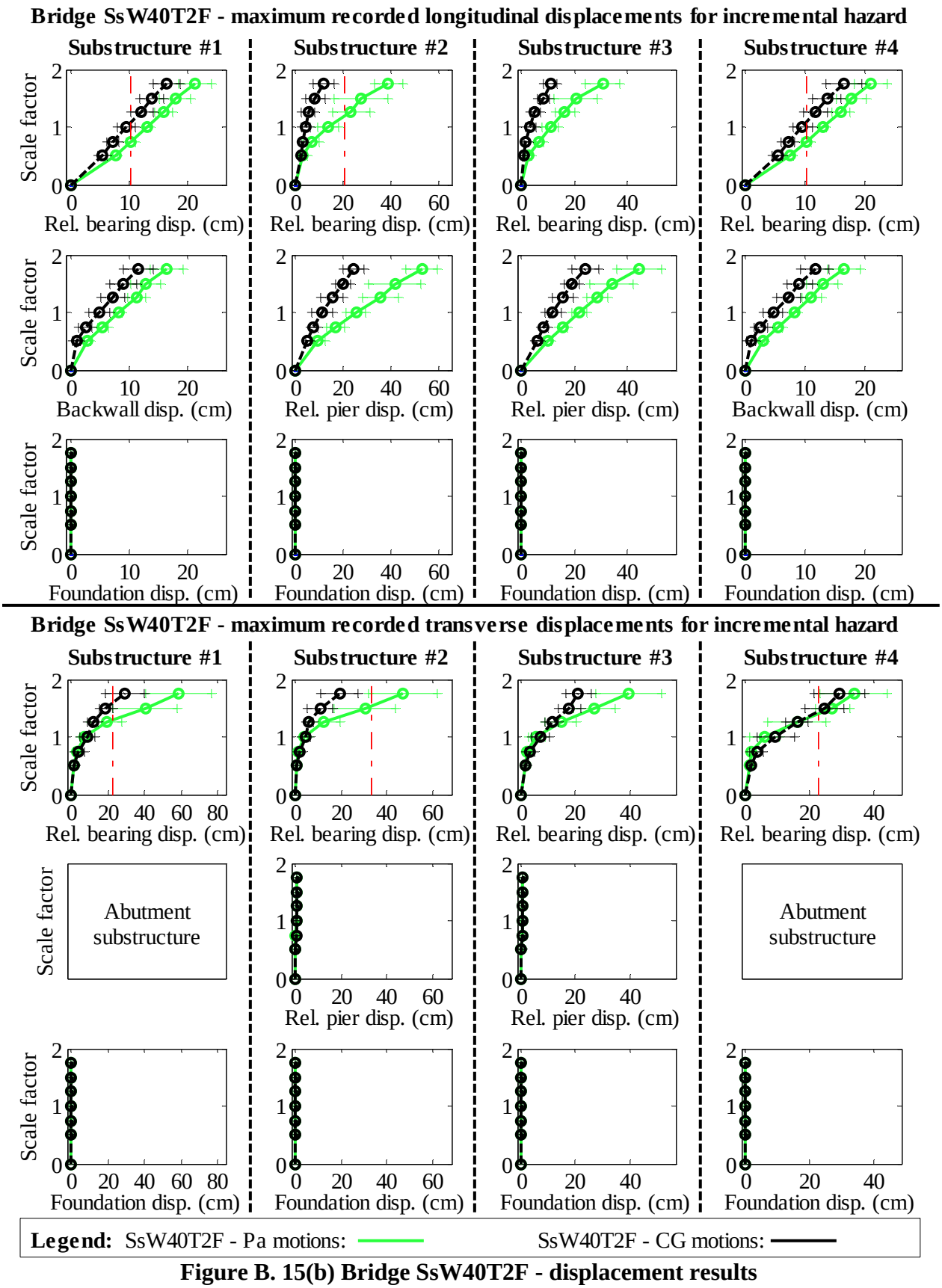

Figure B. 15(b) Bridge SsW40T2F - displacement results

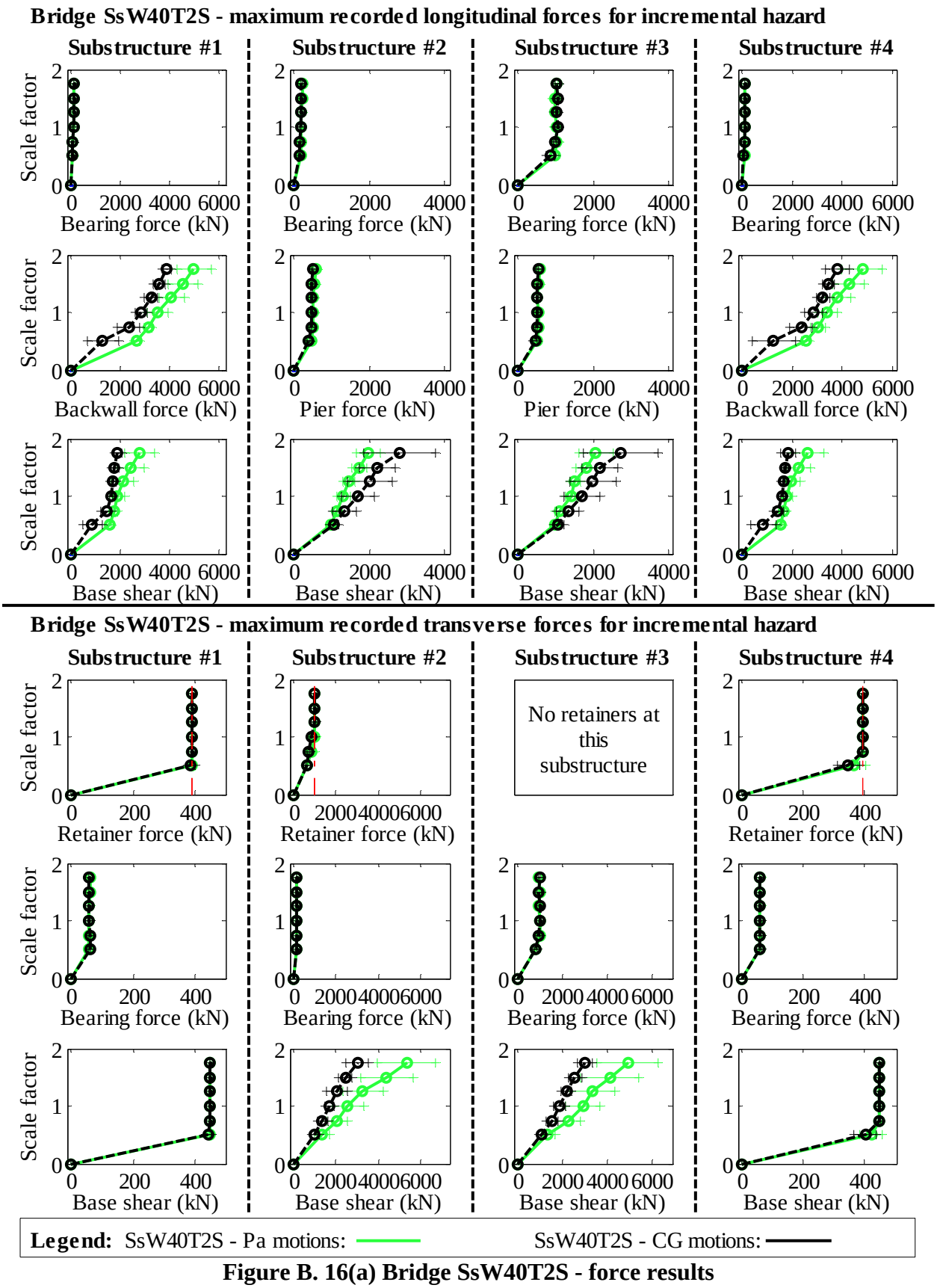

Figure B. 16(a) Bridge SsW40T2S - force results

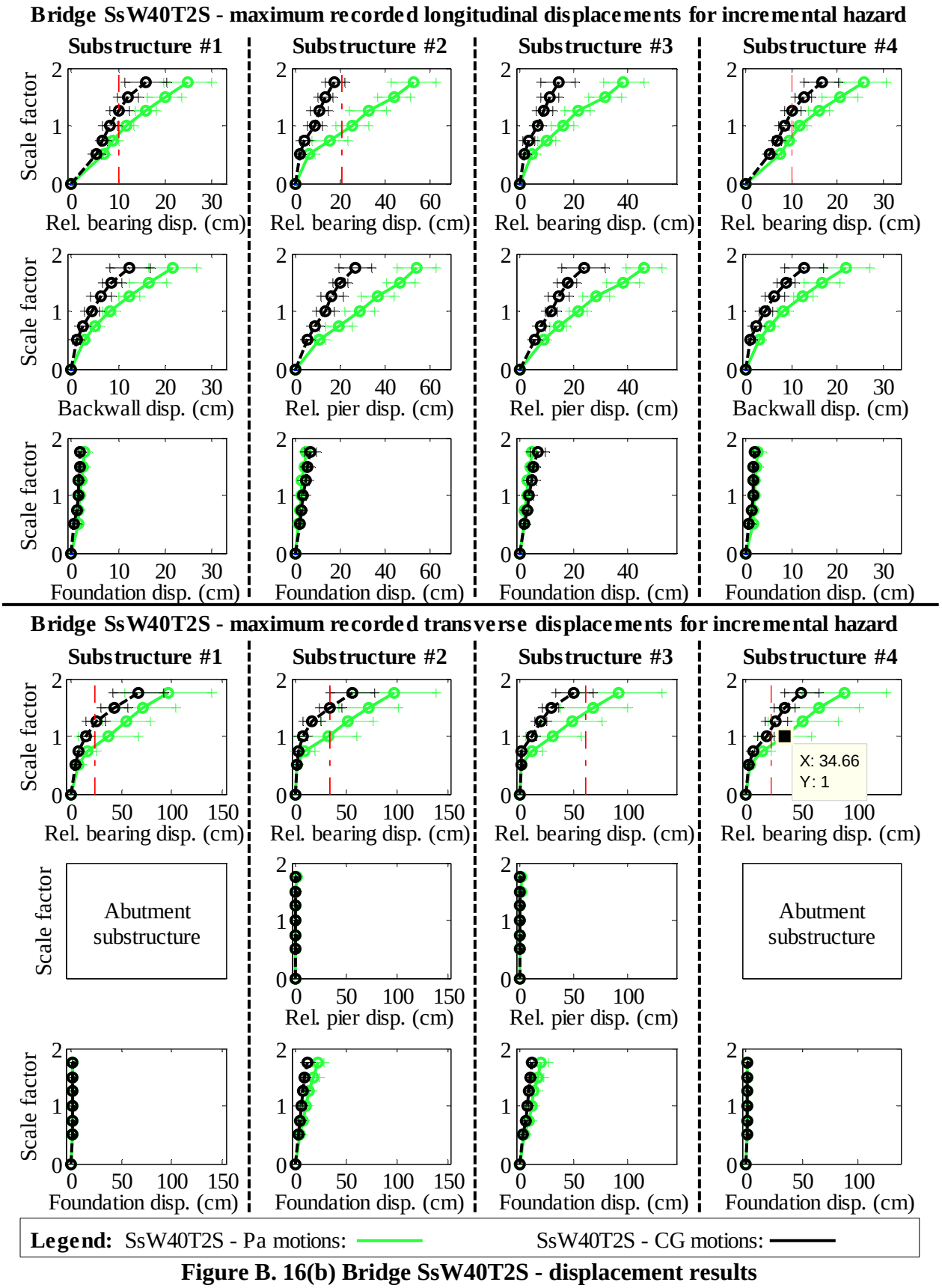

Figure B. 16(b) Bridge SsW40T2S - displacement results

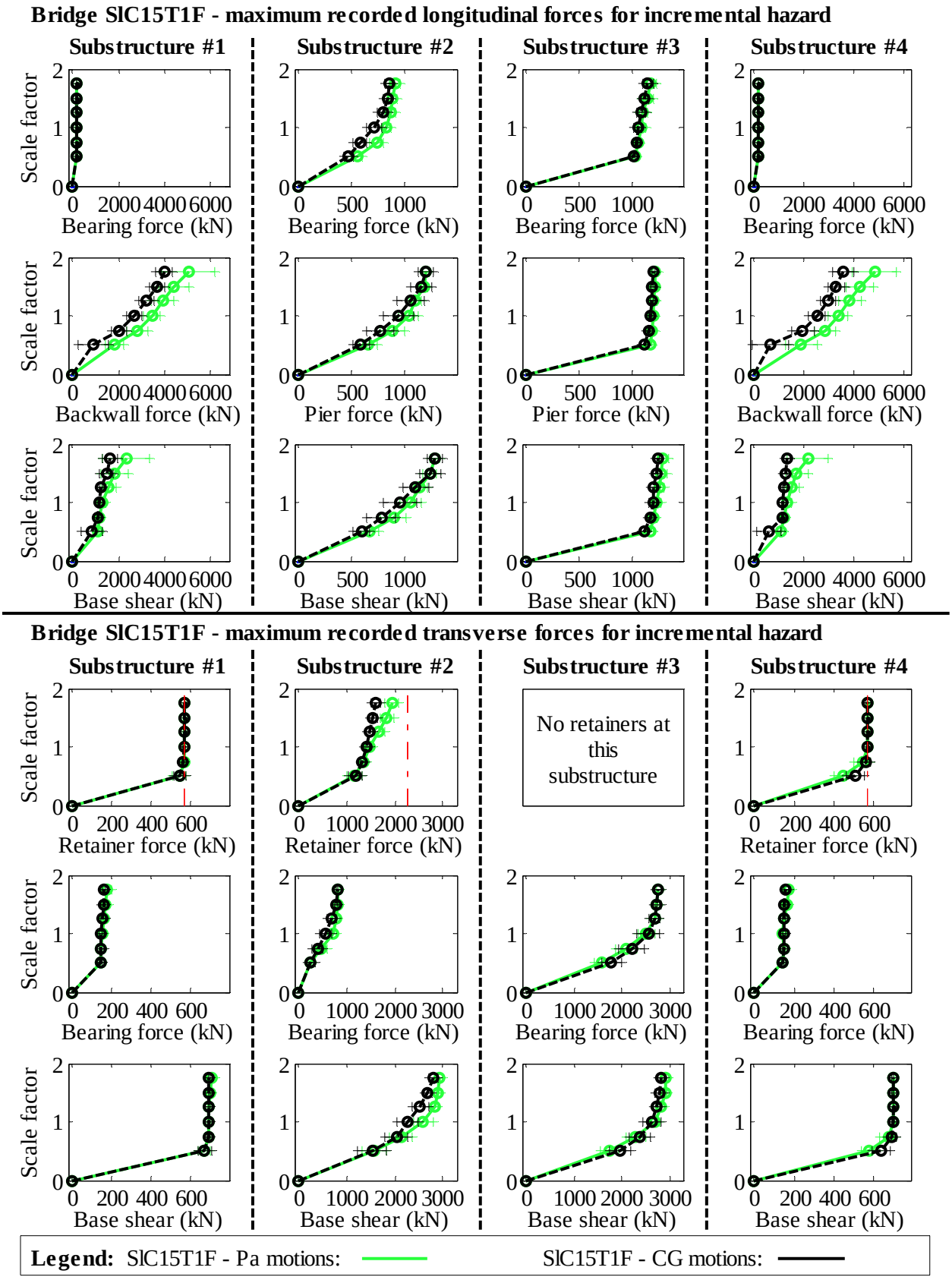

Figure B. 17(a) Bridge SlC15T1F - force results

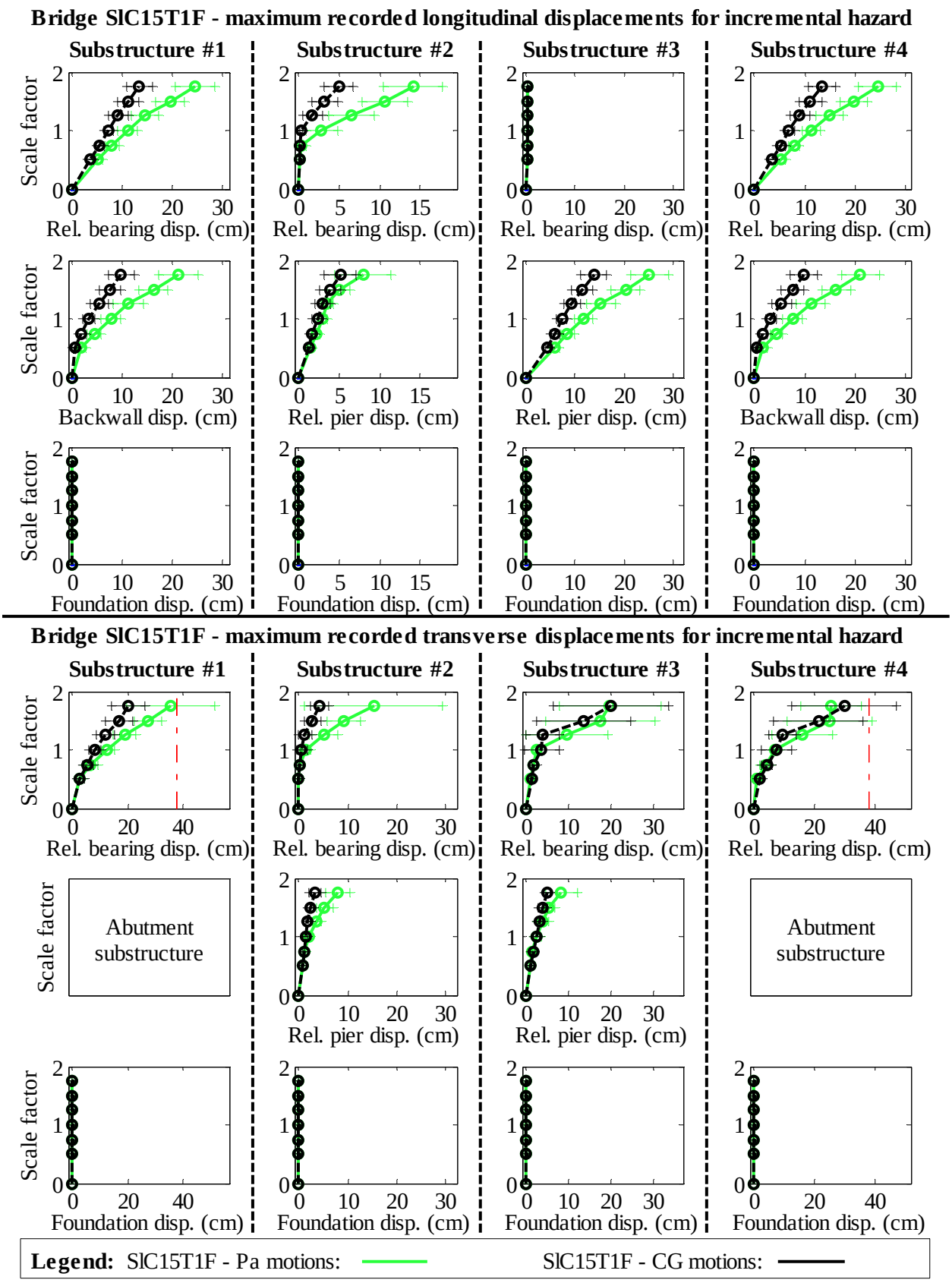

Figure B. 17(b) Bridge SlC15T1F - displacement results

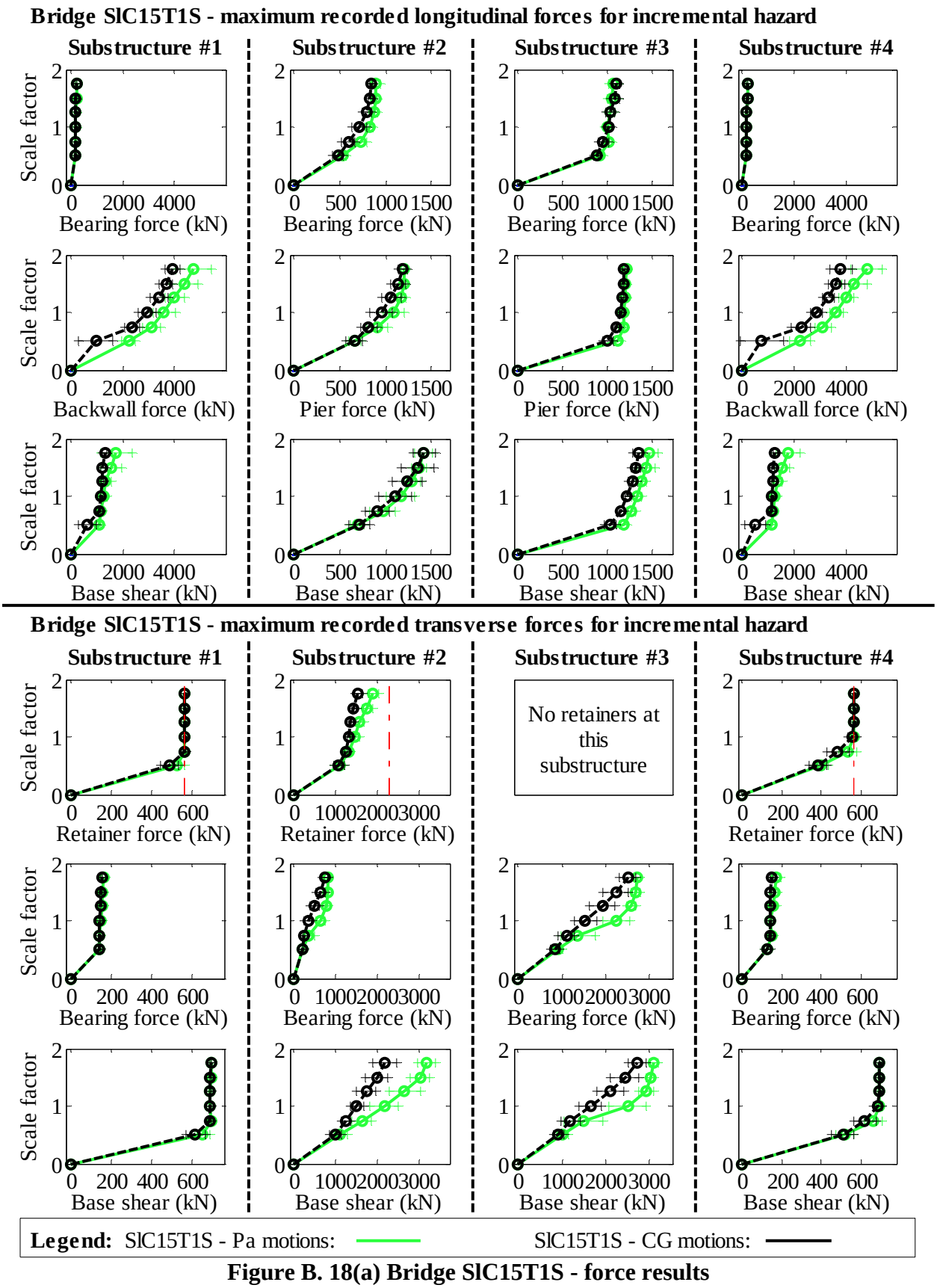

Figure B. 18(a) Bridge SlC15T1S - force results

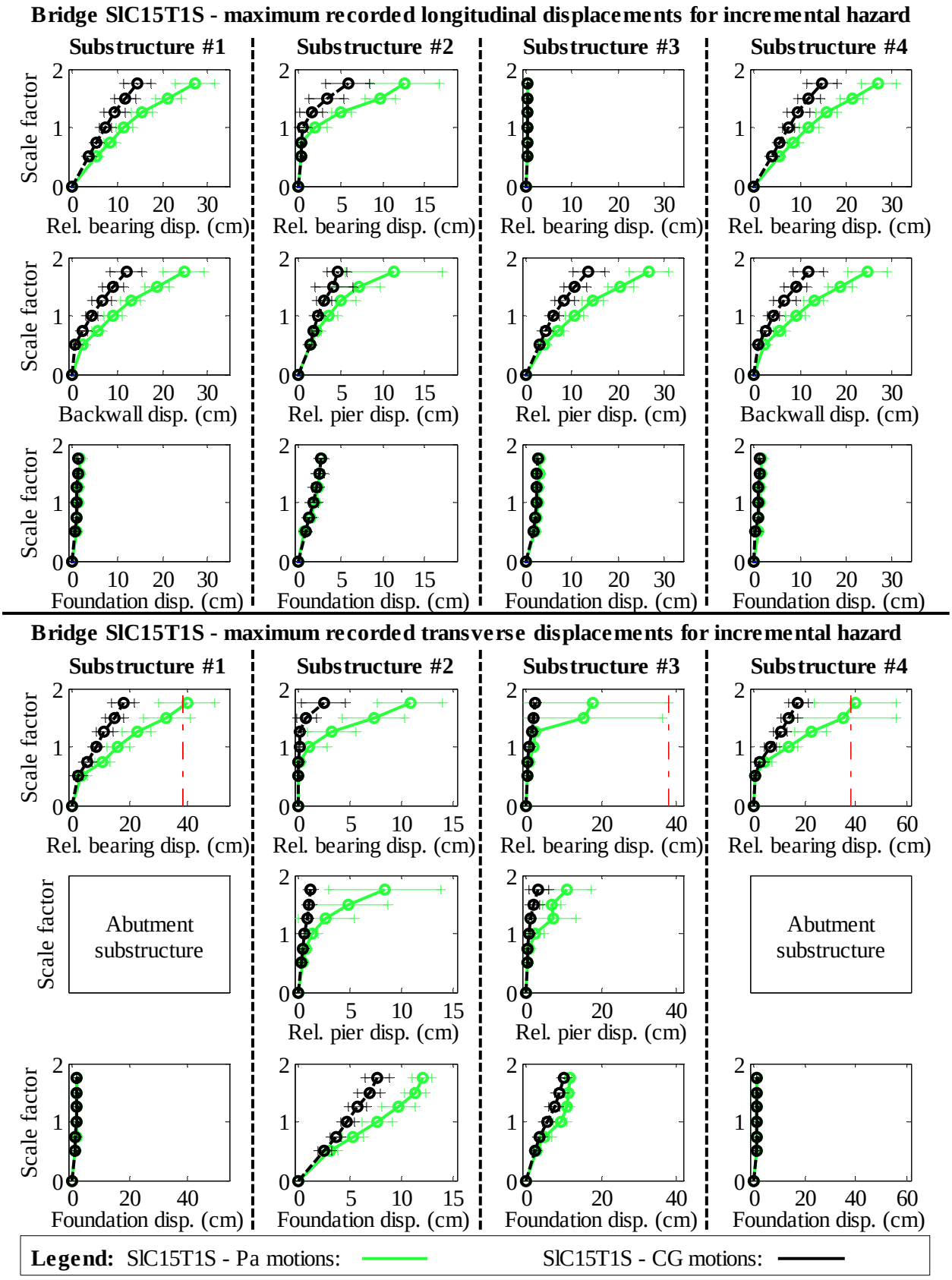

Figure B. 18(b) Bridge SlC15T1S - displacement results

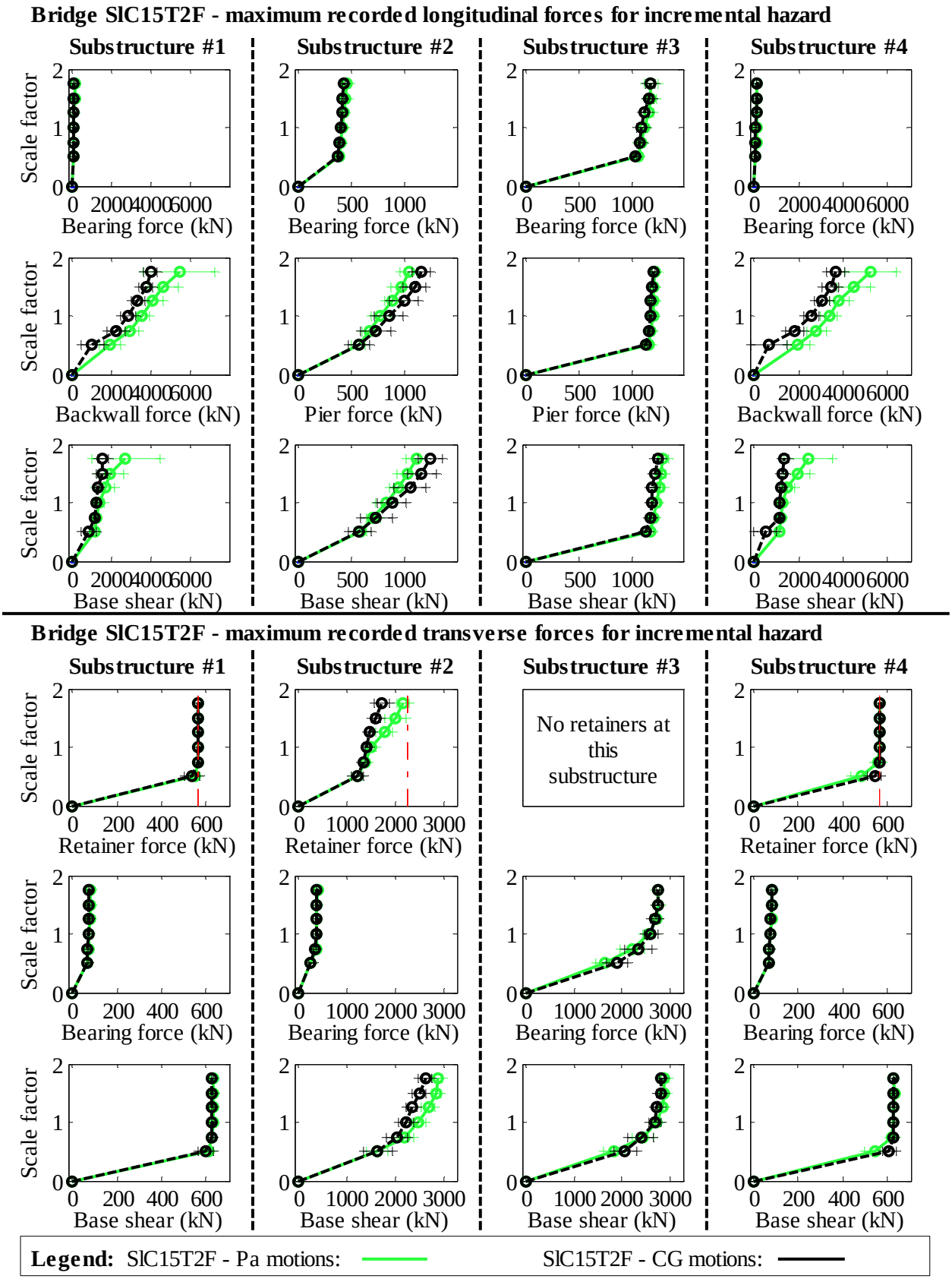

Figure B. 19(a) Bridge SlC15T2F - force results

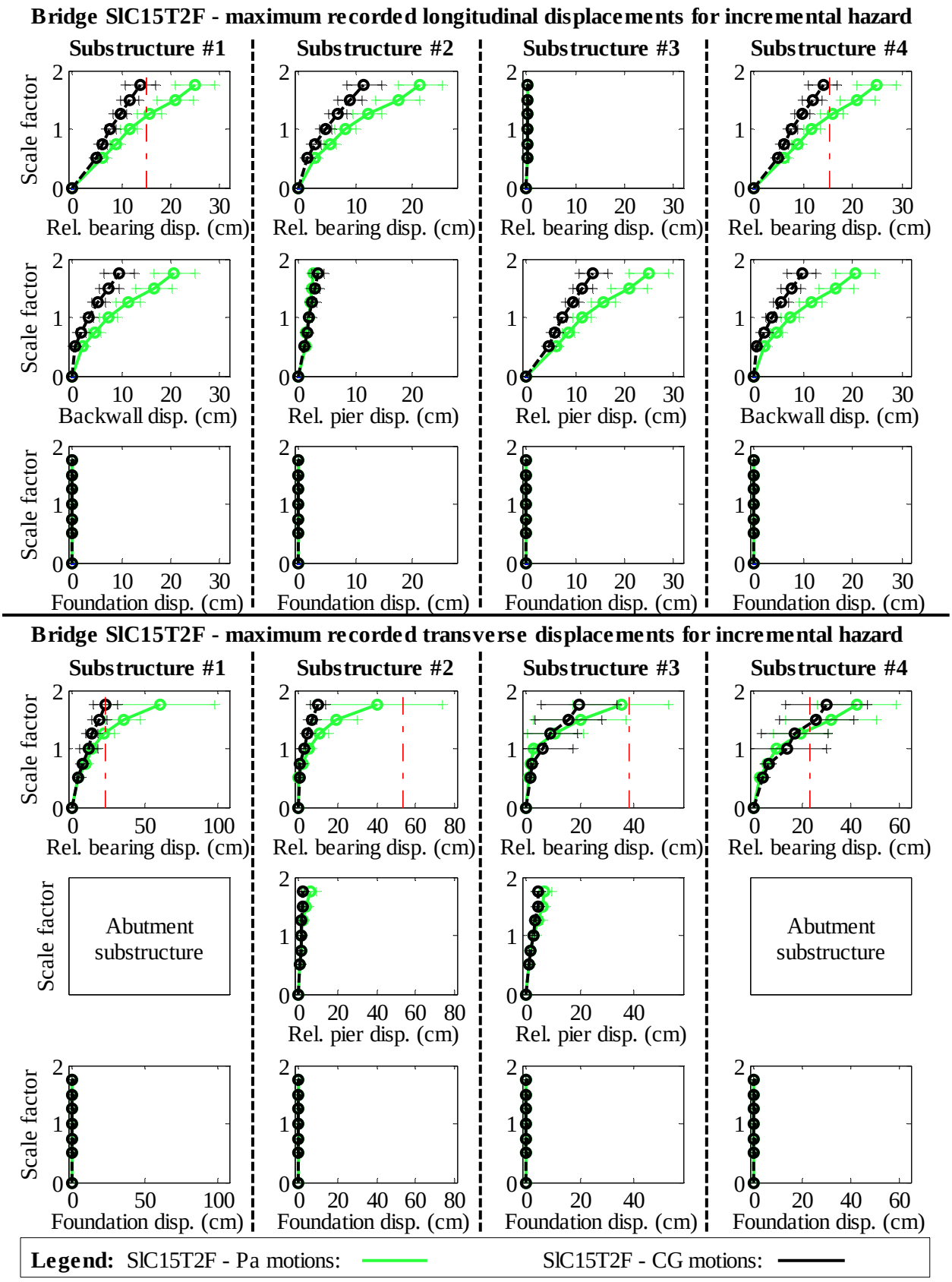

Figure B. 19(b) Bridge SlC15T2F - displacement results

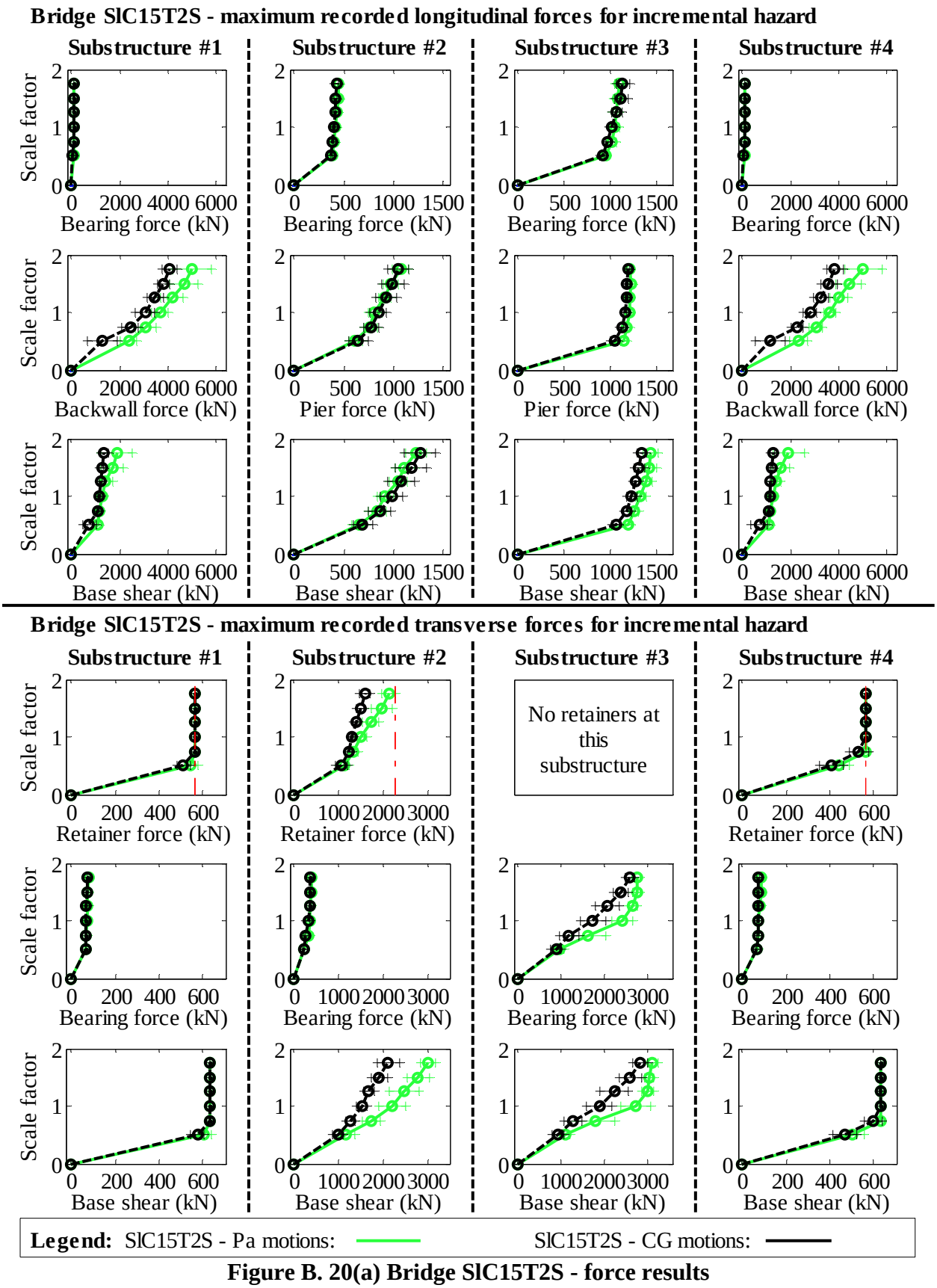

Figure B. 20(a) Bridge SlC15T2S - force results

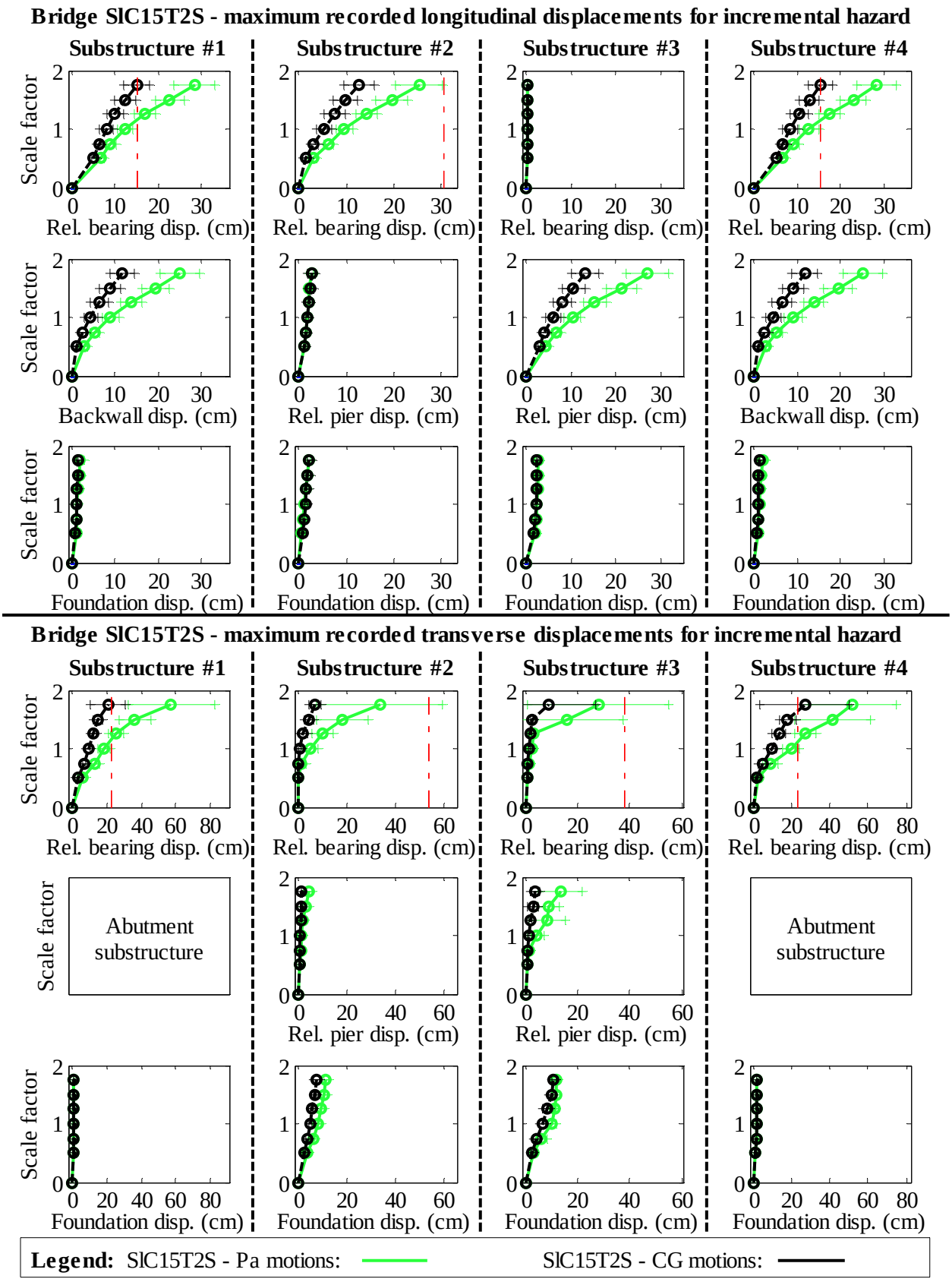

Figure B. 20(b) Bridge SlC15T2S - displacement results

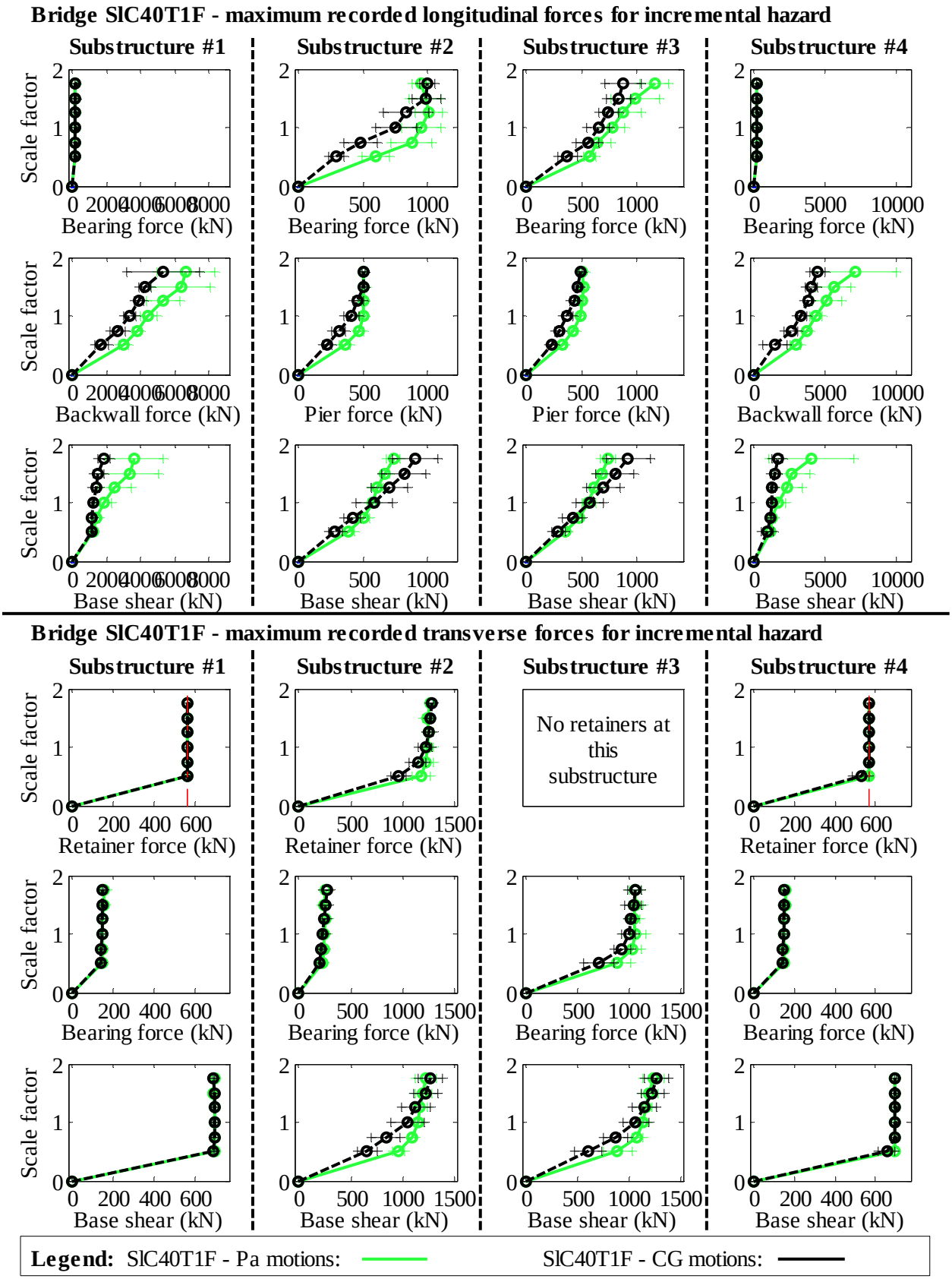

Figure B. 21(a) Bridge SlC40T1F - force results

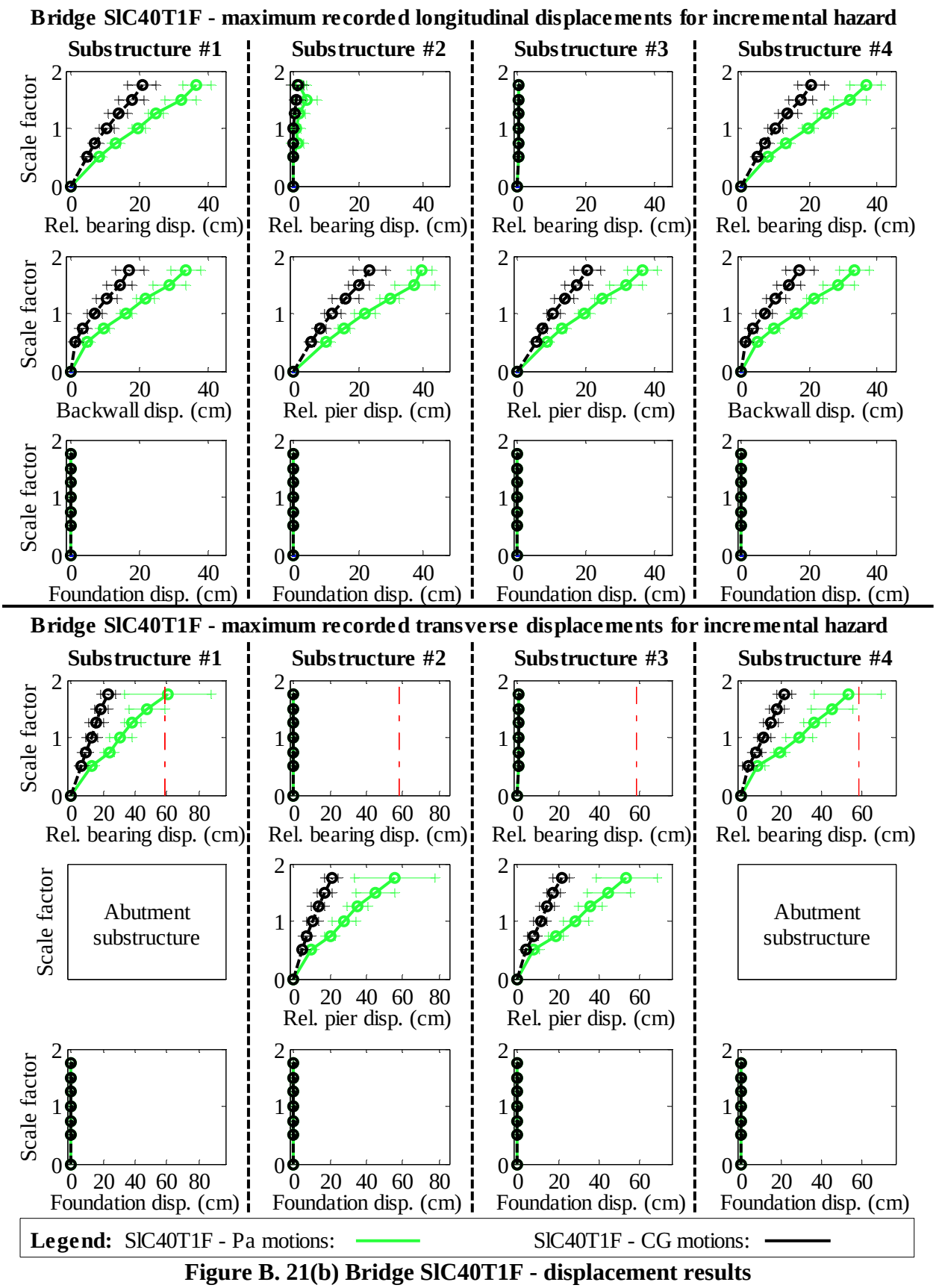

Figure B. 21(b) Bridge SlC40T1F - displacement results

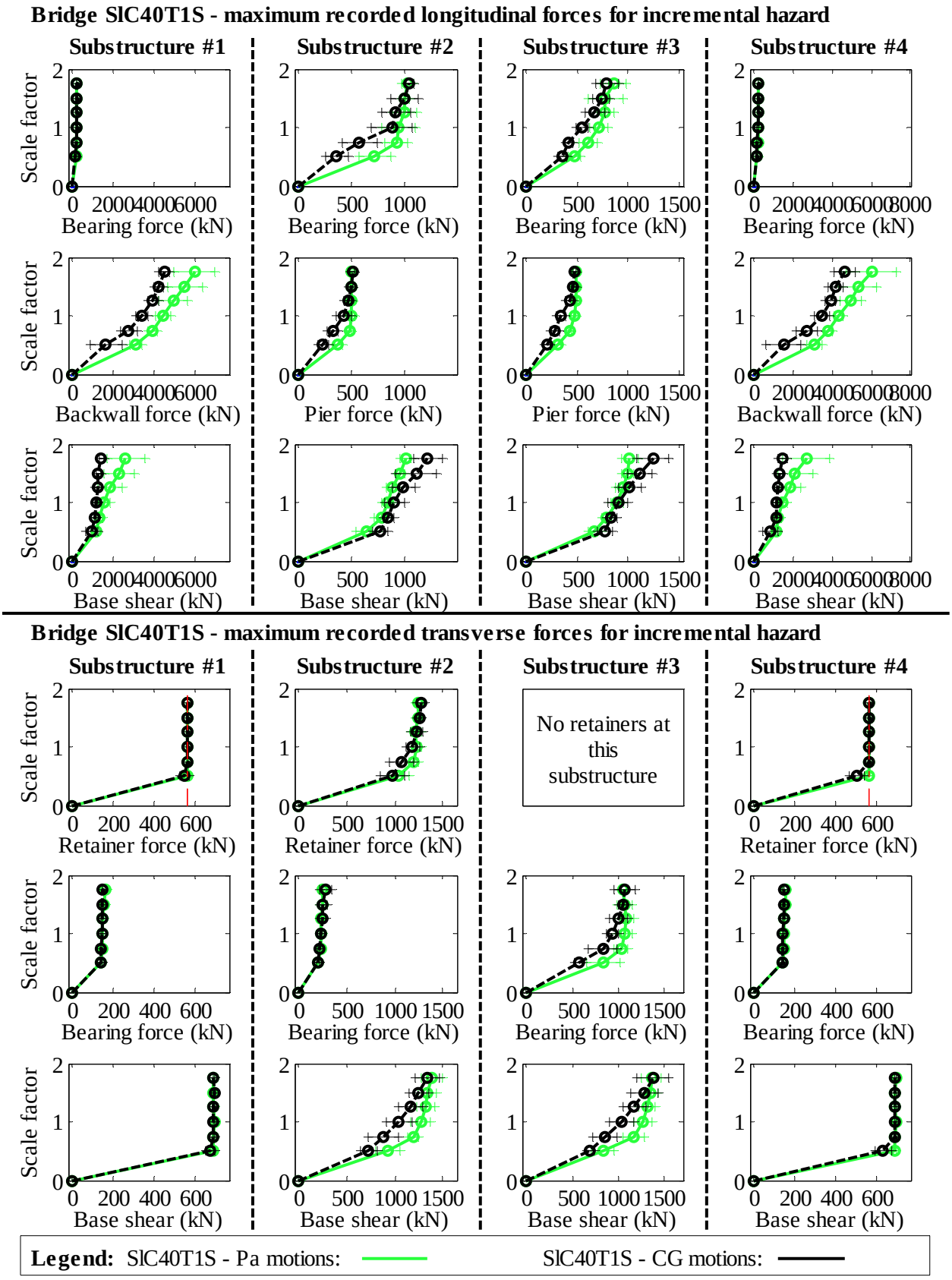

Figure B. 22(a) Bridge SlC40T1S - force results

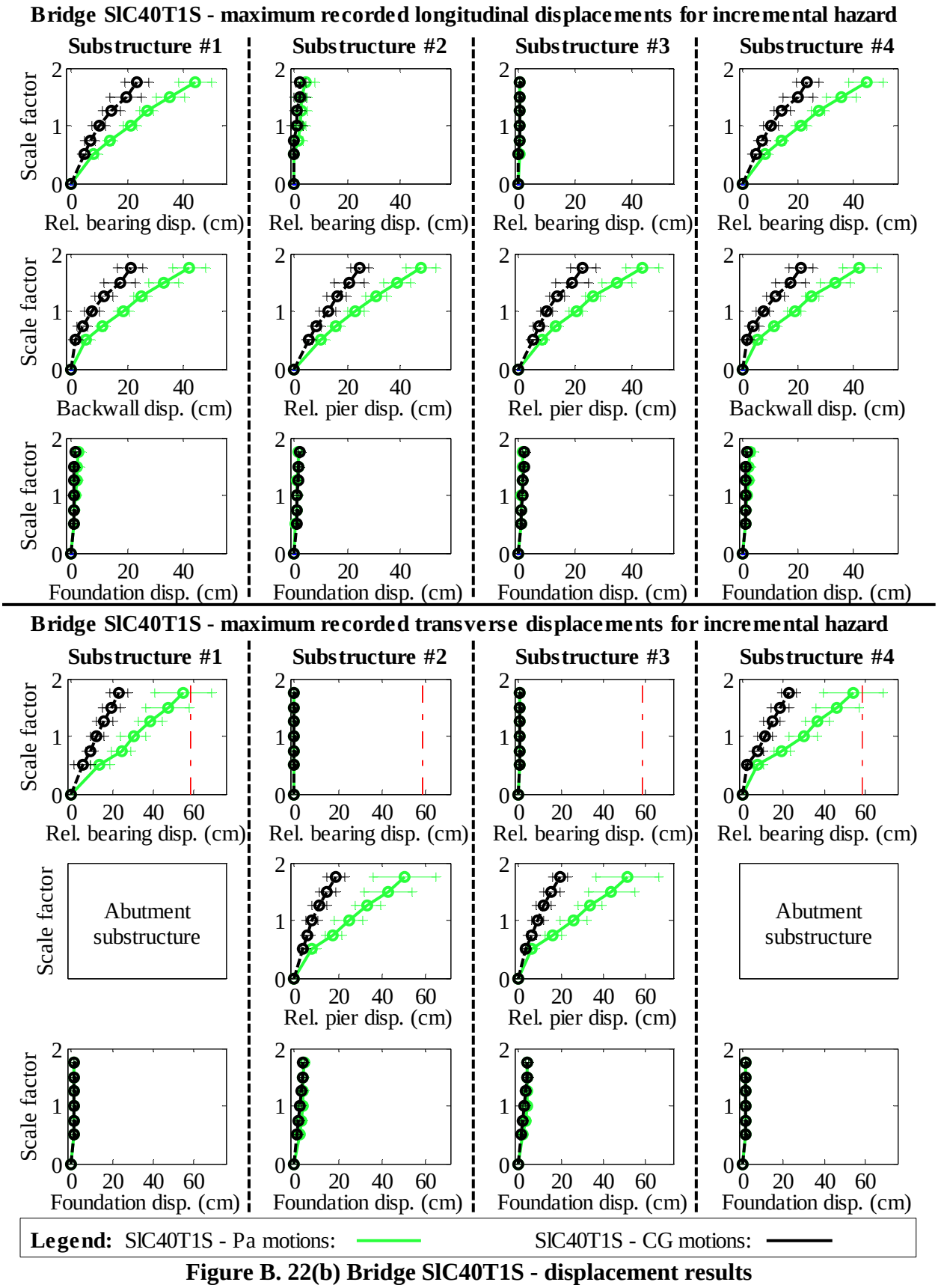

Figure B. 22(b) Bridge SlC40T1S - displacement results

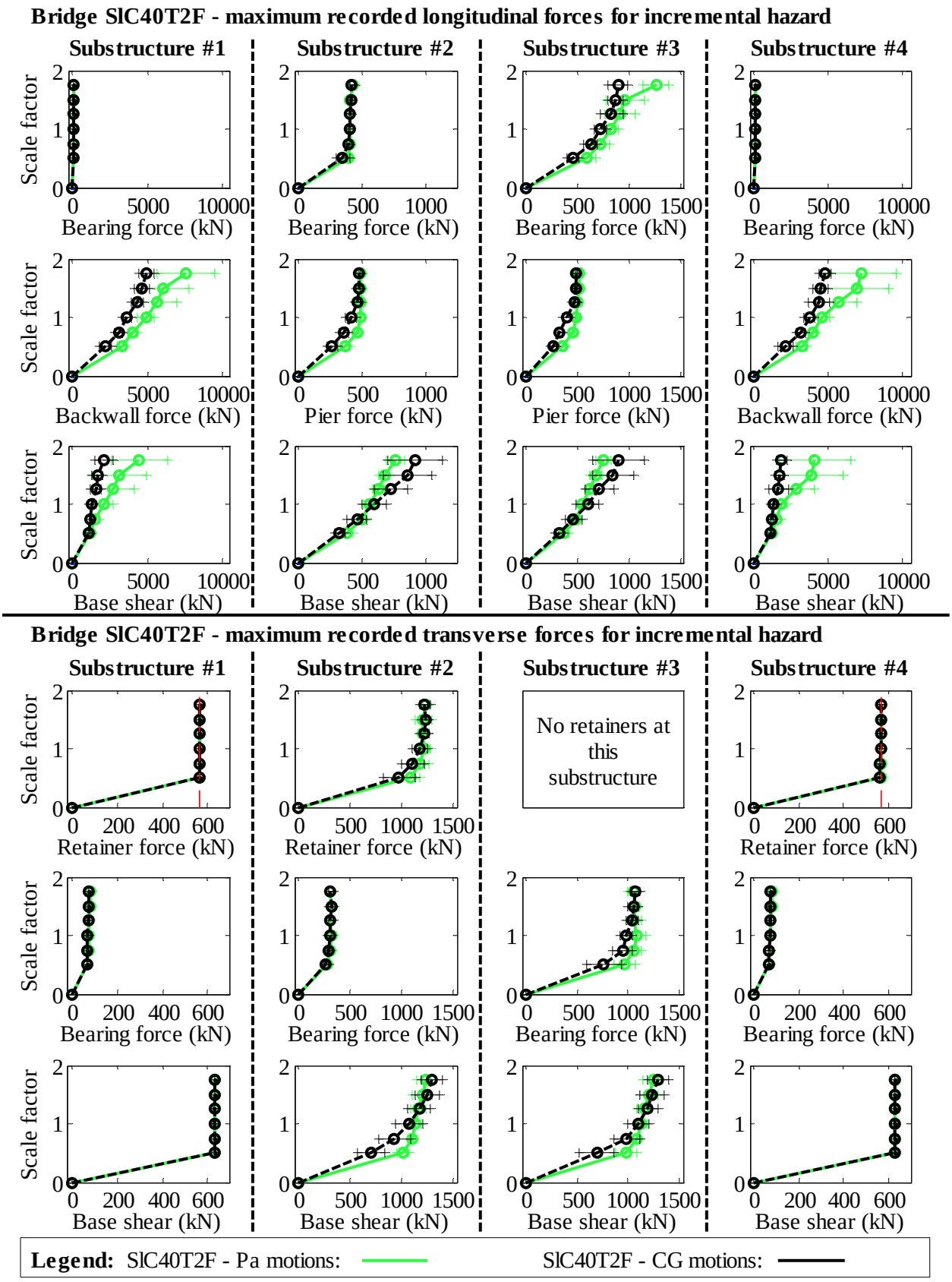

Figure B. 23(a) Bridge SlC40T2F - force results

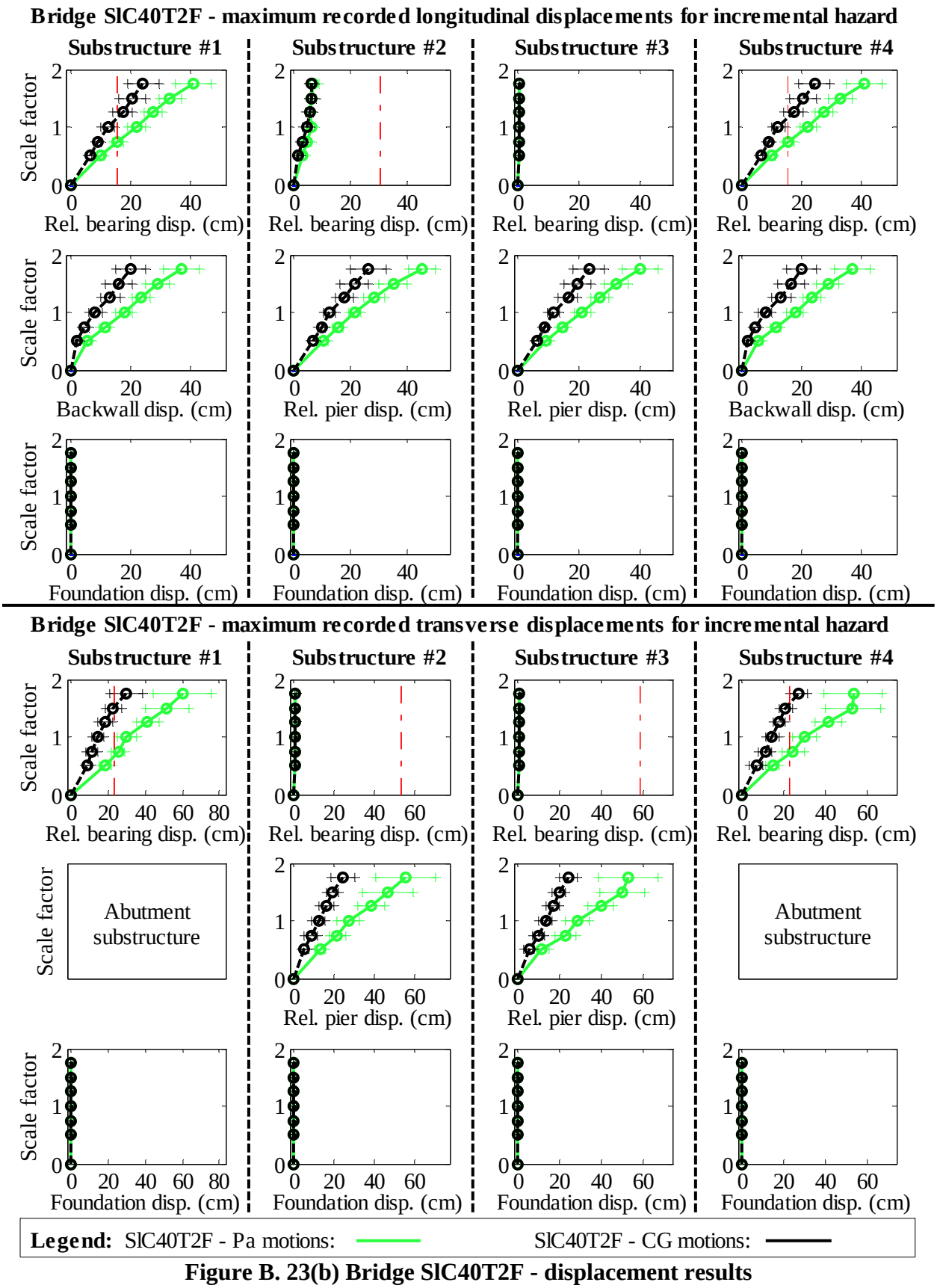

Figure B. 23(b) Bridge SlC40T2F - displacement results

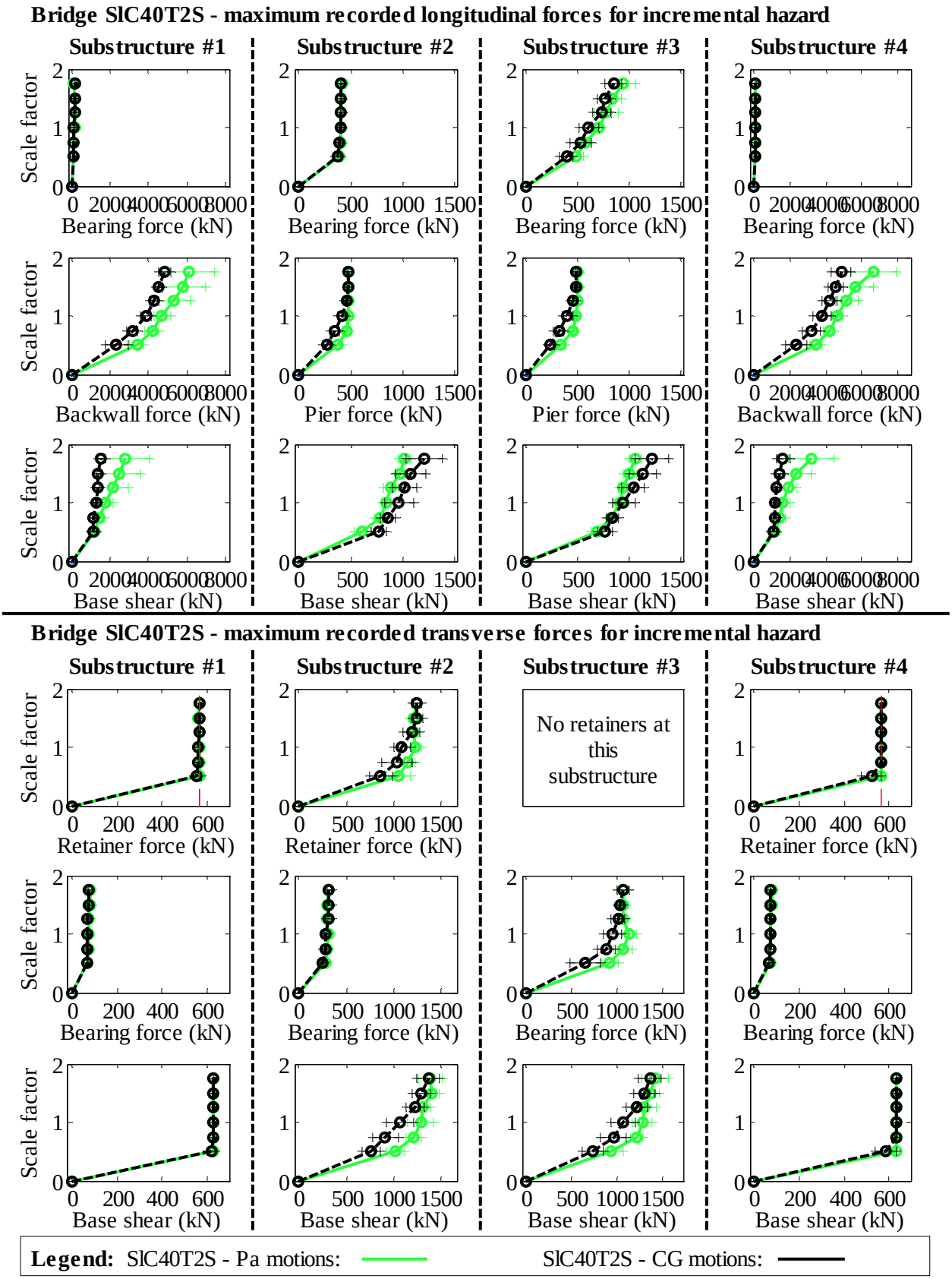

Figure B. 24(a) Bridge SlC40T2S - force results

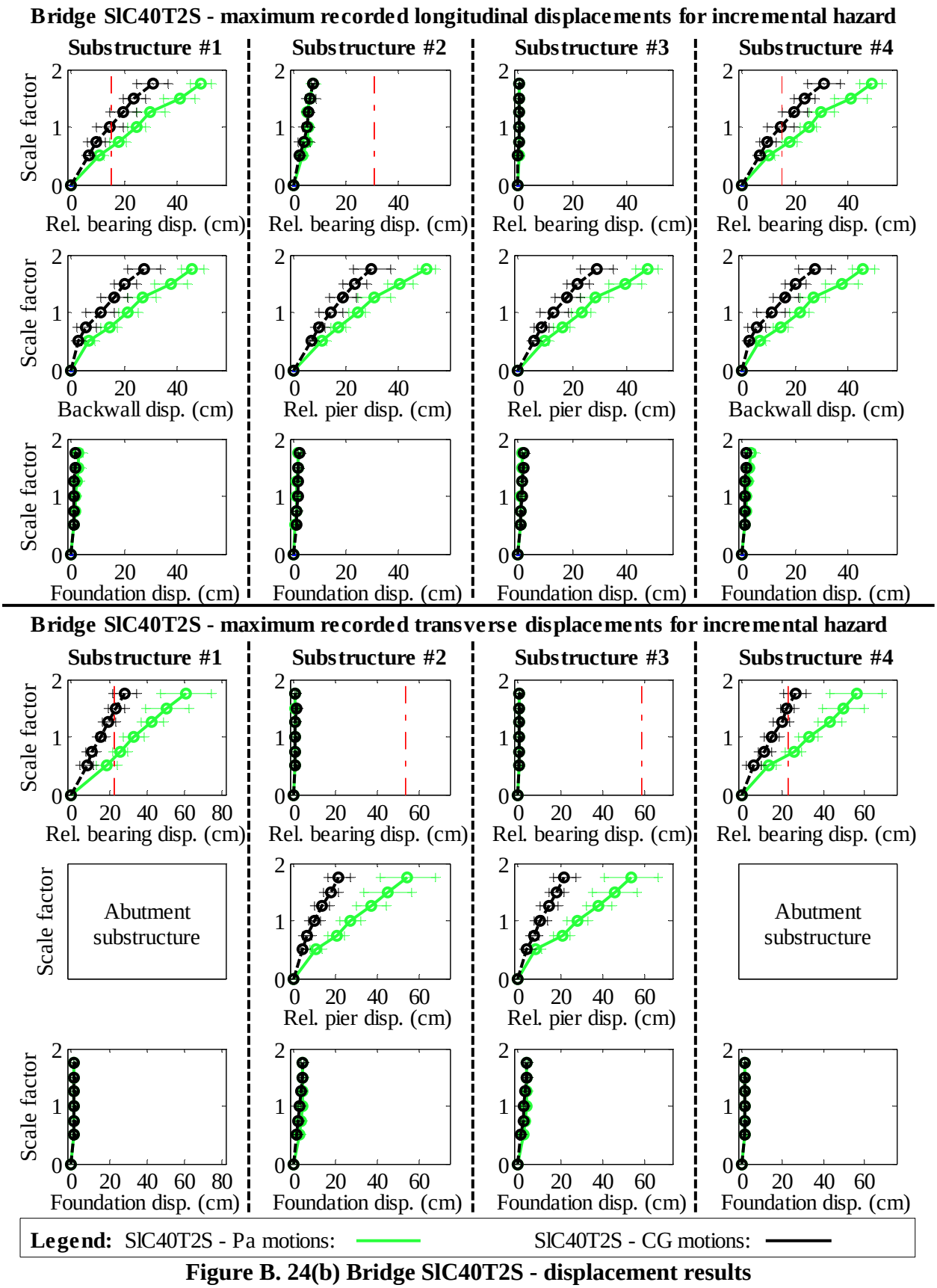

Figure B. 24(b) Bridge SlC40T2S - displacement results

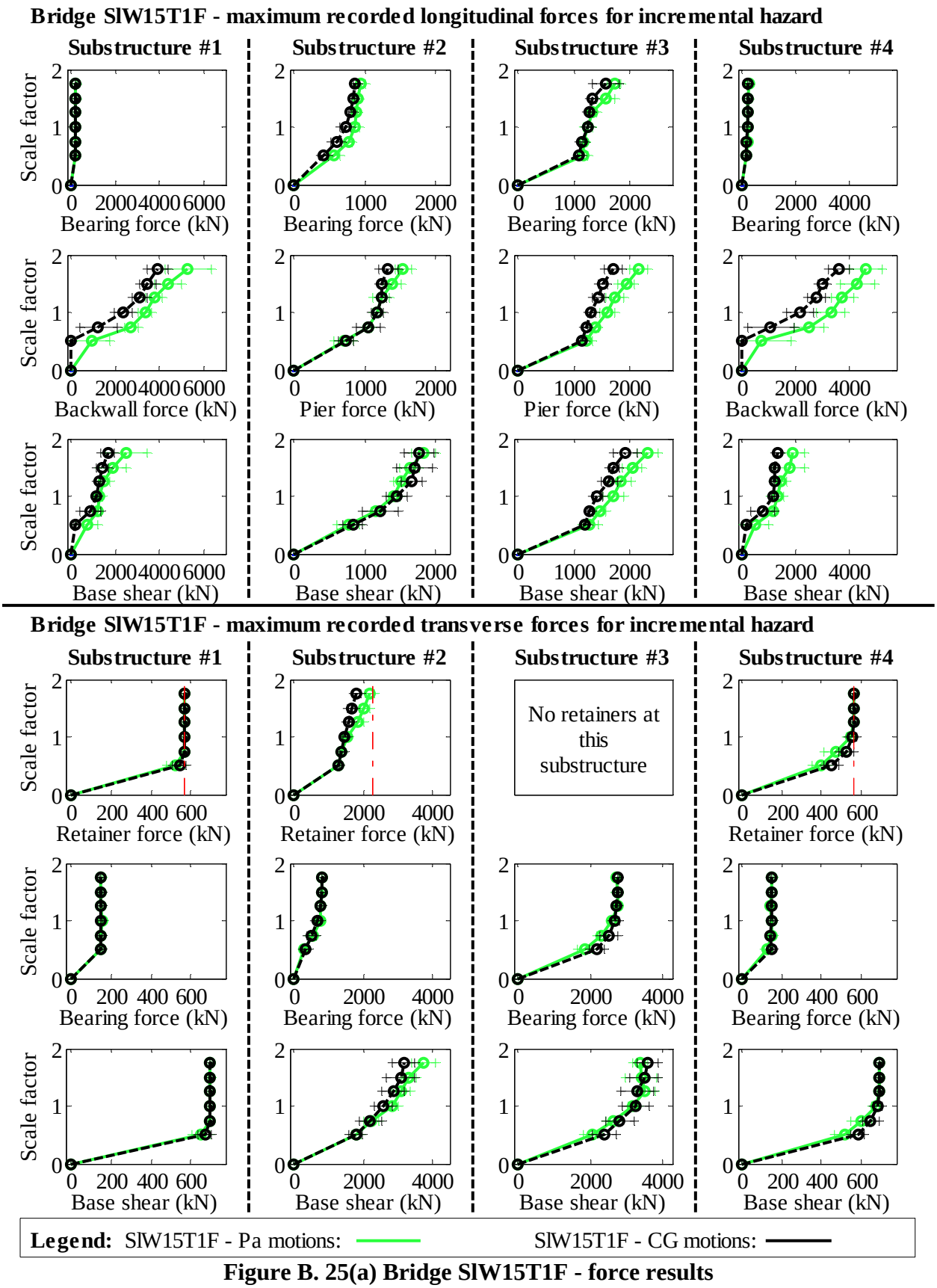

Figure B. 25(a) Bridge SlW15T1F - force results

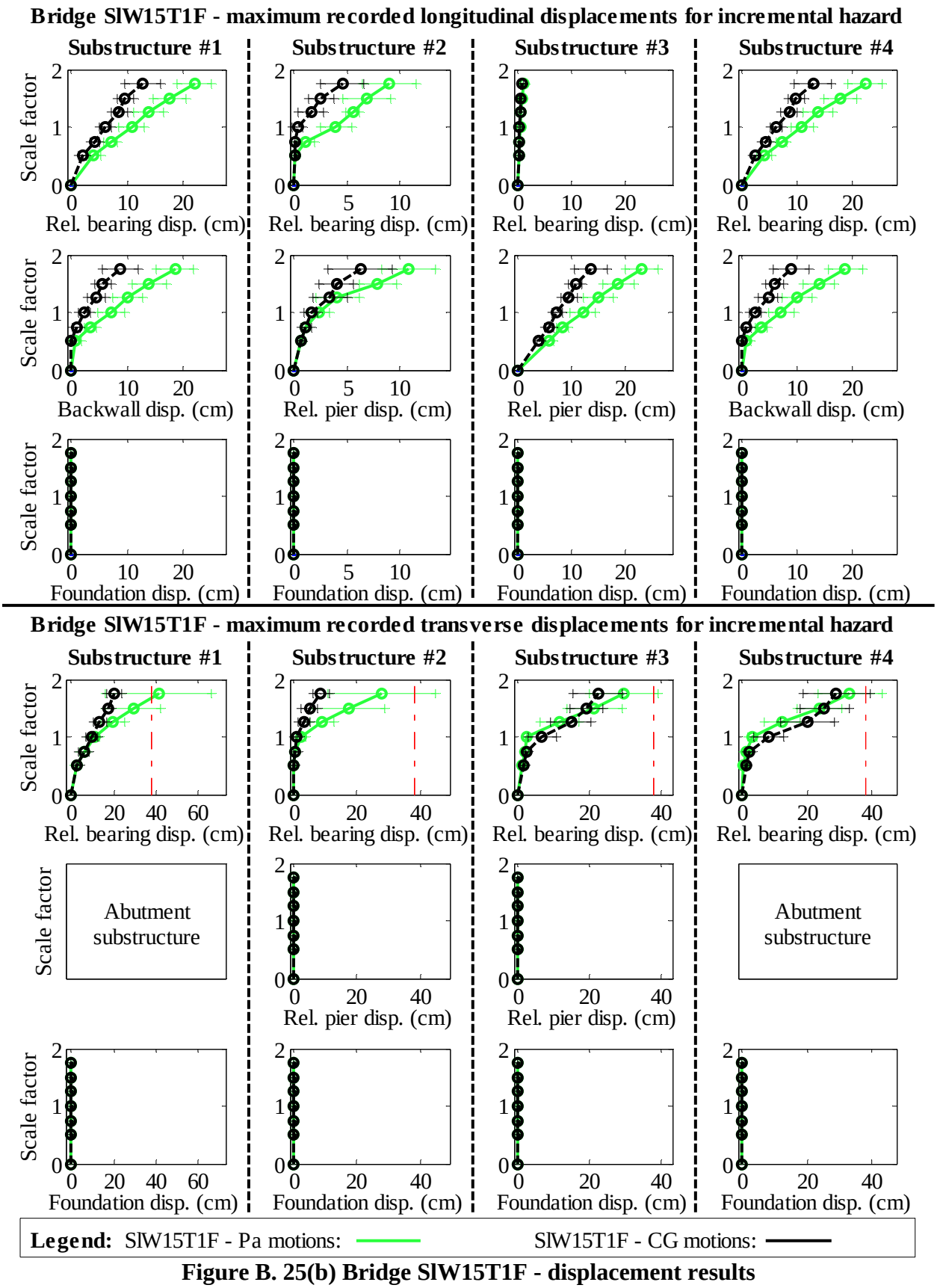

Figure B. 25(b) Bridge SlW15T1F - displacement results

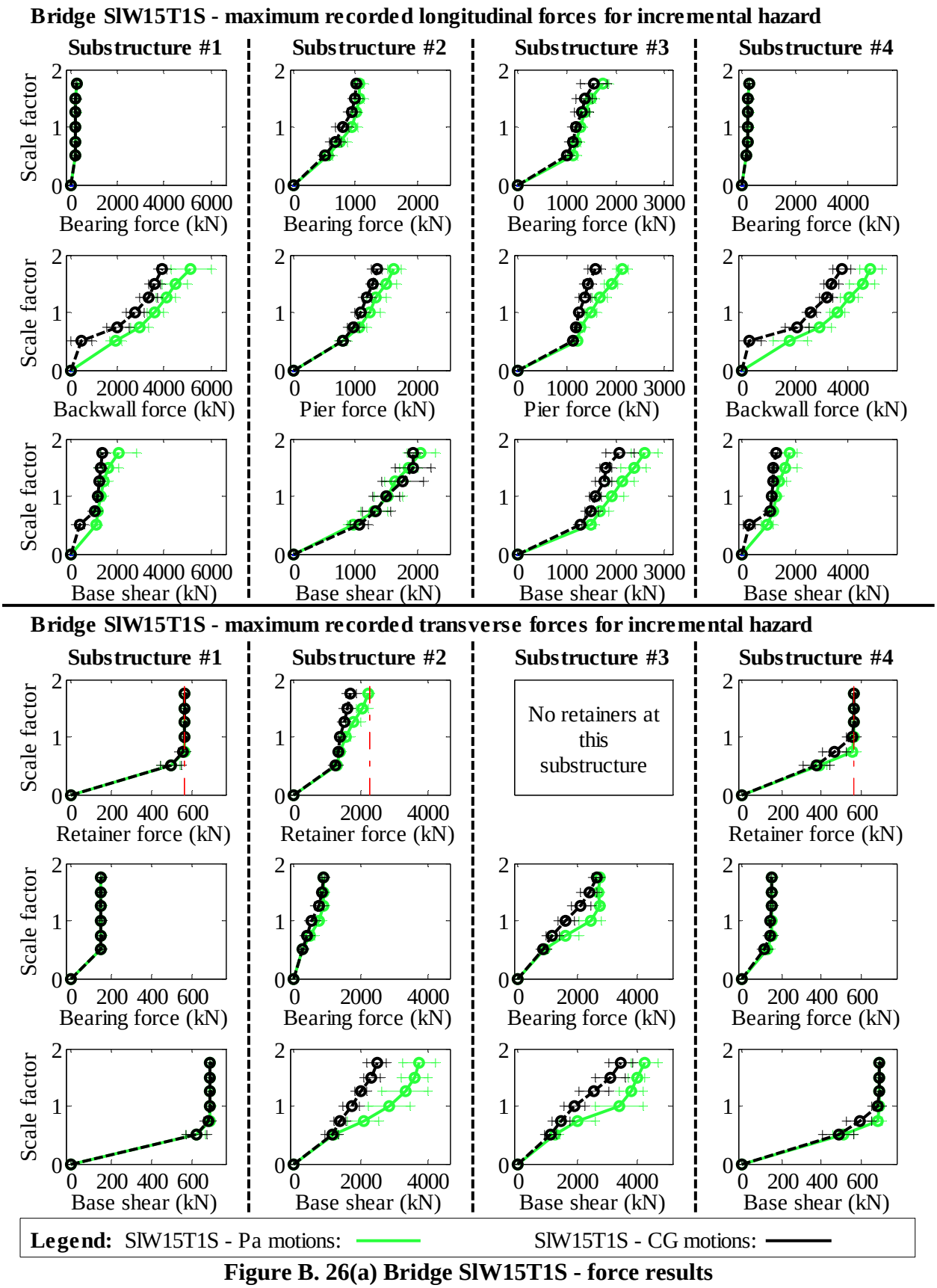

Figure B. 26(a) Bridge SlW15T1S - force results

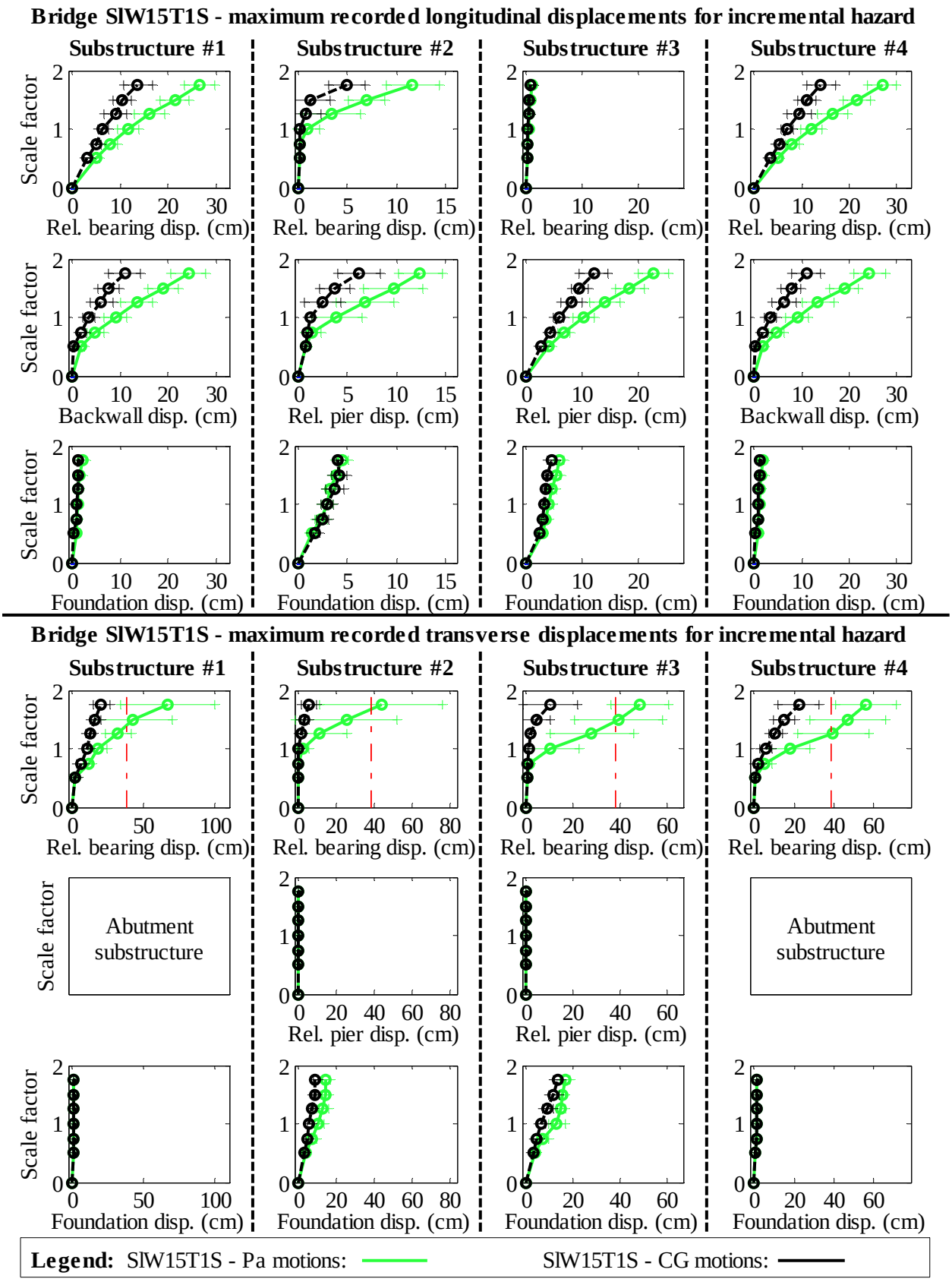

Figure B. 26(b) Bridge SlW15T1S - displacement results

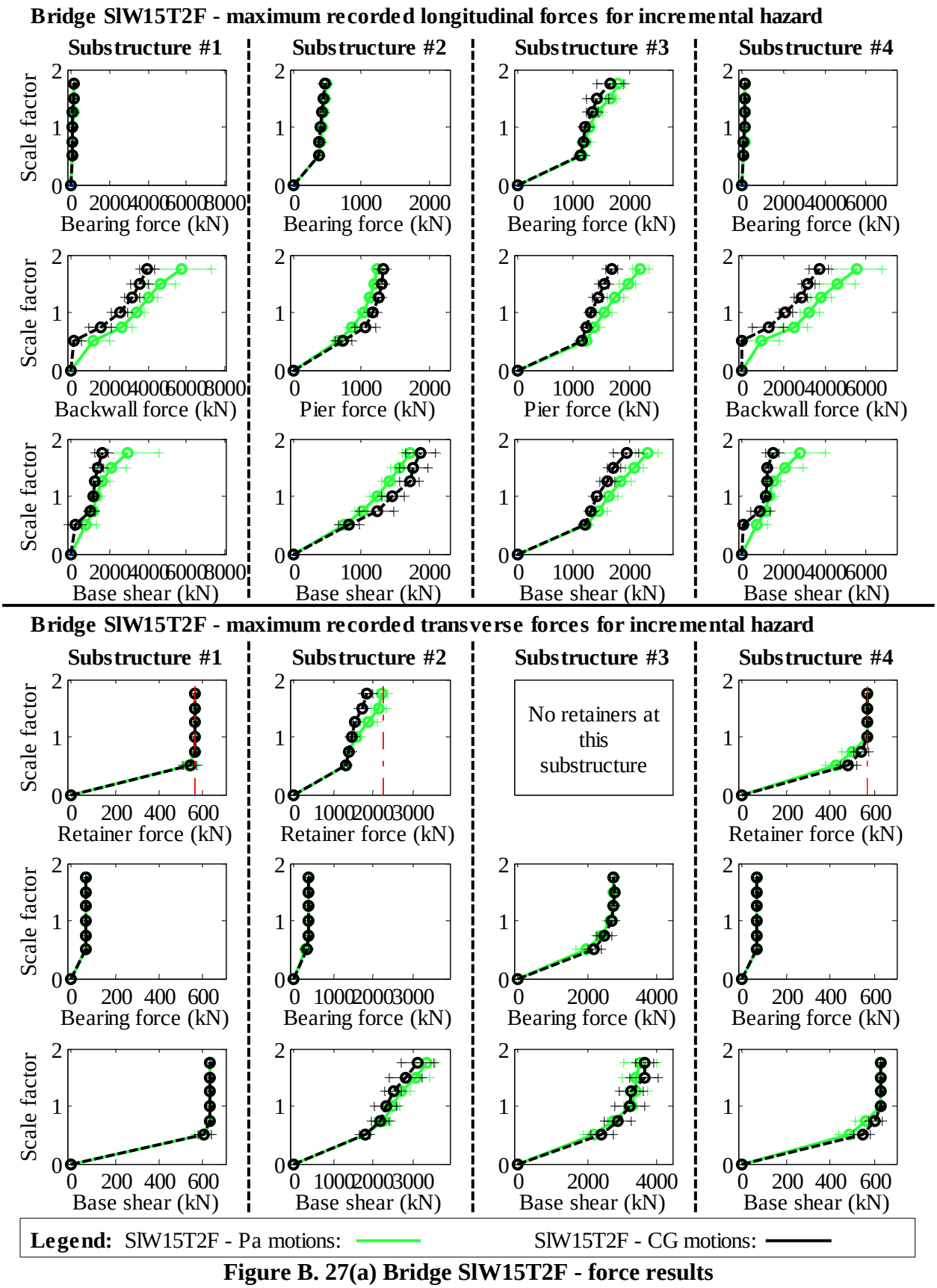

Figure B. 27(a) Bridge SlW15T2F - force results

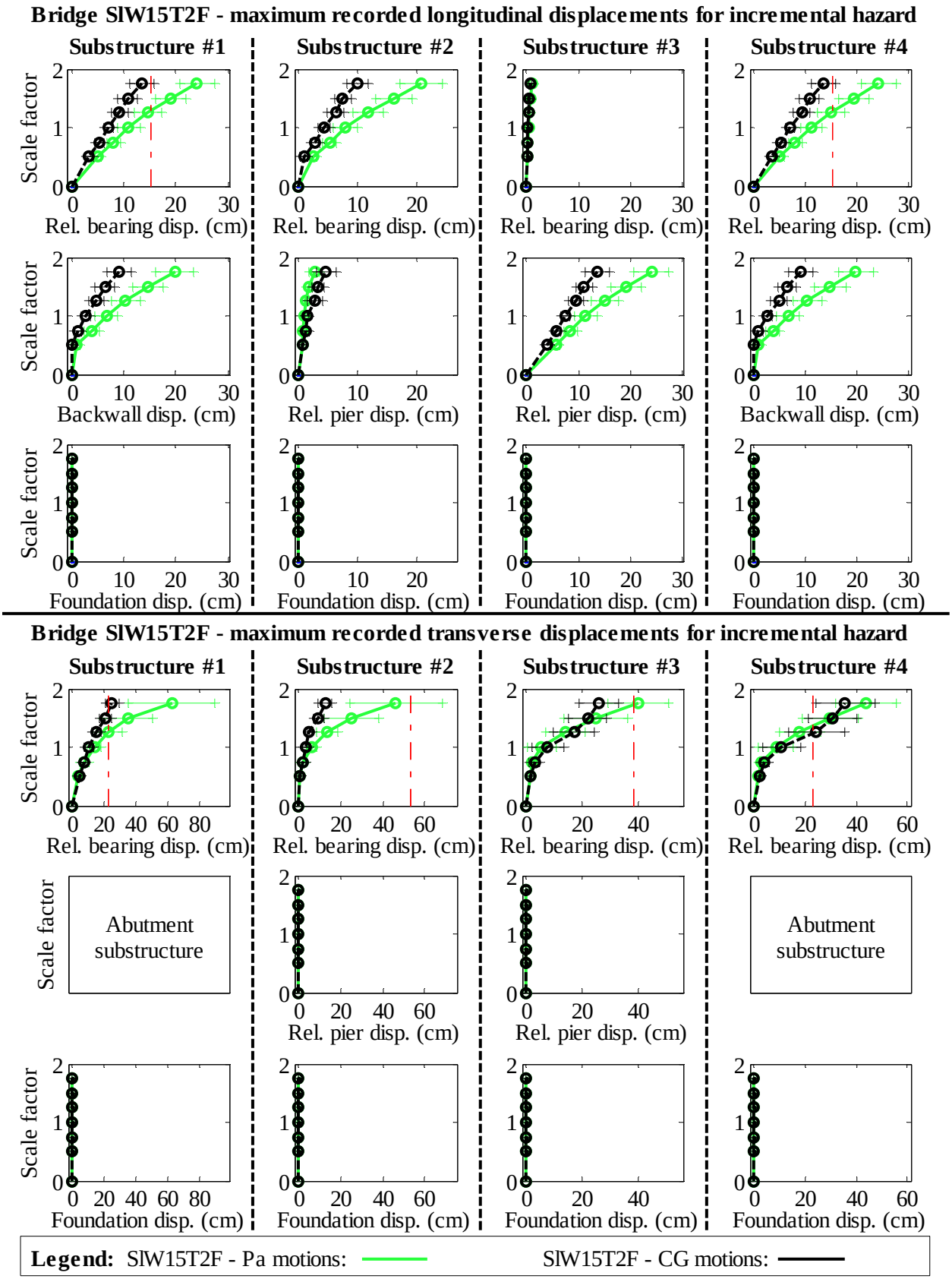

Figure B. 27(b) Bridge SlW15T2F - displacement results

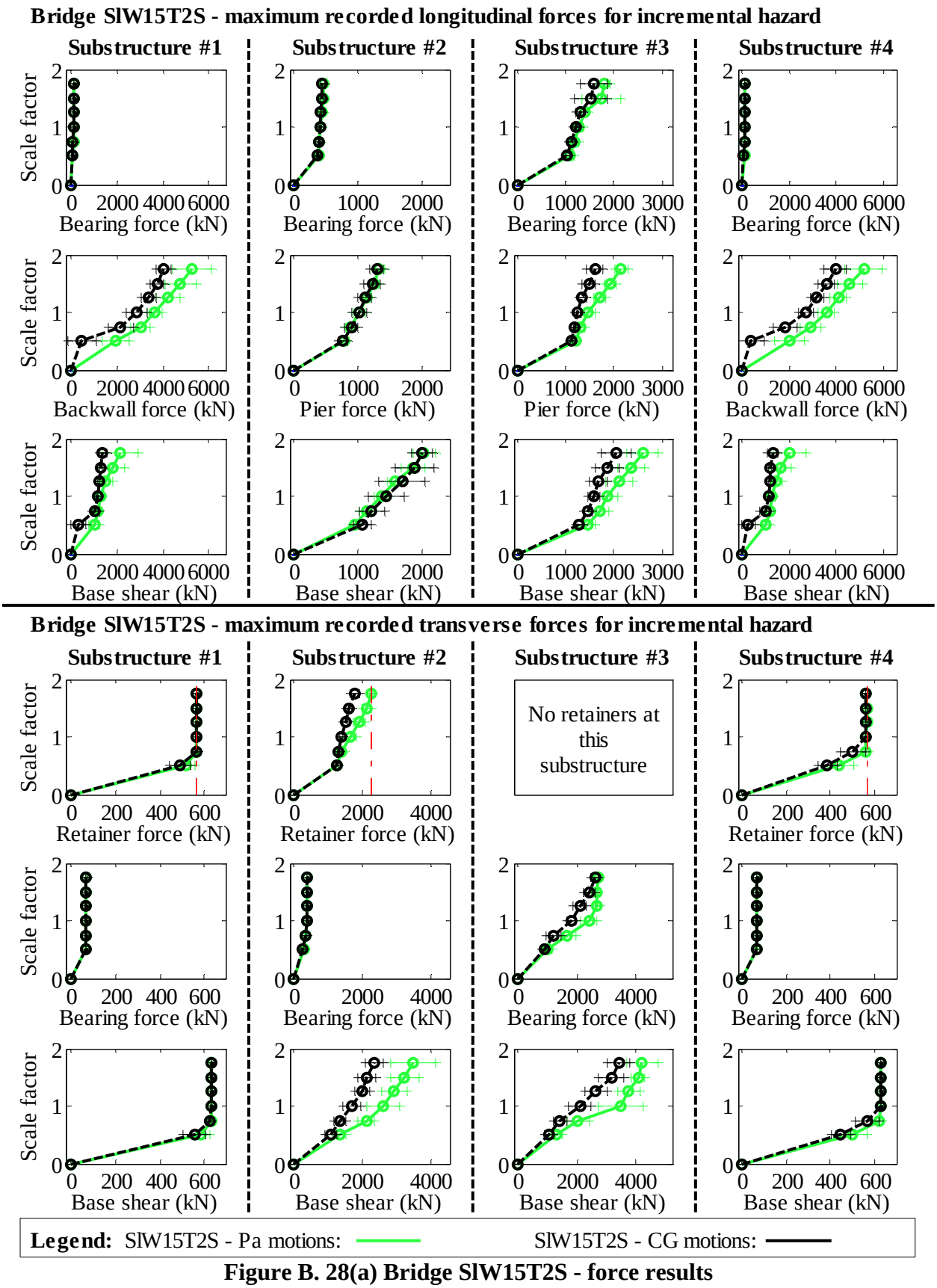

Figure B. 28(a) Bridge SlW15T2S - force results

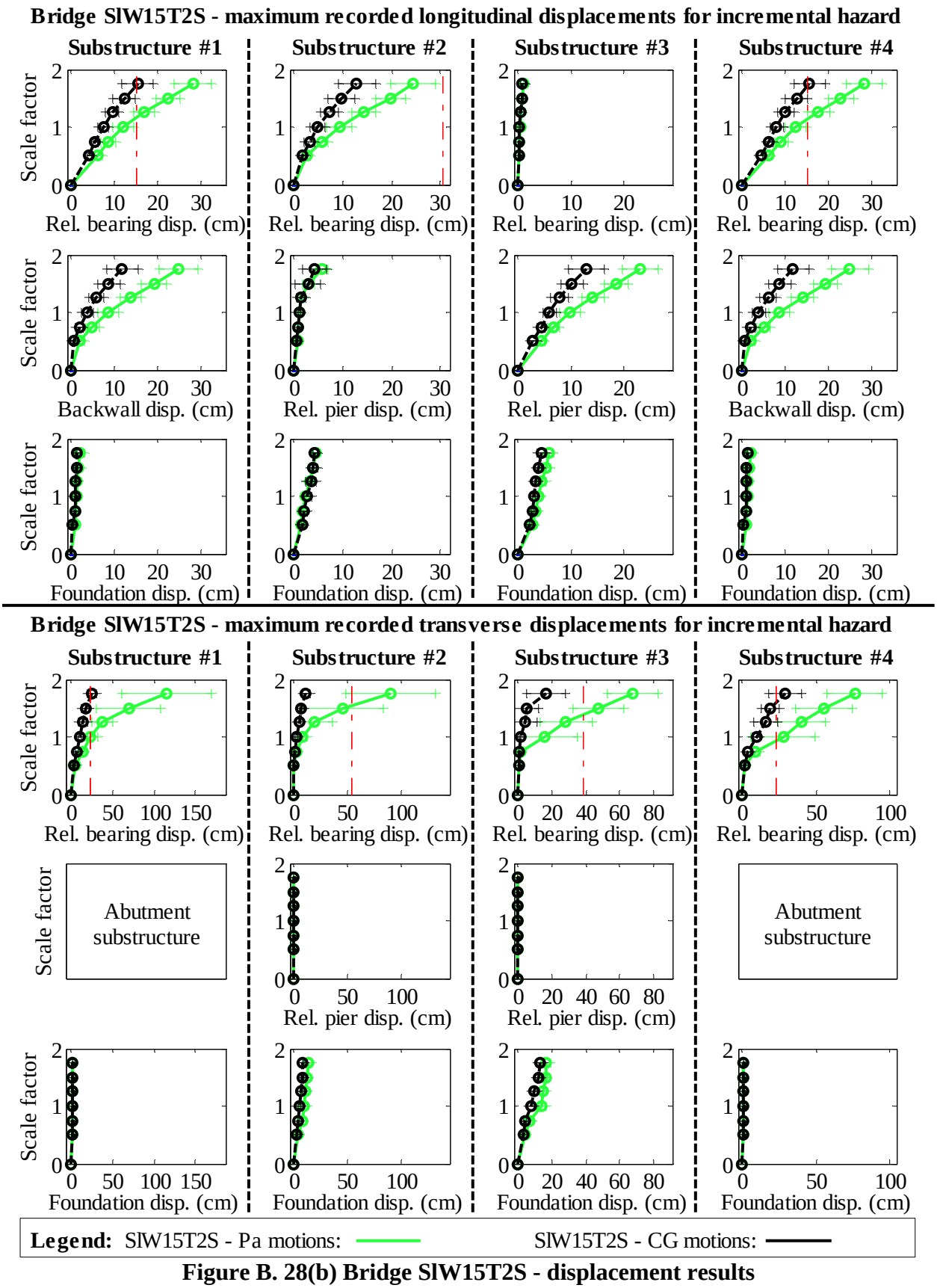

Figure B. 28(b) Bridge SlW15T2S - displacement results

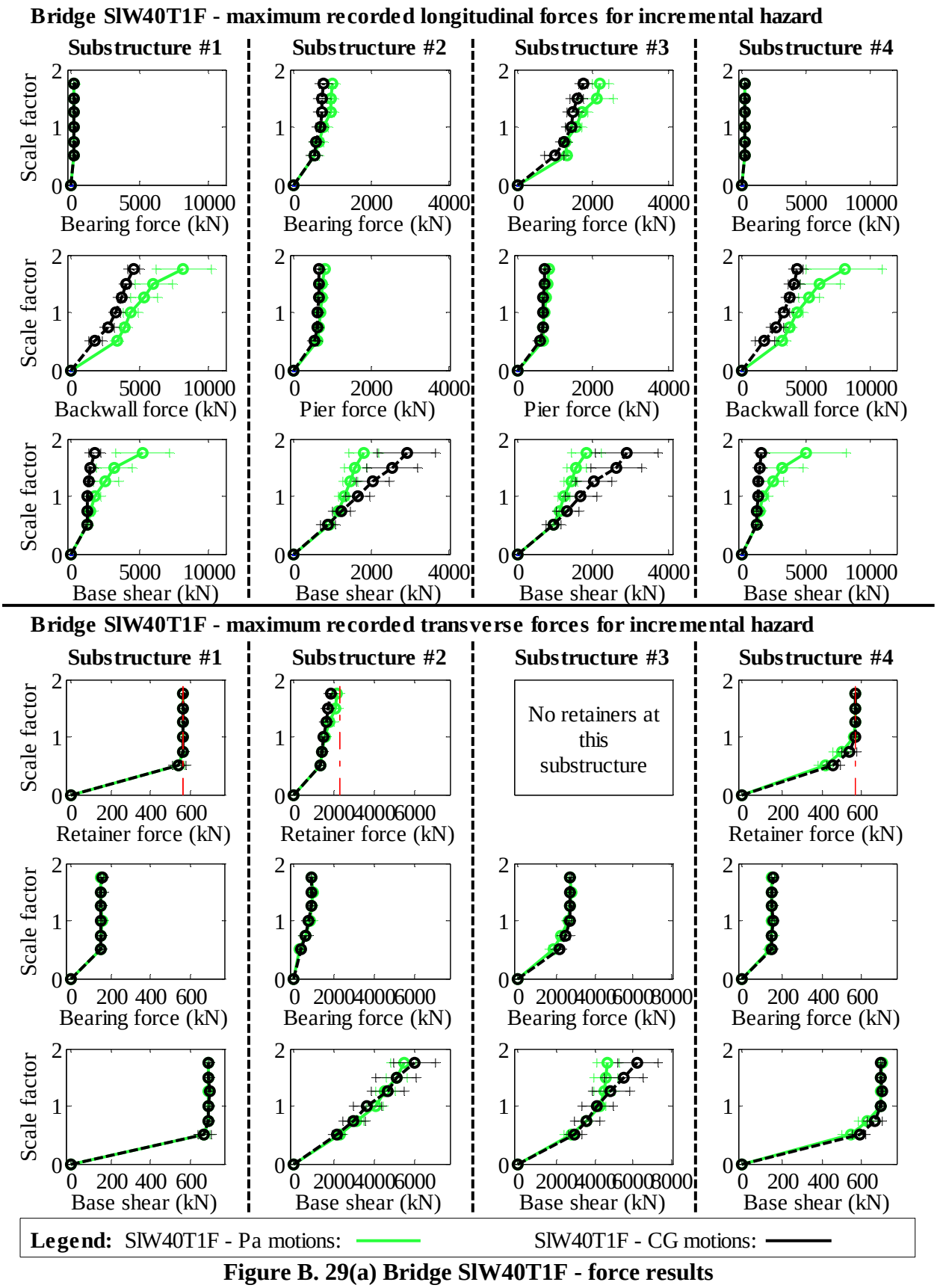

Figure B. 29(a) Bridge SlW40T1F - force results

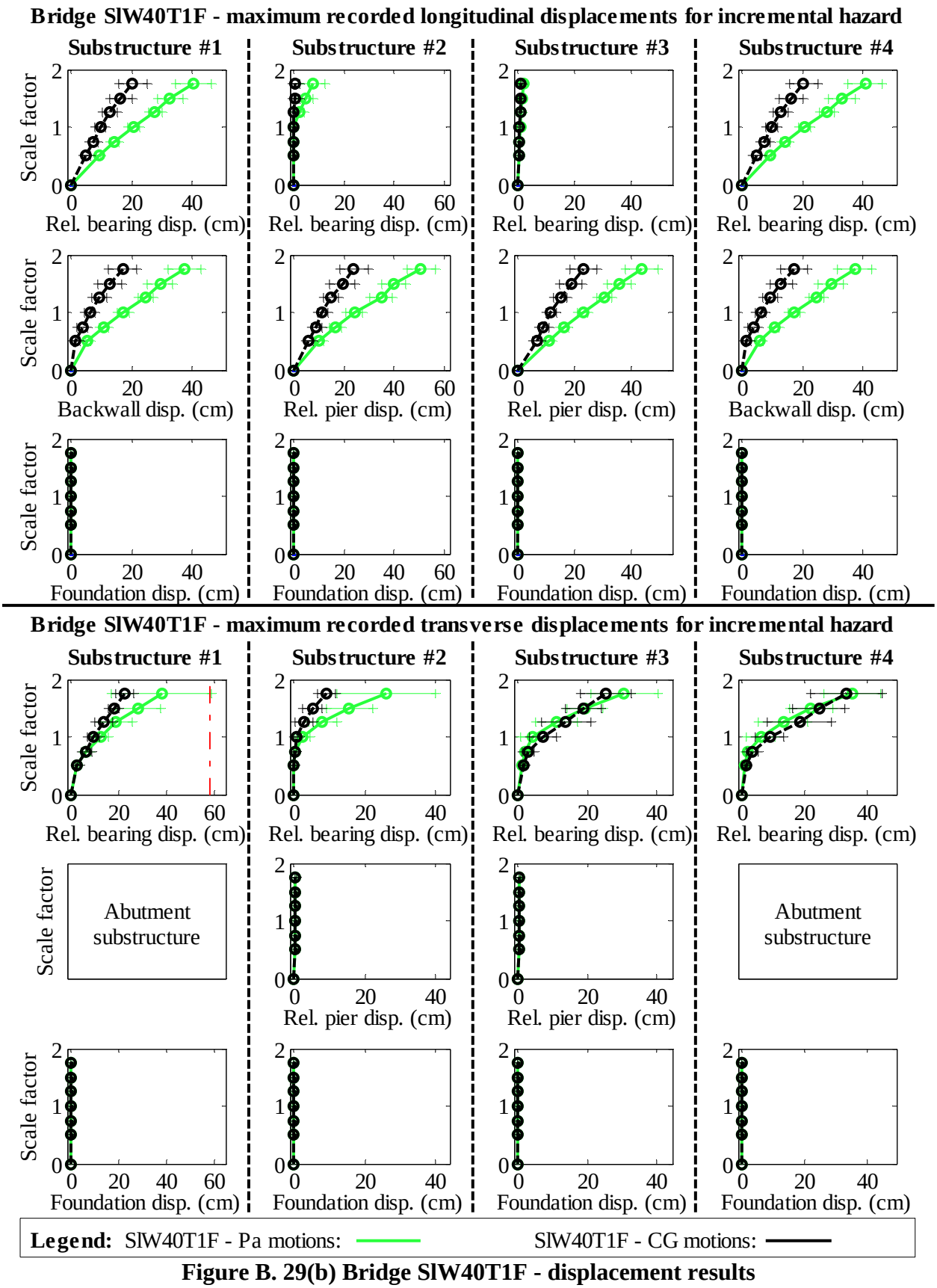

Figure B. 29(b) Bridge SlW40T1F - displacement results

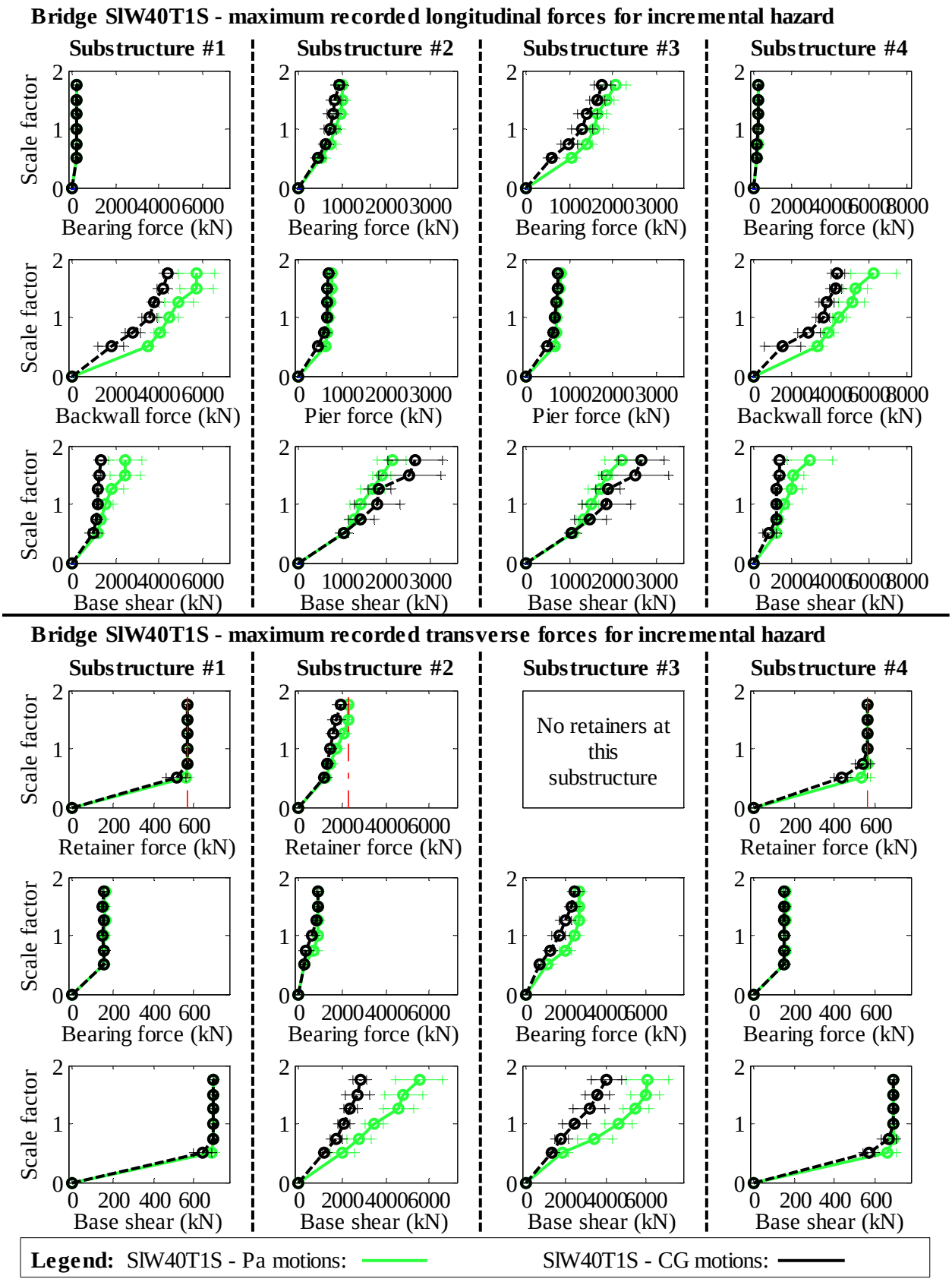

Figure B. 30(a) Bridge SlW40T1S - force results

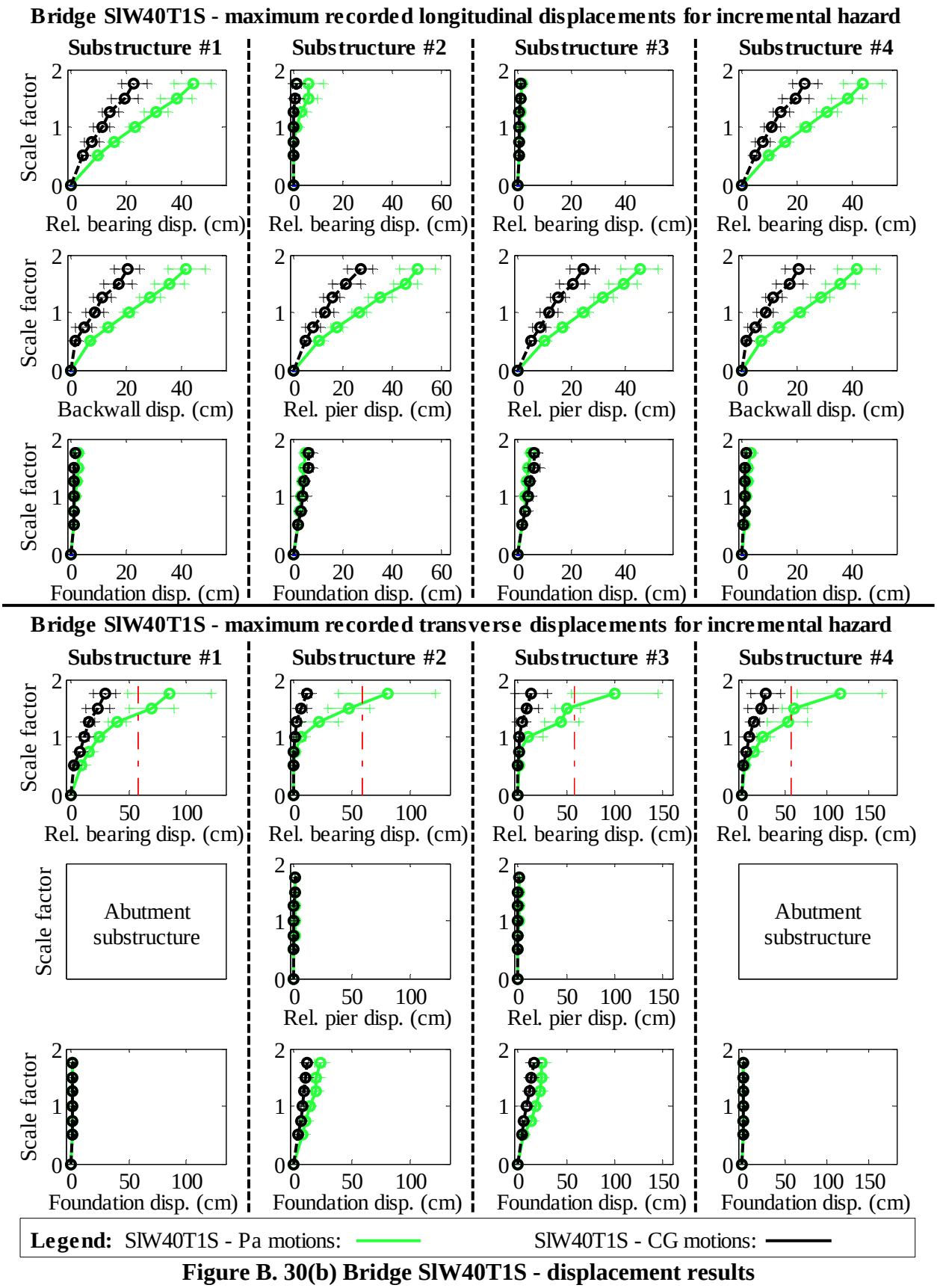

Figure B. 30(b) Bridge SlW40T1S - displacement results

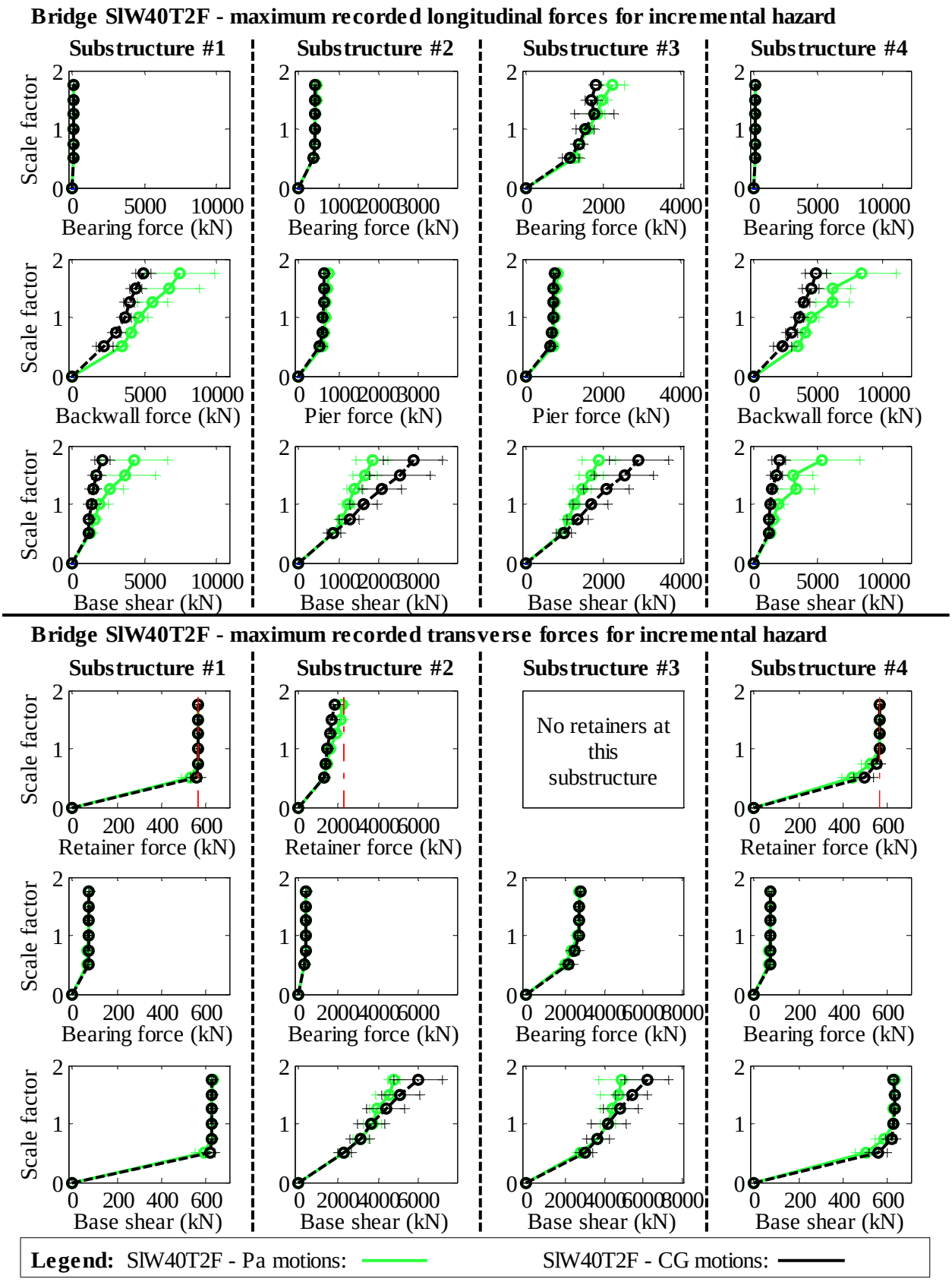

Figure B. 31(a) Bridge SlW40T2F - force results

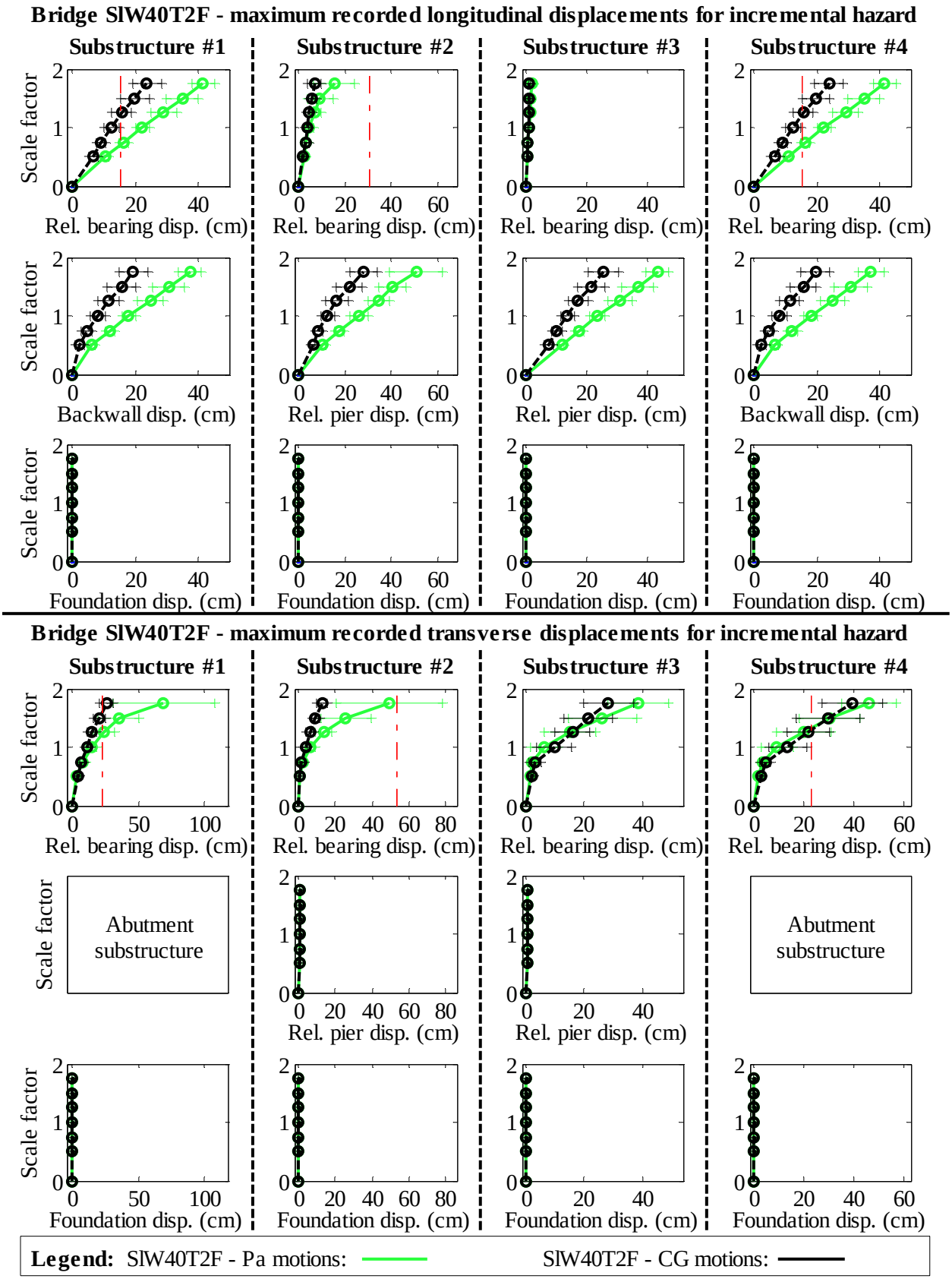

Figure B. 31(b) Bridge SlW40T2F - displacement results

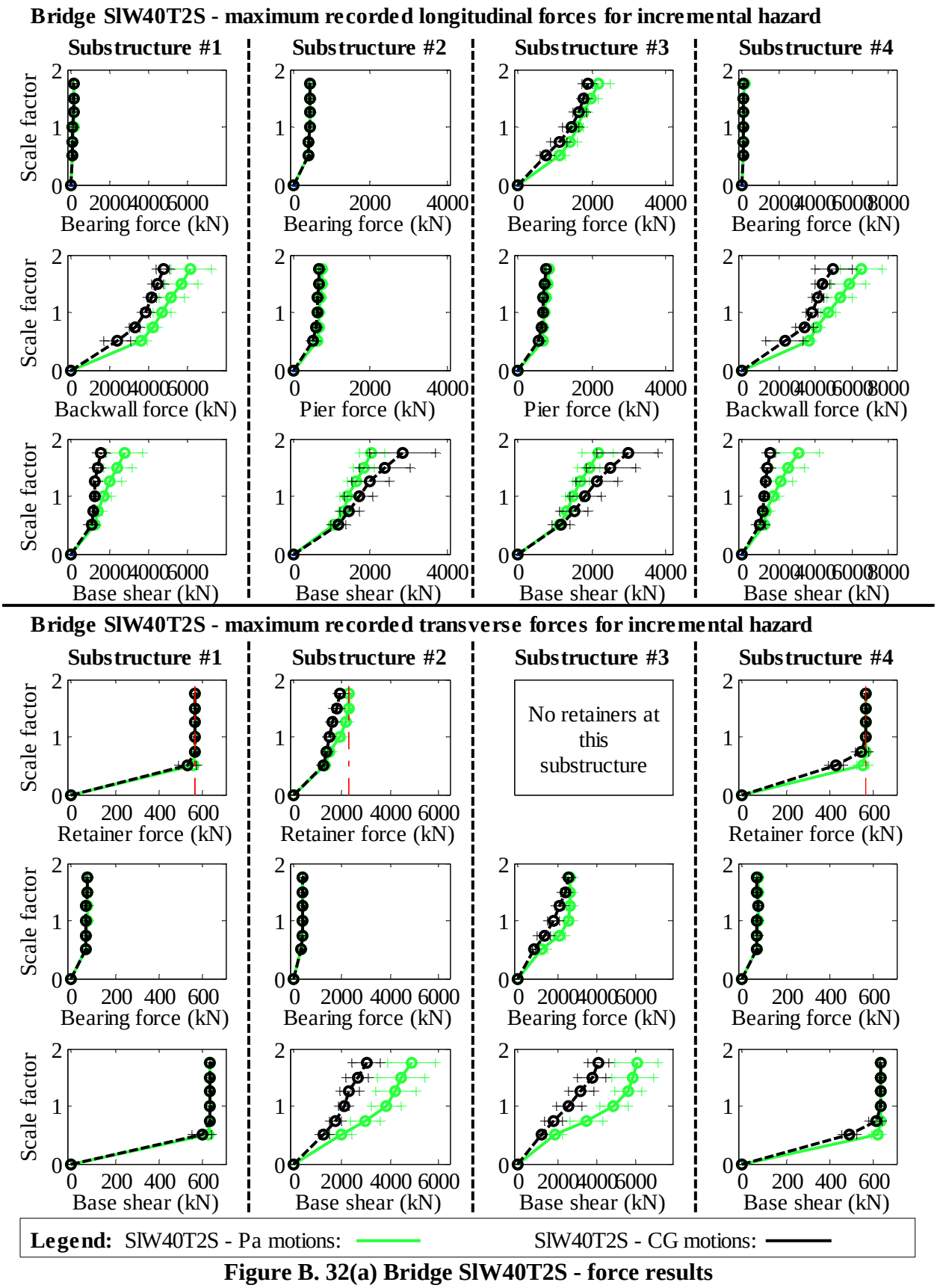

Figure B. 32(a) Bridge SlW40T2S - force results

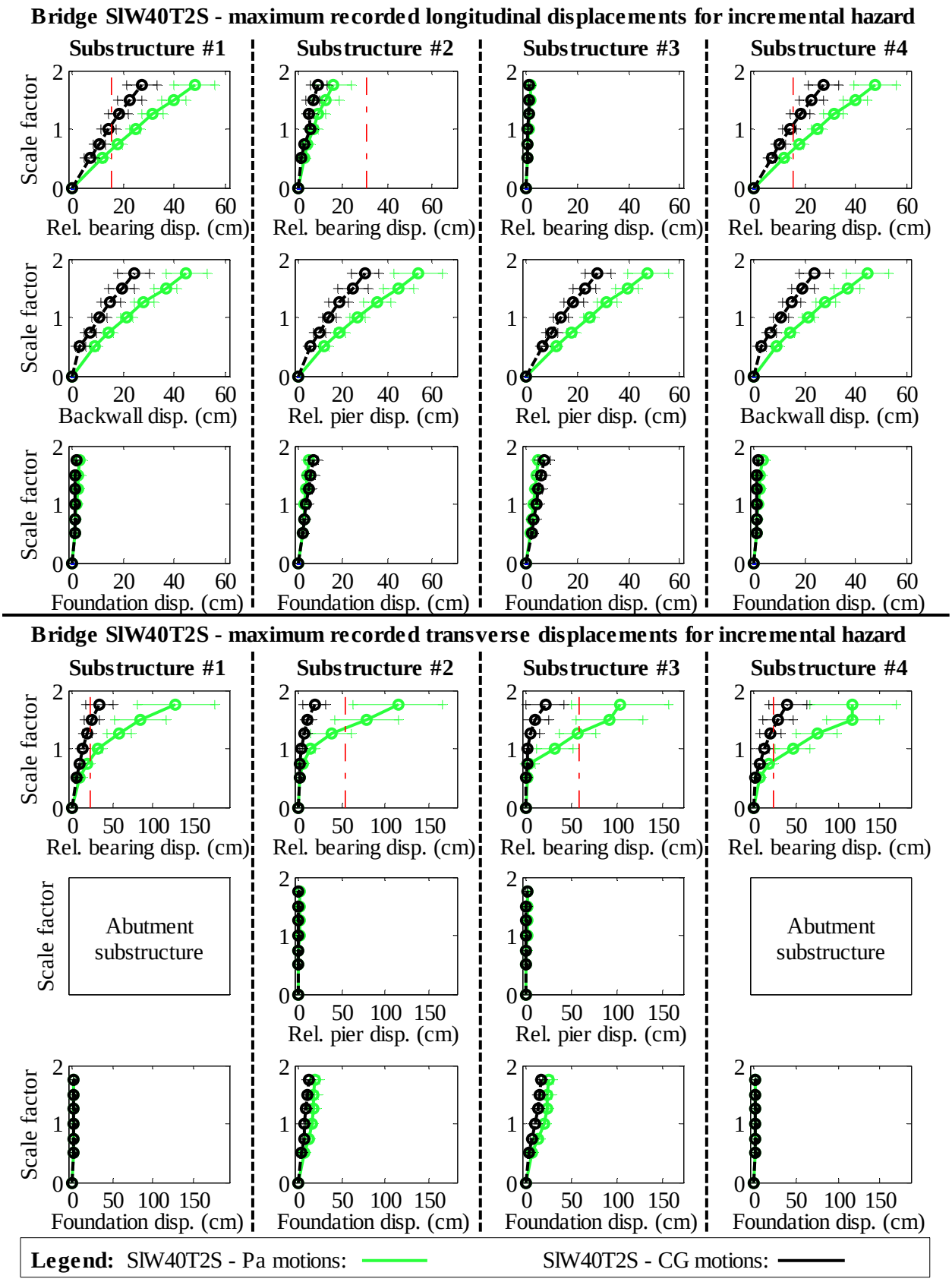

Figure B. 32(b) Bridge SlW40T2S - displacement results

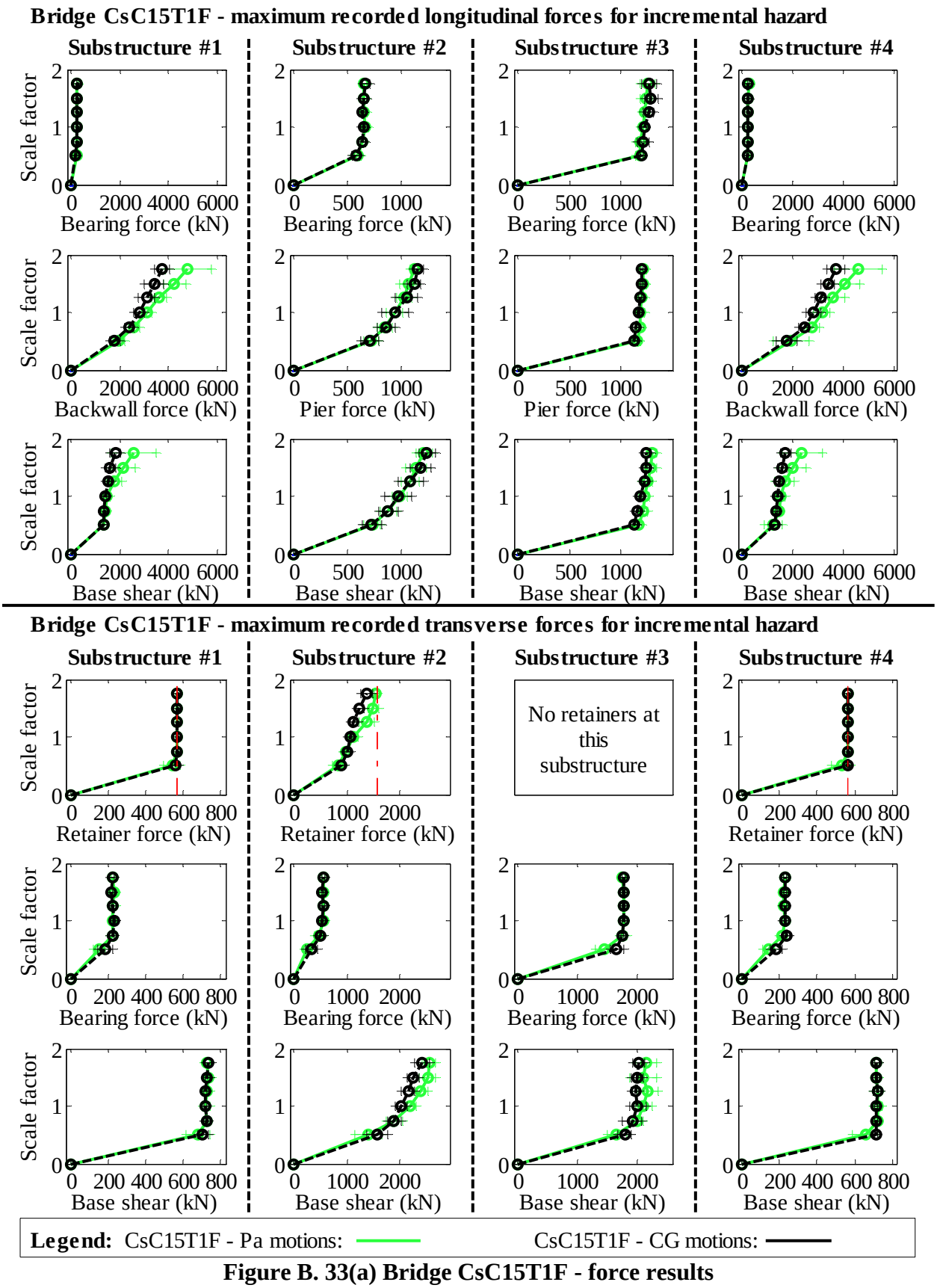

Figure B. 33(a) Bridge CsC15T1F - force results

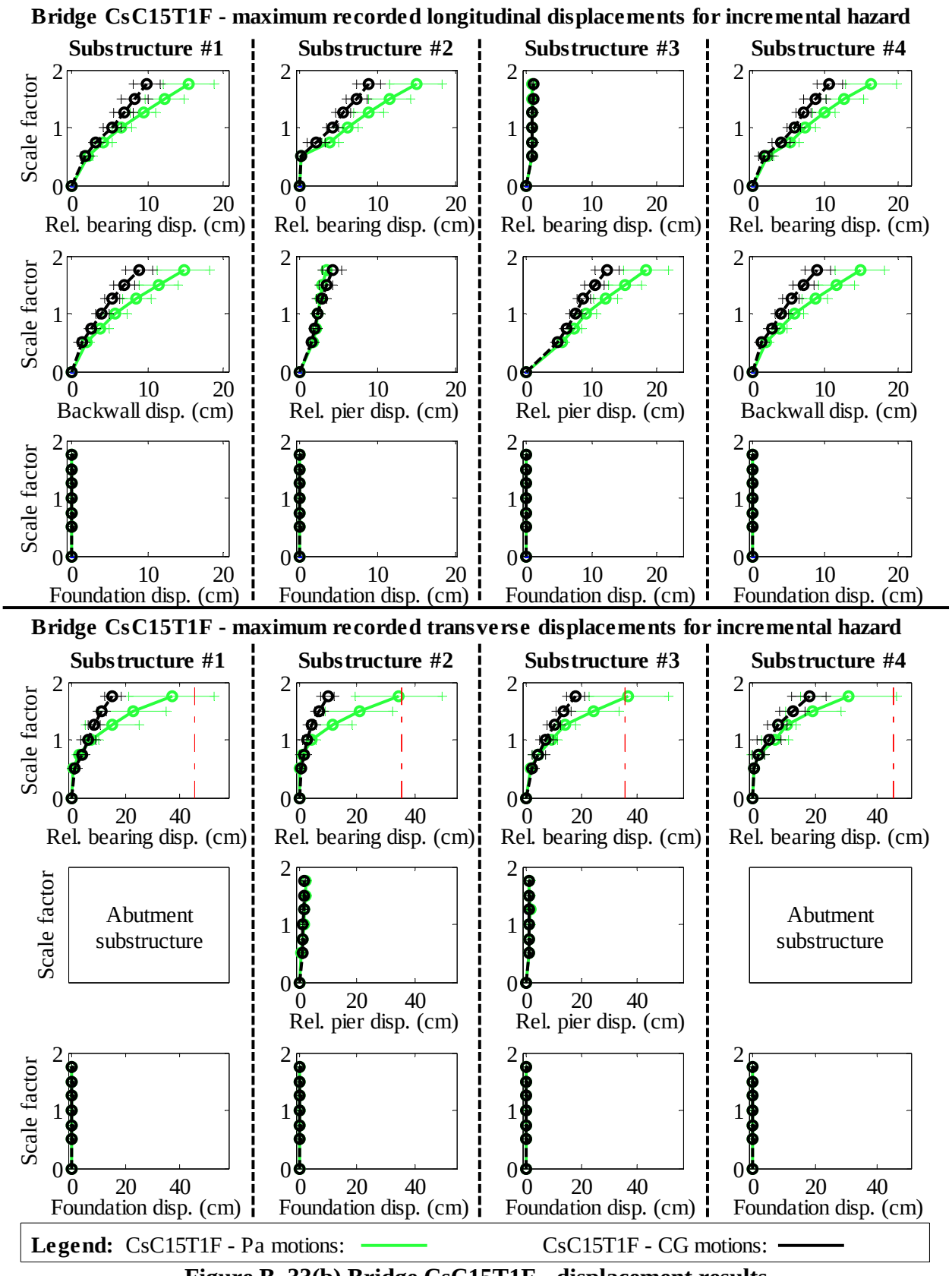

Figure B. 33(b) Bridge CsC15T1F - displacement results

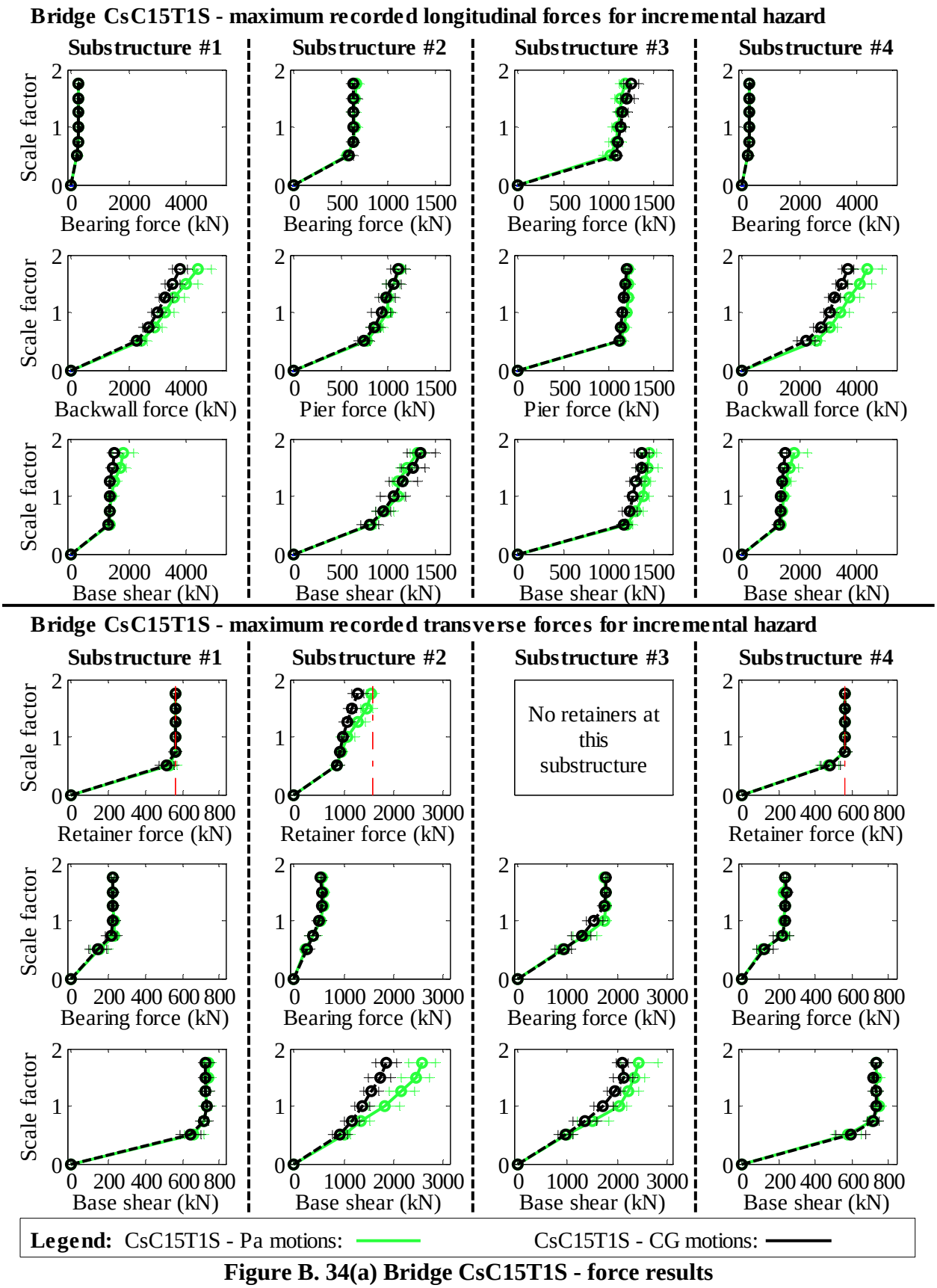

Figure B. 34(a) Bridge CsC15T1S - force results

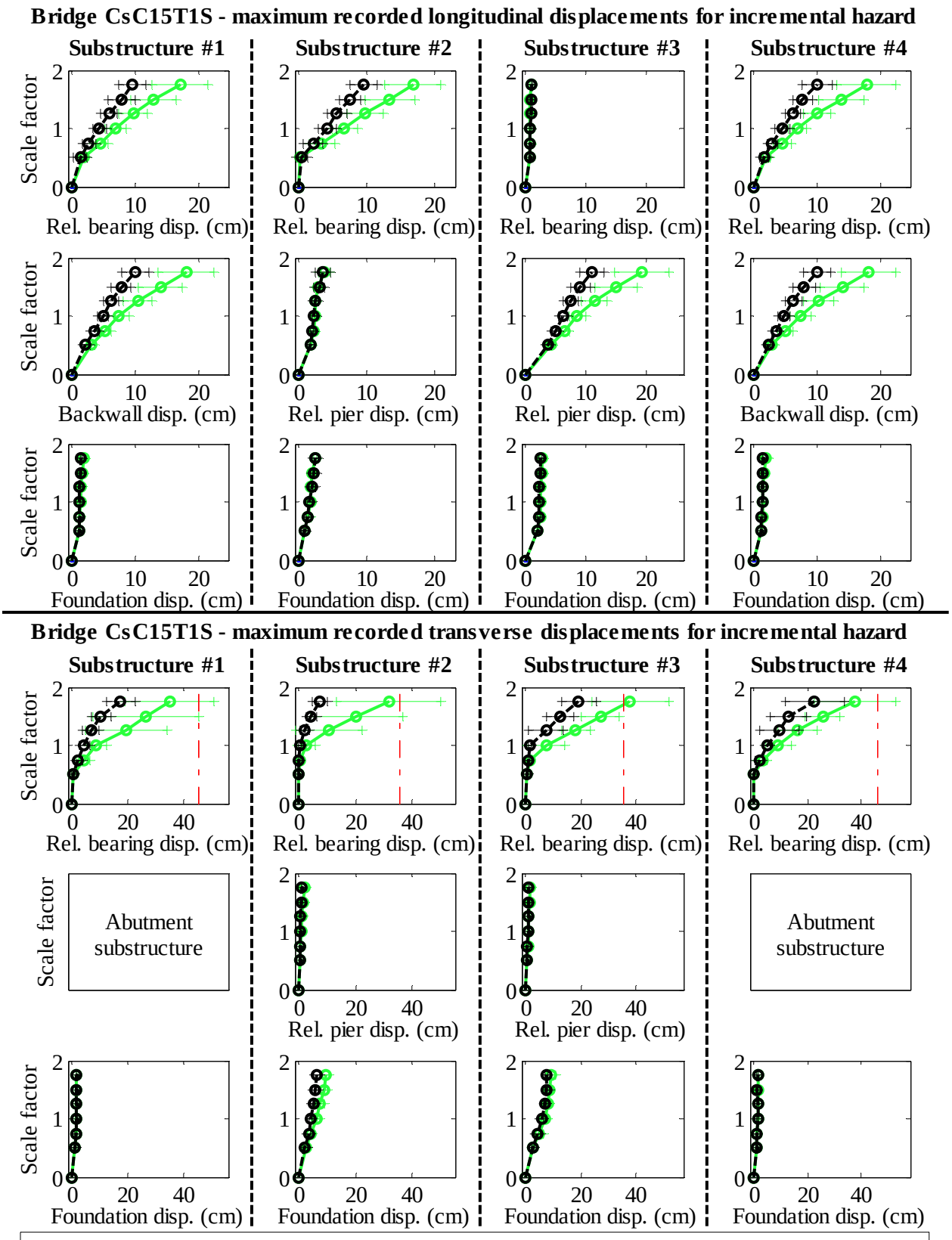

Figure B. 34(b) Bridge CsC15T1S - displacement results

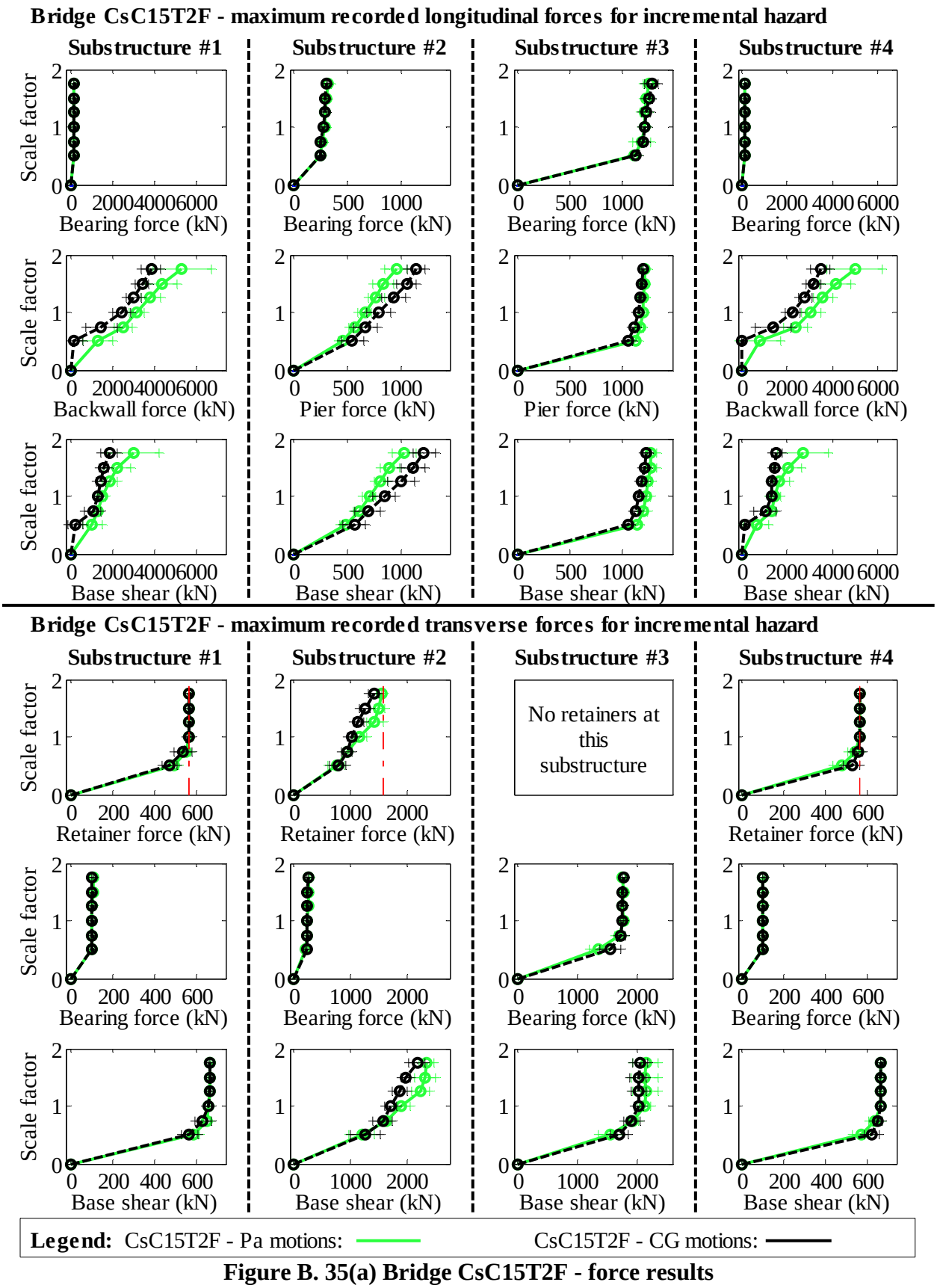

Figure B. 35(a) Bridge CsC15T2F - force results

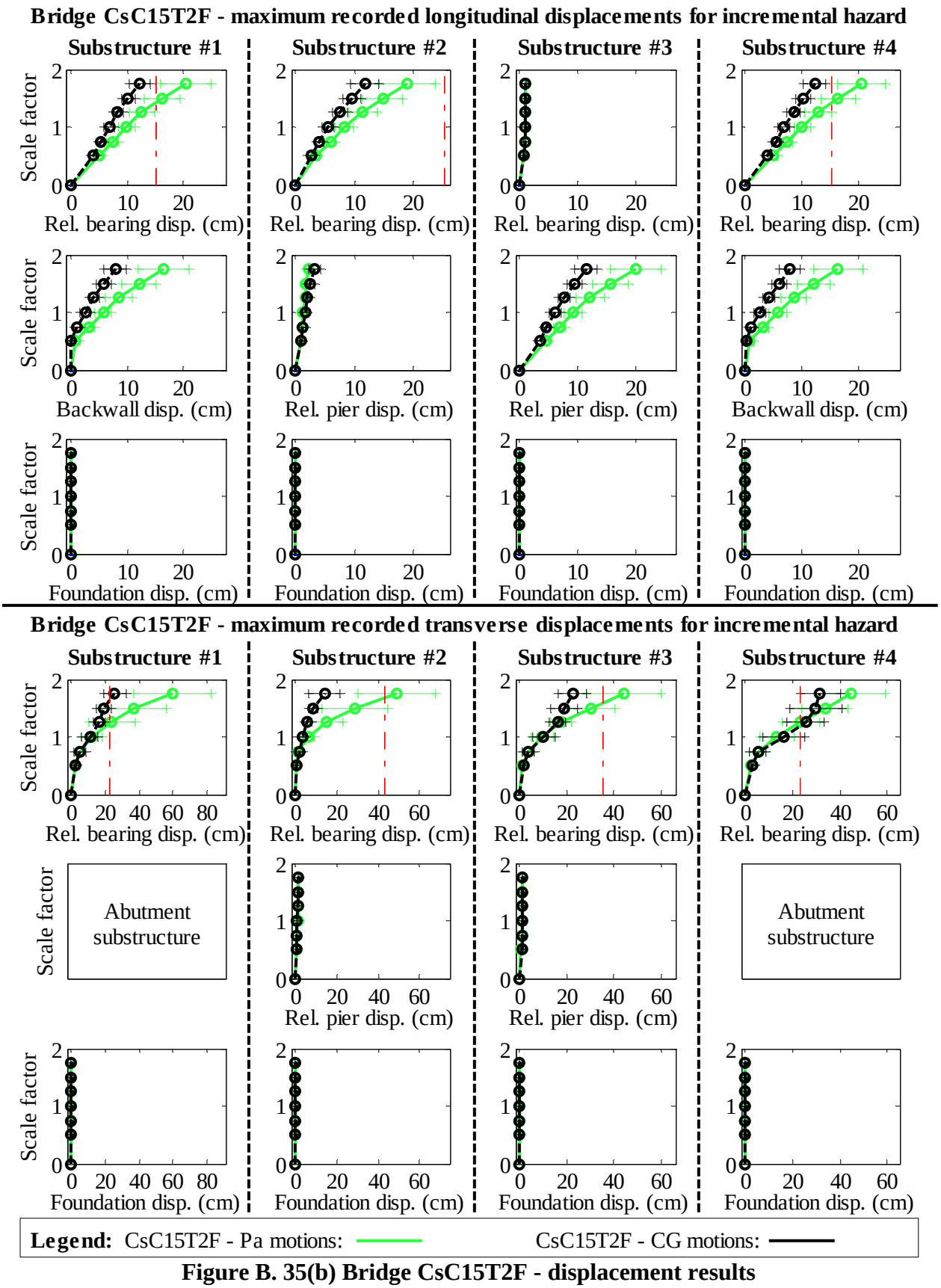

Figure B. 35(b) Bridge CsC15T2F - displacement results

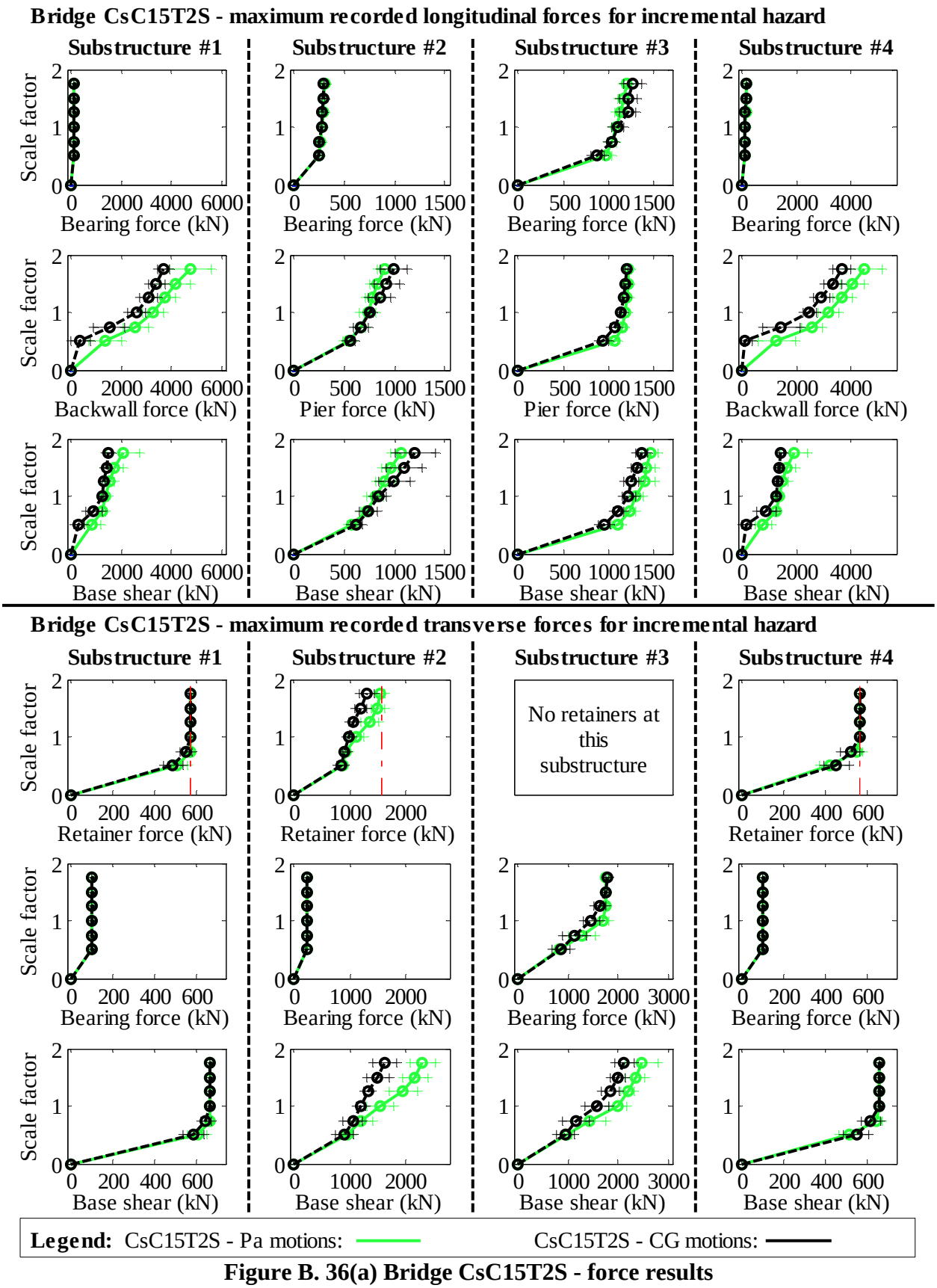

Figure B. 36(a) Bridge CsC15T2S - force results

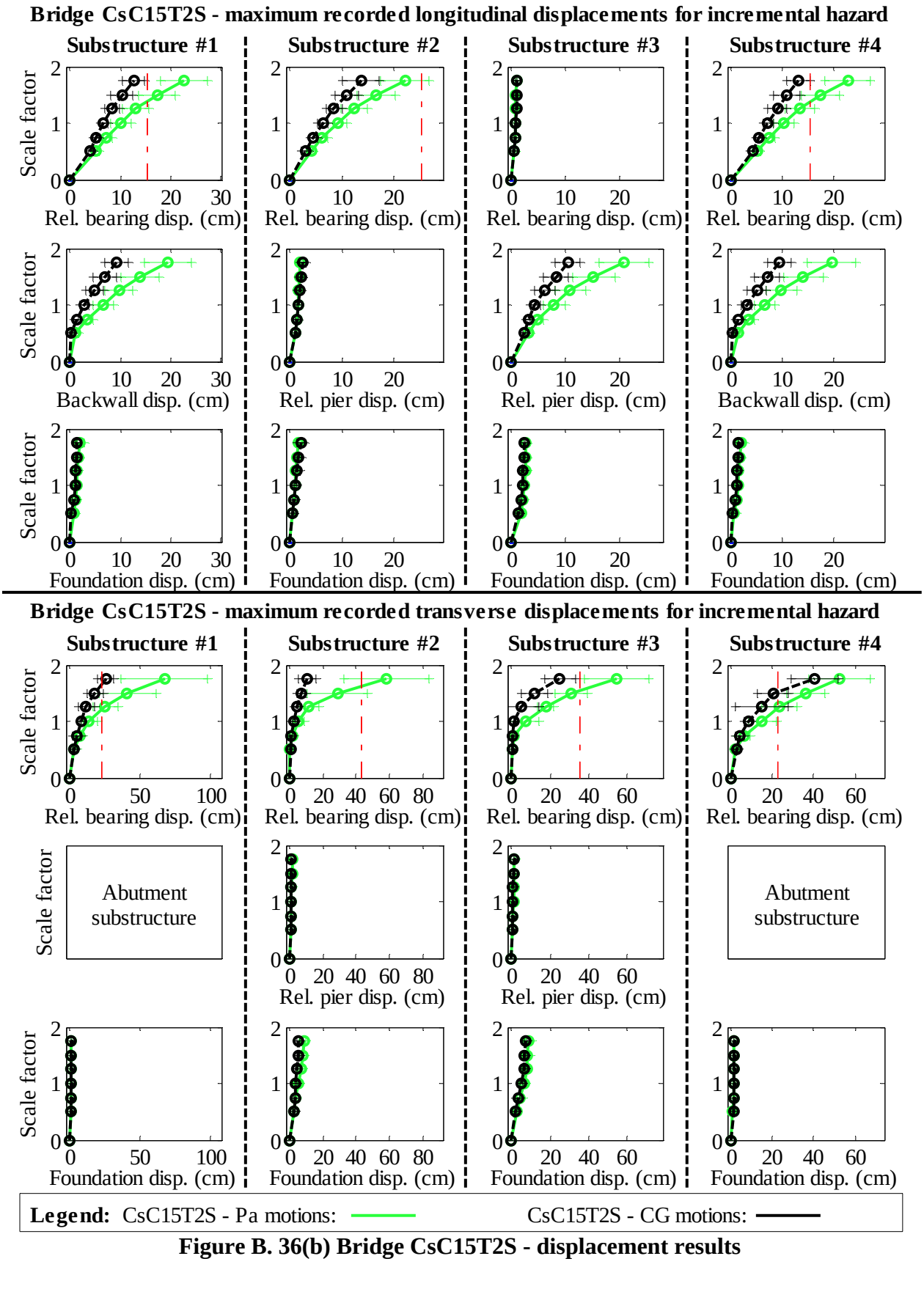

Figure B. 36(b) Bridge CsC15T2S - displacement results

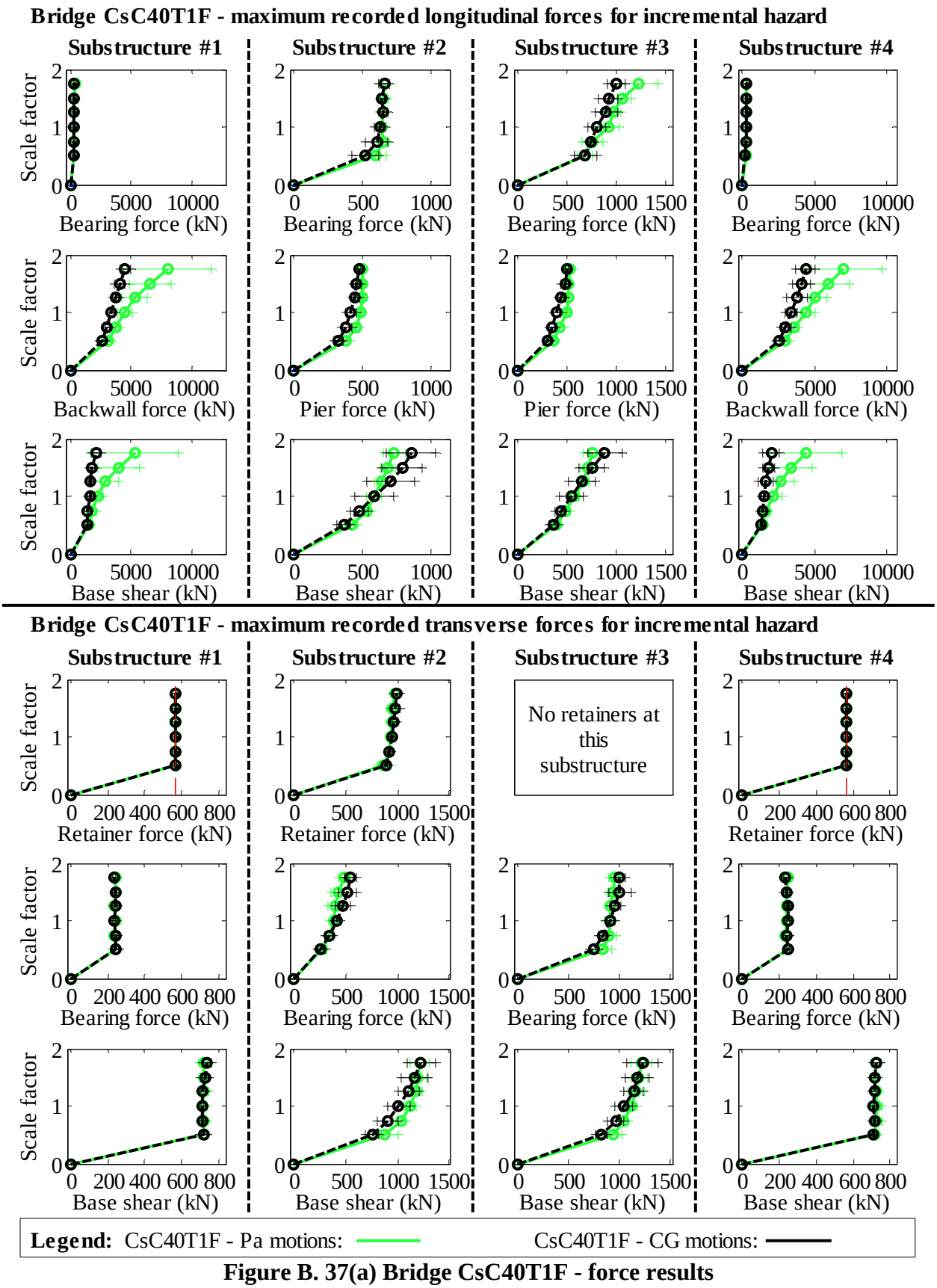

Figure B. 37(a) Bridge CsC40T1F - force results

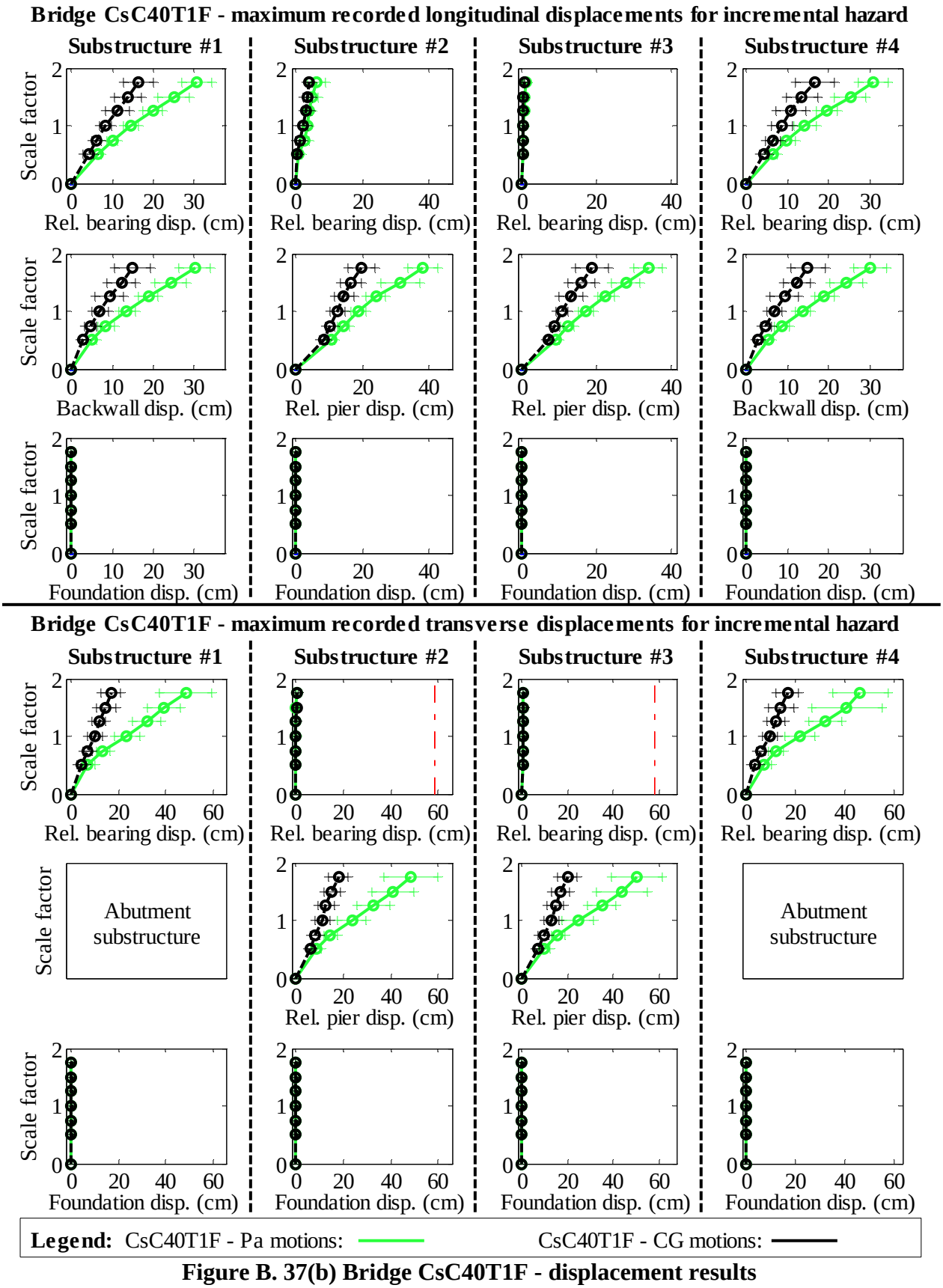

Figure B. 37(b) Bridge CsC40T1F - displacement results

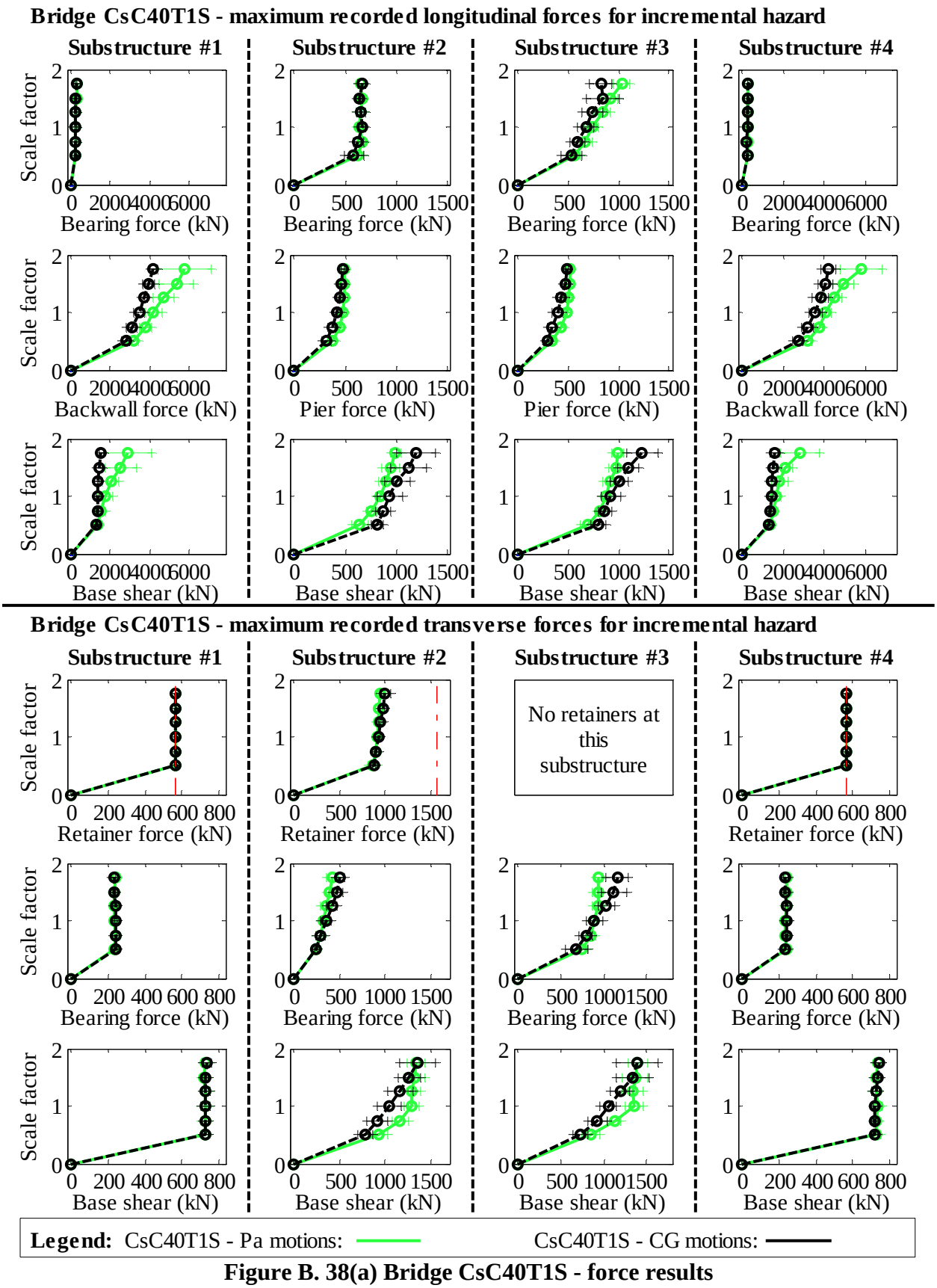

Figure B. 38(a) Bridge CsC40T1S - force results

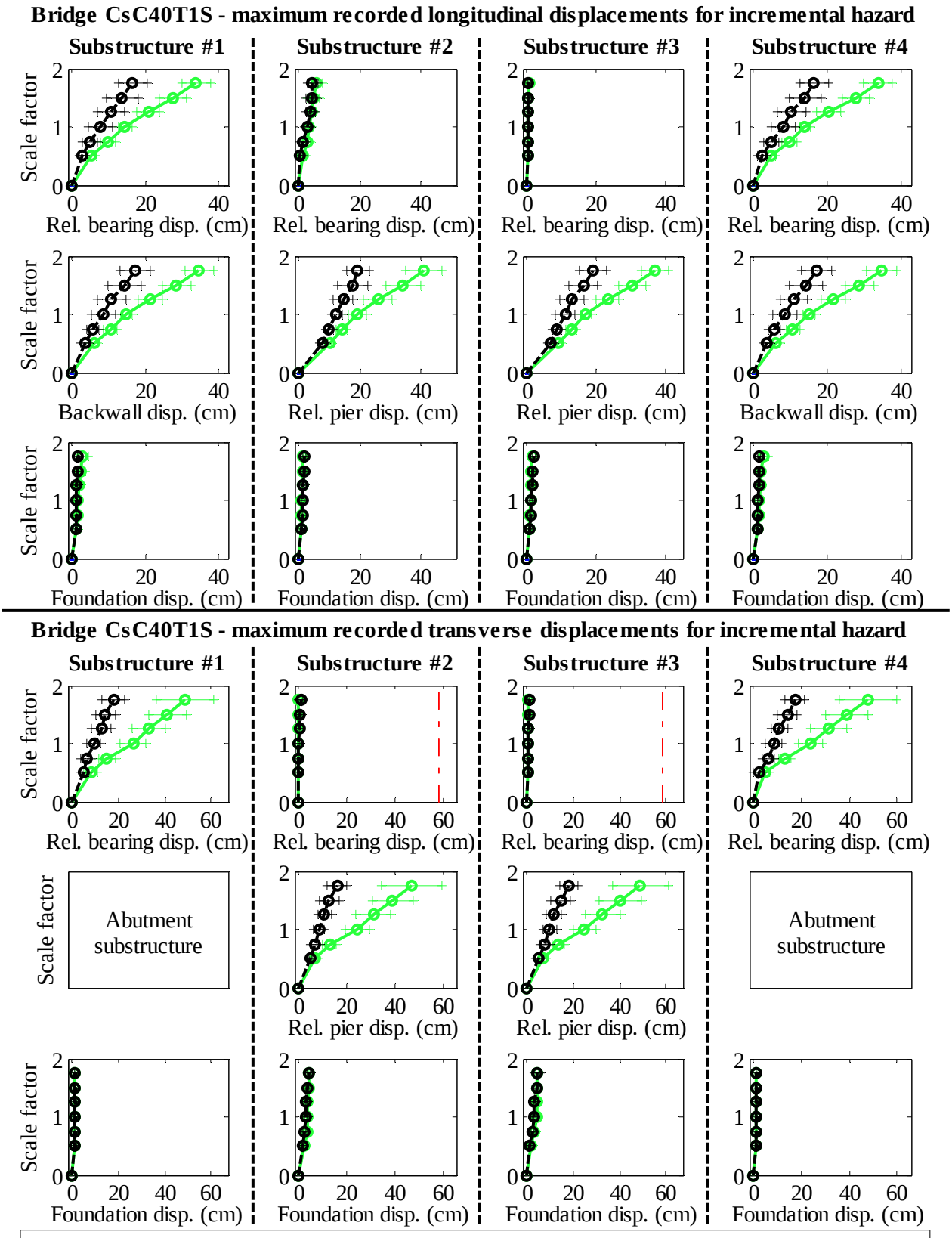

Figure B. 38(b) Bridge CsC40T1S - displacement results

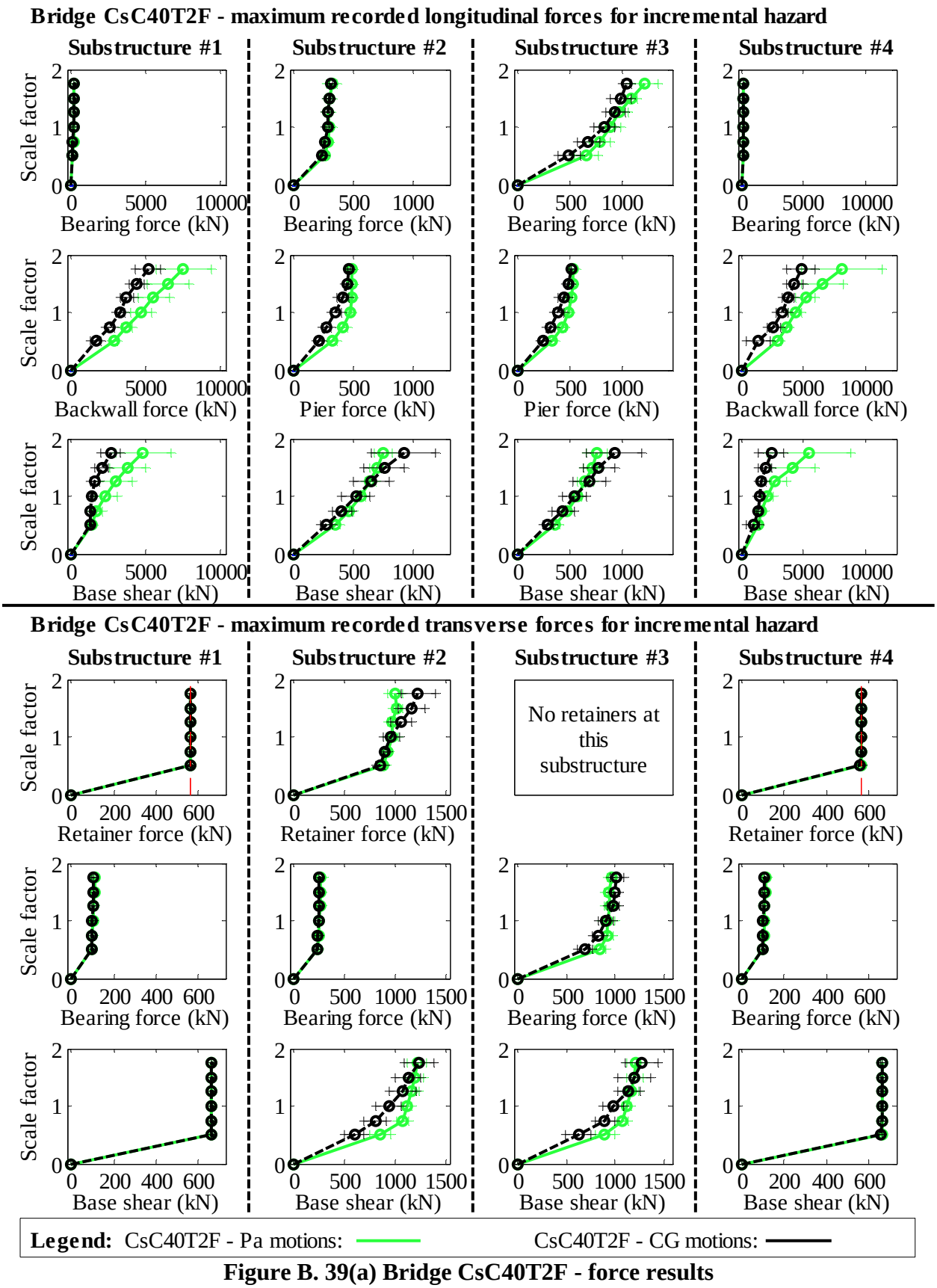

Figure B. 39(a) Bridge CsC40T2F - force results

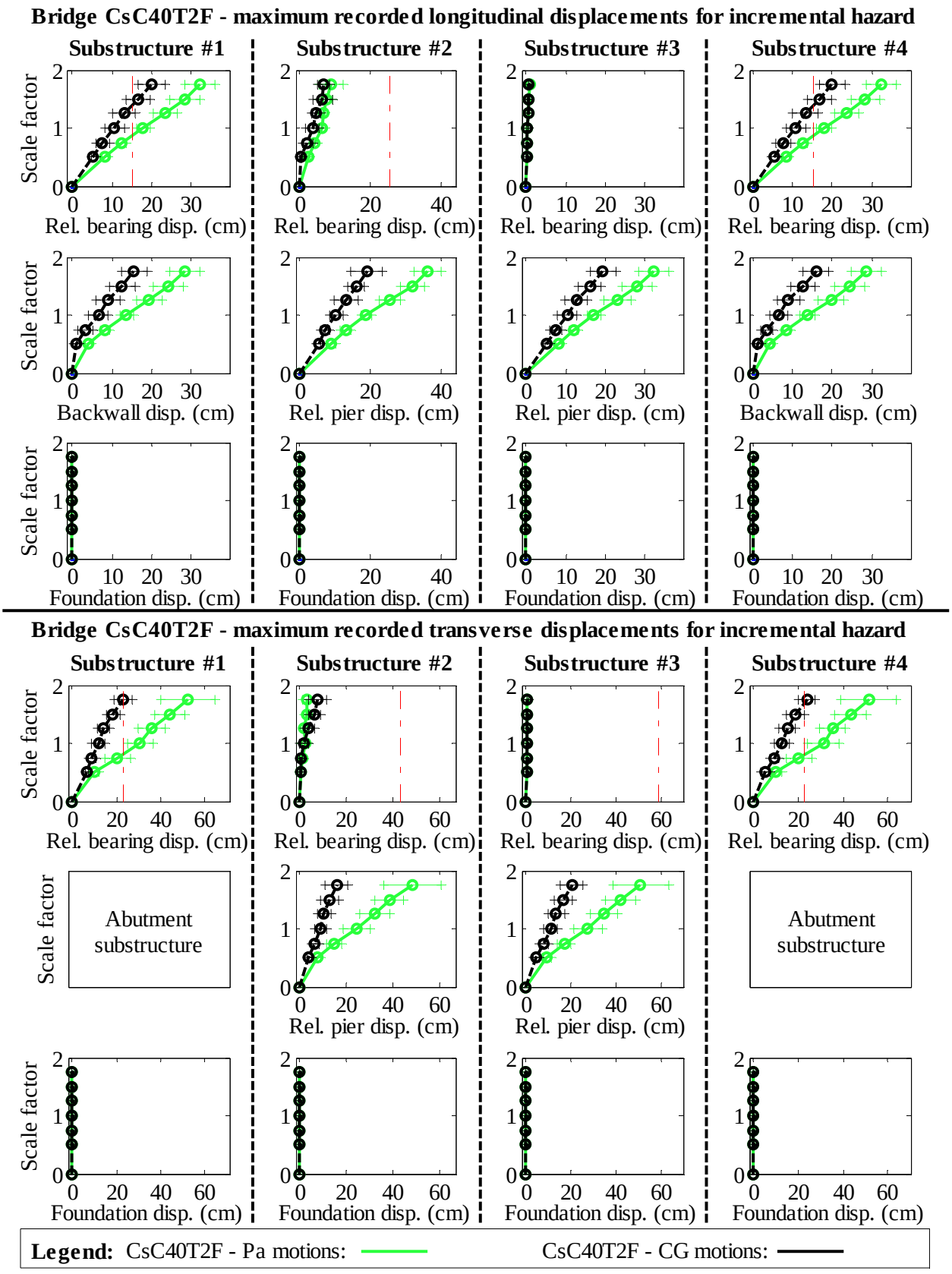

Figure B. 39(b) Bridge CsC40T2F - displacement results

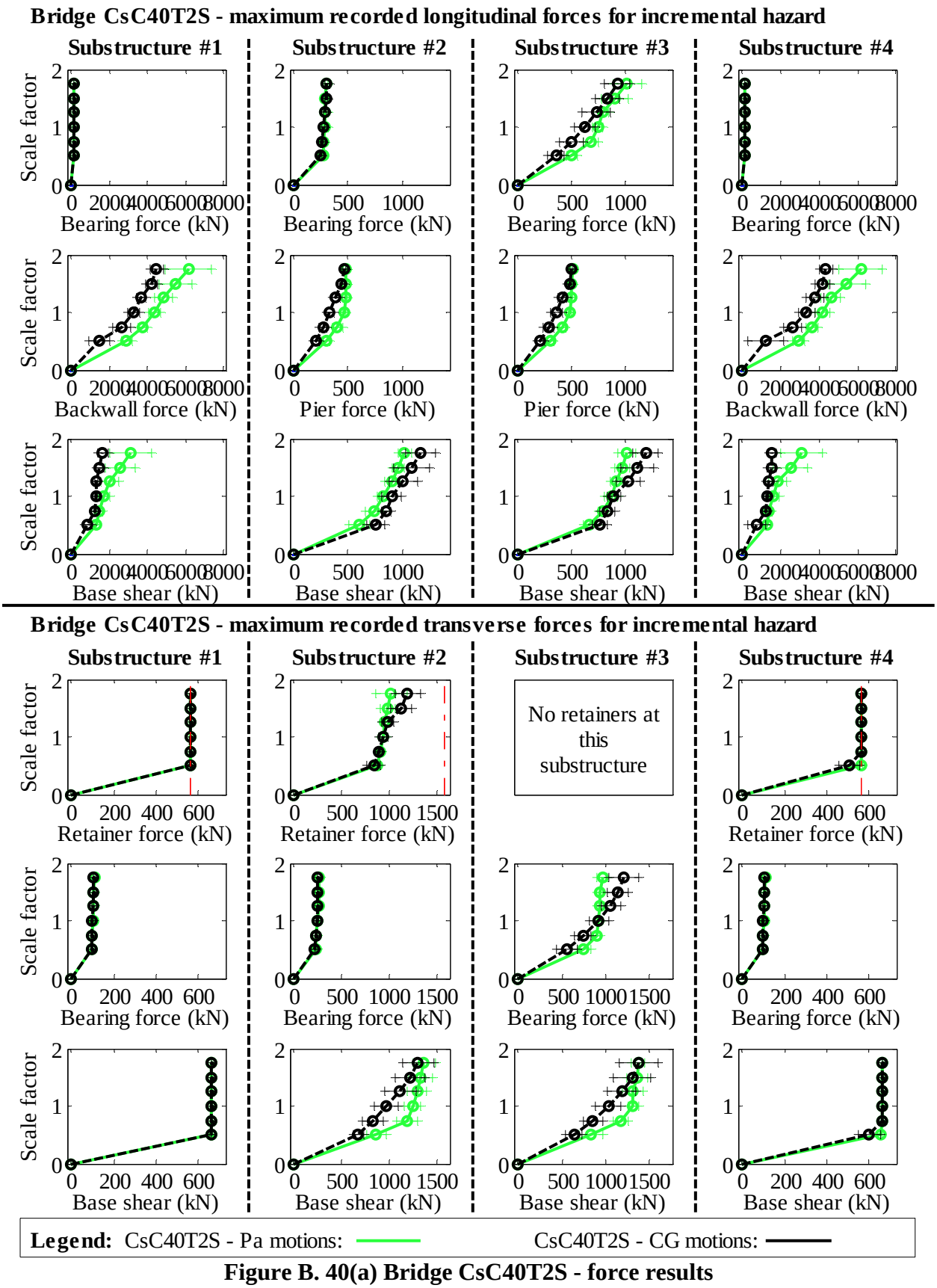

Figure B. 40(a) Bridge CsC40T2S - force results

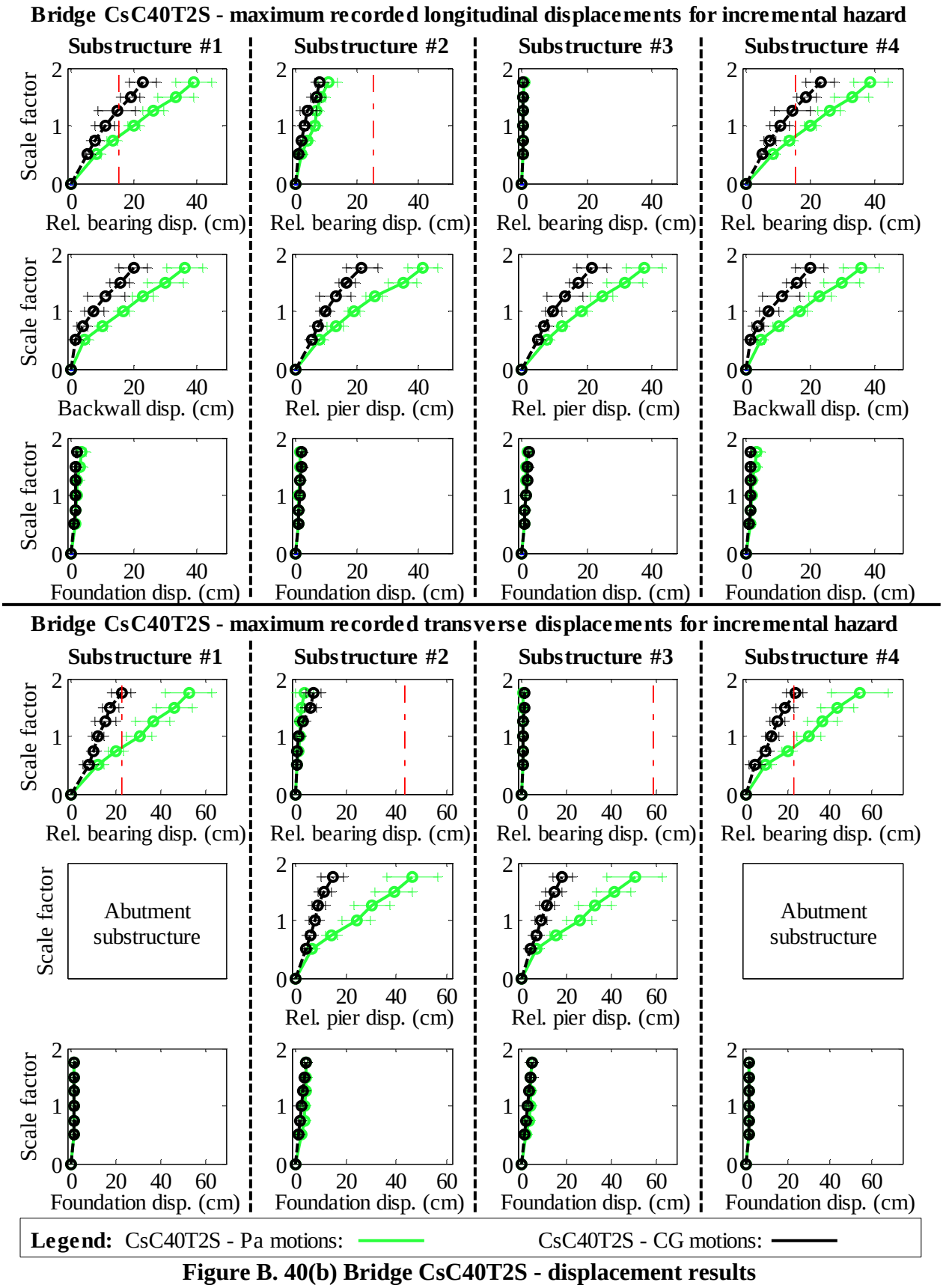

Figure B. 40(b) Bridge CsC40T2S - displacement results

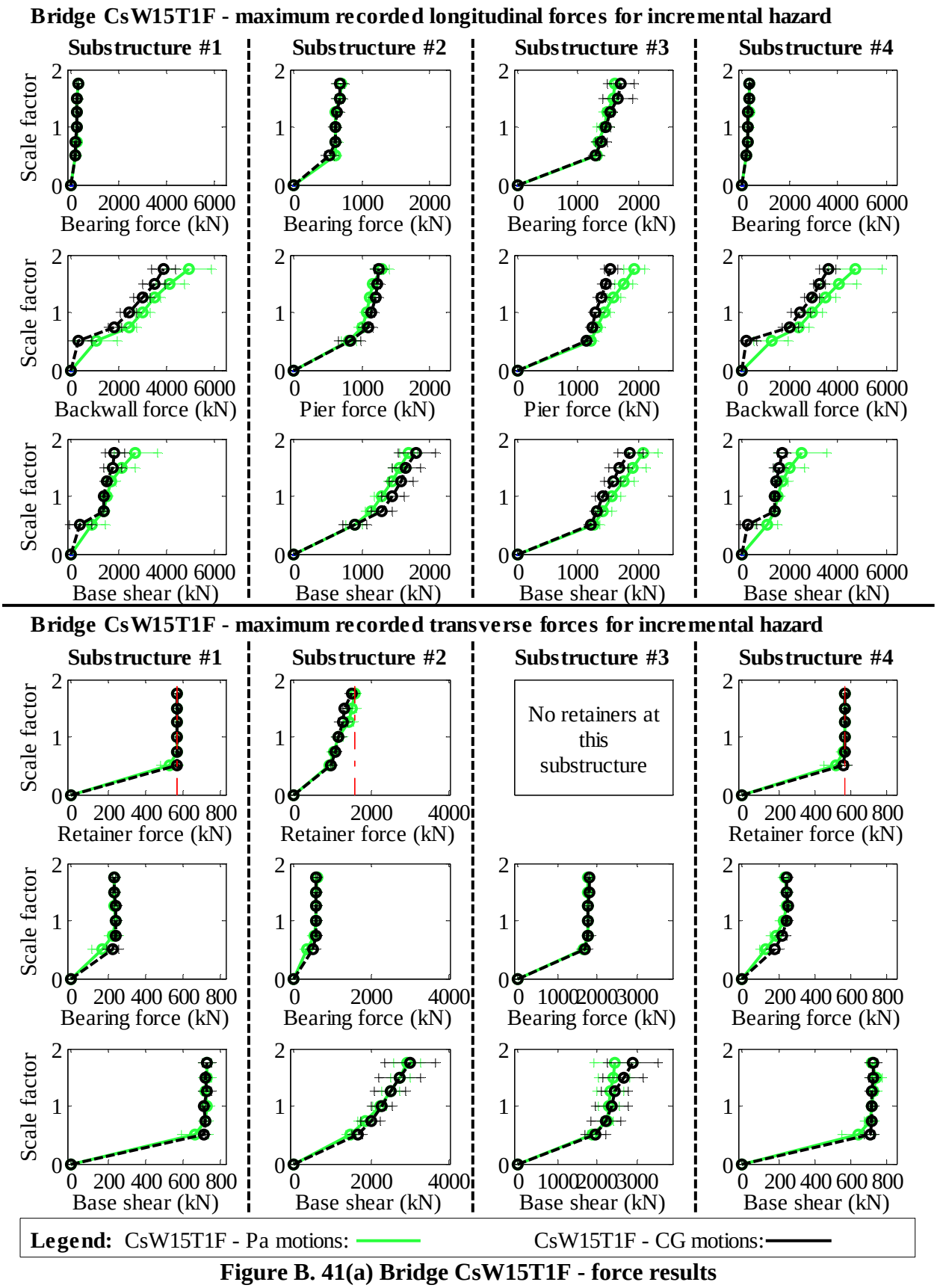

Figure B. 41(a) Bridge CsW15T1F - force results

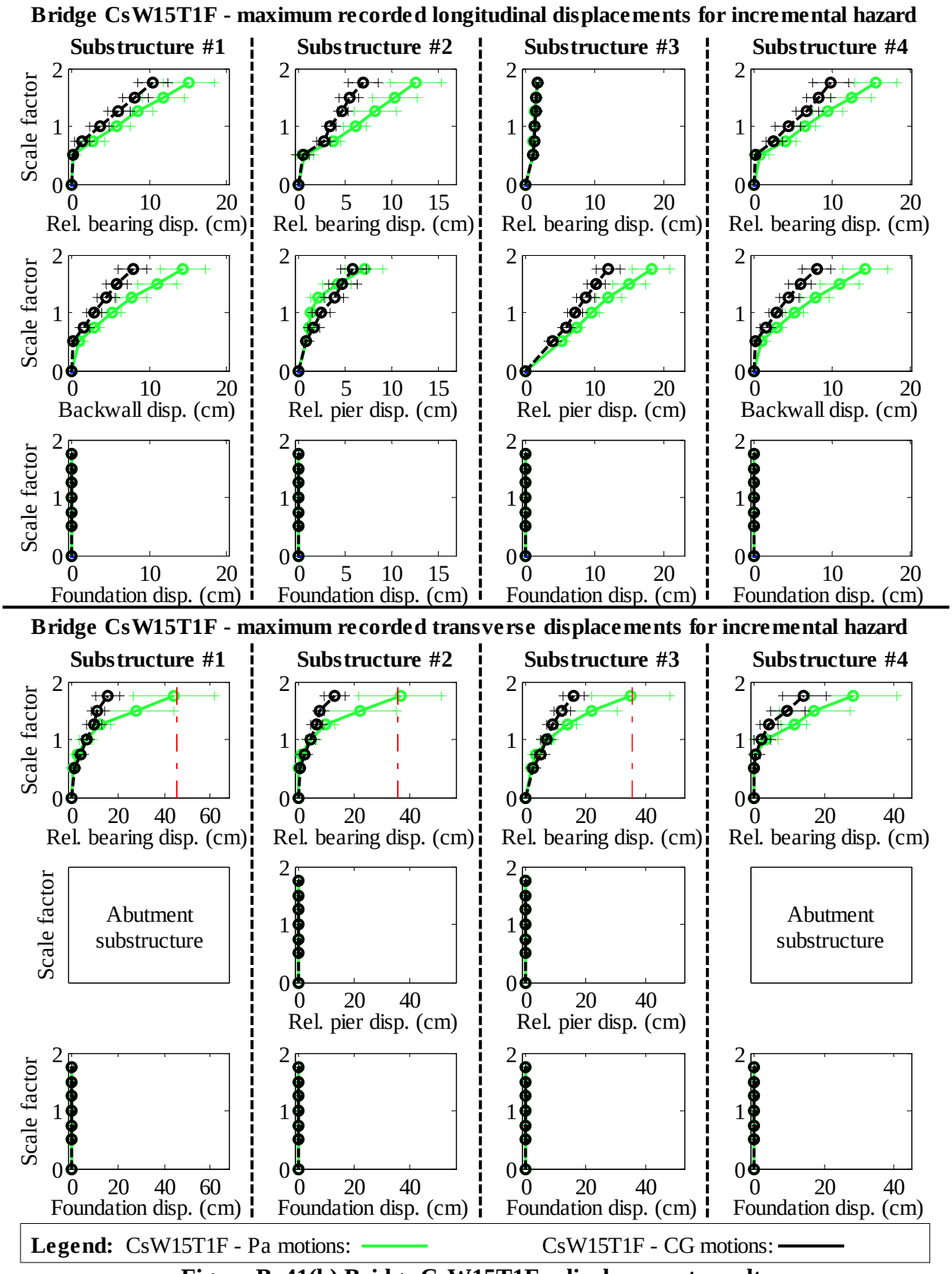

Figure B. 41(b) Bridge CsW15T1F - displacement results

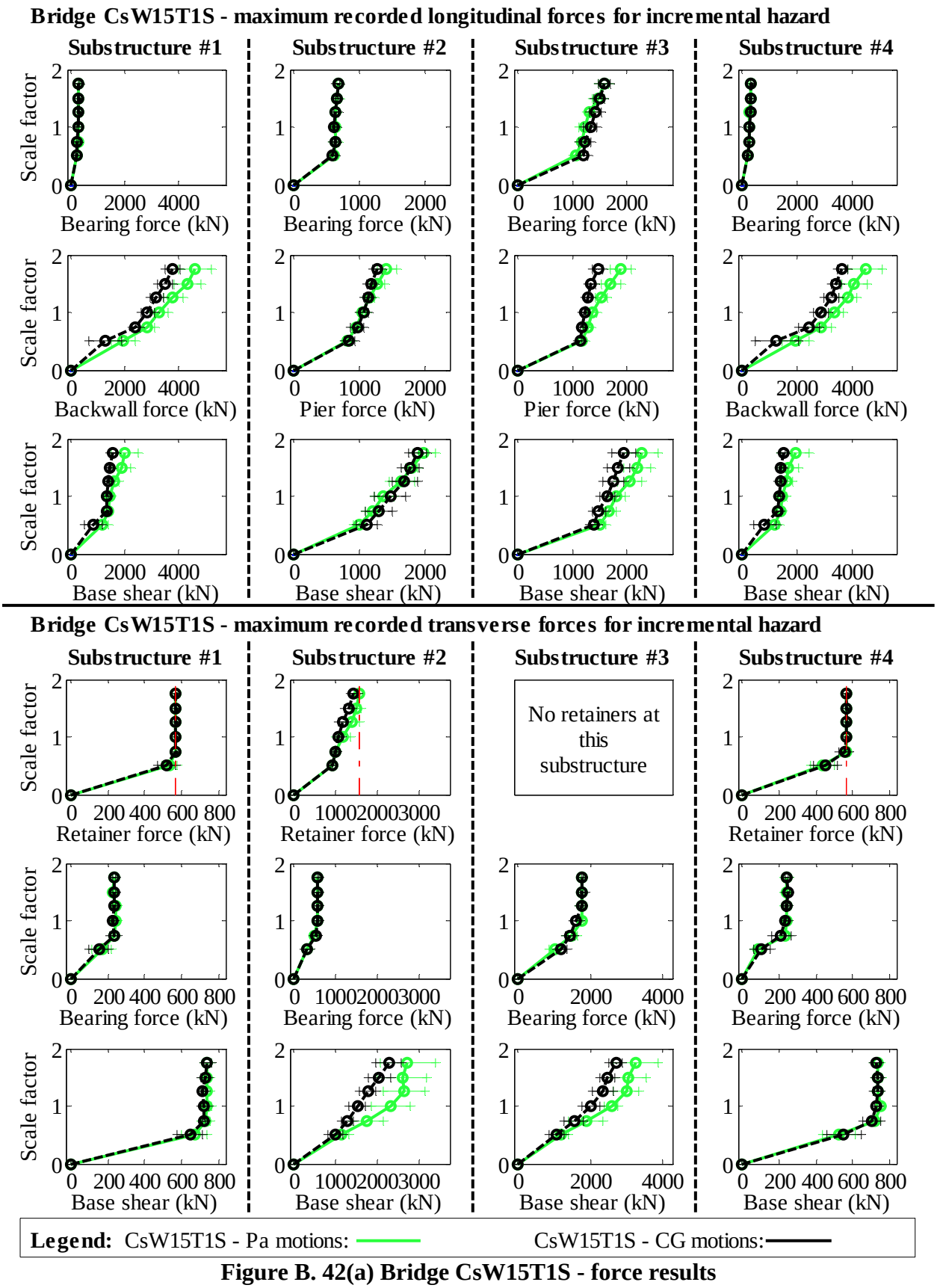

Figure B. 42(a) Bridge CsW15T1S - force results

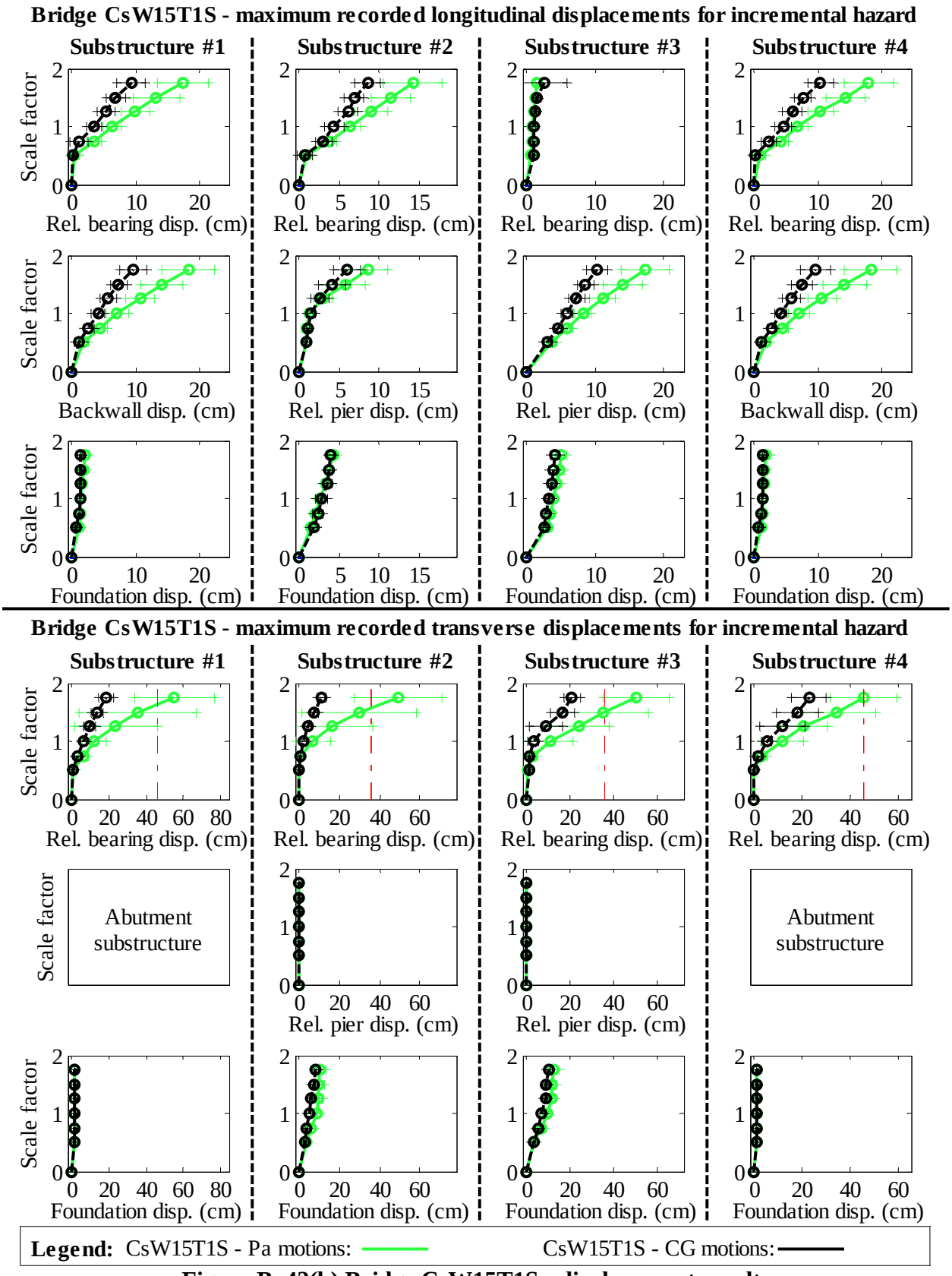

Figure B. 42(b) Bridge CsW15T1S - displacement results

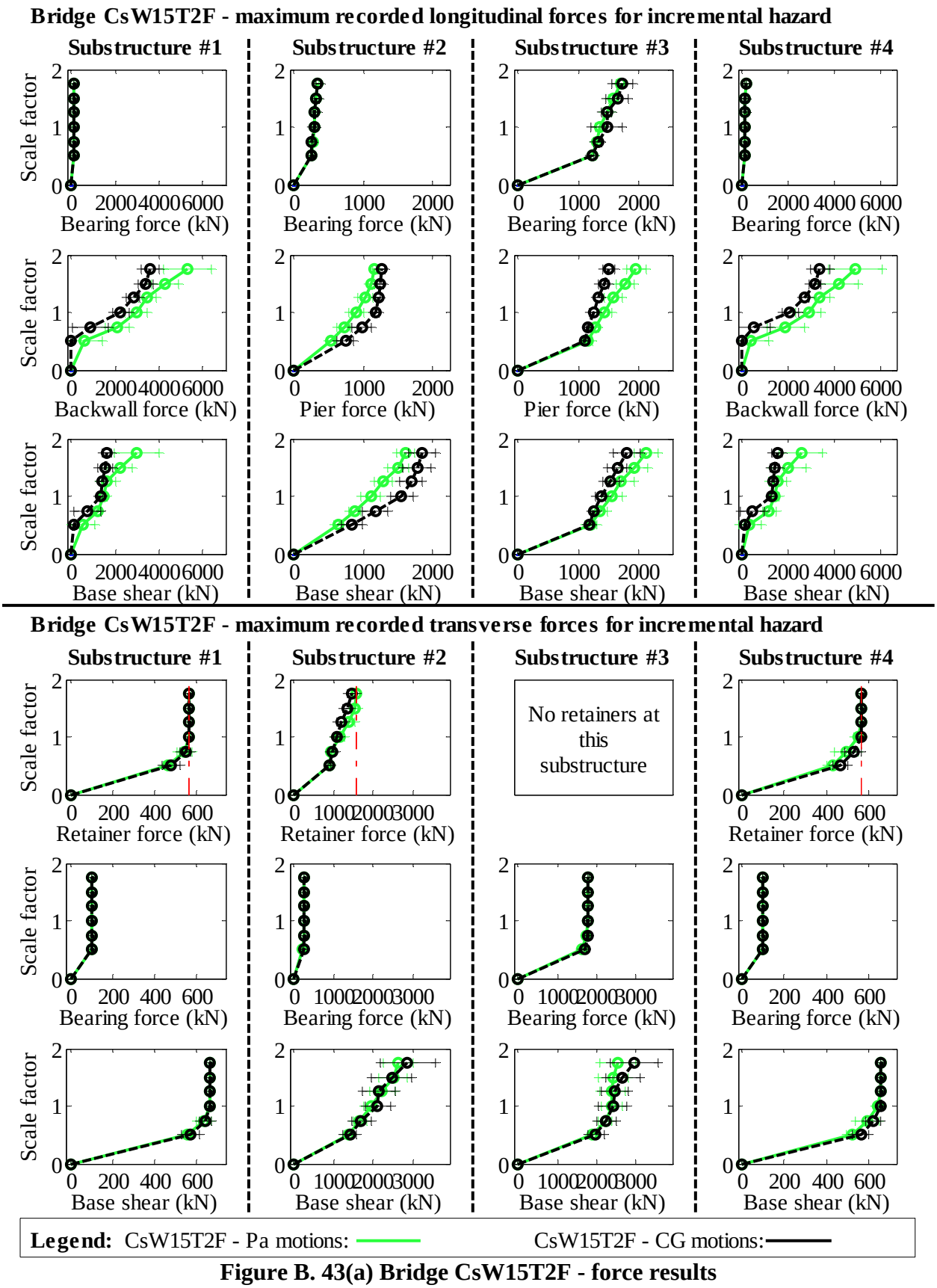

Figure B. 43(a) Bridge CsW15T2F - force results

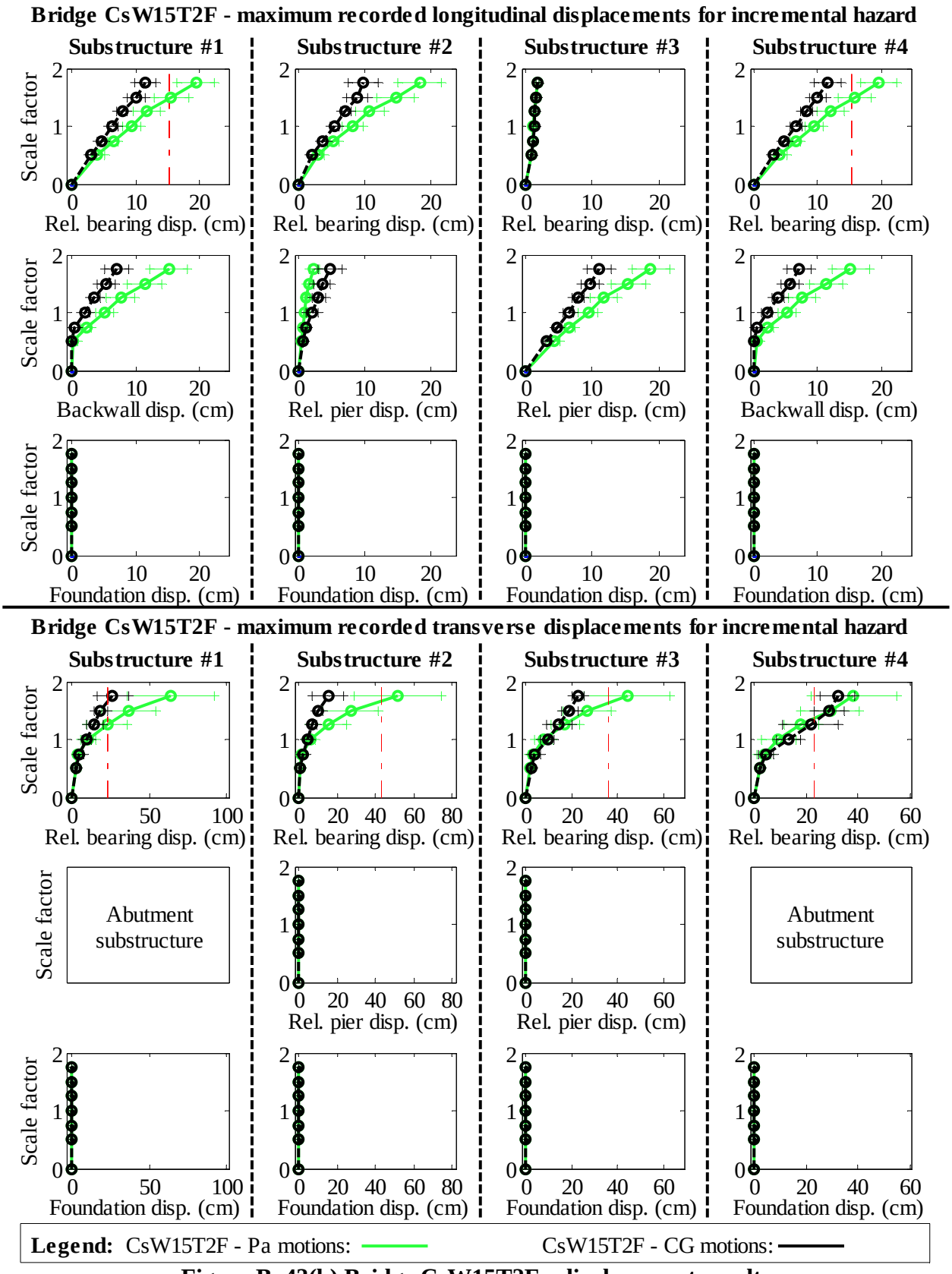

Figure B. 43(b) Bridge CsW15T2F - displacement results

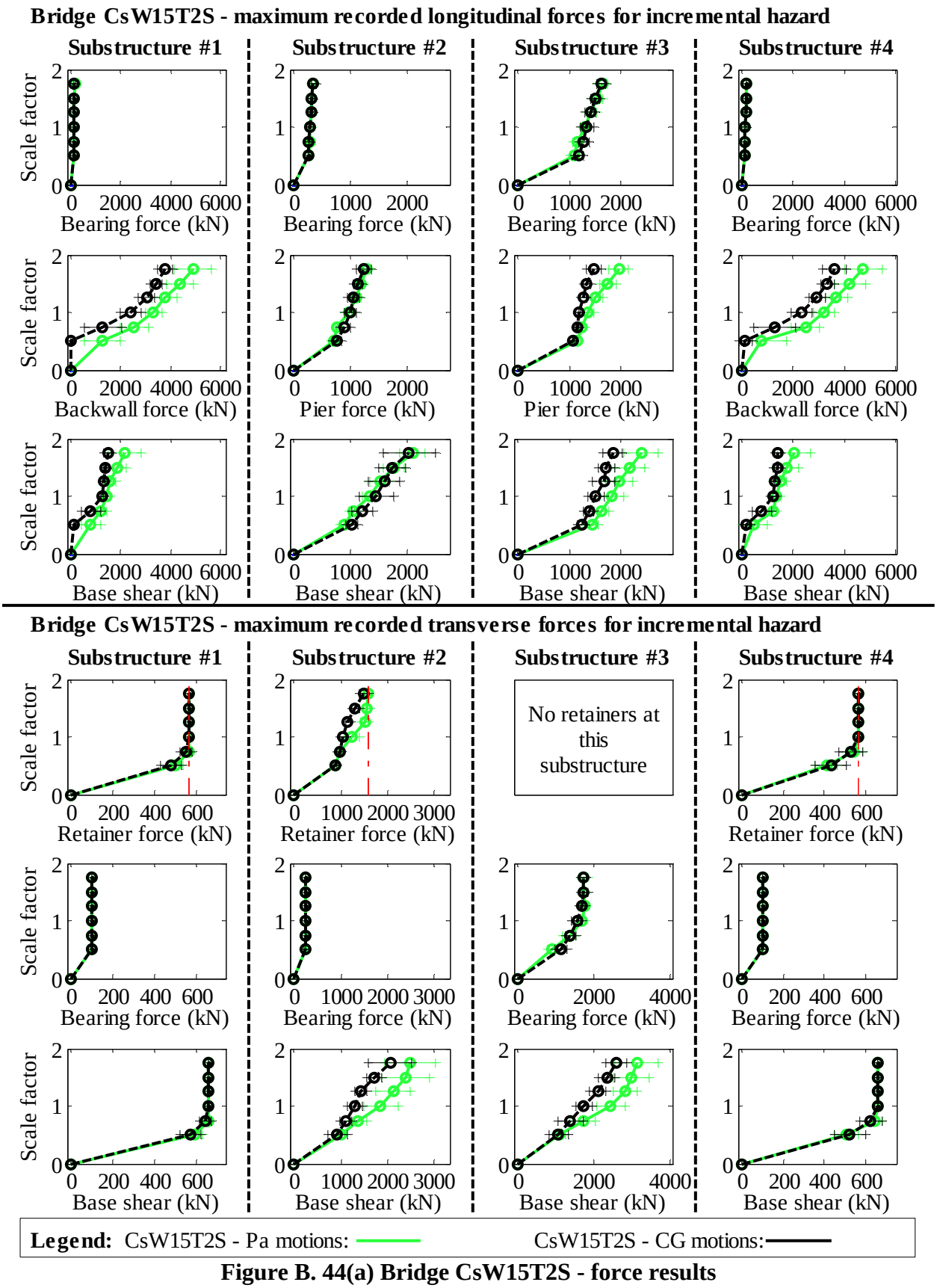

Figure B. 44(a) Bridge CsW15T2S - force results

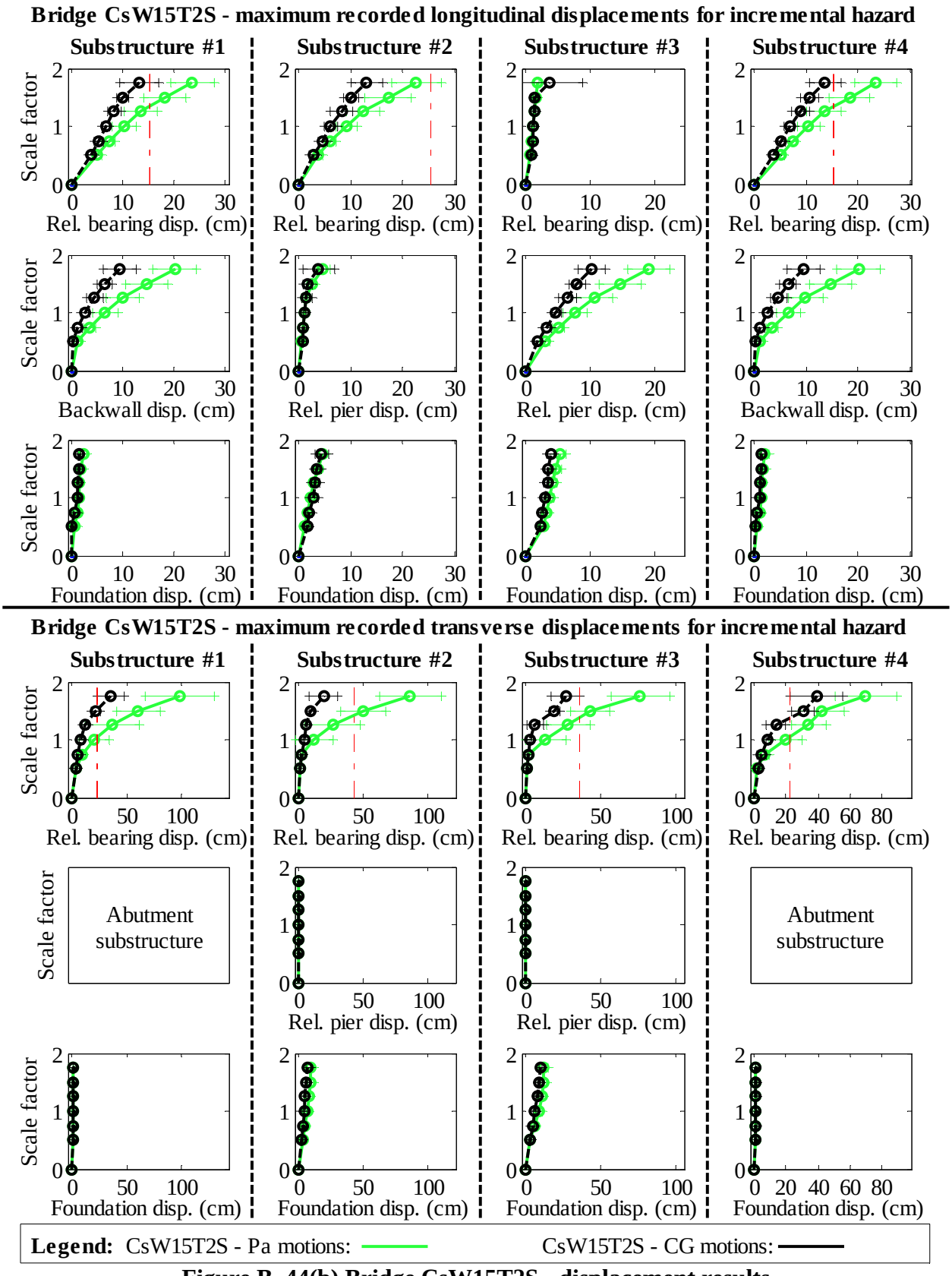

Figure B. 44(b) Bridge CsW15T2S - displacement results

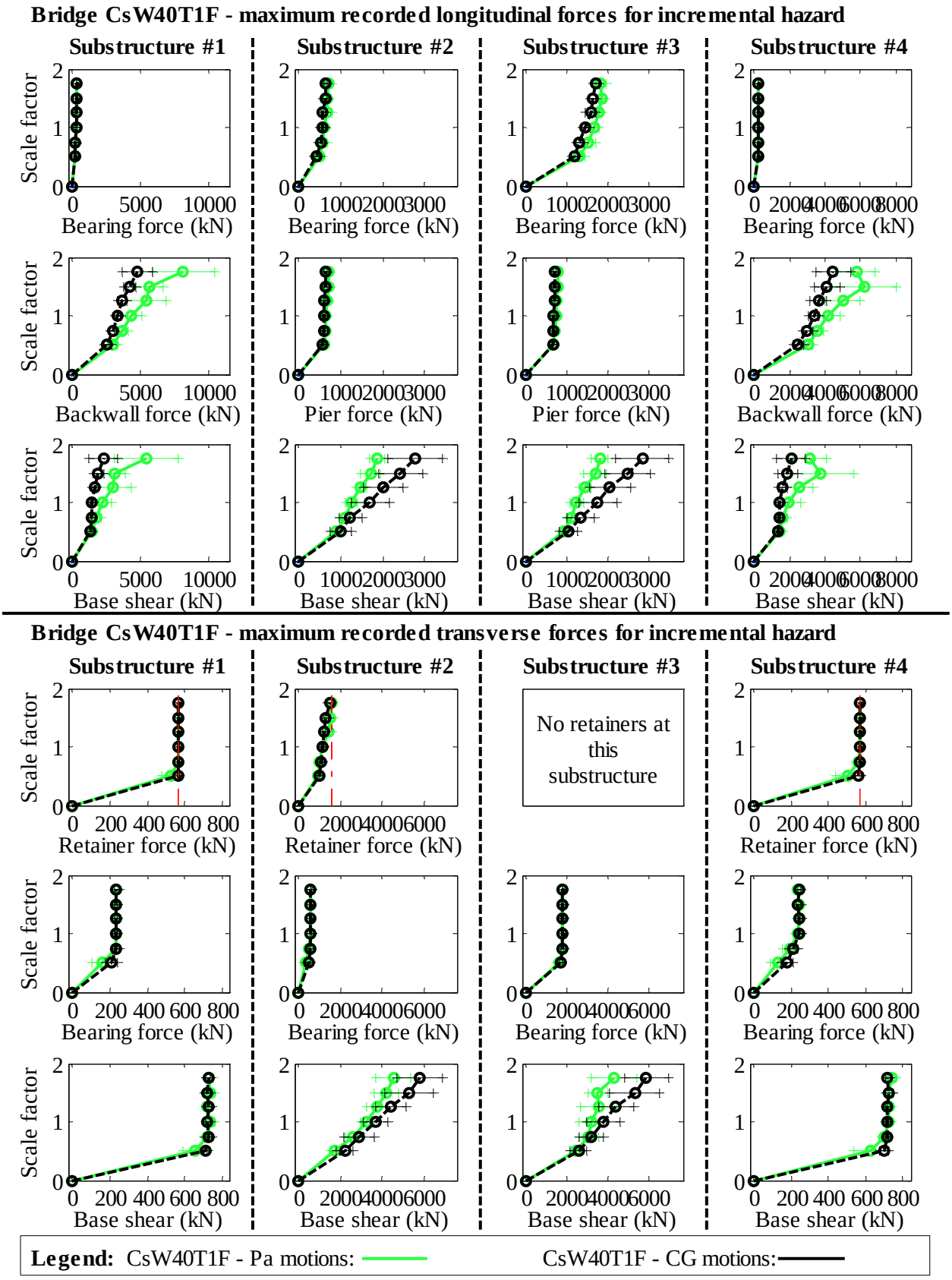

Figure B. 45(a) Bridge CsW40T1F - force results

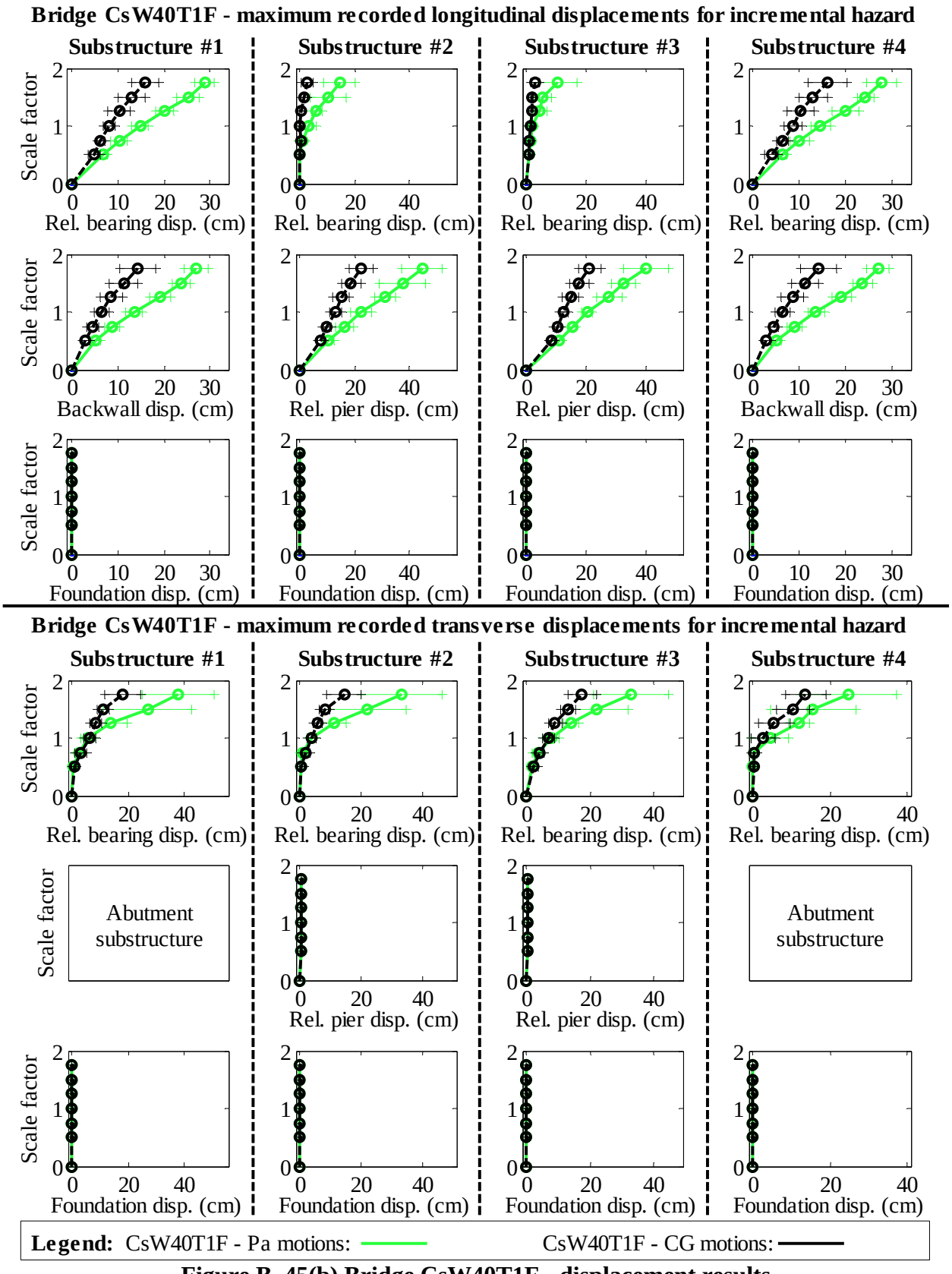

Figure B. 45(b) Bridge CsW40T1F - displacement results

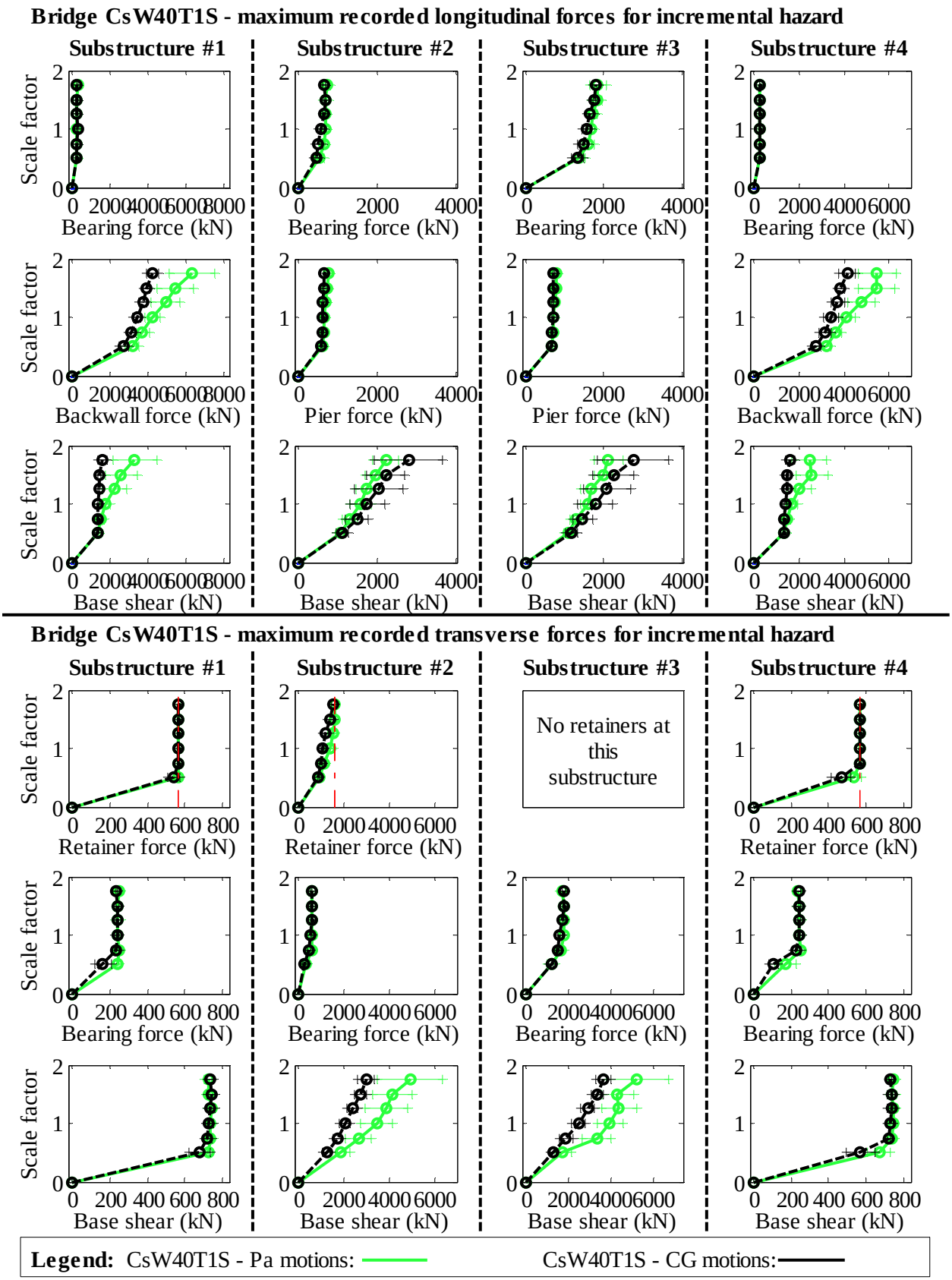

Figure B. 46(a) Bridge CsW40T1S - force results

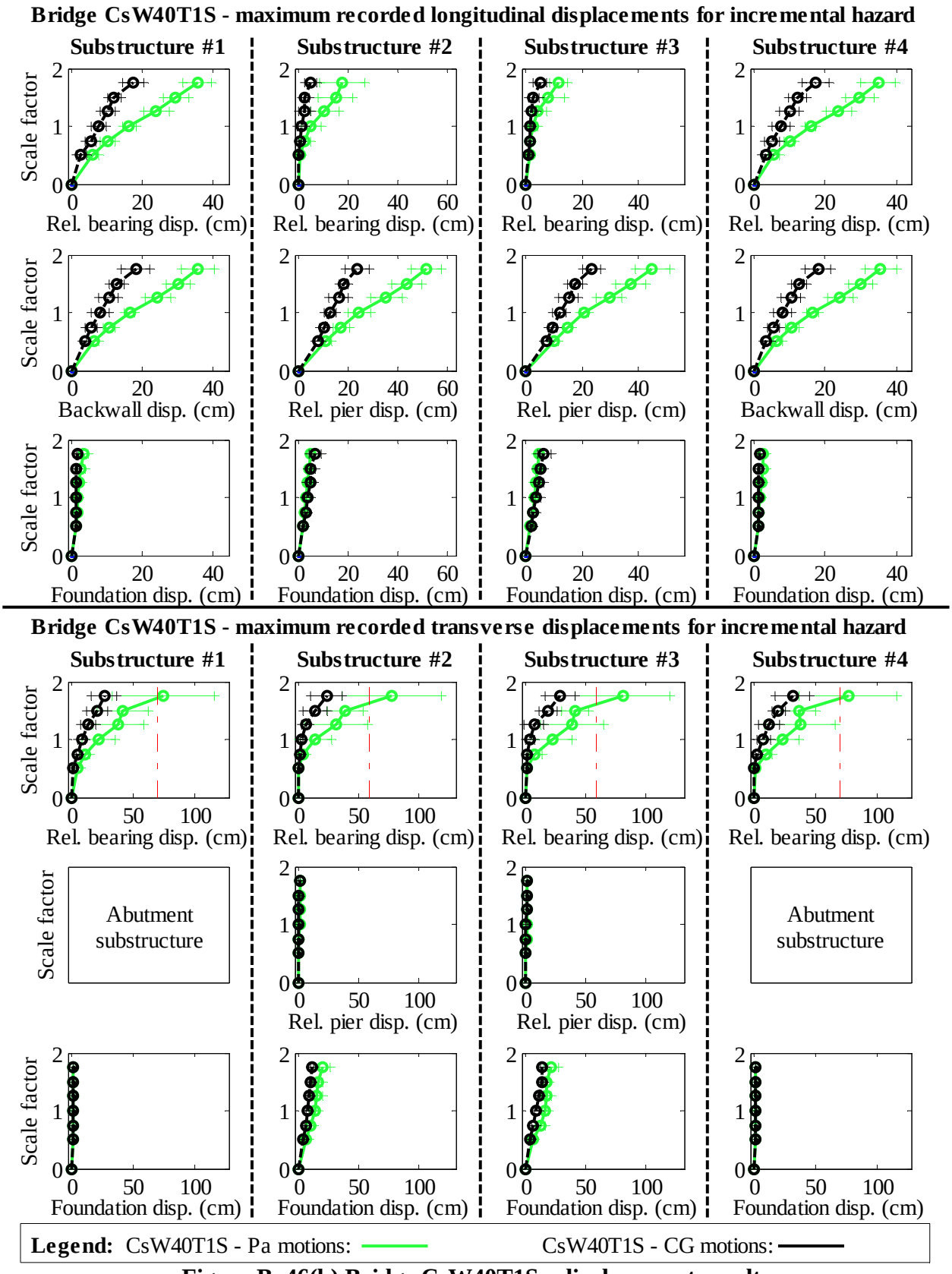

Figure B. 46(b) Bridge CsW40T1S - displacement results

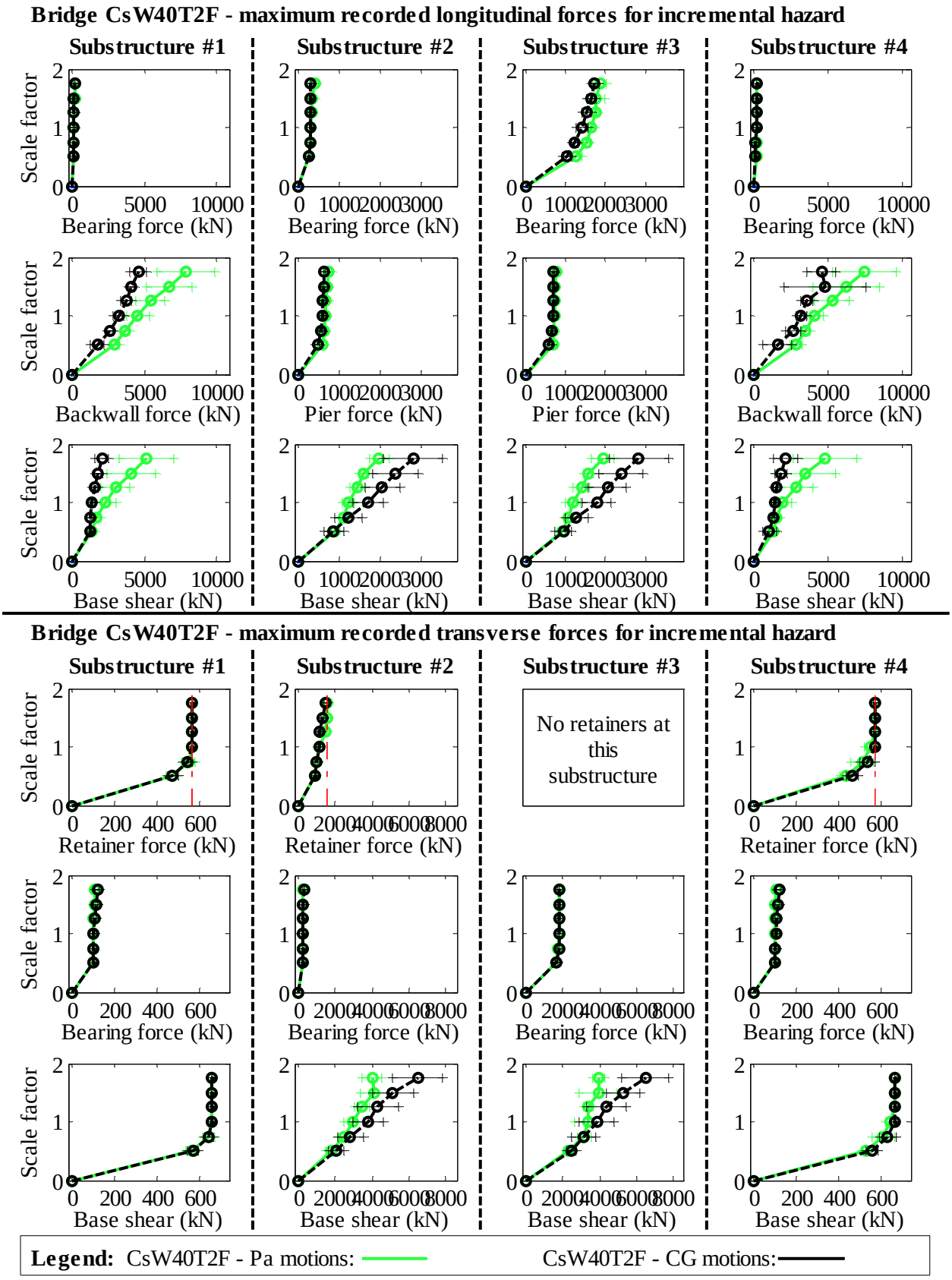

Figure B. 47(a) Bridge CsW40T2F - force results

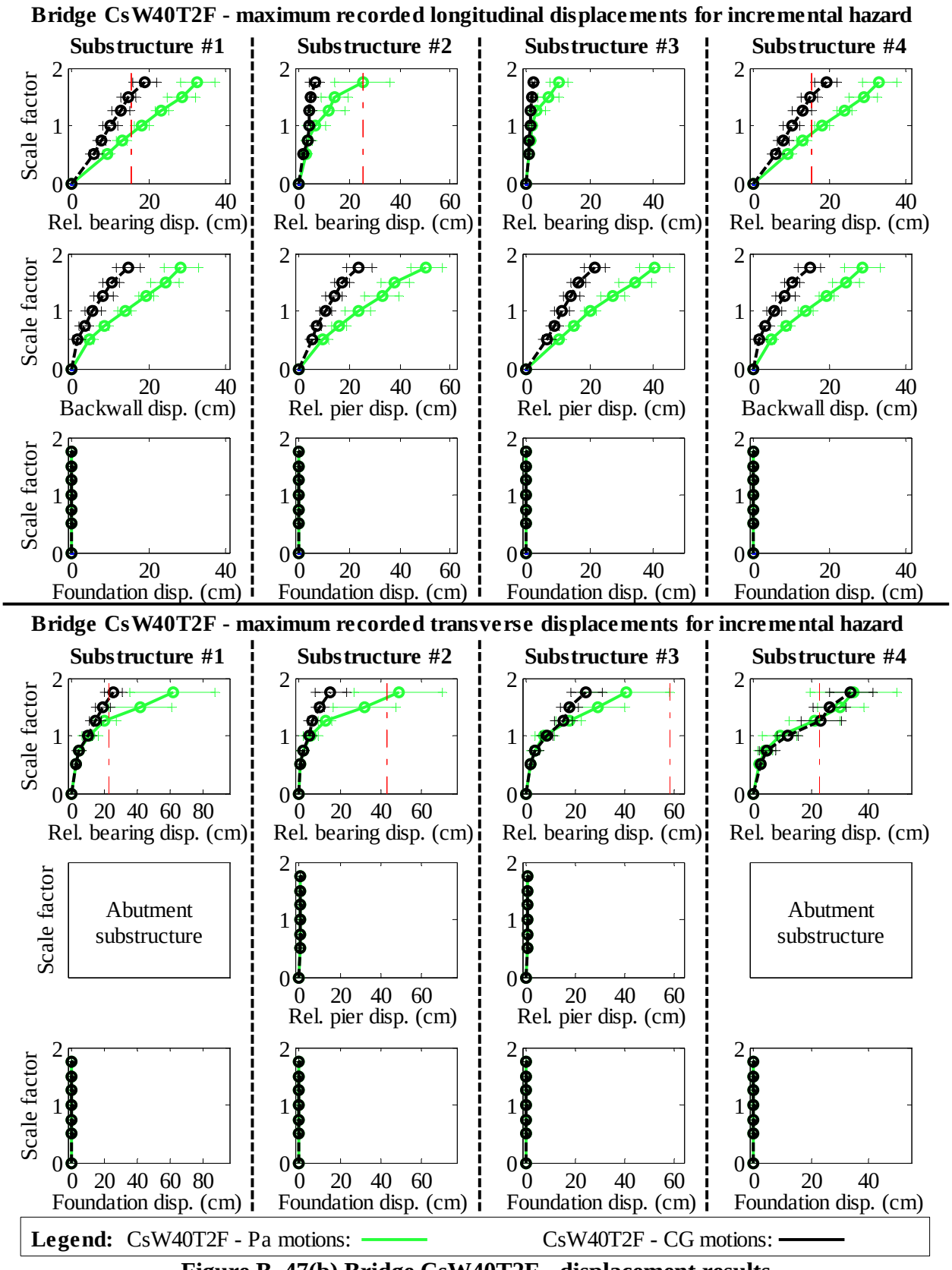

Figure B. 47(b) Bridge CsW40T2F - displacement results

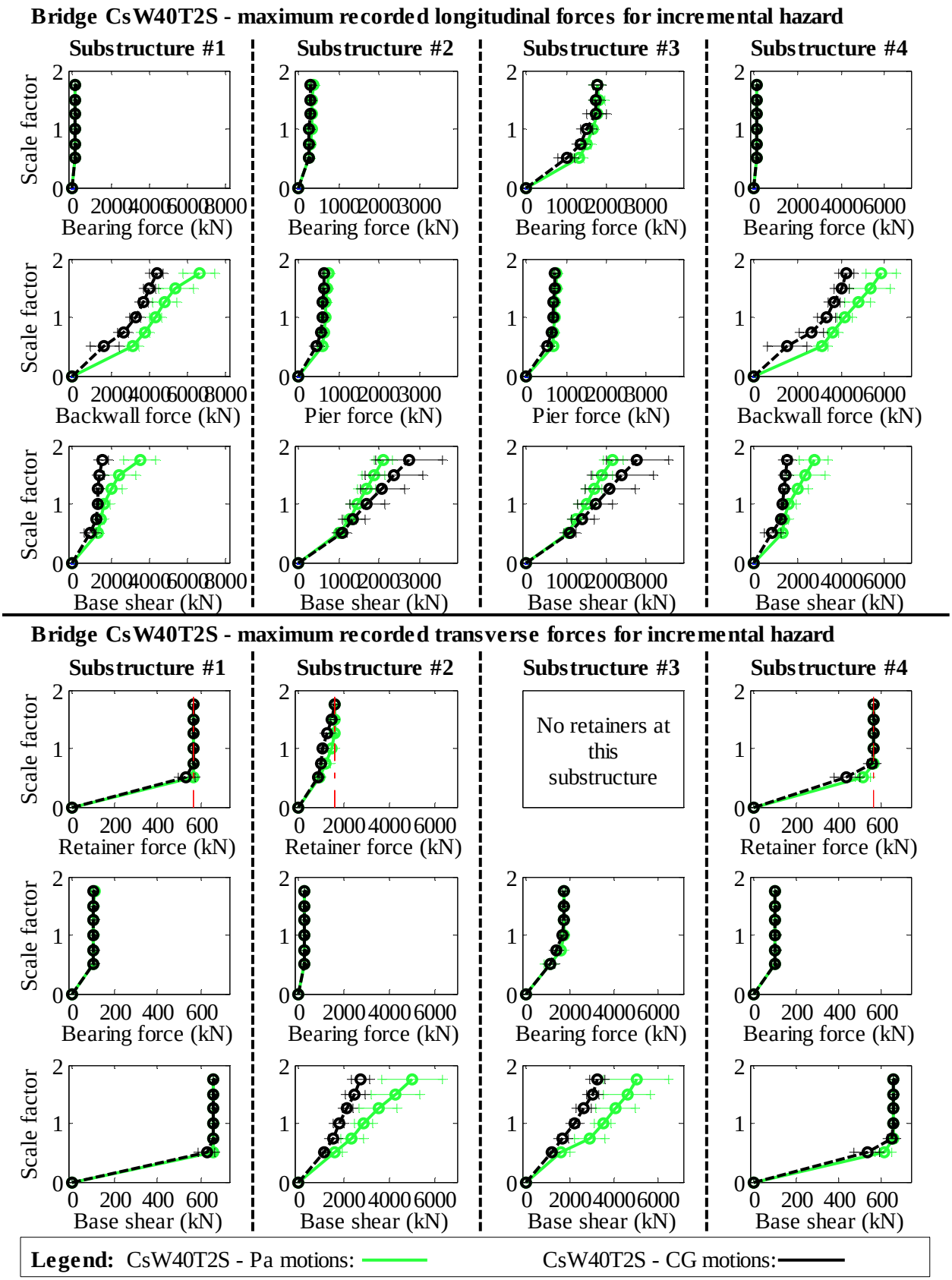

Figure B. 48(a) Bridge CsW40T2S - force results

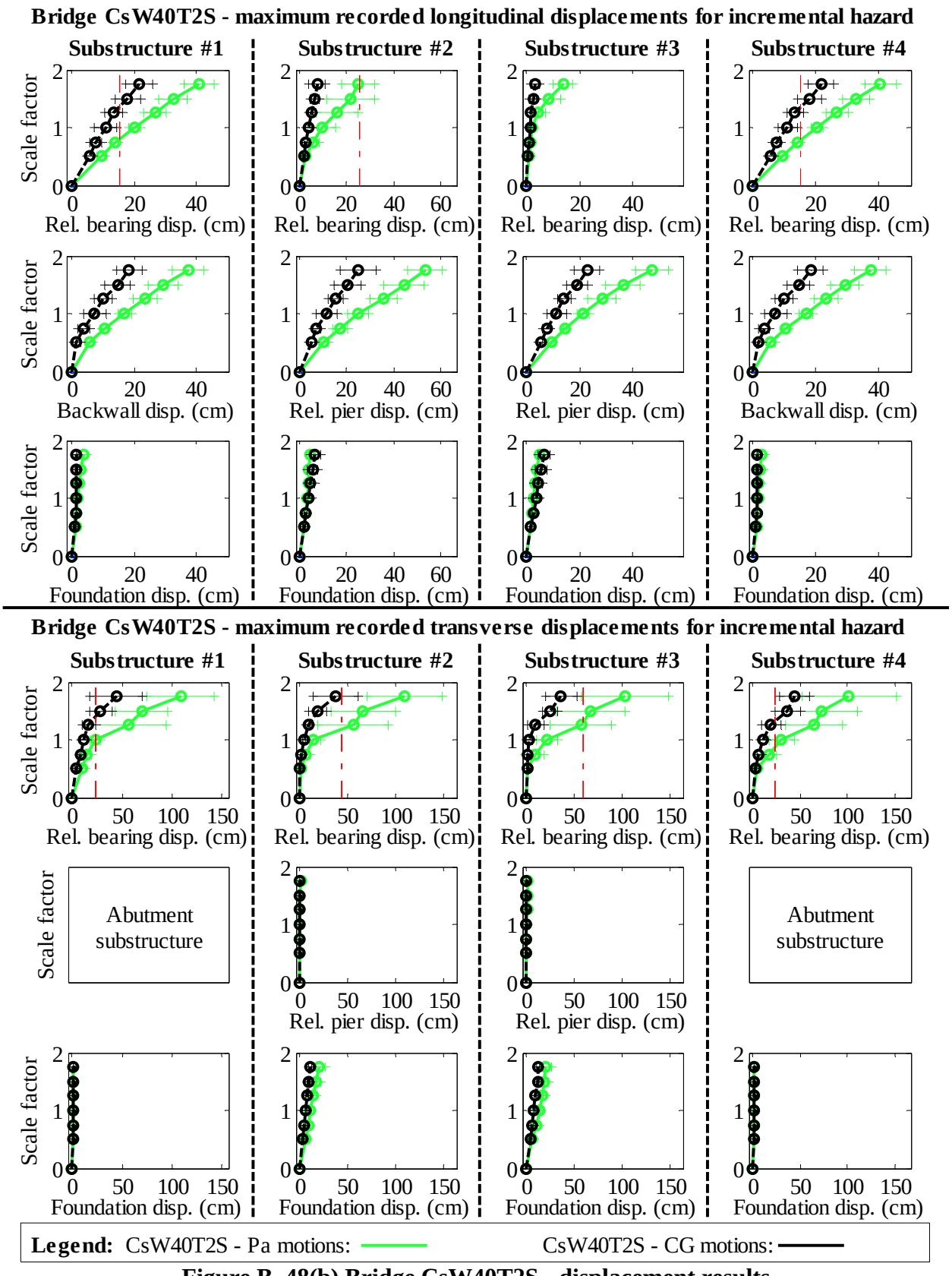

Figure B. 48(b) Bridge CsW40T2S - displacement results

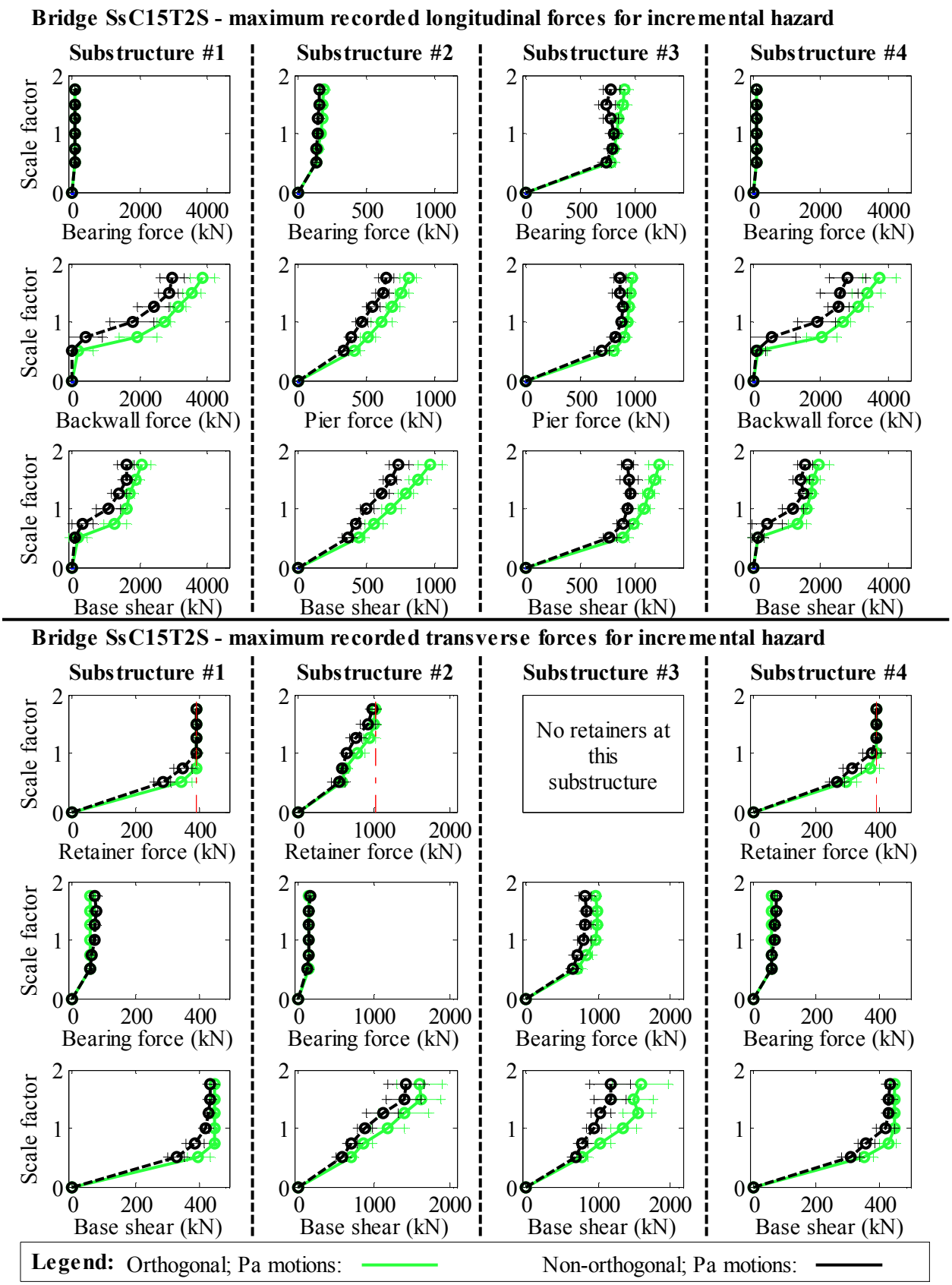

Figure B. 49(a) Bridge SsC15T2S – Non-orthogonal - Pa - force comparison

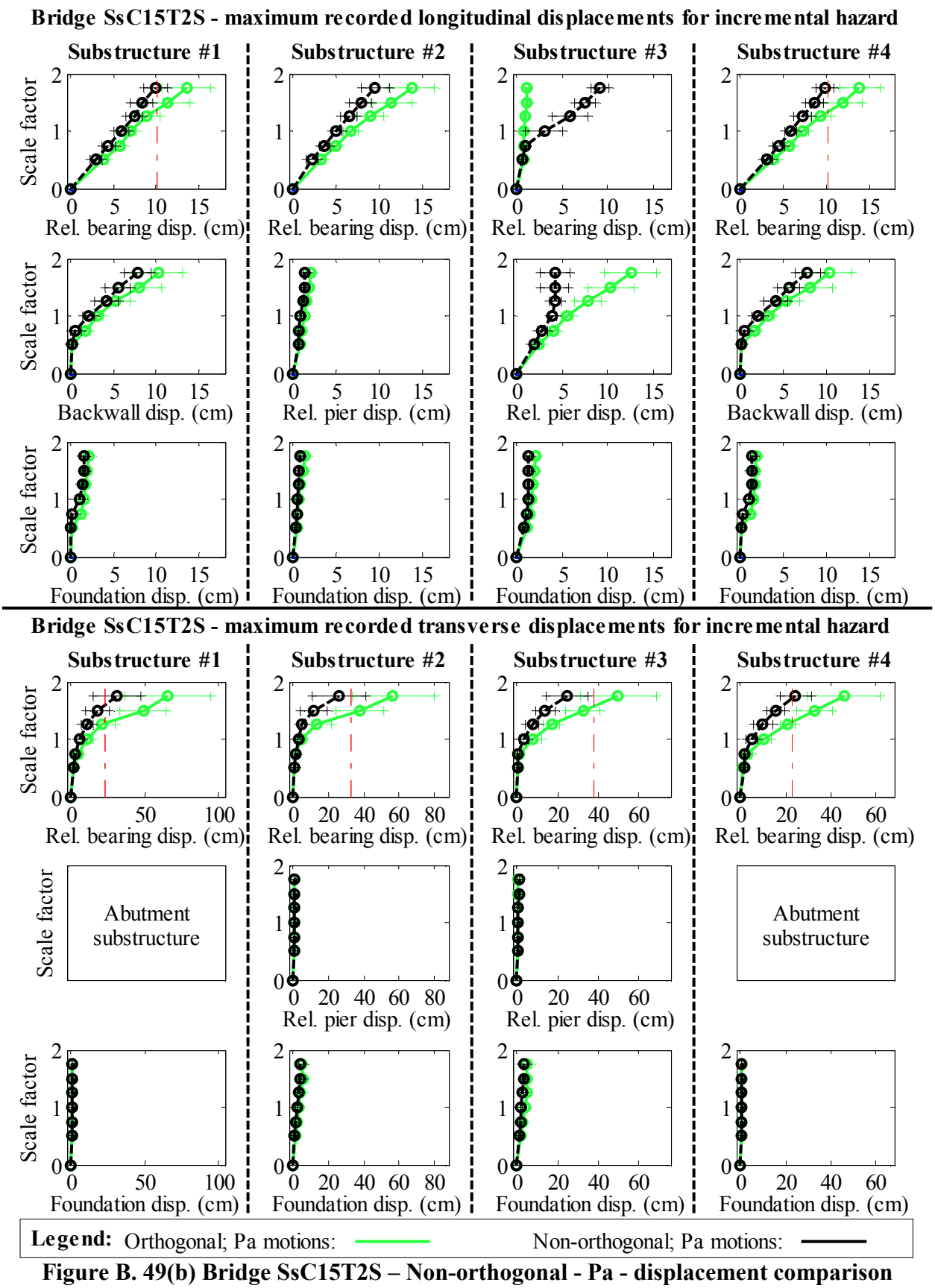

Figure B. 49(b) Bridge SsC15T2S – Non-orthogonal - Pa - displacement comparison

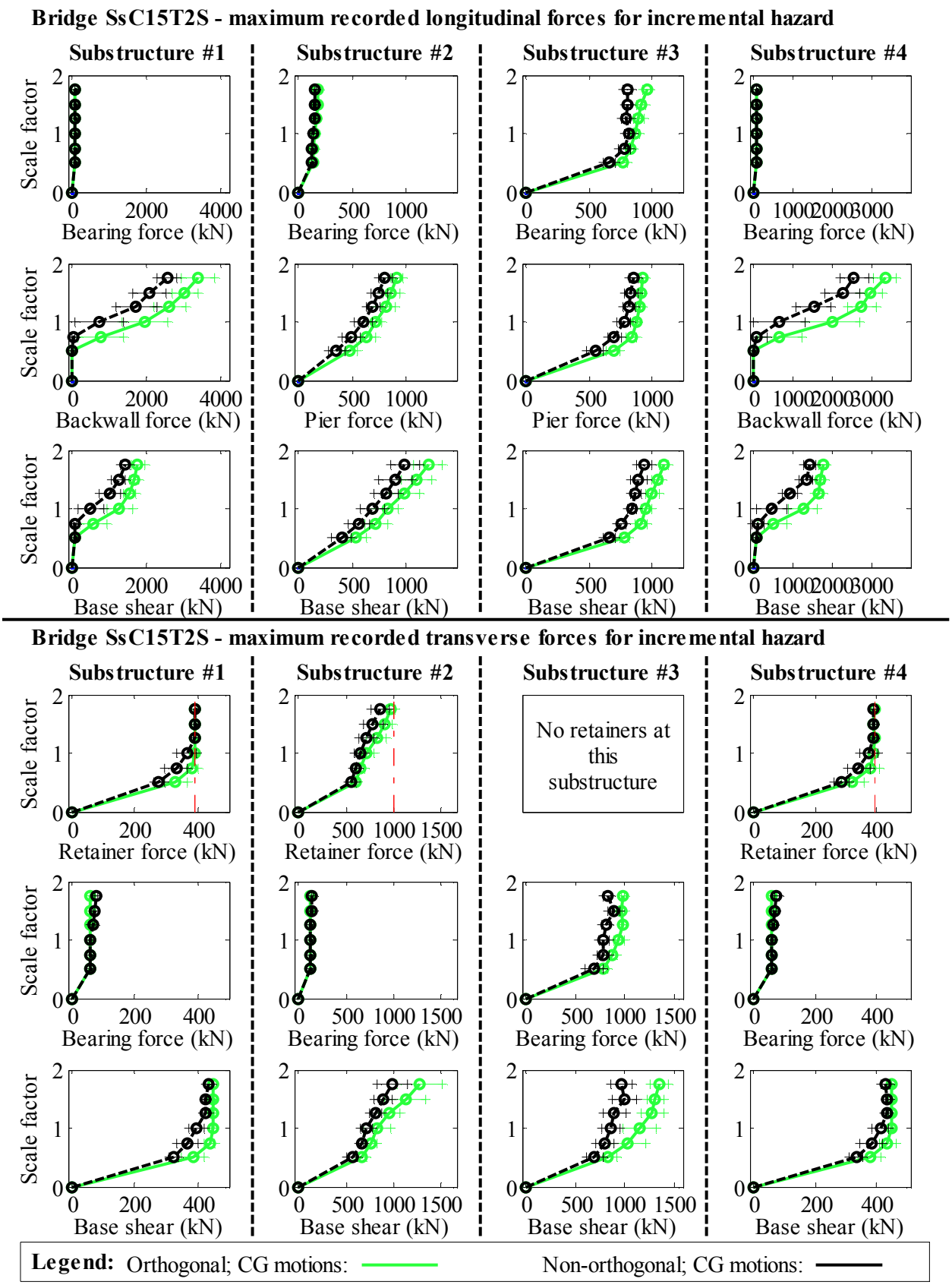

Figure B. 50(a) Bridge SsC15T2S – Non-orthogonal - CG - force comparison

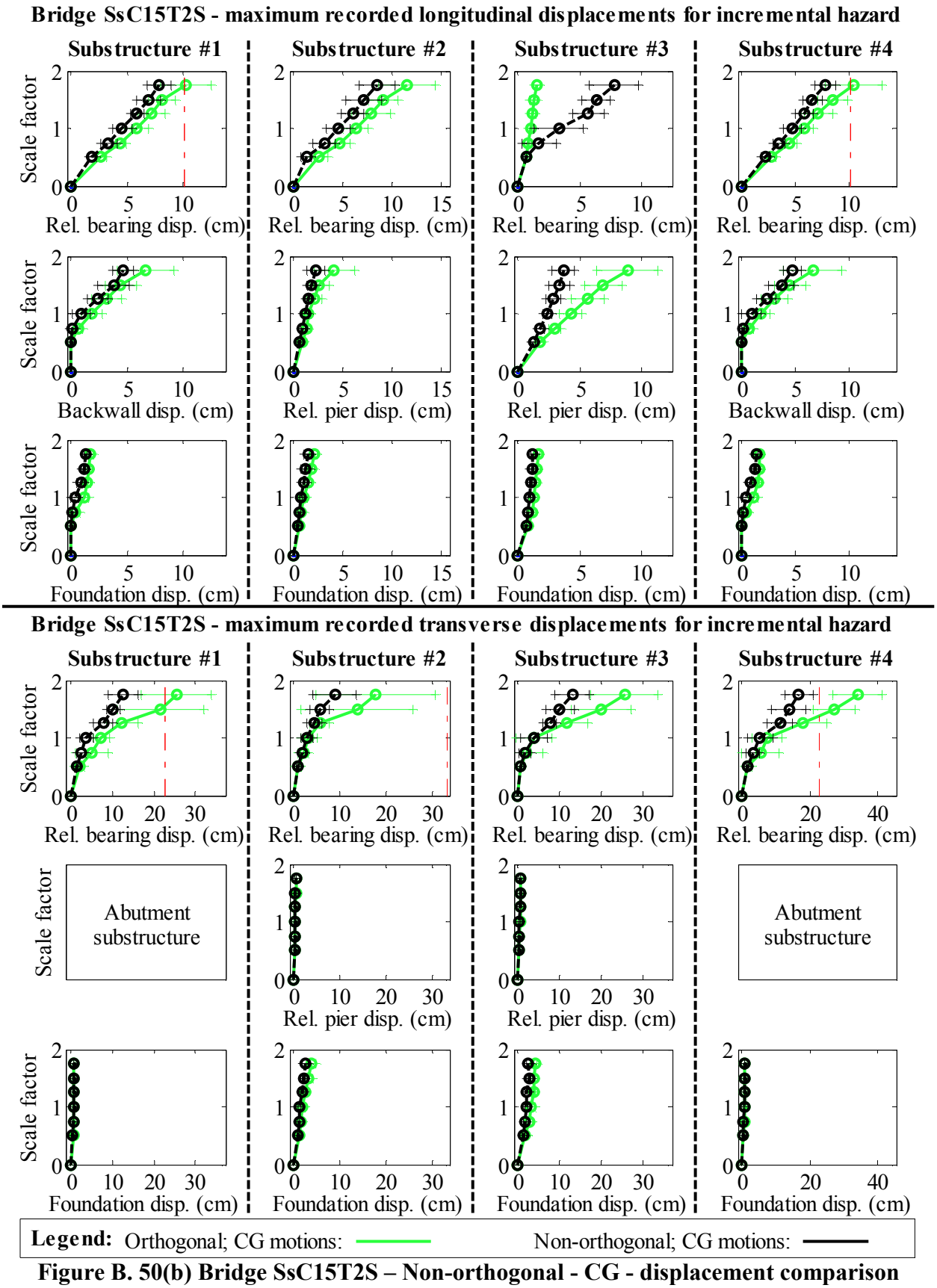

Figure B. 50(b) Bridge SsC15T2S – Non-orthogonal - CG - displacement comparison

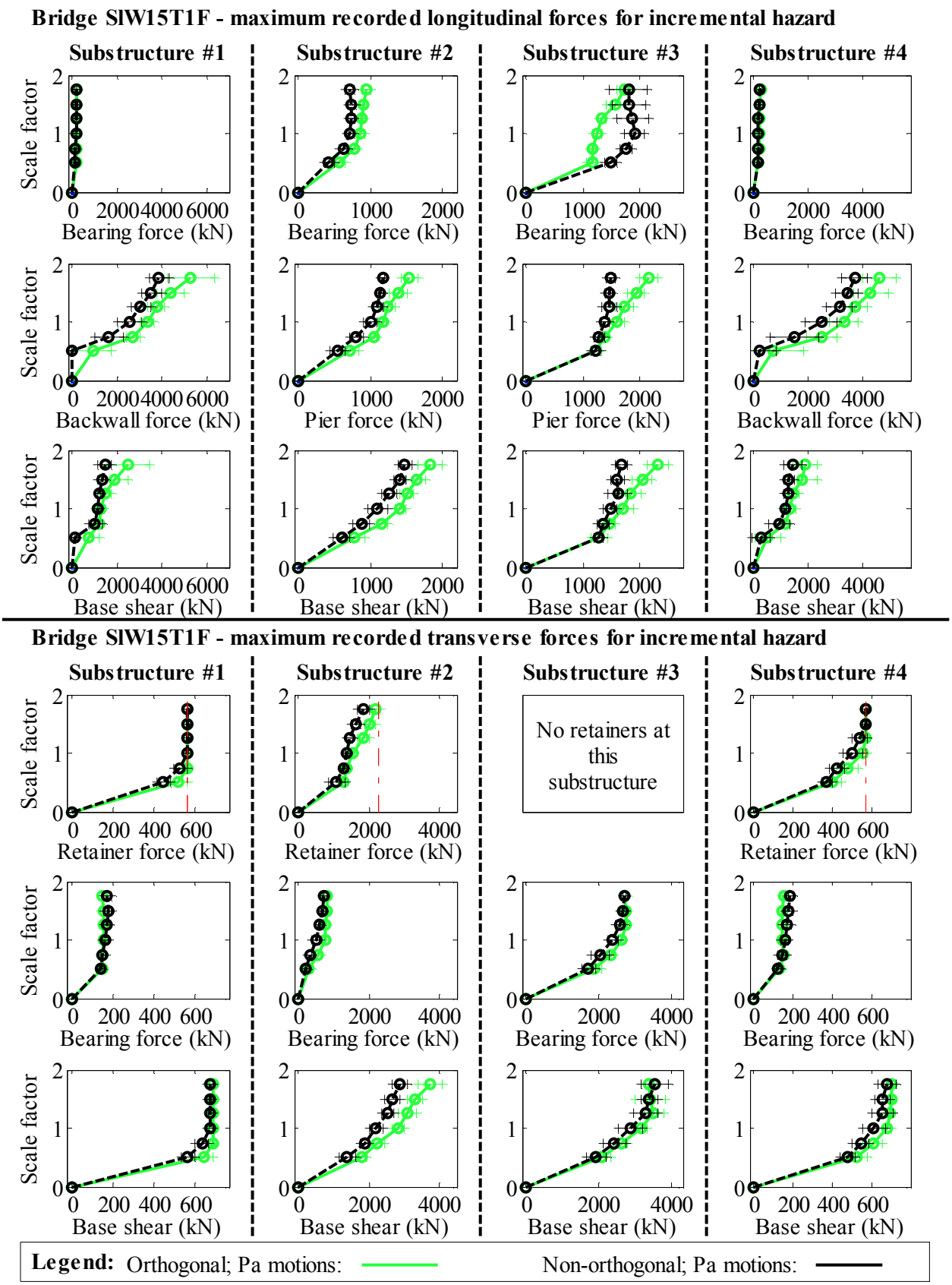

Figure B. 51(a) Bridge SlW15T1F – Non-orthogonal - Pa - force comparison

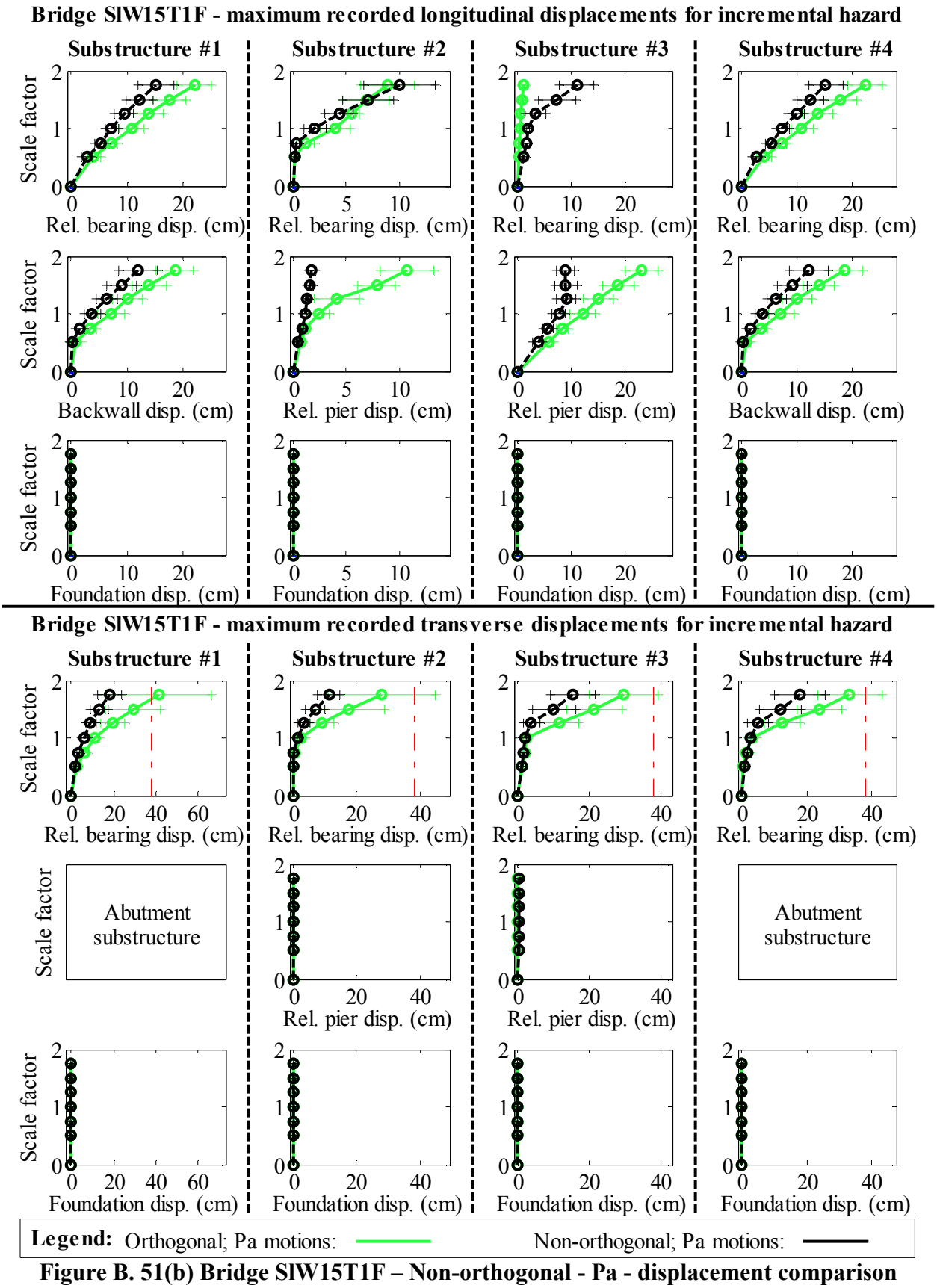

Figure B. 51(b) Bridge SlW15T1F – Non-orthogonal - Pa - displacement comparison

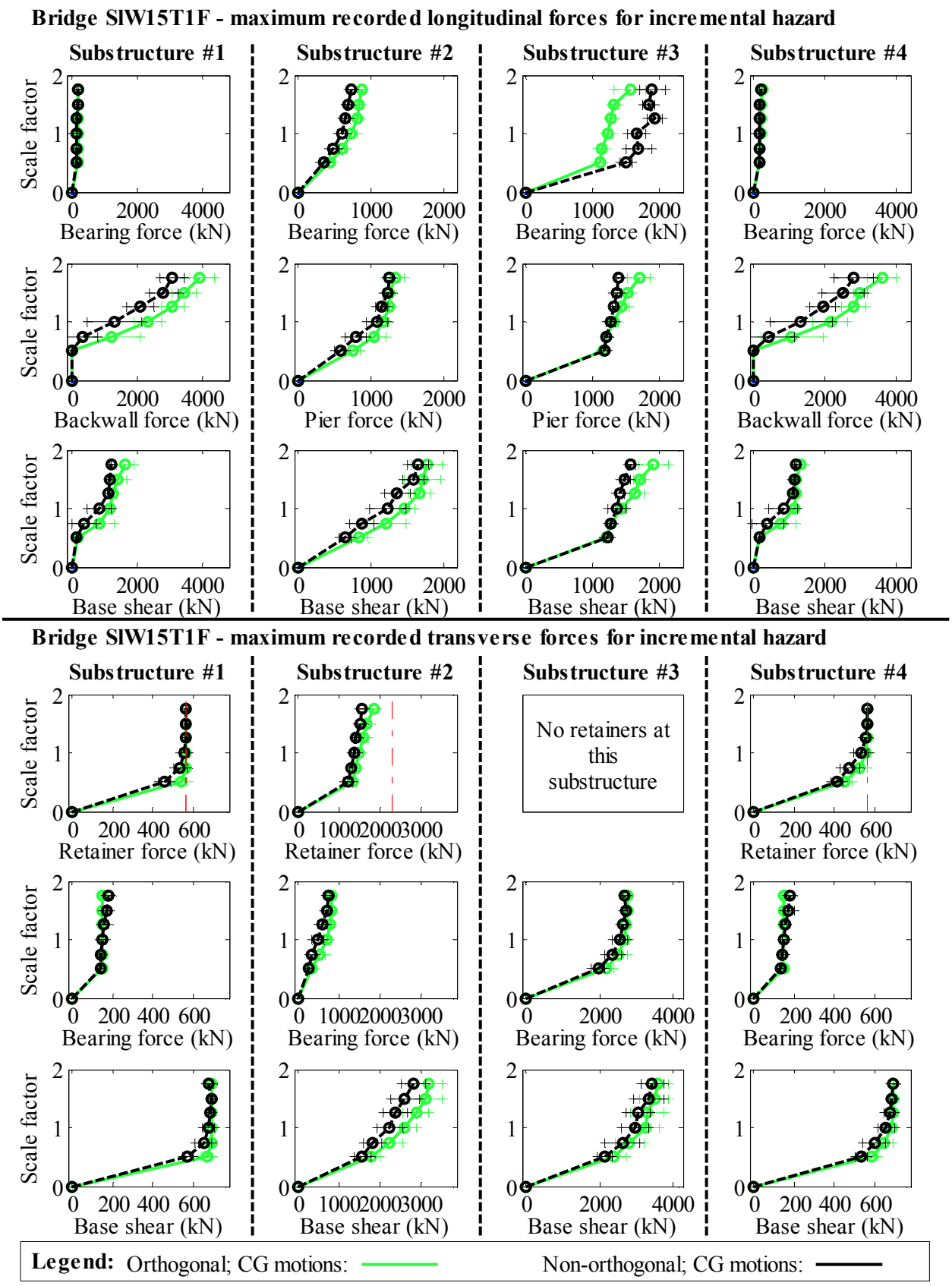

Figure B. 52(a) Bridge SlW15T1F – Non-orthogonal - CG - force comparison

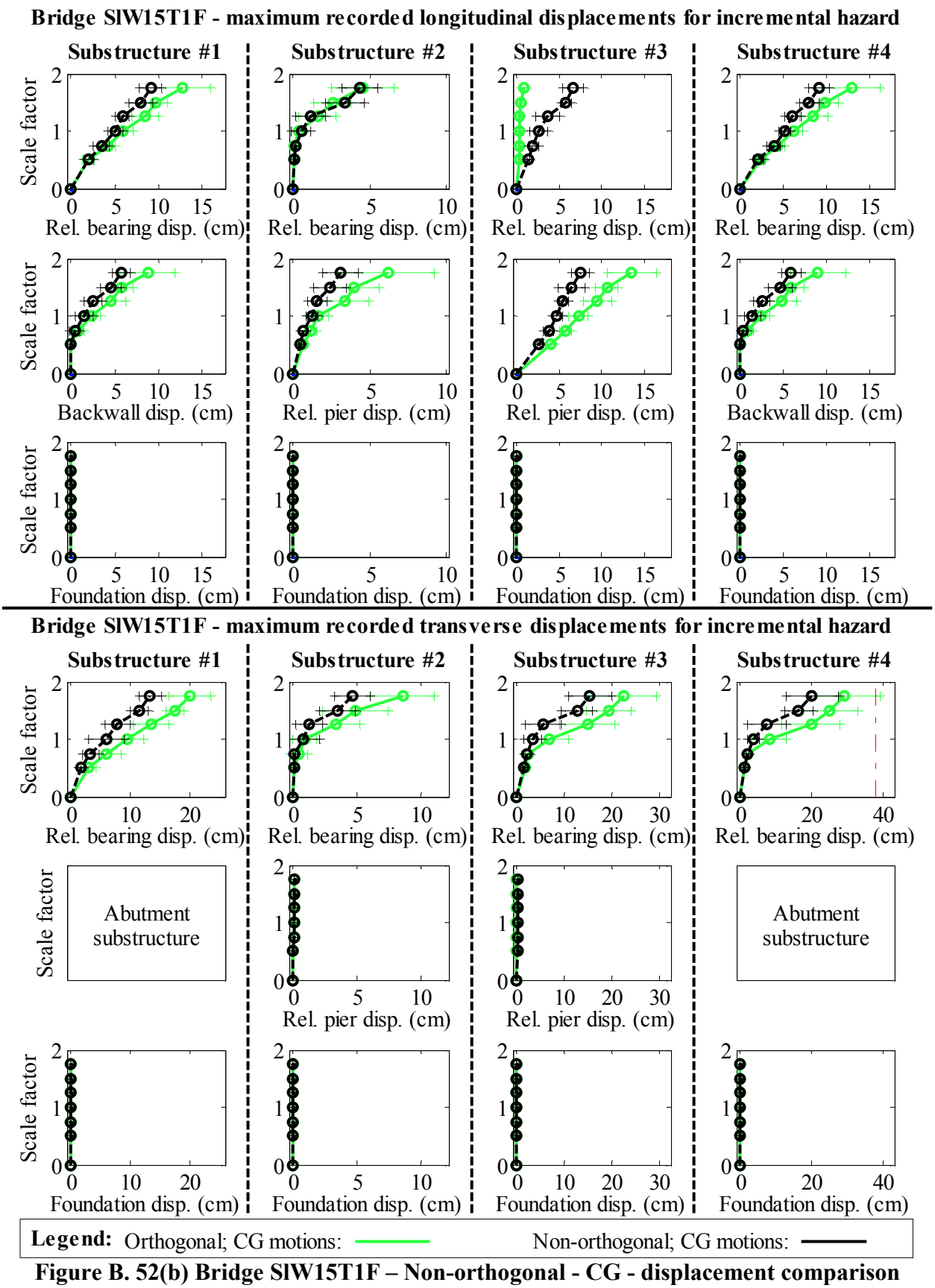

Figure B. 52(b) Bridge SlW15T1F – Non-orthogonal - CG - displacement comparison

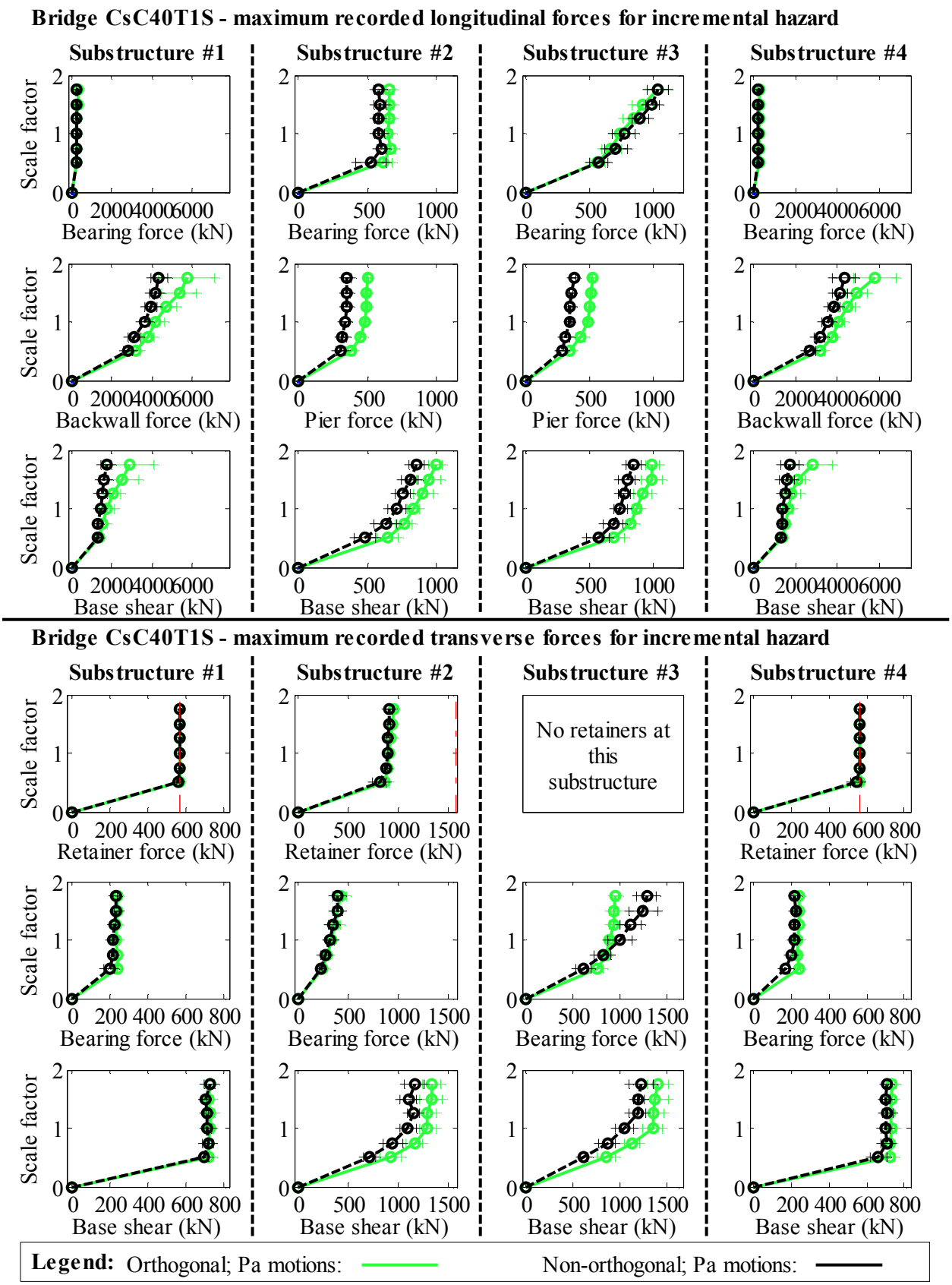

Figure B. 53(a) Bridge CsC40T1S – Non-orthogonal - Pa - force comparison

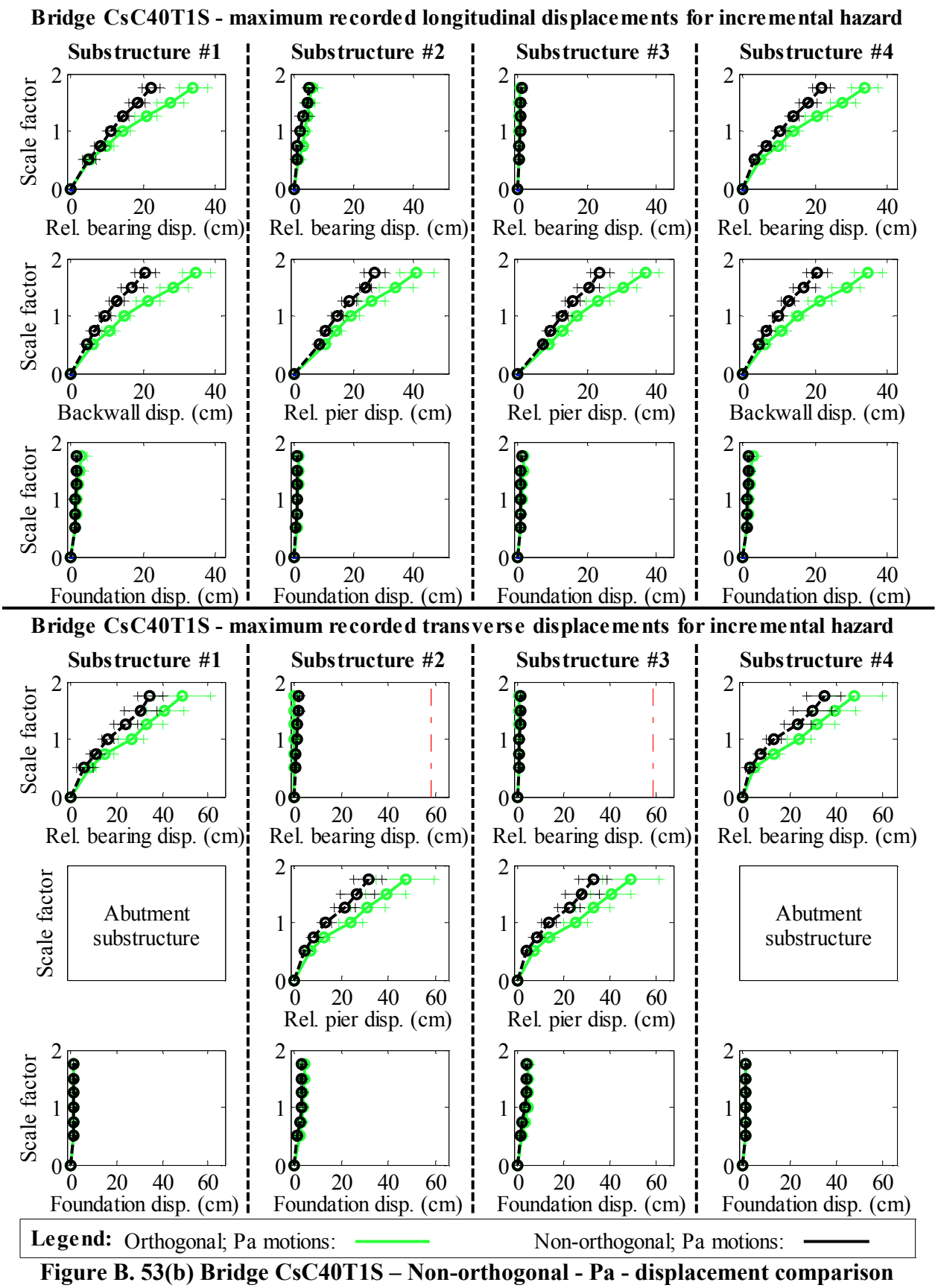

Figure B. 53(b) Bridge CsC40T1S – Non-orthogonal - Pa - displacement comparison

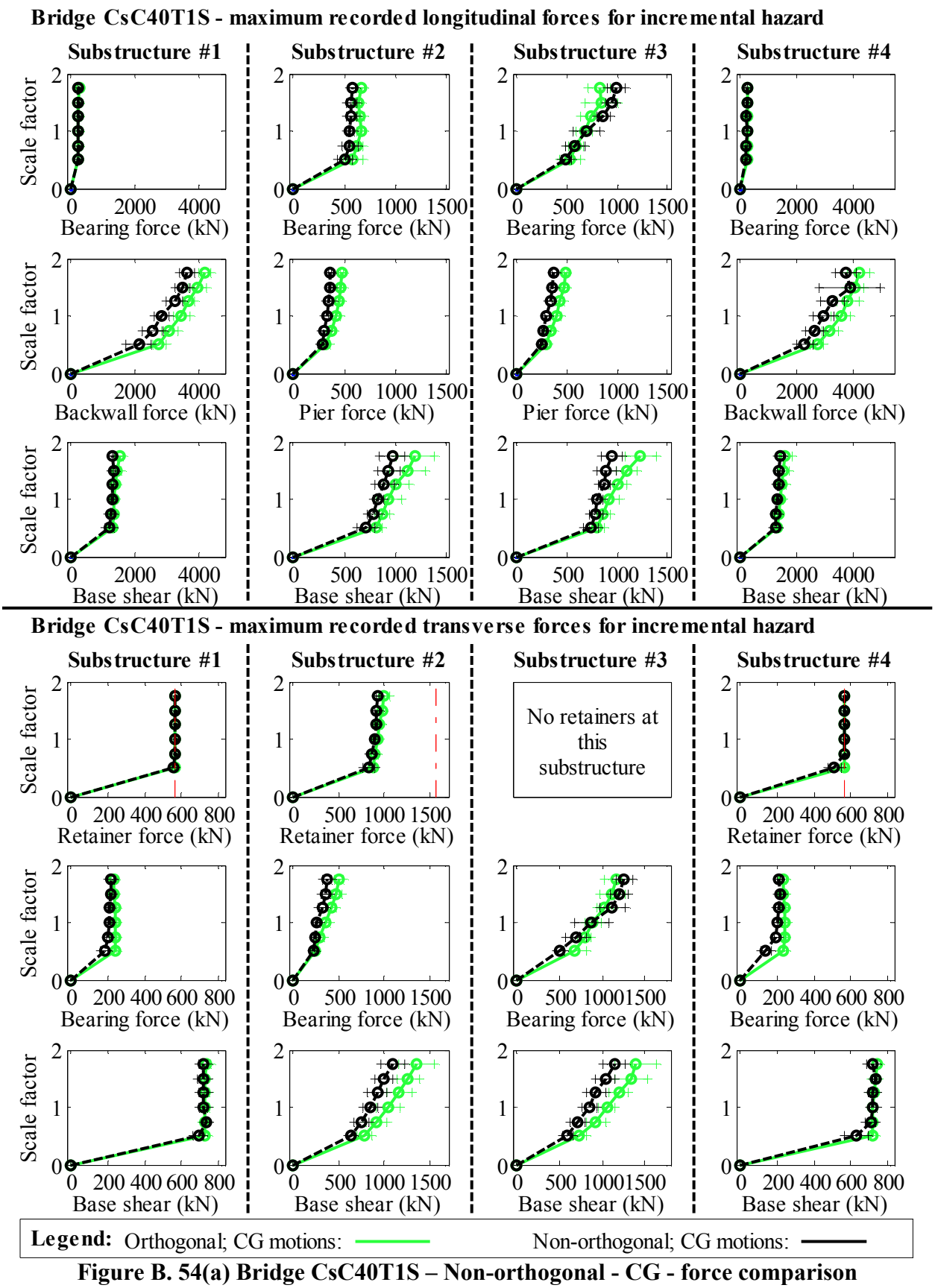

Figure B. 54(a) Bridge CsC40T1S – Non-orthogonal - CG - force comparison

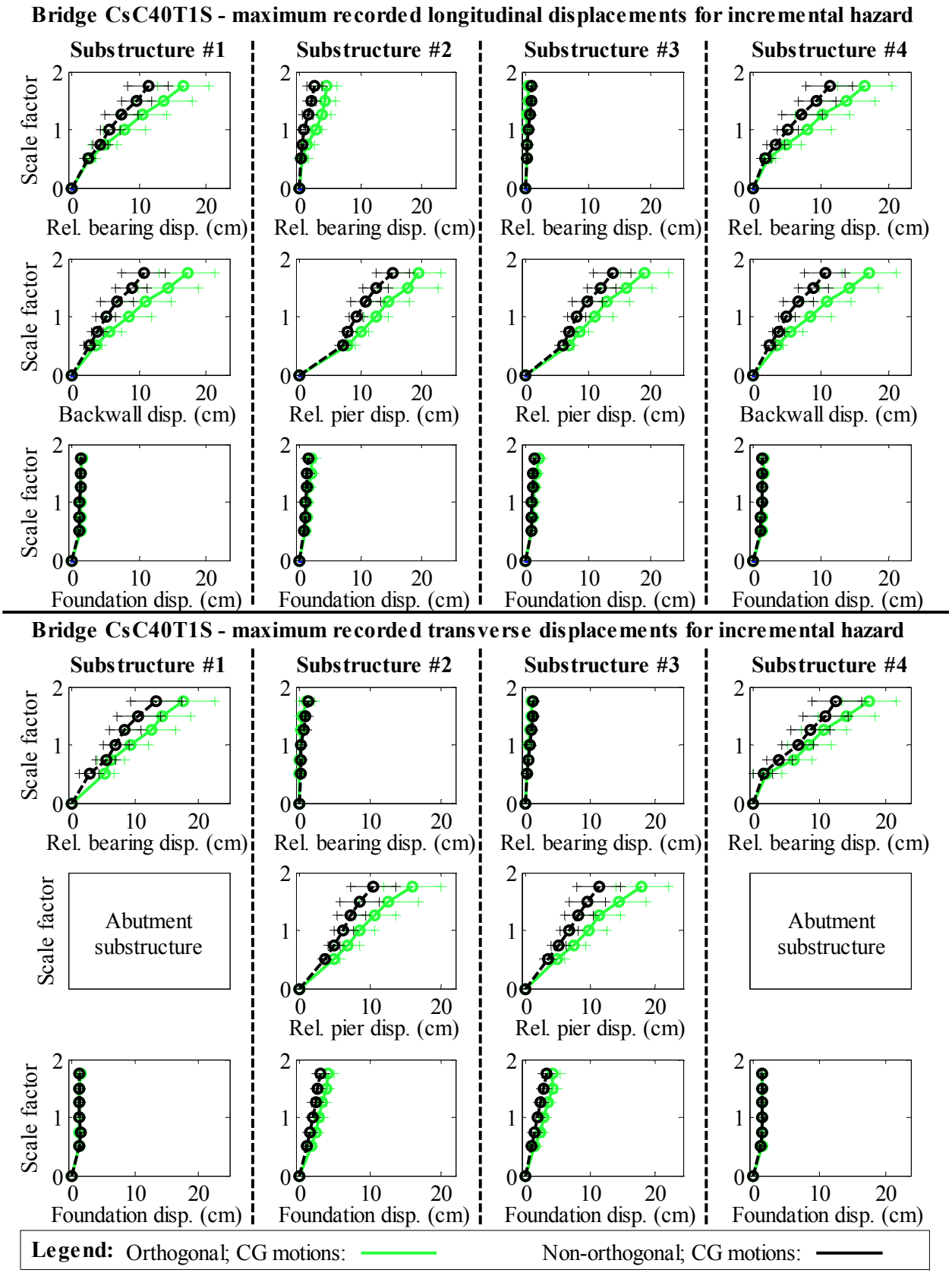

Figure B. 54(b) Bridge CsC40T1S – Non-orthogonal - CG - displacement comparison

APPENDIX C

REDUCED DATA FROM PARAMETRIC ANALYSES

This appendix contains reduced data from the parametric analyses that is used to evaluate the performance of the different systems. Tables C.1 – C.8 show tabulated displacements for each of the bridge variations, ground motion scale factors of SF =1.0 and 1.75. Tables C.9 – C.16 contain tabulated base shears which are normalized with respect to the vertical load at the base. Base shears for a scale factor of SF =1 are presented for the piers as well as the abutments. Maximum diaphragm forces are presented in Tables C.17 – C.20 and will be compared to the diaphragm capacities at a later stage of this project. Tables C.22 – C.27 at the end of this appendix contain sequence of damage results for each bridge system. These tables provide the reached limit states with the corresponding scale factor for longitudinal and transverse directions for both Pa and CG ground motions.

Table C.1 Average maximum longitudinal system displacements for Pa ground motion excitation at SF =1.0 (cm)

			Steel short (Ss) superstructure		Steel long (Sl) superstructure		Precast Concrete (Cs) superstructure	
			Short 4.5 m (15 ft)	Tall 12.2 m (40 ft)	Short 4.5 m (15 ft)	Tall 12.2 m (40 ft)	Short 4.5 m (15 ft)	Tall 12.2 m (40 ft)
Column pier substructure	Type I Bearings	Fixed Fdn.	6.2	11.3	11.3	19.6	7.2	14.6
		Flex. Fdn.	5.5	10.4	11.9	21.1	6.9	14.5
	Type II Bearings	Fixed Fdn.	7.5	13.0	11.7	22.1	10.1	17.9
		Flex. Fdn.	7.3	12.9	12.6	24.9	10.2	20.1
Wall pier substructure	Type I Bearings	Fixed Fdn.	6.1	11.7	10.8	20.6	6.4	14.7
		Flex. Fdn.	5.3	16.3	12.1	23.1	6.9	16.1
	Type II Bearings	Fixed Fdn.	7.3	13.7	11.1	22.2	9.3	18.2
		Flex. Fdn.	7.2	24.9	12.4	24.7	10.5	20.4

Table C.2 Average maximum longitudinal system displacements for CG ground motion excitation at SF =1.0 (cm)

			Steel short (Ss) superstructure		Steel long (Sl) superstructure		Precast Concrete (Cs) superstructure	
			Short 4.5 m (15 ft)	Tall 12.2 m (40 ft)	Short 4.5 m (15 ft)	Tall 12.2 m (40 ft)	Short 4.5 m (15 ft)	Tall 12.2 m (40 ft)
Column pier substructure	Type I Bearings	Fixed Fdn.	5.8	8.3	7.1	10.3	5.7	8.7
		Flex. Fdn.	4.8	6.7	7.5	10.1	4.5	8.0
	Type II Bearings	Fixed Fdn.	5.8	9.2	7.8	12.2	6.9	10.7
		Flex. Fdn.	6.3	9.0	8.4	14.6	7.2	10.7
Wall pier substructure	Type I Bearings	Fixed Fdn.	5.3	8.5	6.1	9.7	4.3	8.6
		Flex. Fdn.	4.6	6.3	6.8	11.0	4.5	7.6
	Type II Bearings	Fixed Fdn.	6.7	9.6	7.0	12.4	6.6	9.9
		Flex. Fdn.	5.9	8.4	8.0	14.0	6.8	11.0

Table C.3 Average maximum transverse system displacements for Pa ground motion excitation at SF =1.0 (cm)

			Steel short (Ss) superstructure		Steel long (Sl) superstructure		Precast Concrete (Cs) superstructure	
			Short 4.5 m (15 ft)	Tall 12.2 m (40 ft)	Short 4.5 m (15 ft)	Tall 12.2 m (40 ft)	Short 4.5 m (15 ft)	Tall 12.2 m (40 ft)
Column pier substructure	Type I Bearings	Fixed Fdn.	7.0	19.9	12.5	30.8	9.1	23.5
		Flex. Fdn.	6.9	21.1	15.8	30.6	9.1	26.3
	Type II Bearings	Fixed Fdn.	9.3	24.9	13.4	29.9	13.1	31.2
		Flex. Fdn.	10.9	25.1	19.6	33.2	15.1	30.5
Wall pier substructure	Type I Bearings	Fixed Fdn.	5.9	6.0	11.0	12.3	7.2	7.7
		Flex. Fdn.	8.5	23.1	18.2	24.8	12.0	23.1
	Type II Bearings	Fixed Fdn.	7.2	7.4	13.9	14.3	10.2	10.9
		Flex. Fdn.	19.2	36.9	27.7	46.0	20.5	30.4

Table C.4 Average maximum transverse system displacements for CG ground motion excitation at SF =1.0 (cm)

			Steel short (Ss) superstructure		Steel long (Sl) superstructure		Precast Concrete (Cs) superstructure	
			Short 4.5 m (15 ft)	Tall 12.2 m (40 ft)	Short 4.5 m (15 ft)	Tall 12.2 m (40 ft)	Short 4.5 m (15 ft)	Tall 12.2 m (40 ft)
Column pier substructure	Type I Bearings	Fixed Fdn.	5.8	9.6	8.2	12.6	7.0	9.8
		Flex. Fdn.	7.7	10.1	8.0	12.6	5.0	9.3
	Type II Bearings	Fixed Fdn.	12.4	12.6	13.4	14.6	16.3	12.4
		Flex. Fdn.	7.4	12.8	9.6	15.4	8.1	12.1
Wall pier substructure	Type I Bearings	Fixed Fdn.	5.8	5.8	9.5	9.3	6.8	6.7
		Flex. Fdn.	8.2	9.8	10.0	11.6	6.0	8.1
	Type II Bearings	Fixed Fdn.	9.8	9.4	10.7	13.5	13.1	11.6
		Flex. Fdn.	18.2	17.7	10.2	11.8	8.5	11.6

Table C.5 Average maximum longitudinal system displacements for Pa ground motion excitation at SF =1.75 (cm)

			Steel short (Ss) superstructure		Steel long (Sl) superstructure		Precast Concrete (Cs) superstructure	
			Short 4.5 m (15 ft)	Tall 12.2 m (40 ft)	Short 4.5 m (15 ft)	Tall 12.2 m (40 ft)	Short 4.5 m (15 ft)	Tall 12.2 m (40 ft)
Column pier substructure	Type I Bearings	Fixed Fdn.	12.3	22.8	24.4	36.7	16.4	30.9
		Flex. Fdn.	12.2	23.7	27.1	44.6	17.7	33.9
	Type II Bearings	Fixed Fdn.	14.1	22.7	25.0	41.2	20.6	32.5
		Flex. Fdn.	13.9	28.9	28.6	48.9	22.7	38.9
Wall pier substructure	Type I Bearings	Fixed Fdn.	11.9	31.3	22.4	40.8	15.6	28.8
		Flex. Fdn.	12.7	37.9	26.9	44.1	18.0	35.5
	Type II Bearings	Fixed Fdn.	13.2	38.9	24.2	41.4	19.6	32.9
		Flex. Fdn.	16.4	52.3	28.3	47.9	23.5	40.7

Table C.6 Average maximum longitudinal system displacements for CG ground motion excitation at SF =1.75 (cm)

			Steel short (Ss) superstructure		Steel long (Sl) superstructure		Precast Concrete (Cs) superstructure	
			Short 4.5 m (15 ft)	Tall 12.2 m (40 ft)	Short 4.5 m (15 ft)	Tall 12.2 m (40 ft)	Short 4.5 m (15 ft)	Tall 12.2 m (40 ft)
Column pier substructure	Type I Bearings	Fixed Fdn.	10.3	15.0	13.4	20.6	10.6	16.6
		Flex. Fdn.	8.5	14.6	14.8	23.6	9.9	16.6
	Type II Bearings	Fixed Fdn.	11.2	17.5	14.0	24.3	12.3	20.0
		Flex. Fdn.	11.5	17.9	15.3	30.8	13.7	23.0
Wall pier substructure	Type I Bearings	Fixed Fdn.	10.9	14.5	12.9	20.3	10.4	16.1
		Flex. Fdn.	9.7	14.9	14.0	22.9	10.4	17.4
	Type II Bearings	Fixed Fdn.	12.1	16.7	13.6	23.7	11.6	19.0
		Flex. Fdn.	10.7	17.4	15.5	27.2	13.6	21.8

Table C.7 Average maximum transverse system displacements for Pa ground motion excitation at SF =1.75 (cm)

			Steel short (Ss) superstructure		Steel long (Sl) superstructure		Precast Concrete (Cs) superstructure	
			Short 4.5 m (15 ft)	Tall 12.2 m (40 ft)	Short 4.5 m (15 ft)	Tall 12.2 m (40 ft)	Short 4.5 m (15 ft)	Tall 12.2 m (40 ft)
Column pier substructure	Type I Bearings	Fixed Fdn.	38.5	47.7	35.9	60.5	36.9	48.4
		Flex. Fdn.	47.0	47.7	39.7	55.0	37.7	48.8
	Type II Bearings	Fixed Fdn.	62.5	60.9	60.5	59.9	59.6	52.2
		Flex. Fdn.	65.5	57.2	57.4	60.6	66.9	54.3
Wall pier substructure	Type I Bearings	Fixed Fdn.	40.4	37.6	41.3	38.1	44.3	38.1
		Flex. Fdn.	70.9	76.7	67.3	114.9	55.3	80.6
	Type II Bearings	Fixed Fdn.	66.5	58.8	62.4	69.5	63.8	61.6
		Flex. Fdn.	97.5	97.4	114.7	128.2	98.3	109.1

Table C.8 Average maximum transverse system displacements for CG ground motion excitation at SF =1.75 (cm)

			Steel short (Ss) superstructure		Steel long (Sl) superstructure		Precast Concrete (Cs) superstructure	
			Short 4.5 m (15 ft)	Tall 12.2 m (40 ft)	Short 4.5 m (15 ft)	Tall 12.2 m (40 ft)	Short 4.5 m (15 ft)	Tall 12.2 m (40 ft)
Column pier substructure	Type I Bearings	Fixed Fdn.	17.7	20.2	29.8	23.4	18.1	16.8
		Flex. Fdn.	20.8	20.7	17.5	23.3	22.5	17.8
	Type II Bearings	Fixed Fdn.	31.6	27.1	29.9	29.9	31.6	23.7
		Flex. Fdn.	33.9	24.8	26.6	27.9	40.3	23.3
Wall pier substructure	Type I Bearings	Fixed Fdn.	18.0	22.6	29.0	33.3	16.1	18.2
		Flex. Fdn.	36.9	40.9	22.2	28.8	22.6	31.0
	Type II Bearings	Fixed Fdn.	37.7	29.4	35.7	39.7	32.1	34.0
		Flex. Fdn.	52.4	66.4	28.9	39.3	39.1	44.1

Table C.9 Average maximum normalized longitudinal pier base shear for Pa ground motion excitation at SF =1

			Steel short (Ss) superstructure				Steel long (Sl) superstructure				Precast Concrete (Cs) superstructure			
			Short 4.5 m (15 ft)		Tall 12.2 m (40 ft)		Short 4.5 m (15 ft)		Tall 12.2 m (40 ft)		Short 4.5 m (15 ft)		Tall 12.2 m (40 ft)	
			Pier 1	Pier 2	Pier 1	Pier 2	Pier 1	Pier 2	Pier 1	Pier 2	Pier 1	Pier 2	Pier 1	Pier 2
Column pier substructure	Type I Bearings	Fixed Fdn.	0.31	0.45	0.19	0.20	0.24	0.28	0.12	0.12	0.33	0.41	0.17	0.17
		Flex. Fdn.	0.37	0.50	0.31	0.31	0.27	0.30	0.17	0.18	0.37	0.46	0.24	0.25
	Type II Bearings	Fixed Fdn.	0.27	0.46	0.19	0.21	0.19	0.28	0.12	0.11	0.23	0.41	0.16	0.16
		Flex. Fdn.	0.32	0.51	0.31	0.32	0.21	0.30	0.17	0.19	0.27	0.43	0.24	0.25
Wall pier substructure	Type I Bearings	Fixed Fdn.	0.38	0.46	0.25	0.24	0.27	0.33	0.18	0.18	0.34	0.42	0.23	0.22
		Flex. Fdn.	0.41	0.54	0.31	0.29	0.30	0.37	0.21	0.21	0.36	0.48	0.28	0.29
	Type II Bearings	Fixed Fdn.	0.34	0.44	0.24	0.23	0.24	0.32	0.18	0.18	0.29	0.41	0.22	0.22
		Flex. Fdn.	0.40	0.53	0.28	0.30	0.27	0.36	0.20	0.21	0.35	0.48	0.27	0.28

Table C.10 Average maximum normalized longitudinal pier base shear for CG ground motion excitation at SF =1

			Steel short (Ss) superstructure				Steel long (Sl) superstructure				Precast Concrete (Cs) superstructure			
			Short 4.5 m (15 ft)		Tall 12.2 m (40 ft)		Short 4.5 m (15 ft)		Tall 12.2 m (40 ft)		Short 4.5 m (15 ft)		Tall 12.2 m (40 ft)	
			Pier 1	Pier 2	Pier 1	Pier 2	Pier 1	Pier 2	Pier 1	Pier 2	Pier 1	Pier 2	Pier 1	Pier 2
Column pier substructure	Type I Bearings	Fixed Fdn.	0.40	0.43	0.20	0.20	0.22	0.27	0.12	0.12	0.32	0.39	0.17	0.15
		Flex. Fdn.	0.44	0.48	0.35	0.34	0.25	0.28	0.19	0.19	0.35	0.42	0.27	0.26
	Type II Bearings	Fixed Fdn.	0.37	0.43	0.20	0.20	0.20	0.27	0.12	0.12	0.28	0.39	0.15	0.15
		Flex. Fdn.	0.39	0.45	0.35	0.34	0.22	0.28	0.20	0.19	0.28	0.40	0.26	0.26
Wall pier substructure	Type I Bearings	Fixed Fdn.	0.51	0.44	0.36	0.35	0.28	0.28	0.24	0.24	0.38	0.37	0.31	0.31
		Flex. Fdn.	0.53	0.49	0.37	0.36	0.29	0.31	0.26	0.27	0.39	0.43	0.31	0.32
	Type II Bearings	Fixed Fdn.	0.51	0.44	0.38	0.38	0.28	0.27	0.23	0.24	0.41	0.36	0.31	0.32
		Flex. Fdn.	0.47	0.45	0.37	0.36	0.28	0.31	0.25	0.26	0.38	0.40	0.31	0.31

Table C.11 Average maximum normalized transverse pier base shear for Pa ground motion excitation at SF =1

			Steel short (Ss) superstructure				Steel long (Sl) superstructure				Precast Concrete (Cs) superstructure			
			Short 4.5 m (15 ft)		Tall 12.2 m (40 ft)		Short 4.5 m (15 ft)		Tall 12.2 m (40 ft)		Short 4.5 m (15 ft)		Tall 12.2 m (40 ft)	
			Pier 1	Pier 2	Pier 1	Pier 2	Pier 1	Pier 2	Pier 1	Pier 2	Pier 1	Pier 2	Pier 1	Pier 2
Column pier substructure	Type I Bearings	Fixed Fdn.	0.69	0.61	0.35	0.35	0.59	0.61	0.23	0.23	0.74	0.70	0.32	0.32
		Flex. Fdn.	0.56	0.63	0.39	0.40	0.49	0.57	0.26	0.26	0.60	0.68	0.37	0.39
	Type II Bearings	Fixed Fdn.	0.63	0.62	0.34	0.36	0.57	0.62	0.23	0.23	0.63	0.70	0.32	0.32
		Flex. Fdn.	0.56	0.64	0.38	0.42	0.50	0.62	0.26	0.26	0.51	0.66	0.36	0.38
Wall pier substructure	Type I Bearings	Fixed Fdn.	0.56	0.54	0.56	0.55	0.55	0.62	0.59	0.62	0.58	0.61	0.59	0.57
		Flex. Fdn.	0.47	0.59	0.61	0.68	0.55	0.65	0.50	0.67	0.62	0.68	0.62	0.71
	Type II Bearings	Fixed Fdn.	0.54	0.57	0.55	0.54	0.48	0.63	0.54	0.61	0.51	0.63	0.54	0.60
		Flex. Fdn.	0.47	0.58	0.56	0.63	0.51	0.68	0.56	0.70	0.49	0.65	0.52	0.63

Table C.12 Average maximum normalized transverse pier base shear for CG ground motion excitation at SF =1

			Steel short (Ss) superstructure				Steel long (Sl) superstructure				Precast Concrete (Cs) superstructure			
			Short 4.5 m (15 ft)		Tall 12.2 m (40 ft)		Short 4.5 m (15 ft)		Tall 12.2 m (40 ft)		Short 4.5 m (15 ft)		Tall 12.2 m (40 ft)	
			Pier 1	Pier 2	Pier 1	Pier 2	Pier 1	Pier 2	Pier 1	Pier 2	Pier 1	Pier 2	Pier 1	Pier 2
Column pier substructure	Type I Bearings	Fixed Fdn.	0.63	0.58	0.30	0.33	0.52	0.60	0.21	0.22	0.67	0.66	0.29	0.30
		Flex. Fdn.	0.46	0.57	0.34	0.36	0.34	0.37	0.21	0.21	0.45	0.57	0.30	0.30
	Type II Bearings	Fixed Fdn.	0.58	0.59	0.28	0.33	0.51	0.62	0.22	0.23	0.57	0.68	0.27	0.28
		Flex. Fdn.	0.39	0.54	0.30	0.34	0.35	0.43	0.22	0.22	0.40	0.52	0.28	0.30
Wall pier substructure	Type I Bearings	Fixed Fdn.	0.58	0.64	0.75	0.74	0.50	0.63	0.53	0.60	0.60	0.62	0.67	0.68
		Flex. Fdn.	0.42	0.50	0.38	0.43	0.33	0.37	0.30	0.35	0.40	0.53	0.37	0.44
	Type II Bearings	Fixed Fdn.	0.60	0.66	0.76	0.73	0.45	0.62	0.53	0.61	0.56	0.64	0.68	0.70
		Flex. Fdn.	0.41	0.49	0.37	0.40	0.33	0.41	0.30	0.37	0.34	0.46	0.32	0.40

Table C.13 Average maximum normalized longitudinal abutment base shear for Pa ground motion excitation at SF =1

			Steel short (Ss) superstructure				Steel long (Sl) superstructure				Precast Concrete (Cs) superstructure			
			Short 4.5 m (15 ft)		Tall 12.2 m (40 ft)		Short 4.5 m (15 ft)		Tall 12.2 m (40 ft)		Short 4.5 m (15 ft)		Tall 12.2 m (40 ft)	
			Abut. 1	Abut. 2	Abut. 1	Abut. 2	Abut. 1	Abut. 2	Abut. 1	Abut. 2	Abut. 1	Abut. 2	Abut. 1	Abut. 2
Column pier substructure	Type I Bearings	Fixed Fdn.	2.45	2.42	3.38	2.98	1.92	1.92	2.63	2.48	1.49	1.56	2.22	2.18
		Flex. Fdn.	2.30	2.32	2.59	2.61	1.81	1.81	2.23	2.08	1.43	1.48	1.74	1.63
	Type II Bearings	Fixed Fdn.	2.50	2.55	3.58	3.55	2.00	1.86	3.11	2.61	1.50	1.45	2.34	2.07
		Flex. Fdn.	2.34	2.32	2.73	2.68	1.83	1.83	2.48	2.33	1.40	1.34	1.76	1.61
Wall pier substructure	Type I Bearings	Fixed Fdn.	2.35	2.17	3.63	3.23	1.89	1.91	2.48	2.40	1.49	1.47	2.16	2.01
		Flex. Fdn.	2.22	2.30	2.67	2.59	1.85	1.84	2.24	2.23	1.45	1.46	1.73	1.69
	Type II Bearings	Fixed Fdn.	2.10	2.05	3.32	3.35	1.92	1.89	2.76	2.67	1.47	1.42	2.28	1.93
		Flex. Fdn.	2.24	2.18	2.75	2.65	1.85	1.83	2.40	2.42	1.44	1.37	1.70	1.62

Table C.14 Average maximum normalized longitudinal abutment base shear for CG ground motion excitation at SF =1

			Steel short (Ss) superstructure				Steel long (Sl) superstructure				Precast Concrete (Cs) superstructure			
			Short 4.5 m (15 ft)		Tall 12.2 m (40 ft)		Short 4.5 m (15 ft)		Tall 12.2 m (40 ft)		Short 4.5 m (15 ft)		Tall 12.2 m (40 ft)	
			Abut. 1	Abut. 2	Abut. 1	Abut. 2	Abut. 1	Abut. 2	Abut. 1	Abut. 2	Abut. 1	Abut. 2	Abut. 1	Abut. 2
Column pier substructure	Type I Bearings	Fixed Fdn.	2.45	2.40	2.62	2.49	1.70	1.70	1.75	1.78	1.42	1.42	1.54	1.54
		Flex. Fdn.	2.20	2.20	2.35	2.34	1.67	1.64	1.68	1.70	1.36	1.37	1.37	1.42
	Type II Bearings	Fixed Fdn.	2.14	2.07	2.73	2.53	1.72	1.68	1.86	1.93	1.31	1.29	1.40	1.40
		Flex. Fdn.	1.85	1.83	2.36	2.38	1.68	1.65	1.78	1.74	1.27	1.27	1.30	1.33
Wall pier substructure	Type I Bearings	Fixed Fdn.	2.21	1.90	2.50	2.48	1.69	1.68	1.72	1.75	1.38	1.39	1.45	1.49
		Flex. Fdn.	1.87	2.00	2.33	2.32	1.65	1.63	1.66	1.71	1.35	1.36	1.37	1.40
	Type II Bearings	Fixed Fdn.	2.34	2.23	2.55	2.54	1.70	1.65	1.92	1.77	1.33	1.28	1.40	1.41
		Flex. Fdn.	1.50	1.82	2.37	2.33	1.67	1.64	1.73	1.73	1.25	1.24	1.31	1.33

Table C.15 Average maximum normalized transverse abutment base shear for Pa ground motion excitation at SF =1

			Steel short (Ss) superstructure				Steel long (Sl) superstructure				Precast Concrete (Cs) superstructure			
			Short 4.5 m (15 ft)		Tall 12.2 m (40 ft)		Short 4.5 m (15 ft)		Tall 12.2 m (40 ft)		Short 4.5 m (15 ft)		Tall 12.2 m (40 ft)	
			Abut. 1	Abut. 2	Abut. 1	Abut. 2	Abut. 1	Abut. 2	Abut. 1	Abut. 2	Abut. 1	Abut. 2	Abut. 1	Abut. 2
Column pier substructure	Type I Bearings	Fixed Fdn.	0.76	0.76	0.76	0.76	1.01	1.02	1.01	1.02	0.73	0.73	0.73	0.74
		Flex. Fdn.	0.75	0.76	0.76	0.76	1.01	1.02	1.02	1.02	0.74	0.76	0.74	0.75
	Type II Bearings	Fixed Fdn.	0.66	0.65	0.66	0.66	0.92	0.92	0.92	0.92	0.67	0.67	0.67	0.67
		Flex. Fdn.	0.66	0.66	0.66	0.66	0.92	0.92	0.92	0.92	0.67	0.67	0.67	0.67
Wall pier substructure	Type I Bearings	Fixed Fdn.	0.76	0.75	0.76	0.75	1.01	0.99	1.01	1.01	0.73	0.72	0.74	0.73
		Flex. Fdn.	0.76	0.76	0.77	0.76	1.01	1.01	1.01	1.02	0.75	0.76	0.74	0.75
	Type II Bearings	Fixed Fdn.	0.66	0.65	0.66	0.65	0.92	0.91	0.92	0.92	0.67	0.66	0.67	0.65
		Flex. Fdn.	0.66	0.66	0.66	0.66	0.92	0.92	0.92	0.92	0.67	0.67	0.67	0.67

Table C.16 Average maximum normalized transverse abutment base shear for CG ground motion excitation at SF =1

			Steel short (Ss) superstructure				Steel long (Sl) superstructure				Precast Concrete (Cs) superstructure			
			Short 4.5 m (15 ft)		Tall 12.2 m (40 ft)		Short 4.5 m (15 ft)		Tall 12.2 m (40 ft)		Short 4.5 m (15 ft)		Tall 12.2 m (40 ft)	
			Abut. 1	Abut. 2	Abut. 1	Abut. 2	Abut. 1	Abut. 2	Abut. 1	Abut. 2	Abut. 1	Abut. 2	Abut. 1	Abut. 2
Column pier substructure	Type I Bearings	Fixed Fdn.	0.75	0.76	0.76	0.77	1.01	1.02	1.01	1.01	0.73	0.72	0.72	0.72
		Flex. Fdn.	0.75	0.76	0.76	0.76	1.01	1.00	1.01	1.02	0.74	0.75	0.74	0.73
	Type II Bearings	Fixed Fdn.	0.65	0.66	0.66	0.66	0.92	0.92	0.92	0.92	0.67	0.67	0.67	0.67
		Flex. Fdn.	0.66	0.66	0.66	0.66	0.92	0.92	0.92	0.92	0.67	0.67	0.67	0.67
Wall pier substructure	Type I Bearings	Fixed Fdn.	0.76	0.76	0.76	0.77	1.01	1.00	1.01	1.01	0.72	0.73	0.73	0.72
		Flex. Fdn.	0.75	0.76	0.76	0.76	1.01	1.00	1.01	1.02	0.74	0.74	0.74	0.74
	Type II Bearings	Fixed Fdn.	0.66	0.66	0.66	0.66	0.92	0.92	0.92	0.92	0.67	0.67	0.67	0.67
		Flex. Fdn.	0.66	0.66	0.66	0.66	0.92	0.92	0.92	0.92	0.67	0.67	0.67	0.67

Table C.17 Average maximum transverse diaphragm force at pier for Pa ground motion excitation at SF =1 (kN)

			Steel short (Ss) superstructure				Steel long (Sl) superstructure				Precast Concrete (Cs) superstructure			
			Short 4.5 m (15 ft)		Tall 12.2 m (40 ft)		Short 4.5 m (15 ft)		Tall 12.2 m (40 ft)		Short 4.5 m (15 ft)		Tall 12.2 m (40 ft)	
			Pier 1	Pier 2	Pier 1	Pier 2	Pier 1	Pier 2	Pier 1	Pier 2	Pier 1	Pier 2	Pier 1	Pier 2
Column pier substructure	Type I Bearings	Fixed Fdn.	1011	973	1036	718	2186	2514	1487	1063	1687	1764	1322	910
		Flex. Fdn.	1003	953	1007	712	2090	2228	1466	1060	1612	1749	1233	881
	Type II Bearings	Fixed Fdn.	885	975	1050	721	1880	2569	1531	1088	1394	1774	1212	928
		Flex. Fdn.	901	962	1012	760	1867	2390	1539	1131	1343	1684	1185	921
Wall pier substructure	Type I Bearings	Fixed Fdn.	1049	980	1076	977	2280	2610	2381	2618	1733	1770	1710	1767
		Flex. Fdn.	1106	953	1246	954	2302	2412	2557	2444	1749	1742	1923	1762
	Type II Bearings	Fixed Fdn.	878	987	872	989	1941	2669	1948	2627	1379	1796	1380	1785
		Flex. Fdn.	1011	961	1119	956	2000	2419	2277	2532	1464	1680	1670	1697

Table C.18 Average maximum transverse diaphragm force at pier for CG ground motion excitation at SF =1 (kN)

			Steel short (Ss) superstructure				Steel long (Sl) superstructure				Precast Concrete (Cs) superstructure			
			Short 4.5 m (15 ft)		Tall 12.2 m (40 ft)		Short 4.5 m (15 ft)		Tall 12.2 m (40 ft)		Short 4.5 m (15 ft)		Tall 12.2 m (40 ft)	
			Pier 1	Pier 2	Pier 1	Pier 2	Pier 1	Pier 2	Pier 1	Pier 2	Pier 1	Pier 2	Pier 1	Pier 2
Column pier substructure	Type I Bearings	Fixed Fdn.	980	968	1042	716	1958	2547	1447	998	1604	1757	1358	909
		Flex. Fdn.	1023	954	1019	849	1631	1535	1412	931	1473	1534	1276	890
	Type II Bearings	Fixed Fdn.	845	972	933	756	1777	2609	1469	981	1267	1763	1198	905
		Flex. Fdn.	836	940	912	832	1616	1727	1372	951	1223	1456	1171	922
Wall pier substructure	Type I Bearings	Fixed Fdn.	1071	989	1050	979	2140	2693	2178	2685	1737	1761	1713	1754
		Flex. Fdn.	1084	985	1074	962	1919	1607	2043	1629	1649	1603	1603	1565
	Type II Bearings	Fixed Fdn.	879	987	896	983	1824	2712	1831	2693	1326	1783	1337	1763
		Flex. Fdn.	937	971	984	983	1759	1837	1816	1782	1284	1559	1310	1649

Table C.19 Average maximum transverse diaphragm force at abutment for Pa ground motion excitation at SF =1 (kN)

			Steel short (Ss) superstructure				Steel long (Sl) superstructure				Precast Concrete (Cs) superstructure			
			Short 4.5 m (15 ft)		Tall 12.2 m (40 ft)		Short 4.5 m (15 ft)		Tall 12.2 m (40 ft)		Short 4.5 m (15 ft)		Tall 12.2 m (40 ft)	
			Abut. 1	Abut. 2	Abut. 1	Abut. 2	Abut. 1	Abut. 2	Abut. 1	Abut. 2	Abut. 1	Abut. 2	Abut. 1	Abut. 2
Column pier substructure	Type I Bearings	Fixed Fdn.	521	527	524	526	718	710	710	711	785	790	807	809
		Flex. Fdn.	519	529	523	531	711	709	710	710	795	794	798	801
	Type II Bearings	Fixed Fdn.	450	446	454	455	641	637	638	637	663	664	668	669
		Flex. Fdn.	451	450	453	455	636	637	638	638	664	664	667	668
Wall pier substructure	Type I Bearings	Fixed Fdn.	525	524	525	523	717	696	722	710	800	793	798	801
		Flex. Fdn.	526	531	534	531	714	712	719	717	805	806	810	810
	Type II Bearings	Fixed Fdn.	450	443	450	441	631	627	637	637	664	650	664	647
		Flex. Fdn.	450	450	452	452	632	632	639	636	664	665	666	667

Table C.20 Average maximum transverse diaphragm force at abutment for CG ground motion excitation at SF =1 (kN)

			Steel short (Ss) superstructure				Steel long (Sl) superstructure				Precast Concrete (Cs) superstructure			
			Short 4.5 m (15 ft)		Tall 12.2 m (40 ft)		Short 4.5 m (15 ft)		Tall 12.2 m (40 ft)		Short 4.5 m (15 ft)		Tall 12.2 m (40 ft)	
			Abut. 1	Abut. 2	Abut. 1	Abut. 2	Abut. 1	Abut. 2	Abut. 1	Abut. 2	Abut. 1	Abut. 2	Abut. 1	Abut. 2
Column pier substructure	Type I Bearings	Fixed Fdn.	520	522	523	529	711	714	708	710	794	791	803	812
		Flex. Fdn.	521	528	525	526	707	703	709	709	793	801	804	806
	Type II Bearings	Fixed Fdn.	446	449	452	452	635	637	633	635	659	664	665	666
		Flex. Fdn.	450	450	452	452	633	636	633	635	663	664	665	666
Wall pier substructure	Type I Bearings	Fixed Fdn.	523	532	524	534	717	706	717	719	802	813	798	811
		Flex. Fdn.	525	535	536	533	713	697	717	716	795	802	803	809
	Type II Bearings	Fixed Fdn.	450	450	454	454	630	631	637	638	664	663	667	667
		Flex. Fdn.	451	451	452	452	631	633	634	635	664	664	666	667

Tables C.22 – C.27 contain sequence of damage results for each bridge system. These tables are based on the sequence of failure plots shown in Chapter 6. Table C.21 shows the different limit states that occur with the bridge structures, and the limit states with appropriate scale factors for occurrence are shown. Note that a more compact representation of the sequence of damage for different bridges is shown in Tables 7.5 -7.8 in Chapter 7.

Table C.21 Typical limit states observed in bridge prototypes

Acceptable for quasi-isolation	**Acceptable as Level 3 fusing for quasi-isolation**
EA - Elastomeric bearings slide at abutment	P1 - Pier 1 yields
EP - Elastomeric bearing slides at Pier 1	P2 - Pier 2 yields
RA - Retainer failure at abutment	
RP - Retainer failure at Pier 1	**Discouraged for quasi-isolation**
Fb - Fixed (low-profile) bearing failure	UA - Unseating of bearing at abutment
Bw - Backwall yielding	UP - Unseating of bearing at pier

Table C.22 Detailed Sequence of damage for SsC bridges

Bridge - SsC15T1F

Longitudinal	Pa	LS	EA	P2	EP	Bw							
		SF	0.5	0.75	0.75	0.75							
	CG	LS	EA	P2	EP	Bw							
		SF	0.5	0.75	0.75	0.75							
Transverse	Pa	LS	EA1	EA2	RA1	RA2	Fb	EP	RP				
		SF	0.75	1	0.5	0.75	1	1.25	1.5				
	CG	LS	EA1	EA2	RA1	RA2	Fb	EP	RP				
		SF	0.75	1	0.5	0.75	1	1.25	1.5				

Bridge - SsC40T1F

Longitudinal	Pa	LS	EA	Bw	P2	P1	EP	Fb					
		SF	0.5	0.5	1.25	1.25	1.25	1.5					
	CG	LS	EA	Bw	P2	P1	EP						
		SF	0.5	0.75	1.5	1.5	1.75						
Transverse	Pa	LS	EA1	EA2	RA1	RA2	P2	P1					
		SF	0.5	0.5	0.5	0.5	0.75	0.75					
	CG	LS	EA1	EA2	RA1	RA2	P2	P1	EP				
		SF	0.5	0.5	0.5	0.5	1	1	1.75				

Bridge - SsC15T1S

Longitudinal	Pa	LS	EA	P2	EP	Bw							
		SF	0.5	0.75	0.75	0.75							
	CG	LS	EA	P2	EP	Bw							
		SF	0.5	0.75	0.75	0.75							
Transverse	Pa	LS	EA1	EA2	RA1	RA2	Fb	EP	RP	UA1	UP1		
		SF	0.5	0.75	0.5	0.75	1	1.25	1.5	1.75	1.75		
	CG	LS	EA1	EA2	RA1	RA2	Fb	EP	RP				
		SF	0.5	0.75	0.5	0.75	1	1.25	1.5				

Bridge - SsC40T1S

Longitudinal	Pa	LS	EA	Bw	P2	P1	EP	Fb					
		SF	0.5	0.5	1.25	1.25	1.25	1.5					
	CG	LS	EA	Bw	P2	P1	EP	Fb					
		SF	0.5	0.5	1.25	1.25	1.25	1.5					
Transverse	Pa	LS	EA1	EA2	RA1	RA2	P2	P1					
		SF	0.5	0.5	0.5	0.5	0.75	0.75					
	CG	LS	EA1	EA2	RA1	RA2	P2	P1	EP				
		SF	0.5	0.5	0.5	0.5	1.25	1.25	1.75				

Bridge - SsC15T2F

Longitudinal	Pa	LS	EA	EP	P2	Bw	Fb	UA					
		SF	0.5	0.5	0.75	0.75	1.5	1.5					
	CG	LS	EA	EP	P2	Bw	Fb	UA					
		SF	0.5	0.5	0.75	1	1.5	1.75					
Transverse	Pa	LS	EA1	EA2	EP	RA1	RA2	Fb	RP	UA1	UA2	UP1	UP2
		SF	0.5	0.5	0.5	0.75	1	1	1.5	1.50	1.5	1.75	1.75
	CG	LS	EA1	EA2	EP	RA1	RA2	Fb	RP	UA2	UA1		
		SF	0.5	0.5	0.5	0.75	1	1	1.5	1.5	1.75		

Bridge - SsC40T2F

Longitudinal	Pa	LS	EA	Bw	UA	P2	EP	P1	Fb	UP						
		SF	0.5	0.5	0.75	1	1.25	1.25	1.5	1.75						
	CG	LS	EA	Bw	P2	UA	P1	EP	Fb							
		SF	0.5	0.5	1.25	1.25	1.5	1.5	1.5							
Transverse	Pa	LS	EA1	EA2	RA1	RA2	P2	EP	P1	UA1	UA2	RP	UP1			
		SF	0.5	0.5	0.5	0.5	0.75	1	1	1.00	1	1.5	1.5			
	CG	LS	EA1	EA2	RA1	RA2	P2	EP	P1	RP	UA1	UA2				
		SF	0.5	0.5	0.5	0.5	1.25	1.25	1..5	1.5	1.75	1.75				

Bridge - SsC15T2S

Longitudinal	Pa	LS	EA	EP	P2	Bw	UA						
		SF	0.5	0.5	0.75	0.75	1.5						
	CG	LS	EA	EP	P2	Bw	UA						
		SF	0.5	0.5	0.75	0.75	1.75						
Transverse	Pa	LS	EA1	EA2	EP	RA1	RA2	Fb	RP	UA1	UA2	UP1	UP2
		SF	0.5	0.5	0.5	0.75	1	1.25	1.5	1.50	1.5	1.5	1.75
	CG	LS	EA1	EA2	EP	RA1	RA2	Fb	RP	UA2	UA1		
		SF	0.5	0.5	0.5	0.75	1	1	1.5	1.5	1.75		

Bridge - SsC40T2S

Longitudinal	Pa	LS	EA	Bw	EP	P2	UA	P1	Fb							
		SF	0.5	0.5	1	1	1	1.25	1.5							
	CG	LS	EA	Bw	EP	P2	UA	P1	Fb							
		SF	0.5	0.5	1	1.25	1.25	1.25	1.75							
Transverse	Pa	LS	EA1	EA2	RA1	RA2	P2	EP	P1	UA1	UA2	RP	UP1			
		SF	0.5	0.5	0.5	0.5	0.75	1	1	1.00	1	1.5	1.5			
	CG	LS	EA1	EA2	RA1	RA2	P2	EP	P1	RP	UA1	UA2				
		SF	0.5	0.5	0.5	0.5	1.25	1.25	1..5	1.5	1.75	1.75				

Table C.23 Detailed Sequence of damage for SsW bridges

Bridge - SsW15T1F

Longitudinal	Pa	LS	EA	EP	P2	Fb	Bw	P1					
		SF	0.75	0.75	0.75	0.75	1.00	1.75					
	CG	LS	EA	EP	P2	Fb	Bw	P1					
		SF	0.75	0.75	0.75	0.75	1	1					
Transverse	Pa	LS	EA1	EA2	RA1	RA2	Fb	EP	RP				
		SF	0.75	0.75	0.75	0.75	1	1	1.5				
	CG	LS	EA1	EA2	RA1	RA2	Fb	EP	RP				
		SF	0.75	0.75	0.75	0.75	1	1	1.5				

Bridge - SsW40T1F

Longitudinal	Pa	LS	EA	Bw	EP	P2	P1	Fb					
		SF	0.50	0.50	0.75	0.75	0.75	1.00					
	CG	LS	EA	Bw	P2	P1	EB	Fb					
		SF	0.5	0.5	1	1	1.25	1.25					
Transverse	Pa	LS	EA1	EA2	EP	Fb	RA1	RA2	Fb				
		SF	0.75	0.75	0.75	0.75	0.75	0.75	0.75				
	CG	LS	EA1	EA2	EP	Fb	RA1	RA2	Fb				
		SF	0.75	0.75	0.75	0.75	0.75	0.75	0.75				

Bridge - SsW15T1S

Longitudinal	Pa	LS	EA	EP	P2	Bw	P1	Fb					
		SF	0.5	0.75	0.75	0.75	1.25	1.5					
	CG	LS	EA	EP	P2	Bw	Fb	P1					
		SF	0.5	0.75	0.75	0.75	1	1.25					
Transverse	Pa	LS	EA1	EA2	RA1	RA2	Fb	EP	RP	UA1	UP1	UP2	UA2
		SF	0.5	0.5	0.5	0.75	1	1.25	1.5	1.75	1.75	1.75	1.75
	CG	LS	EA1	EA2	RA1	RA2	Fb	EP	RP				
		SF	0.5	0.5	0.5	0.75	1	1.25	1.5				

Bridge - SsW40T1S

Longitudinal	Pa	LS	EA	Bw	EP	P2	P1	Fb					
		SF	0.5	0.5	0.75	0.75	0.75	1					
	CG	LS	EA	Bw	P2	P1	EP	Fb					
		SF	0.5	0.5	1	1	1.25	1.25					
Transverse	Pa	LS	EA1	EA2	EP	Fb	RA1	RA2	Fb	UA1	UP1	UP2	UA2
		SF	0.75	0.75	0.75	0.75	0.75	0.75	0.75	1.75	1.75	1.75	1.75
	CG	LS	EA1	EA2	EP	Fb	RA1	RA2	Fb				
		SF	0.75	0.75	0.75	0.75	0.75	0.75	0.75				

Bridge - SsW15T2F

Longitudinal	Pa	LS	EA	EP	P2	Fb	Bw	UA1	UA2				
		SF	0.5	0.5	0.5	0.75	0.75	1.5	1.5				
	CG	LS	EA	EP	P2	Fb	Bw	P1	UA1	UA2			
		SF	0.5	0.5	0.5	0.75	0.75	1.75	1.75	1.75			
Transverse	Pa	LS	EA1	EA2	EP	Fb	RA1	RA2	UA1	UA2	RP	UP1	UP2
		SF	0.5	0.5	0.5	0.75	1	1	1.5	1.50	1.5	1.75	1.75
	CG	LS	EA1	EA2	EP	Fb	RA1	RA2	UA1	UA2	RP		
		SF	0.5	0.5	0.5	0.75	1	1	1.5	1.5	1.5		

Bridge - SsW40T2F

Longitudinal	Pa	LS	EA	Bw	EP	P2	P1	Fb	UA1	UA2	UP1		
		SF	0.5	0.5	0.75	0.75	0.75	1	1	1	1.25		
	CG	LS	EA	Bw	P2	P1	EP	Fb	UA1	UA2			
		SF	0.5	0.5	1	1	1.25	1.25	1.25	1.25			
Transverse	Pa	LS	EA1	EA2	EP	RA1	RA2	Fb	UA1	UA2	UP1		
		SF	0.5	0.5	0.5	1	1	1	1.5	1.50	1.75		
	CG	LS	EA1	EA2	EP	Fb	RA1	RA2	Fb	UA2	UA1		
		SF	0.75	0.75	0.75	0.75	0.75	0.75	1	1.5	1.75		

Bridge - SsW15T2S

Longitudinal	Pa	LS	EA	EP	P2	Fb	Bw	UA1	UA2				
		SF	0.5	0.5	0.5	0.75	0.75	1.5	1.5				
	CG	LS	EA	EP	P2	Fb	Bw	P1	UA1	UA2			
		SF	0.5	0.5	0.5	0.75	0.75	1.75	1.75	1.75			
Transverse	Pa	LS	EA1	EA2	EP	Fb	RA1	RA2	UA1	UA2	RP	UP1	UP2
		SF	0.5	0.5	0.5	0.75	1	1	1.25	1.25	1.25	1.5	1.5
	CG	LS	EA1	EA2	EP	Fb	RA1	RA2	UA1	UA2	RP	UP1	UP2
		SF	0.5	0.5	0.5	0.75	1	1	1.5	1.5	1.25	1.75	1.75

Bridge - SsW40T2S

Longitudinal	Pa	LS	EA	Bw	EP	Fb	P2	P1	UA	UP1			
		SF	0.5	0.5	0.75	0.75	0.75	1	1	1			
	CG	LS	EA	Bw	EP	Fb	P2	P1	UA				
		SF	0.5	0.5	1	1	1	1	1.5				
Transverse	Pa	LS	EA1	EA2	EP	RA1	RA2	Fb	UA1	UA2	UP1		
		SF	0.5	0.5	0.5	0.5	0.75	1	1	1.00	1.25		
	CG	LS	EA1	EA2	EP	RA1	RA2	Fb	UA1	UA2	UP1		
		SF	0.5	0.5	0.75	0.5	0.75	1	1.25	1.25	1.75		

Table C.24 Detailed Sequence of damage for SlC bridges

Bridge - SlC15T1F

Longitudinal	Pa	LS	EA	Bw	P2	EP	P1					
		SF	0.5	0.5	0.75	1	1.75					
	CG	LS	EA	Bw	P2	EP	P1					
		SF	0.5	0.5	0.75	1.25	1.75					
Transverse	Pa	LS	EA1	EA2	RA1	RA2	EP	Fb	P1			
		SF	0.5	0.5	0.5	0.75	1.25	1.25	1.75			
	CG	LS	EA1	EA2	RA1	RA2	EP	Fb				
		SF	0.5	0.5	0.5	0.75	1.25	1.5				

Bridge - SlC40T1F

Longitudinal	Pa	LS	EA	Bw	P2	P1				
		SF	0.5	0.5	1	1				
	CG	LS	EA	Bw	P2	P1				
		SF	0.5	0.5	1.25	1.25				
Transverse	Pa	LS	EA1	EA2	RA1	RA2	P2	P1	UA1	
		SF	0.5	0.5	0.75	0.75	0.75	0.75	1.75	
	CG	LS	EA1	EA2	RA1	RA2	P2	P1		
		SF	0.5	0.5	0.75	0.75	1.25	1.25		

Bridge - SlC15T1S

Longitudinal	Pa	LS	EA	Bw	P2	EP	P1					
		SF	0.5	0.5	0.75	1	1.25					
	CG	LS	EA	Bw	P2	EP	P1					
		SF	0.5	0.5	1	1.25	1.75					
Transverse	Pa	LS	EA1	EA2	RA1	RA2	EP	Fb	P2	P1	UA1	UA2
		SF	0.5	0.5	0.5	0.75	1.25	1.5	1.25	1.25	1.75	1.75
	CG	LS	EA1	EA2	RA1	RA2	EP					
		SF	0.5	0.5	0.5	0.75	1.5					

Bridge - SlC40T1S

Longitudinal	Pa	LS	EA	Bw	P2	P1				
		SF	0.5	0.5	1	1				
	CG	LS	EA	Bw	P2	P1				
		SF	0.5	0.5	1.5	1.5				
Transverse	Pa	LS	EA1	EA2	RA1	RA2	P2	P1		
		SF	0.5	0.5	0.75	0.75	0.75	0.75		
	CG	LS	EA1	EA2	RA1	RA2	P2	P1		
		SF	0.5	0.5	0.75	0.75	1.25	1.25		

Bridge - SlC15T2F

Longitudinal	Pa	LS	EA	EP	Bw	P2	UA					
		SF	0.5	0.5	0.5	0.75	1.25					
	CG	LS	EA	EP	Bw	P2						
		SF	0.5	0.5	0.75	1						
Transverse	Pa	LS	EA1	EA2	RA1	RA2	EP	Fb	UA2	UA1	RP	
		SF	0.5	0.5	0.75	0.75	1	1.25	1.5	1.5	1.75	
	CG	LS	EA1	EA2	RA1	RA2	EP	Fb	UA2	UA1		
		SF	0.5	0.5	0.75	0.75	1	1.25	1.5	1.75		

Bridge - SlC40T2F

Longitudinal	Pa	LS	EA	Bw	EP	P2	P1	UA1	UA2		
		SF	0.5	0.5	1	1	1	1	1		
	CG	LS	EA	Bw	EP	P2	P1	UA1	UA1		
		SF	0.5	0.5	1	1.25	1.25	1.25	1.25		
Transverse	Pa	LS	EA1	EA2	RA1	RA2	P2	P1	UA1	UA2	
		SF	0.5	0.5	0.5	0.5	0.75	0.75	0.75	0.75	
	CG	LS	EA1	EA2	RA1	RA2	P2	P1	UA1	UA1	
		SF	0.5	0.5	0.5	0.5	1.25	1.25	1.75	1.75	

Bridge - SlC15T2S

Longitudinal	Pa	LS	EA	EP	Bw	P2	UA					
		SF	0.5	0.5	0.5	0.75	1.25					
	CG	LS	EA	EP	Bw	P2						
		SF	0.5	0.5	0.75	1						
Transverse	Pa	LS	EA1	EA2	RA1	RA2	EP	Fb	UA2	UA1	RP	
		SF	0.5	0.5	0.75	0.75	1	1.5	1.25	1.25	1.75	
	CG	LS	EA1	EA2	RA1	RA2	EP	Fb	UA2	UA1		
		SF	0.5	0.5	0.75	0.75	1.25	1.75	1.75	1.75		

Bridge - SlC40T2S

Longitudinal	Pa	LS	EA	Bw	UA1	UA2	EP	P2	P1		
		SF	0.5	0.5	0.75	0.75	1	1	1		
	CG	LS	EA	Bw	EP	P2	P1	UA1	UA1		
		SF	0.5	0.5	1	1.25	1.25	1.25	1.25		
Transverse	Pa	LS	EA1	EA2	RA1	RA2	P2	P1	UA1	UA2	
		SF	0.5	0.5	0.5	0.5	0.75	0.75	0.75	0.75	
	CG	LS	EA1	EA2	RA1	RA2	P2	P1	UA1	UA1	
		SF	0.5	0.5	0.5	0.5	1.25	1.25	1.75	1.75	

Table C.25 Detailed Sequence of damage for SlW bridges

Bridge - SlW15T1F

Longitudinal	Pa	LS	EA	P2	Bw	EP	P1						
		SF	0.5	0.5	0.75	1	1.25						
	CG	LS	EA	P2	Bw	EP	P1						
		SF	0.5	0.5	0.75	1.25	1.25						
Transverse	Pa	LS	EA1	EA2	RA1	RA2	EP	Fb	RP	UA1			
		SF	0.5	0.5	0.5	1	1.25	1.25	1.75	1.75			
	CG	LS	EA1	EA2	RA1	RA2	EP	Fb					
		SF	0.5	0.5	0.5	1	1.25	1.25					

Bridge - SlW40T1F

Longitudinal	Pa	LS	EA	Bw	P2	P1	EP						
		SF	0.5	0.5	0.5	0.75	1.75						
	CG	LS	EA	Bw	P2	P1							
		SF	0.5	0.5	1	1							
Transverse	Pa	LS	EA1	EA2	RA1	RA2	Fb	EP	RP				
		SF	0.75	0.75	0.75	0.75	1	1.25	1.75				
	CG	LS	EA1	EA2	RA1	RA2	Fb	EP	RP				
		SF	0.75	0.75	0.75	1	1	1.25	1.75				

Bridge - SlW15T1S

Longitudinal	Pa	LS	EA	Bw	P2	P1	EP						
		SF	0.5	0.5	0.75	1	1.25						
	CG	LS	EA	Bw	P2	P1	EP						
		SF	0.5	0.75	0.75	1.25	1.5						
Transverse	Pa	LS	EA1	EA2	RA1	RA2	Fb	EP	UA2	UP2	RP	UP1	UA1
		SF	0.5	0.5	0.75	0.75	1	1.25	1.25	1.5	1.75	1.75	1.75
	CG	LS	EA1	EA2	RA1	RA2	EP	Fb					
		SF	0.5	0.5	0.75	1	1.25	1.25					

Bridge - SlW40T1S

Longitudinal	Pa	LS	EA	Bw	P2	P1	EP						
		SF	0.5	0.5	0.5	0.75	1.75						
	CG	LS	EA	Bw	P2	P1							
		SF	0.5	0.5	1	1							
Transverse	Pa	LS	EA1	EA2	RA1	RA2	Fb	EP	RP				
		SF	0.75	0.75	0.75	0.75	1.25	1.25	1.25				
	CG	LS	EA1	EA2	RA1	RA2	Fb						
		SF	0.75	0.75	0.75	0.75	1.75						

Bridge - SlW15T2F

Longitudinal	Pa	LS	EA	P2	EP	Bw	UA1						
		SF	0.5	0.5	0.75	0.75	1.5						
	CG	LS	EA	P2	EP	Bw							
		SF	0.5	0.5	0.75	0.75							
Transverse	Pa	LS	EA1	EA2	RA1	RA2	Fb	EP	UA2	UA1	RP	UP2	
		SF	0.5	0.75	0.5	0.75	1.25	1.25	1.5	1.5	1.5	1.75	
	CG	LS	EA1	EA2	RA1	RA2	Fb	EP	UA2				
		SF	0.5	0.5	0.75	1	1.25	1.25	1.75				

Bridge - SlW40T2F

Longitudinal	Pa	LS	EA	Bw	P2	P1	UA	EP							
		SF	0.5	0.5	0.5	0.75	0.75	1.75							
	CG	LS	EA	Bw	P2	P1	UA								
		SF	0.5	0.5	0.75	1	1.25								
Transverse	Pa	LS	EA1	EA2	RA1	RA2	Fb	EP	RP	UA2	UA1				
		SF	0.5	0.5	0.5	0.75	1	1.25	1.25	0.75	0.75				
	CG	LS	EA1	EA2	RA1	RA2	Fb	EP	RP	UA2	UA1				
		SF	0.5	0.5	0.5	0.75	1	1.25	1.25	1.25	1.25				

Bridge - SlW15T2S

Longitudinal	Pa	LS	EA	EP	Bw	P2	UA1						
		SF	0.5	0.5	0.5	0.5	1.25						
	CG	LS	EA	EP	P2	Bw	UA1						
		SF	0.5	0.5	0.5	0.75	1.75						
Transverse	Pa	LS	EA1	EA2	RA1	RA2	Fb	EP	UA2	UA1	RP	UP2	UP1
		SF	0.5	0.75	0.75	0.75	1	1.25	1	1	1.5	1.5	1.75
	CG	LS	EA1	EA2	RA1	RA2	EP	Fb	UA2				
		SF	0.5	0.5	0.75	1	1.5	1.75	1.75				

Bridge - SlW40T2S

Longitudinal	Pa	LS	EA	Bw	P2	P1	UA	EP							
		SF	0.5	0.5	0.5	0.75	0.75	1.5							
	CG	LS	EA	Bw	P2	P1	UA								
		SF	0.5	0.5	0.75	1	1.25								
Transverse	Pa	LS	EA1	EA2	RA1	RA2	Fb	UA2	UA1	EP	RP				
		SF	0.5	0.5	0.75	0.75	1	1	1	1.25	1.5				
	CG	LS	EA1	EA2	RA1	RA2	Fb	UA2	EP	RP	UA1				
		SF	0.5	0.5	0.75	0.75	1	1.5	1.75	1.75	1.75				

Table C.26 Detailed Sequence of damage for CsC bridges

Bridge - CsC15T1F

Longitudinal	Pa	LS	EA	Bw	P2	EP							
		SF	0.5	0.5	0.5	0.75							
	CG	LS	EA	Bw	P2	EP							
		SF	0.5	0.5	0.5	0.75							
Transverse	Pa	LS	RA1	RA2	EA1	EA2	Fb	EP	RP	UP2			
		SF	0.5	0.5	0.75	0.75	0.75	1.25	1.75	1.75			
	CG	LS	RA1	RA2	EA1	EA2	Fb	EP					
		SF	0.5	0.5	0.75	0.75	0.75	1.25					

Bridge - CsC40T1F

Longitudinal	Pa	LS	EA	Bw	EP	P2	P1			
		SF	0.5	0.5	1	1.25	1.25			
	CG	LS	EA	Bw	EP	P2	P1			
		SF	0.5	0.5	1	1.75	1.75			
Transverse	Pa	LS	EA1	EA2	RA1	RA2	P2	P1		
		SF	0.5	0.5	0.5	0.5	1	1		
	CG	LS	EA1	EA2	RA1	RA2	P2	P1		
		SF	0.5	0.5	0.5	0.5	1.25	1.25		

Bridge - CsC15T1S

Longitudinal	Pa	LS	EA	Bw	EP	P2							
		SF	0.5	0.5	0.75	0.75							
	CG	LS	EA	Bw	EP	P2							
		SF	0.5	0.5	0.75	0.75							
Transverse	Pa	LS	EA1	EA2	RA1	RA2	Fb	EP	RP	UP2			
		SF	0.75	0.75	0.75	0.75	0.75	1.25	1.75	1.75			
	CG	LS	EA1	EA2	RA1	RA2	Fb	EP					
		SF	0.75	0.75	0.75	0.75	0.75	1.25					

Bridge - CsC40T1S

Longitudinal	Pa	LS	EA	Bw	EP	P2	P1			
		SF	0.5	0.5	1	1.25	1.25			
	CG	LS	EA	Bw	EP	P2	P1			
		SF	0.5	0.5	1	1.75	1.75			
Transverse	Pa	LS	EA1	EA2	RA1	RA2	P2	P1		
		SF	0.5	0.5	0.5	0.5	1	1		
	CG	LS	EA1	EA2	RA1	RA2	P2	P1		
		SF	0.5	0.5	0.5	0.5	1.25	1.25		

Bridge - CsC15T2F

Longitudinal	Pa	LS	EA	EP	Bw	P2	UA						
		SF	0.5	0.5	0.75	0.75	1.5						
	CG	LS	EA	EP	Bw	P2							
		SF	0.5	0.5	0.75	0.75							
Transverse	Pa	LS	EA1	EA2	RA1	RA2	Fb	EP	UA1	UA2	RP	UP2	UP1
		SF	0.5	0.5	0.75	0.75	0.75	1.25	1.25	1.25	1.5	1.75	1.75
	CG	LS	EA1	EA2	RA1	RA2	Fb	EP	UA2	UA1			
		SF	0.5	0.5	0.75	0.75	0.75	1.25	1.25	1.75			

Bridge - CsC40T2F

Longitudinal	Pa	LS	EA	Bw	EP	UA	P2	P1					
		SF	0.5	0.5	0.75	1	1.25	1.25					
	CG	LS	EA	Bw	EP	UA	P2	P1					
		SF	0.5	0.5	0.75	1.5	1.75	1.75					
Transverse	Pa	LS	EA1	EA2	RA1	RA2	P2	P1	UA1	UA2			
		SF	0.5	0.5	0.5	0.5	0.75	0.75	1	1.00			
	CG	LS	EA1	EA2	RA1	RA2	P2	P1	UA1	UA2			
		SF	0.5	0.5	0.5	0.5	1.25	1.25	1.75	1.75			

Bridge - CsC15T2S

Longitudinal	Pa	LS	EA	EP	Bw	P2	UA						
		SF	0.5	0.5	0.75	0.75	1.5						
	CG	LS	EA	EP	Bw	P2							
		SF	0.5	0.5	0.75	0.75							
Transverse	Pa	LS	EA1	EA2	RA1	RA2	EP	Fb	UA1	UA2	RP	UP2	UP1
		SF	0.5	0.5	0.75	0.75	1.25	1.25	1.25	1.25	1.5	1.75	1.75
	CG	LS	EA1	EA2	RA1	RA2	EP	Fb	UA2	UA1			
		SF	0.5	0.5	0.75	0.75	1.25	1.25	1.75	1.75			

Bridge - CsC40T2S

Longitudinal	Pa	LS	EA	Bw	EP	UA	P2	P1					
		SF	0.5	0.5	0.75	1	1.25	1.25					
	CG	LS	EA	Bw	EP	UA	P2	P1					
		SF	0.5	0.5	0.75	1	1.75	1.75					
Transverse	Pa	LS	EA1	EA2	RA1	RA2	P2	P1	UA1	UA2			
		SF	0.5	0.5	0.5	0.5	0.75	0.75	1	1.00			
	CG	LS	EA1	EA2	RA1	RA2	P2	P1	UA1	UA2			
		SF	0.5	0.5	0.5	0.5	1.25	1.25	1.75	1.75			

Table C.27 Detailed Sequence of damage for CsW bridges

Bridge - CsW15T1F

Longitudinal	Pa	LS	P2	EA	EP	Bw	P1						
		SF	0.50	0.75	0.75	0.75	1.00						
	CG	LS	P2	EA	EP	Bw	P1						
		SF	0.5	0.75	0.75	0.75	1.75						
Transverse	Pa	LS	RA1	RA2	EA1	EA2	EP	Fb	RP	UP1			
		SF	0.5	0.5	0.75	0.75	0.75	0.75	1.5	1.75			
	CG	LS	RA1	RA2	EA1	EA2	EP	Fb	RP				
		SF	0.5	0.5	0.75	0.75	0.75	0.75	1.75				

Bridge - CsW40T1F

Longitudinal	Pa	LS	EA	Bw	P2	P1	EP	Fb					
		SF	0.50	0.50	0.75	0.75	1.50	1.75					
	CG	LS	EA	Bw	P2	P1							
		SF	0.5	0.5	1	1							
Transverse	Pa	LS	EA1	RA1	RA2	Fb	EA2	EP					
		SF	0.75	0.75	0.75	0.75	1	1					
	CG	LS	EA1	RA1	RA2	Fb	EA2	EP					
		SF	0.75	0.75	0.75	0.75	1	1					

Bridge - CsW15T1S

Longitudinal	Pa	LS	P2	EA	EP	Bw	P1						
		SF	0.5	0.75	0.75	0.75	1.5						
	CG	LS	P2	EA	EP	Bw	P1						
		SF	0.5	0.75	0.75	0.75	1.5						
Transverse	Pa	LS	EA1	EA2	RA1	RA2	Fb	EP	RP	UA1	UA2	UP1	UP2
		SF	0.75	0.75	0.75	0.75	0.75	1	1.5	1.75	1.75	1.75	1.75
	CG	LS	EA1	EA2	RA1	RA2	EP	Fb	RP				
		SF	0.75	0.75	0.75	0.75	1	1	1.75				

Bridge - CsW40T1S

Longitudinal	Pa	LS	EA	Bw	P2	P1	EP	Fb					
		SF	0.5	0.5	0.75	0.75	1.5	1.75					
	CG	LS	EA	Bw	P2	P1							
		SF	0.5	0.5	1	1							
Transverse	Pa	LS	EA1	EA2	RA1	RA2	Fb	EP	UA1	UA2	UP1	UP2	
		SF	0.75	0.75	0.75	0.75	1	1	1.75	1.75	1.75	1.75	
	CG	LS	EA1	EA2	RA1	RA2	Fb	EP					
		SF	0.75	0.75	0.75	0.75	1.25	1.25					

Bridge - CsW15T2F

Longitudinal	Pa	LS	EA	EP	P2	Bw	UA1	UA2					
		SF	0.5	0.5	0.5	0.75	1.5	1.5					
	CG	LS	EA	EP	P2	Bw							
		SF	0.5	0.5	0.5	0.75							
Transverse	Pa	LS	EA1	EA2	EP	RA1	RA2	Fb	RP	UA1	UA2	UP1	UP2
		SF	0.5	0.5	0.5	0.75	0.75	0.75	1.5	1.50	1.5	1.75	1.75
	CG	LS	EA1	EA2	EP	RA1	RA2	Fb	UA2	RP	UA1		
		SF	0.5	0.5	0.5	0.75	0.75	0.75	1.5	1.75	1.75		

Bridge - CsW40T2F

Longitudinal	Pa	LS	EA	Bw	P2	P1	UA1	UA2	EP	Fb			
		SF	0.5	0.5	0.75	0.75	1	1	1.25	1.75			
	CG	LS	EA	Bw	P2	P1	UA1	UA2					
		SF	0.5	0.5	1	1	1.75	1.75					
Transverse	Pa	LS	EA1	EA2	EP	RA1	RA2	Fb	RP	UA1	UA2	UP1	
		SF	0.5	0.5	0.5	0.75	0.75	0.75	1.5	1.50	1.5	1.75	
	CG	LS	EA1	EA2	EP	RA1	RA2	Fb	UA2	UA1			
		SF	0.5	0.5	0.5	0.75	0.75	1.25	1.5	1.75			

Bridge - CsW15T2S

Longitudinal	Pa	LS	EA	EP	P2	Bw	UA1	UA2					
		SF	0.5	0.5	0.5	0.75	1.5	1.5					
	CG	LS	EA	EP	P2	Bw							
		SF	0.5	0.5	0.5	0.75							
Transverse	Pa	LS	EA1	EA2	EP	RA1	RA2	Fb	RP	UA1	UA2	UP1	UP2
		SF	0.5	0.5	0.5	0.75	0.75	1	1.25	1.25	1.25	1.5	1.5
	CG	LS	EA1	EA2	EP	RA1	RA2	Fb	UA2	RP	UA1		
		SF	0.5	0.5	0.5	0.75	0.75	1.25	1.5	1.75	1.75		

Bridge - CsW40T2S

Longitudinal	Pa	LS	EA	Bw	P2	P1	UA1	UA2	EP	Fb			
		SF	0.5	0.5	0.75	0.75	1	1	1.25	1.75			
	CG	LS	EA	Bw	P2	P1	UA1	UA2					
		SF	0.5	0.5	1	1	1.75	1.75					
Transverse	Pa	LS	EA1	EA2	EP	RA1	RA2	Fb	RP	UA1	UA2	UP1	UP2
		SF	0.5	0.5	0.5	0.75	0.75	1	1	1.25	1.25	1.25	1.25
	CG	LS	EA1	EA2	EP	RA1	RA2	Fb	UA1	UA2	RP		
		SF	0.5	0.5	0.5	0.75	0.75	1.25	1.5	1.5	1.5		